Aim & Scope
The journal publishes original papers in the extensive field of Electrical-Electronics and Computer engineering. It accepts contributions which are fundamental for the development of electrical engineering, computer engineering and its applications, including overlaps to physics. Manuscripts on both theoretical and experimental work are welcome. Review articles and letters to the editors are also included.

Application areas include (but are not limited to): Electrical & Electronics Engineering, Computer Engineering, Software Engineering, Biomedical Engineering, Electrical Power Engineering, Control Engineering, Signal and Image Processing, Communications & Networking, Sensors, Actuators, Remote Sensing, Consumer Electronics, Fiber-Optics, Radar and Sonar Systems, Artificial Intelligence and its applications, Expert Systems, Medical Imaging, Biomedical Analysis and its applications, Computer Vision, Pattern Recognition, Robotics, Industrial Automation.

Balkan Journal of Electrical & Computer Engineering

BAJECE

An International Peer Reviewed, Indexed and Open Access Journal

CONTENTS

The Effect of Increases in User Weight and Road Slope on Energy Consumption in Disabled Vehicle Driven with PMSM

F. A. KAZAN* and R. AKKAYA

Abstract—**In this study, the effect of increases in user weight and road slope on energy consumption (Wh/km) value of a disabled vehicle driven with permanent magnet synchronous motor (PMSM) was investigated. In order to digitize this effect, a test system consisting of a data reading card and an interface program prepared in Visual C # was developed. In this way, information about the disabled vehicle and the road was collected instantly during the test process and visualized in the interface. Then experimental studies were carried out on two roads with different slopes with users of different weights. Finally, by using the obtained results, the effect of increases in road slope and user weight on the energy consumption of the vehicle was demonstrated by numerical data. By using these results, the numerical simulations of battery-operated disabled vehicles can be calibrated and much more realistic simulation results can be obtained in future studies.**

I. INTRODUCTION

ENERGY CONSUMPTION (Wh/km) values of disabled vehicles are very important issues for people who use these vehicles. Because disabled vehicle users want to go as far as possible on a single charge. To achieve this, either a larger capacity battery or a more efficient motor must be used in the vehicle. These are additional costs. However, choosing a motor taking into account the environment where the vehicle will be used, and user weight are solutions that are simple and do not incur any additional costs. In order to implement these simple solutions, it is necessary to know the effect of the

FATİH ALPASLAN KAZAN, is with Department of Aviation Electrical and Electronic of Selçuk University, Konya, Turkey, (e-mail: akazan@selcuk.edu.tr).

https://orcid.org/0000-0002-5461-0117
*Corresponding Author.

RAMAZAN AKKAYA, is with Department of Electrical and Electronic Engineering of Konya Technical University, Konya, Turkey, (e-mail: rakkaya@ktun.edu.tr).

https://orcid.org/0000-0002-6314-1500

increase in road slope and user weight on the energy consumption of the disabled vehicle.

The powers of the motors to be mounted on electric vehicles are determined by taking into account the climbing angle of the vehicle and some forces affecting the vehicle. These forces that oppose the movement of the vehicle; aerodynamic (air) resistance, rolling resistance, acceleration resistance and uphill resistance.

Similar points need to be taken into account when determining the power of the motor to be fitted on battery-operated wheelchairs. In [1], the power of a motor designed to carry 120 kg load on the battery-operated wheelchair was calculated by considering the above-mentioned forces. As a result of the calculations, it has been found that the motor to be mounted to the disabled vehicle should produce 16.25 Nm, 10 Nm and 3.75 Nm of torque on + 20°, 0° and -20° roads, respectively. This means that every 1° change in road slope causes a change by 3.125% in torque. The literature was searched to find similar studies examining the change of the vehicle's parameters in relation to the road slope in the battery-operated disabled vehicles.

In [2], the effect of road slope on the energy drawn from the battery in electric cars is theoretically investigated. In the investigation, it is foreseen that the total electricity consumption of the vehicle will increase by 13.58% on 1° road slope. However, since the simulated vehicle is a car, the reflection of the change in user weight on this value has not taken into consideration.

In the literature searches made for this purpose, studies in which different solutions are produced for those who do not have hands or arms attract attention. For example, controlling of the disabled vehicle with mouth movement [3], sound [4-7], eyes [8-11], and head movements [12-16] are some of them. Using fuzzy logic controller instead of traditional controller [17, 18], examining the human factor [19], examining the vibration of the vehicle under different road conditions [20], measuring the mechanical and electrical impedances of the vehicle with sensors [21], using efficient motors to increase the vehicle's range [22, 23], detection of road slope with sensor [24] or without sensor [25] are some of the other studies in this area.

In this study, the effect of road slope and user weight on energy consumption in a disabled vehicle driven with permanent magnet synchronous motor (PMSM) was obtained

by conducting experimental studies. For this purpose, the test system, which was previously designed by the authors [26] to test disabled vehicles driven by permanent magnet direct motor in the laboratory, has been developed to allow disabled vehicles driven with PMSM to be tested in real environments conditions. Then experimental studies were carried out on different sloped roads with users of different weights. Using the obtained data, the effect of the increases in road slope and user weight on energy consumption has been revealed with numerical data.

II. DESIGNED TEST SYSTEM AND COMPONENTS

In the designed test system, battery current, inverter current, motor current, battery and inverter voltages, ambient and motor surface temperatures, road slope and vehicle speed are measured every second and sent to the computer. The data sent to the computer are both monitored and recorded at an interface prepared in C #. The block diagram of the designed test system is given in Fig. 1. The components of the system are also detailed below.
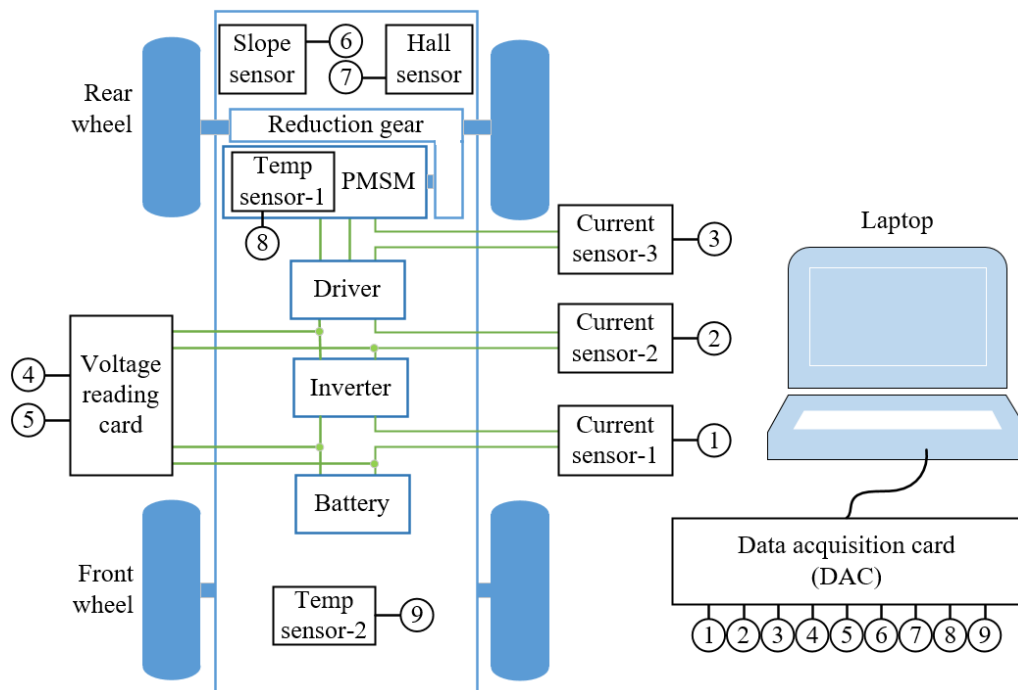
Fig. 1. The block diagram of the designed test system.

A. Measurement of Vehicle Speed

In order to obtain the energy consumption values of the disabled vehicle, the distance travelled by the vehicle must be known. This information can be obtained by performing experimental studies on a route whose distance is known, or the distance travelled on any route can be obtained by measuring the vehicle speed. Speed measurement can be achieved by fixing the encoder directly or indirectly to the wheel shaft. However, this will require additional changes to the wheel shaft. In this study, it was preferred to measure by using the Hall sensor and magnets instead of speed measurement by making any changes in the physical structure of the vehicle. For this purpose, the A1101 series Hall sensor manufactured by the company named Allegro was used.

To minimize the error in speed measurement as much as possible, it is necessary to place the magnets on the wheel as often as possible. To minimize the error in speed measurement as much as possible, it is necessary to place the magnets on the wheel as often as possible. However, if the distance between the magnets goes below a certain value, the sensor gives an erroneous output. In the tests performed to determine the most suitable magnet number, the number has determined to be 24. For this reason, 24 magnets have placed on the rim of the right

rear wheel. The sensor has placed closest to the wheel so that the distance between them is less than 1 cm when the sensor is aligned with the magnet. The placed sensor and magnets are shown in Fig. 2.
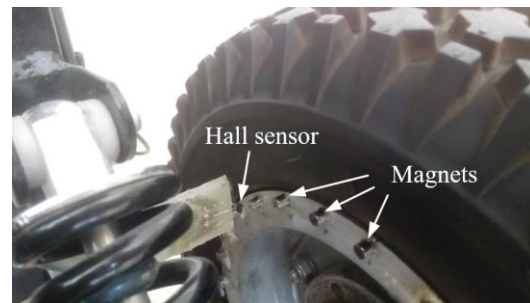
Fig. 2. Physical location of the Hall sensor and magnets.

B. Current Measurement

ACS712 series current sensors, which can be procured as a module for current measurement, have been chosen. It is sufficient to connect the outputs of the sensors to the analogue inputs of the microcontroller to be used for measurement.

C. Voltage Measurement

In order to both minimize the effect of temperature and provide insulation, LV25P type voltage sensor produced by the company named LEM has used for voltage measurement. LV25P, which can measure AC and DC voltage and needs symmetrical supply, produces an output current that varies according to the magnitude of the voltage at its input. The voltage at the ends of the resistor connected to the low voltage side of this sensor can be easily measured by connecting it to any analogue input of the microcontroller to be used. The voltage reading card, which designed and realized for measuring the voltages of the battery and inverter, is given in Fig. 3.

(a)

(b)
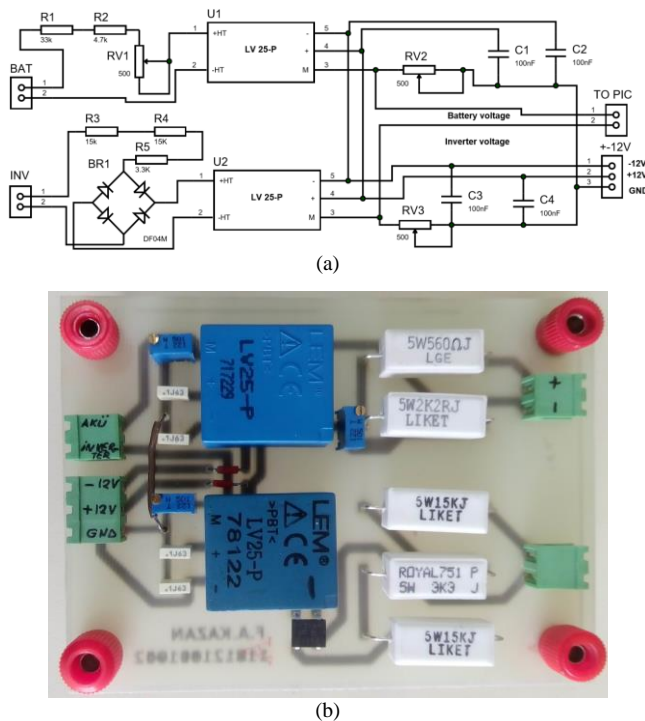
Fig. 3. Circuit board designed to measure the voltages (a) The open-circuit diagram (b) Final form of the board.

D. Measurement of Road Slope

SCA61T-FAHH1G inclination sensor, which can measure the slope within ± 30° limits and with a precision of 0.0025°, was used in order to detect the slope of the road where disabled vehicles are used. This sensor, which can give analogue output, produces an oscillating output when used on a vibrating surface or when exposed to accelerated motion.

E. Data Acquisition Card

A data acquisition card was designed to ensure that both the data is displayed on the LCD screen and transferred to the computer via USB in real-time after reading the voltages, currents, temperatures, road slope and vehicle speed. PIC18F4550 was preferred as the microcontroller on the board and was operated at 48 MHz by using PLL (Phase Locked Loop) feature. The data acquisition card are given in Fig. 4.

(a)

(b)
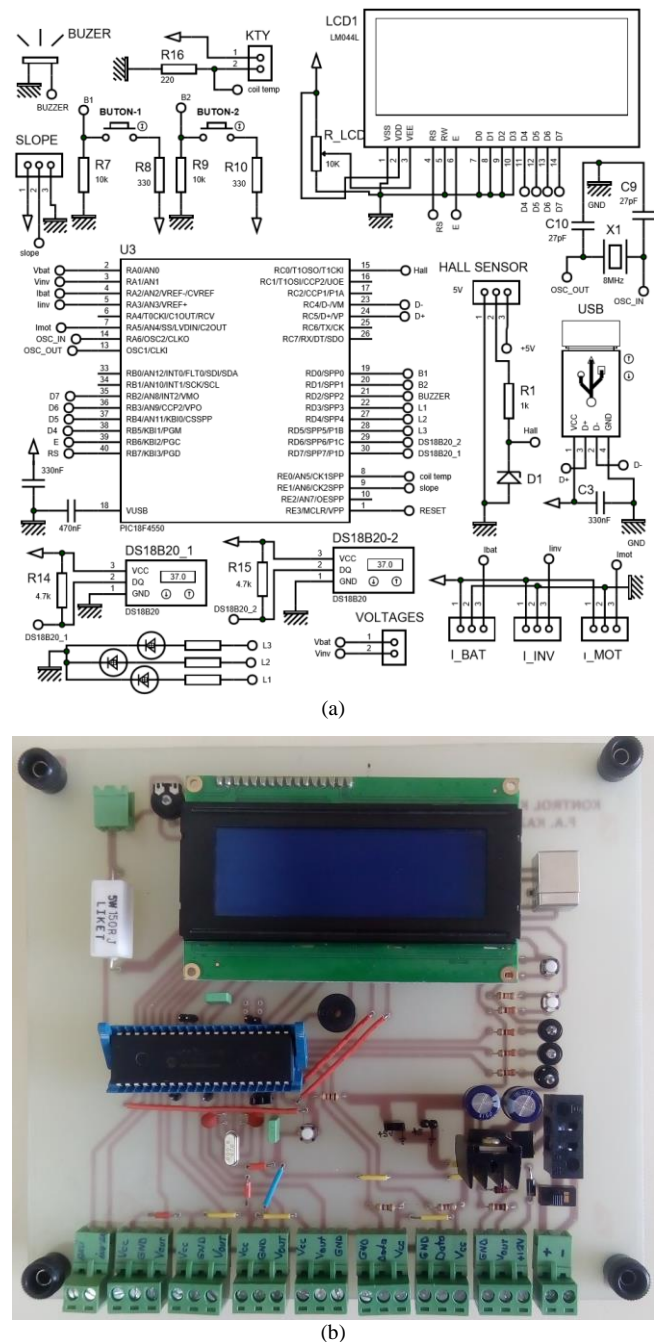
Fig. 4. The data acquisition card (a) The open-circuit diagram (b) Final form of the board.

F. Data Reading Interface Program

An interface was designed in the Visual C# program to receive the data to be sent by the data acquisition card, to display and store it on the computer, and to graph some required data simultaneously. The interface was designed according to electric mobility scooter models which have different wheel diameters and different reducer ratios and driven by PMSM. The screenshot taken at the moment of the simulation of the data acquisition card from the designed data reading interface program is given in Fig. 5.

Fig. 5. Designed interface program.

The designed interface consists of 4 main sections: parameters section to be entered, measured and calculated values section, table section and graphic section.

In the parameters section to be entered, the battery voltage warning level can be determined in order to protect the batteries from deep discharge during the test or to examine the process until the battery voltage decreases to a certain value. When the battery voltage drops to the entered value, the user is warned with an audible warning. In order to prevent the motor from overheating or to examine the process until it reaches a certain value, the maximum allowable motor temperature section has also been added. In addition, in order to examine the effect of user weight on the measured parameters of the vehicle, it has also possible to enter the weight information of the person sitting in the vehicle seat during the test.

The instantaneous values of the measured and calculated total 13 quantities are displayed in the measured and calculated values section. The quantities are also recorded in the table section. A data number is assigned to each data set during recording. Thus, it is possible to examine the data both during and after the test. Moreover, the time, which elapsed from the moment the first data is received until the moment the last data is received, can be computed precisely. Thus, it is also possible to calculate the energy consumption value per km of the vehicle. All the data saved in the table section can be exported to Excel at any time.

10 of the measured and calculated quantities have grouped among themselves and collected in 6 graphs. The graphics, which are updated automatically after each incoming data, show how the change of the relevant quantity from the beginning of the test. In these graphs, the data are on the y-axis whereas the data numbers are on the x-axis. Since the data is updated every second, the data number also represents the total time in seconds since the start of the test.

9 out of 13 quantities (currents, voltages, temperatures, road slope and the number of pulses per second) in the measured and calculated values section are directly measurable quantities. The other 4 quantities (power drawn from the battery, motor speed, speed of the vehicle and the total road taken by the vehicle) are the quantities that should be calculated using the measured values.

The power drawn from the battery (P_{bat}), which is one of the calculated quantities, is calculated as in Eq. (1). V_{bat} and I_{bat} in Eq. (1) represent battery voltage and current drawn from the battery, respectively.

$$P_{bat} = V_{bat} \cdot I_{bat} \tag{1}$$

In order to calculate the other three quantities, the revolution per second of the wheel (N_w) must first be calculated using Eq. (2). In Eq. (2), p_t refers to the total number of pulses produced by the Hall sensor in one second while m_n indicates the total number of magnets mounted on the rear wheel.

$$N_w = p_t / m_n \tag{2}$$

In order to find the travelled total distance (x_t) by the vehicle, the distance (x_s) that was taken in one second must firstly be calculated. According to this, the distance travelled by the vehicle in meters in one second is calculated as in (3). C_w in (3) refers to the circumference of the rear wheel in cm.

$$x_s = (N_w \cdot C_w) / 100 \tag{3}$$

The total covered distance that is updated every second is calculated as in (4). ($x_{(t-1)}$) in (4) indicates the previous total covered distance value.

$$x_t = x_{(t-1)} + x_s \tag{4}$$

The instantaneous speed of the disabled vehicle in km/h is:

$$v = x_s \cdot 3.6 \qquad (5)$$

When considering the reducer ratio (p_g), the motor's revolutions per minute (N_m) is:

$$N_m = 60 \cdot N_w \cdot p_g \qquad (6)$$

III. EXPERIMENTAL STUDIES

In the experimental studies, the disabled vehicle, which is seen in Fig. 6 and previously introduced in [23] by the authors, was used. The vehicle was driven using the PMSM manufactured by Lenze with the code MCS06I41L.
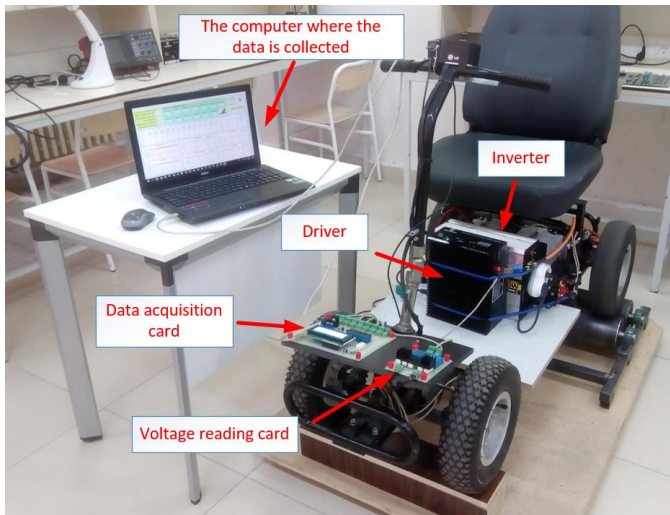
Fig. 6. Disabled vehicle and other components used in the experimental study.

Experimental studies were done in Alaeddin Keykubat Campus of Selçuk University. During the experiments, the motor was operated at 1000 rpm. Batteries were fully charged before each test to obtain more accurate comparison results. Experimental studies were carried out primarily without users, then with users of 35 kg, 50 kg, 70 kg and 95 kg respectively.

In order to examine the effect of the user's weight and the road slope, Route-1 in Fig. 7, where the slope is very close to zero and constant, was chosen. The average value of the slope on this route of 187 m is 0.21°. The slope sensor, which gives an analogue output, produces oscillating results due to the vibration and acceleration of the vehicle. To prevent the slope sensor from producing oscillating results due to the vibrating and accelerating movement of the vehicle, the vehicle was moved before point A, was stopped after passing point B.

Fig. 7. Route-1.

The changes in the road slope of the Route-1 and in the power drawn from the battery along this route are given in Fig. 8.
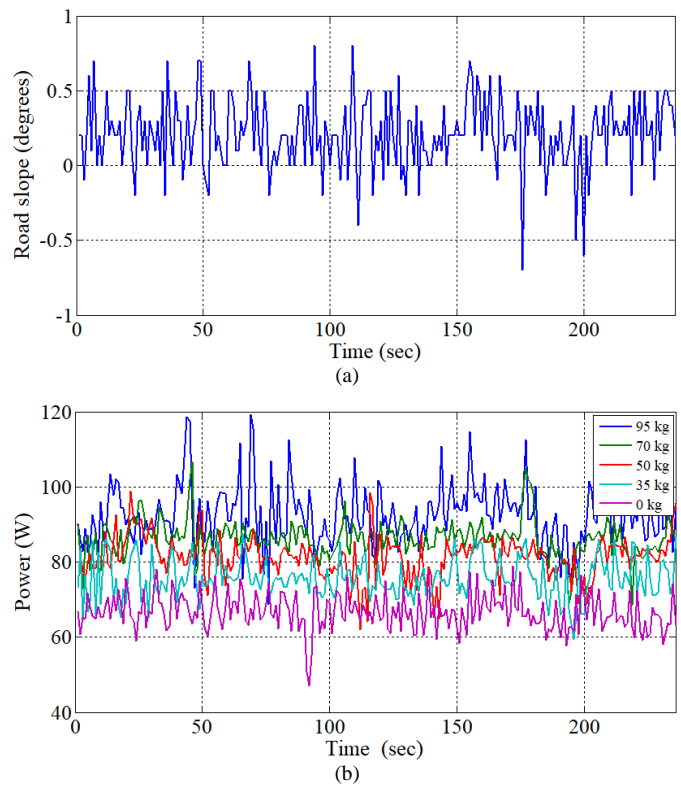
Fig. 8. Graphs of tests performed with users of different weights on Route-1. (a) The road slope, (b) Power drawn from the battery.

When the power graphs in Fig. 8.(b) are examined, it is clearly seen that the power values drawn from the battery increase in parallel with the increasing user weight. The average value of the instantaneous power drawn from the battery in the test conducted along this route without a user is 66.68 W. The average values of instantaneous power drawn from the battery at user weights of 35 kg, 50 kg, 70 kg and 95 kg are also 75.72 W, 81.34 W, 86.21 W and 92.53 W, respectively. This relationship between user weight and average instantaneous power can also be seen in the graph in Fig. 9.

Fig. 9. Change of the average instantaneous power drawn from the battery according to the user weight in the tests performed in Route-1.

The total distance (x_t), user weight (m), total energy drawn from the battery (W) and the energy that the vehicle must draw from the battery (W/x_t) to travel 1 km are summarized in Table 1. The percentage increases in W/x_t and W/x_t values per kilogram obtained from the calculations based on the $m = 0$ kg state are also given in Table 1 as $\Delta (W/x_t)$ and $\Delta(W/x_t)/\Delta m$, respectively.

TABLE I
ENERGY CONSUMPTION DATA OBTAINED FROM THE TEST
PERFORMED IN ROUTE-1 (0.21°).

m (kg)	x_t (km)	W (Wh)	W/x_t (Wh/km)	$\Delta(W/x_t)$ (%)	$\Delta(W/x_t)/\Delta m$ (%)
0	0.187	4.45	23.80	0.00	0.00
35	0.187	5.05	27.01	13.49	0.39
50	0.187	5.33	28.50	19.75	0.39
70	0.187	5.75	30.75	29.20	0.42
95	0.187	6.17	32.99	38.61	0.41

Undoubtedly, the increase in road slope will also have an effect on these rates. In order to see the effect of the road slope on these rates, this time the tests were performed on the 246 m long Route-2 seen in Fig. 10. The average road slope of Route-2 is 1.44°. The tests were carried out from point A to point B.

Fig. 10. Route-2.

The changes in the road slope of the Route-2 and in the power drawn from the battery along this route are given in Fig. 11.
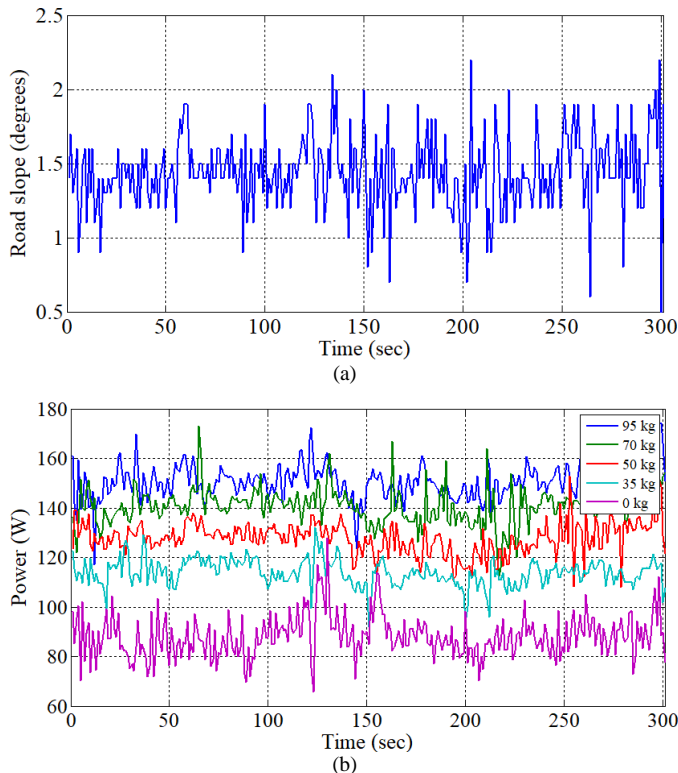
Fig. 11. Graphs of tests performed with users of different weights on Route-2. (a) The road slope, (b) Power drawn from the battery.

The average value of the instantaneous power drawn from the battery in the test conducted on Route-2 without a user is 88.3 W. The average values of instantaneous power drawn from the battery at user weights of 35 kg, 50 kg, 70 kg and 95 kg are also 113.83 W, 127.70 W, 140.75 W and 150.97 W, respectively. This relationship between user weight and average instantaneous power can also be seen in the graph in Fig. 12.
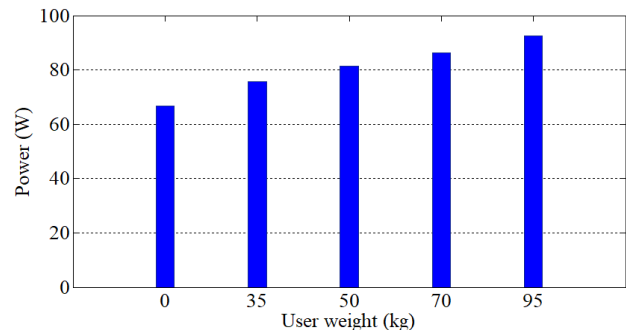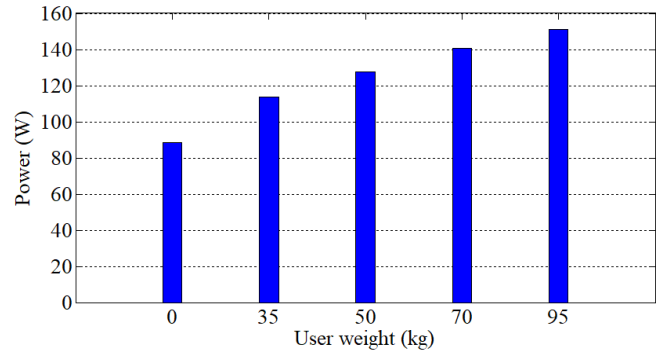

Fig. 12. Change of the average instantaneous power drawn from the battery according to the user weight in the tests performed in Route-2.

Energy consumption data of the tests performed in Route-2 are summarized in Table-2. The percentage increases in values, in which Wh/km and Wh/km per kilogram compared to test without users, are also given in Table 2.

TABLE II
ENERGY CONSUMPTION DATA OBTAINED FROM THE TEST
PERFORMED IN ROUTE-2 (1.44°).

m (kg)	x_t (km)	W (Wh)	W/x_t (Wh/km)	$\Delta(W/x_t)$ (%)	$\Delta(W/x_t)/\Delta m$ (%)
0	0.246	7.37	29.96	0.00	0.00
35	0.246	9.52	38.70	29.17	0.83
50	0.246	10.68	43.41	44.89	0.90
70	0.246	11.77	47.85	59.71	0.85
95	0.246	12.84	52.18	74.17	0.78

IV.   CONCLUSION AND DISCUSSION

In this study, the effects of both road slope and user weight on the vehicle's energy consumption value in the disabled vehicle driven with PMSM were examined together. In this context, firstly, on the Route-1 with an average slope of 0.21°, tests were carried out both with no load and with user weights of 35 kg, 50 kg, 70 kg and 95 kg. In these tests on the Route-1, it was observed that every 1 kg increase in user weight caused an average increase of 0.40 % in the amount of energy drawn from the battery per km.

Then the same tests were repeated on the Route-2 with a slope of 1.44°. In the test carried out on the Route-2, it was observed that every 1 kg increase in user weight caused an average increase of 0.84% in the amount of energy drawn from the battery per km. When considering that this value is 0.40% on the road slope of 0.21°, it is seen that the increase in the road slope of 1.23° causes a 110 % increase in the energy consumption value per kg.

By using these results, the numerical simulations of battery-operated disabled vehicles can be calibrated and much more realistic simulation results can be obtained in future studies.

REFERENCES

[1] A. Akpunar, "Ergonomik Bir Elektrikli Tekerlekli Sandalye İçin Dişlisiz Ve Direkt Sürmeli Bir Elektrik Motor Tasarımı" Yüksek Lisans, Fen Bilimleri Enstitüsü, Muğla Üniversitesi, Muğla, 2007.

[2] S. Yang, M. Li, Y. Lin, and T. Tang, "Electric vehicle's electricity consumption on a road with different slope," Physica A: Statistical Mechanics and its Applications, vol. 402, pp. 41-48, 2014.

[3] J. Ju, Y. Shin, and E. Kim, "Intelligent wheelchair using head tilt and mouth shape," IET Electronics letters, vol. 45, no. 17, pp. 873-875, 2009.

[4] P. Ghule, M. Bhalerao, R. Chile, and V. G. Asutkar, "Wheelchair control using speech recognition," in 9th International Conference on Contemporary Computing (IC3), 2016: IEEE, pp. 1-6.

[5] R. Chauhan, Y. Jain, H. Agarwal, and A. Patil, "Study of implementation of Voice Controlled Wheelchair," in 3rd International Advanced Computing and Communication Systems (ICACCS), 2016, vol. 1: IEEE, pp. 1-4.

[6] D. Wang and H. Yu, "Development of the control system of a voice-operated wheelchair with multi-posture characteristics," in Intelligent Robot Systems (ACIRS), 2017 2nd Asia-Pacific Conference on, 2017: IEEE, pp. 151-155.

[7] M. F. Ruzaij, S. Neubert, N. Stoll, and K. Thurow, "Design and testing of low cost three-modes of operation voice controller for wheelchairs and rehabilitation robotics," in 2015 IEEE 9th International Symposium on Intelligent Signal Processing Proceedings, 2015: IEEE, pp. 1-6.

[8] P. S. Gajwani and S. A. Chhabria, "Eye motion tracking for wheelchair control," International Journal of Information Technology, vol. 2, no. 2, pp. 185-187, 2010.

[9] M. Jain, S. Puri, and S. Unishree, "Eyeball motion controlled wheelchair using IR sensors," World Acad. Sci. Eng. Technol. Int. J. Comput. Electr. Autom. Control Inf. Eng, vol. 9, no. 4, pp. 906-909, 2015.

[10] J. Sharma, M. Anbarasu, C. Chakraborty, and M. Shanmugasundaram, "Iris movement based wheel chair control using raspberry Pi—A state of art," in Power and Advanced Computing Technologies (i-PACT), 2017: IEEE, pp. 1-5.

[11] K. Arai and R. Mardiyanto, "Eyes based eletric wheel chair control system," International Journal of Advanced Computer Science and Applications (IJACSA), vol. 2, no. 12, 2011.

[12] G. Marins, D. Carvalho, A. Marcato, and I. Junior, "Development of a control system for electric wheelchairs based on head movements," in Intelligent Systems Conference (IntelliSys), 2017, 2017: IEEE, pp. 996-1001.

[13] Ö. Deniz, A. A. Süzen, and A. Çetin, "Kafa Hareketleri İle Kontrol Edilebilen Tekerlekli Sandalye," in 4. Ulusal Meslek Yüksekokulları Sosyal Ve Teknik Bilimler Kongresi Burdur, Türkiye, 11-13 Mayıs 2017 2017.

[14] D. Kupetz, S. Wentzell, and B. BuSha, "Head motion controlled power wheelchair," in Proceedings of the 2010 IEEE 36th Annual Northeast Bioengineering Conference (NEBEC), 2010: IEEE, pp. 1-2.

[15] J. M. Ford and S. J. Sheredos, "Ultrasonic head controller for powered wheelchairs," Journal of Rehabilitation Research and Development, vol. 32, no. 3, pp. 280-284, 1995.

[16] F. A. Kondori, S. Yousefi, L. Liu, and H. Li, "Head operated electric wheelchair," in 2014 Southwest Symposium on Image Analysis and Interpretation, 2014: IEEE, pp. 53-56.

[17] V. Sankardoss and P. Geethanjali, "Design and low-cost implementation of an electric wheelchair control," IETE Journal of Research, pp. 1-10, 2019.

[18] N. Tanohata, H. Murakami, and H. Seki, "Battery friendly driving control of electric power-assisted wheelchair based on fuzzy algorithm," in Proceedings of SICE Annual Conference 2010, 2010: IEEE, pp. 1595-1598.

[19] N. Hashimoto, K. Tomita, A. Boyali, Y. Takinami, and O. Matsumoto, "Experimental study of the human factors when riding an automated wheelchair: supervision and acceptability of the automated system," IET Intelligent Transport Systems, vol. 12, no. 3, pp. 236-241, 2018.

[20] T. Wang, J. i. Kaneko, and K. Kojima, "Study on relevance between electric wheelchair riding comfort and user exposure to whole-body vibration," in Consumer Electronics (GCCE), 2017 IEEE 6th Global Conference on, 2017: IEEE, pp. 1-2.

[21] H. M. Hondori, P. Q. Trung, and L. Shih-Fu, "Simultaneous sensing and actuating for path condition monitoring of a power wheel chair," in Robotics and Mechatronics (ICRoM), 2013 First RSI/ISM International Conference on, 2013: IEEE, pp. 343-346.

[22] Y.-K. Kim, Y.-H. Cho, N.-C. Park, S.-H. Kim, and H.-S. Mok, "In-Wheel motor drive system using 2-phase PMSM," in Power Electronics and Motion Control Conference, 2009. IPEMC'09. IEEE 6th International, 2009: IEEE, pp. 1875-1879.

[23] F. A. Kazan and R. Akkaya, "Use of PMSM in Electric Mobility Scooter Propulsion," in International Conference on Engineering Technologies (ICENTE'19), Konya, Turkey, October 25-27, 2019.

[24] M. F. Ruzaij, S. Neubert, N. Stoll, and K. Thurow, "A speed compensation algorithm for a head tilts controller used for wheelchairs and rehabilitation applications," in 2017 IEEE 15th International Symposium on Applied Machine Intelligence and Informatics (SAMI), 2017: IEEE, pp. 000497-000502.

[25] B. Li, J. Zhang, H. Du, and W. Li, "Two-layer structure based adaptive estimation for vehicle mass and road slope under longitudinal motion," Measurement, vol. 95, pp. 439-455, 2017.

[26] R. Akkaya and F. A. Kazan, "Design and implementation of a test setup for electric mobility scooter for the disabled," Measurement and Control, vol. 52, no. 9-10, pp. 1434-1444, 2019.

BIOGRAPHIES

FATIH ALPASLAN KAZAN was born in Amasya, Turkey, in 1977. In 2002, he graduated from Electrical Education Department of Gazi University and started to work as a lecturer at Selçuk University. He completed his master's degree in Selcuk University, Institute of Science, Electrical and Electronics Engineering in 2009. He received his PhD degree from the Department of Electrical and Electronics Engineering of Konya Technical University in 2019. He has been working as Asst. Prof. in the Department of Aviation Electrical and Electronic of Selçuk University since 2020. His main interests are Avionic Systems, Microcontroller Applications, Measurement Systems, Circuit Design, and Motor Control.

RAMAZAN AKKAYA was born in Aksaray, Turkey, in 1963. He received the B.S., M.S., and PhD degrees from Electrical Engineering of Yıldız Technical University, Istanbul, Turkey in 1986, 1988, and 1995, respectively. He worked as a Research Assistant between 1987 and 1995 and as an Assistant Professor between 1996 and 1998 at Yıldız Technical University Electrical Engineering Department. In 1998, he started to work at Selçuk University Electrical and Electronics Engineering Department. He became Associate Professor in 2010 and Professor in 2016 at the same university. He has been working as a Prof. Dr. in the Department of Electrical and Electronics Engineering at Konya Technical University since 2018. His main interests are Power Electronics and Applications, Control of Electric Drives, Electric Power Quality, and Renewable Energy Systems.

An Image Enhancement Method For Night-Way Images

BÜLENT TURAN

Abstract—Image processing has a wide range of applications especially in our daily lives. Image processing is not common in sensitive industrial applications. Because of these applications, very high percentage of success is requested. Also these applications work in real-time. However, it can be widely used in many daily routines (driving, entrance to the workplace/ exit, control of multimedia devices, security applications, identification applications, etc.). Especially Advanced Driver Assistance Systems (ADAS) is a popular working area for image processing. Strip tracking systems, pedestrian detection systems, reading of traffic signs and signals are based on image processing.

In this study, a new method has been developed to increase the visibility levels of road images at night driving. In these images, the brightness level is low because of insufficient of light sources (headlights and road lighting) which are often used to increase the driver's view. On the other hand, adversely affects the view of driver which the headlight of coming vehicles from opposite directions, poorly structured road lighting and etc. Especially the vehicle headlights coming from the opposite direction take the eye of the drivers and cause the level of view to decrease.

Intense dark areas and light sources are in the image together. By so, special to these images requires the use of an adaptive improvement method. This is because, when classical image enhancement methods are used, the visibility levels of the dark areas are increased, and the shining regions are more likely to shine and the visibility level decreases in these regions.

The developed method aims at enhancement these images that drivers be exposed to. For this purpose, the light sources in the image and the magnitudes of these light sources, the distance of the pixels to be calculated from the light sources, the value of the pixel itself and the neighboring pixels are used as separate parameters. Images are enhancement with the equations developed using these parameters. When the output images obtained with the use of the developed equations and the obtained Structural Similarity İndex Maps (SSIM) are examined, it is seen that the developed method gives good results.

Index Terms— ADAS, early warning, image enhancement, night road images, pedestrian detection.

BÜLENT TURAN, is with Department of Computer Engineering Tokat Gaziosmanpasa University, Tokat, Turkey,(e-mail: bulent.turan@gop.edu.tr).

https://orcid.org/ 0000-0003-0673-469X

I. INTRODUCTION

NIGHT DRIVING support systems for drivers are now a new study area for Advanced Driver Assistance Systems (ADAS). When night driving support systems in the literature are examined; The driver is intended to perceive factors such as pedestrian, animal, warning sign, or road condition which the driver cannot perceive (such as being dark, the headlights can only illuminate certain areas, other light sources in the field of view adversely affect the driver's view, etc.). It is seen that night driving support systems are considered as transferring the warning information obtained using sensors (infrared / thermal vision, radar, ultrasonic sensors, etc.) that can detect these factors. The data is transferred to the driver via audio/visual warning systems or screen. The need for different analyzes and syntheses on the image for different road conditions, will cause the use of many different sensors or image processing methods / classifiers / machine learning methods. For example, infrared / thermal cameras can be used to detect pedestrian / animals or other objects. Infrared / thermal image will not be affected by the visible light in the environment, it provides us with information on the identification of pedestrians, animals, and objects. However, it does not include some data that we can obtain in a visible light environment. In this case, the driver needs to look at the infrared image being transmitted to the road and to the screen at the same time in order to receive all the information. but its continuity is not possible. Therefore, the warning system developed should automatically alert the driver.

However, the warning system cannot differentiate for different situations. The support system to be developed will warn the driver in the same way for an adult, child, elderly, or animal at the side of the road considering the current technologies. This will lead the driver to question the effectiveness of the warning level of the support system.

Whereas, all of these data can be used to improve the quality of the driver's view. The driver can make his own decision without the need for another support system for the analysis and synthesis of the image. Thus, the data obtained can be used effectively. At this point, it would be more useful to provide the driver with night vision support instead of or in addition to night driving support to prevent traffic accidents. Night Vision Assistance Systems (NVAS), the driver to provides driving the vehicle by looking at the enhancement image. In this case, the driver will not look at the road. Instead the driver looking at the screen presented to him will use the vehicle. There are advantages to using a screen view instead of

a road view. At the same time, there are also disadvantages. Any problems that may occur on the screen may cause the sight to disappear completely. In addition, the change of the driver's point of view does not have an effect on the image, this is also may make it difficult to use.

With another approach, NVASs can also be used via transparent screen glasses which can be used as screens but do not obstruct normal view. Thus, even if the NVAS is switched off completely, the driver does not experience any loss of view. However, he can adjust the viewpoint and orientation as he wishes. The data obtained by the sensors and cameras are created on the glasses and added to the normal view. To use this method effectively, transparent screen technologies need to work decisively. In addition, these technologies need to be accessible in terms of cost. But it is clear that it will not be an appropriate method unless these conditions are met.

Drivers, in case of hesitation or low visibility, can be imaging an enhancement image via on a screen besides the your field of views, until the technology level is available for the aforementioned applications. This way, the driver can continue his journey by looking at the view support screen when the road view is too low or When the sight is completely absent. Or, when the field of view is limited, can follow the enhancement view of the dark areas by the occasionally view looking at the support screen.

Driver night vision support areas:

• Light sources that cause glare: Pupils are growing to collect better data in a structurally dark environment. However, if an intense light from any light source in the dark environment is directed towards the eye, the pupil becomes smaller and the perception becomes weaker because the light from other objects is less.

a- Front and rear headlights of traffic vehicles: Front headlights of vehicles which coming from the opposite direction (long-short). Divided roads bring down in a positively this glare, while traffic density increases in a negatively this glare.

b- Road lightings: Although road lighting is intended to provide driver view support, there are places where it may adversely affect view. Especially when over-lighting in urban road lighting.

c- Illuminated billboards: The billboards of the facilities / businesses, emitting a large amount of light unconsciously located at the side of the road adversely affect the driver's view.

d- Field lighting: Intense and incorrect lighting of roadside construction sites, factories, private properties and so on. adversely affects the view of the driver.

e- Sunlight: during the daytime driving the vehicle towards the sun (east-west) during certain hours, the quality of vision is very low due to the intense light.

• Areas outside the illumination area: There are areas within the driver's field of view that are not illuminated by the vehicle headlights. Providing opinion support in these areas will affect traffic safety positively. For example, a long headlight provides driver support by illuminating the area that

the short headlight cannot illuminate, but adversely affects the traffic safety, as to dazzle the opposite direction driver eye. For this reason, NVASs can be developed with image processing methods or infrared illumination for these regions without using visible light.

In the study, it was aimed to eliminate the decrease in the quality of vision caused by the light sources that caused the glare at night driving and to increase the quality of vision in areas outside the lighting area.

II.   PRIOR WORK

As the main subject of the study is to improve road images at night. Therefore, one of the objectives is to increase the visibility levels of pedestrians (all living beings) on the road. Because night-time driving is unsafe due to poor view of low contrast in the road image[1]. There are many studies in the literature about pedestrian detection [2,3,4,5,6]. In some of these studies fixed camera [2] and in the other studies car-camera [3,4,5,6] have been used. As a common feature, it was used IR images in all studies. In some of them near-IR (NIR) imager and far-IR (FIR) images [3], in others visible images and FIR images are used and compared. Especially when the aim is pedestrian detection, it is seen that FIR images came to the fore. Good results in areas where the visible light is very low in night road images and the fact that no IR light source is needed is a great advantage for the studies with FIR. However, if the FIR images which since there are visible off-band images are transferred to the driver as it is, it is difficult for the driver to drive the vehicle just by looking at these images. But, images can be processed and transferred to the driver via a separate screen with machine learning methods that detect pedestrians.

ADAS is an popular study area in recent years for researchers. Academic studies have been carried out to examine the close history of driver support systems [7] and to examine systems developed to strengthen night vision [8]. Some driver assistance systems to enhance night vision, that pedestrian (all vivid forms) images obtained from thermal cameras should be added onto the non-thermal camera image and suggest transferred to drivers [9]. In this way,, thermal and non-thermal camera images are added to each other and a driver support system is created and patented [10]. In these studies, the non-thermal camera images are enhancement and then the pedestrian images obtained with FIR cameras are added to the enhancement non-thermal camera image and support is provided to the driver by increasing the visibility of low visibility pedestrians images. One of the reasons for the decrease in visibility on night trips is the opposite headlights. Studies have been conducted to prevent the headlights from taking the eyes of the drivers coming from the opposite direction [11]. In some of these studies, the aim is not only to improve the image but also to support the driver in different areas (Lane monitoring and warning) [12,13]. In general, ADAS aims to warn the driver in many different areas (lane tracking and warning, distance tracking and warning, pedestrian detection, identification and warning of traffic information sign, detection and warning of traffic signals, and etc.) and to operate these systems on the same platform.

The topic discussed in the study is related to image enhancement. For this reason, during the preliminary study, image enhancement studies were examined. Especially complex images [14,15,16,17], foggy images [18,19] night images [20,21,22] / night road images [23,24,25], dimmed images with local bright areas [26,27], infrared images [28] were examined. There is no standard enhancement method (contrast enhancement, histogram equalization, sharpening, time / frequency domain filters and others) that can be applied to each image (dark, light, foggy, complex, and etc.) and can be given good results. Therefore, researchers are working on new / adaptive enhancement methods. However, better results can be obtained when specific methods are developed for specific images instead of adaptive enhancement methods for all images.

III. Material and Method

a.   b.

Fig.1. night road image a - original image b - light sources filtered image [31]

On night trips (usually these trips are intercity), we can find and filter the light sources which into the driver's pointview image. Thus, the filtered image can be transferred to the driver by means of augmented reality applications to provide feedback to the driver. However, it is clearly seen in Fig.1 and Video 1 (clickhere) that the glare caused by the source cannot be obstructed even if the light source is filtered (dimmed). Because the glare has already occured on the camera sensor during image capture. In order to prevent glare, the light from the light sources must never reach the camera sensor. For example, it is very difficult to enhancement of the image given in figure (see Fig.2c) and to perform this process using simple image processing methods. Light source at the image given in figure (see Fig.2d), can also be filtered by simple image processing methods. However, the source is filtered, although the glare caused by the source cannot be prevented. Using a larger filter or an adaptive filter when the location of the source is detected will complicate the process. And filtering on larger areas will reduce the field of view. Because in this case, the filter means that all data in the filtered region is lost.

Therefore, instead of improving the captured image interfering during the capture of the image can lead to a more efficient solution. Figures (see Fig.3a) and (see Fig.3b) images were captured in a similar manner to the image of figure (see Fig.2d) when the camera's flash was on and there was a light source in the environment. However, an object is placed in front of the source during image capture. As a result of this process, the resulting image appears to be of similar quality to that of figure (see Fig.2b) (no light source in the captured image). Figure (see Fig.3c) and (see Fig.3d) images were captured in a similar manner to the image of figure (see Fig.2c) when the camera's flash was off and there was a light source in the environment. However, an object was placed in front of the source during image capture. Even if obtained image is not in quality image in the figure (see Fig.2b) (no light source in the received image) as a result of this operation, It is clearly seen that it is much better quality than the image in figure (see Fig.2c).

.   b.   c.   d.
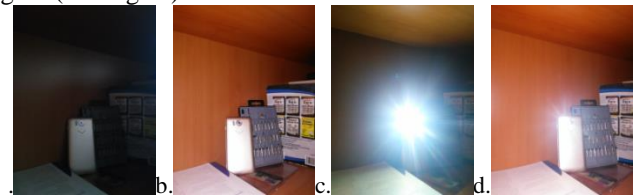
Fig. 2. Examples of images captured with the phone camera in the dark environment
a- The camera's flash is off, there is no light source in the image captured,
b- The camera's flash is on, there is no light source in the image captured,
c- The camera's flash is off, there is light source in the image captured,
d- The camera's flash is on, there is light source in the image captured,

a.   b.   c.   d.

Fig. 3. Examples of images captured with the phone camera in the dark environment when the front of the incoming light is covered with physical material
a-The camera flash is on, there is a blocking object in front of the source of light and there is light source in the image captured,
b- The camera flash is on, there is a blocking object in front of the source of light and there is light source in the image captured,
c- The camera flash is off, there is a blocking object in front of the source of light and there is light source in the image captured,
d- The camera flash is off, there is a blocking object in front of the source of light and there is light source in the image captured,

It is aimed to improve the night road images recorded in the study. Therefore, the effect of glare on the camera sensor during recording has already been recorded. Therefore, eliminate glare is not included in the study. Instead, it is the ultimate goal of the study to reduce glare in glare-forming images, and also to improve image quality in poorly damaged areas due to glare or insufficient light intensity.

a.
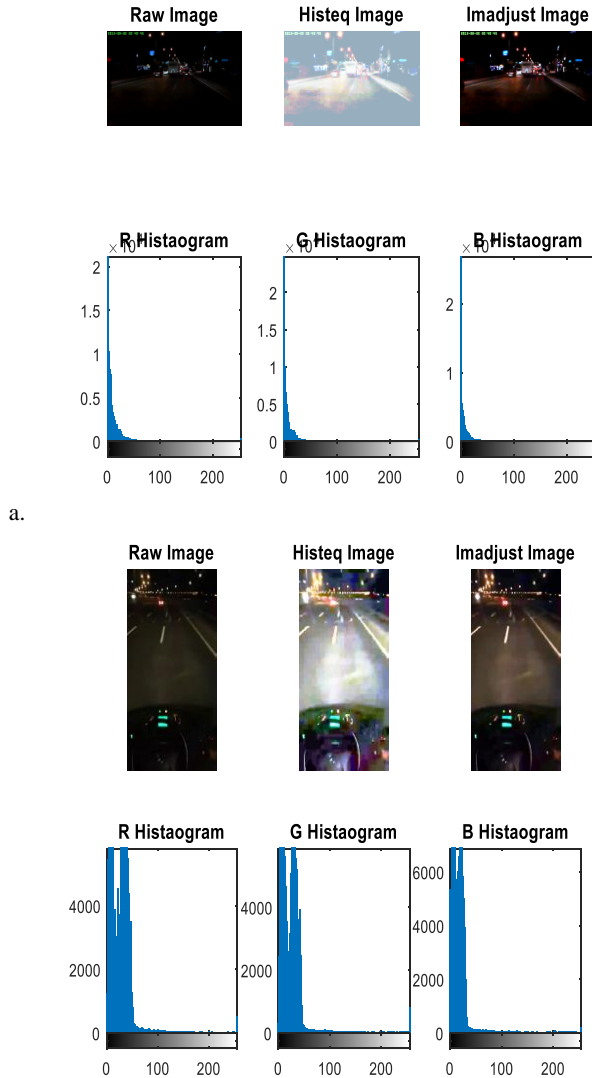
b.

Fig. 4. Night road image histograms [31,32]

When the histograms of the night road images given in figure (see Fig.4) are examined, it is generally seen that there is an agglomeration in the dark area. For such images, contrast stretching, histogram equalization, sharpening can usually be sufficient to improve the image. However, as can be seen in figure (see Fig.3), standard contrast stretching, histogram equalization, sharpening, and etc. image processing applications are not sufficient to improve such images. These images are usually dark, but also include light sources directed to the driver in different paths and time zones. Thus, the driver's view is negatively influenced by the lack of light sources that support his view, and by the presence of light sources that negatively affect his view. The focus of the study is the adaptive improvement of these images, which are constantly changing.

A. Recommended Method

In the study to enhancement images, when calculating the new value of pixel:

• The light sources size in the image,
• Of the pixels whose value is to be calculated, distance to the light source.
• Neighboring pixels value's
It is thought that it should be used as parameter of each. Thus, for each pixel, the new pixel value can be calculated in an adaptive manner. As a result, unnecessary glare and dark areas can be removed within the enhanced image.
To run the method, the color image is first converted to a binary image using a gray image followed by a threshold value of 0,9. In this image the center coordinates, boundaries and fields of light sources are calculated.
The edges, numbers, center coordinates, and area covered of the light sources in the image were found using the Matlan funtions (bwboundaries, bwlabel, regionprops). Matlab codes prepared are below.

```
for k = 1 : 1310
    image = read(vidObj,k);
    gray_image =rgb2gray(image);
    bwImage=(im2bw(gray_image,0.9)).*255;
    fill_Image = imfill(bwImage,'holes');
    Edges= bwboundaries(fill_Image);
    [Data Number]=bwlabel(fill_Image);
    Prop = regionprops (Data, 'Area',
'Centroid');
```

The developed equations are applied to pixels other than pixels with RGB intensity values> = 200. These pixels are assumed to be the source's pixels.
The image enhancement process is performed for each pixel. For this to be done

$r(i,j) = input\ image\ pixels\ values$

$s(i,j) = output\ image\ pixels\ values$

$K = Source\ of\ light$

$K_x = Distance\ to\ the\ light\ source\ nearest\ the\ pixel$
$\quad to\ be\ processed$ (The difference between the pixel coordinate and the light source center point was calculated)

$K_r = Radius\ of\ light\ source\ located\ nearest\ the\ pixel$
$\quad to\ be\ processed$

$pFour_R(i,j) = Calculate\ the\ matrix\ values$
$\quad containing\ the\ 4\ neighboring\ averages$
$\quad of\ the\ pixel\ to\ be\ processed$

As far as is observed, the glare in the night road images occurs around the light source. The glare is inversely proportional with the distance from the light source, and it is proportional the size of the light source. In accordance with this information, it is tried to develop an equation which uses the distance of the pixel from light sources, the size of these light sources as parameter and operates according to the intensity level of the pixels within the image.

$$s(i,j) = \left(1 \Big/ \left(1 + e^{-\left(\frac{Kx-2K_r}{20}\right)} \right) \right) r(i,j) \qquad (1)$$

In the equation (1), the distance of the pixel to the nearest light source and the radius of this source are used as parameters.

The equation produces results in the range 0-1. It is normalized with 1/20 due to its logarithmic properties. Has a sigmoid structure. Thus, it performs an effective classification in the range in which it is normalized. As K_x grows (as the distance from the source increases), the multiplier converges to 1. As K_x decreases, the multiplier converges to 0. Convergence to 0 does not cause problems because the pixels remaining within the light source limits are not processed during the process. Since it produces results in O-1 range, it decreases the glare of the glowing regions and ensures that other regions are not affected. Thus, the parameters used in the equation affect the pixel values as adaptive.

However, in the image processing, constant c coefficient is used when image enhancement is performed by using logarithmic and force transformation.

Logarithmic transformation

$$s(i,j) = c * \log(r(i,j) + 1) \tag{2}$$

Force transformation
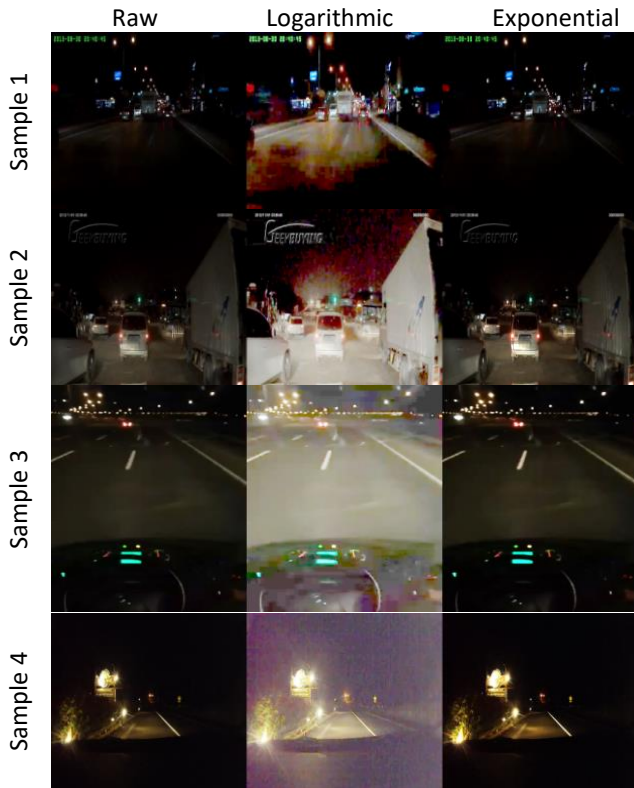
$$s(i,j) = c * r(i,j)^\gamma \tag{3}$$

Fig. 5. Example images processed with logarithmic and force transforms[31,32,33,34]

An adaptive coefficient of improvement in logarithmic and force transformations is not used. Logarithmic or exponential processing of pixel value, it results in a direct proportion to the pixel value. Logarithmic transformation in some images commonly used in the study, some of them give good results in the force conversion, while in some images both are poor. Sample image results processed by logarithmic and force transformation are given in figure (see Fig.5). Images processed by equation (1) are shown in figures (see Fig.7, Fig.8, and Fig.9).

The equation (1) that is used decreases only the brightness of the glowing regions as adaptive. However, another aim of the study is to increase the brightness levels of the regions with low visibility. For this, the equation needs to be developed. It is especially desirable to increase the brightness in areas where the image is dark. Thus, the visibility level of the regions with low visibility is increased, but the visibility levels of other regions will not be affected. It can use the pixels value to achieve of this effect. However, this study, 4 neighboring averages of the pixel were used in order to prevent the process to be negatively affected by noise. The 4 neighboring averages of the pixel was normalized with 1/255. And to the equation was added as $1 + e^{-pFour_R(i,j)/255}$ (4). The value of the added portion converges to 1.36 as the average grows. The average as it shrinks converges to 2. Thus, visibility of regions with low visibility is increased more than in other regions. Equation (4) is obtained by using neighboring pixel averages as parameters. Images processed by equation (4) are given in figures (see Fig.7, Fig.8, and Fig.9).

In such images, setting the value of pixels to increase the visibility level with only 4 neighboring pixel averages is a deficiency. Despite K_x and K_r are used to update the values of glare pixels, they was not used to update the values of pixels with low visibility. $2K_r$ was normalized with K_x and added to the equation as $1 + e^{-(\frac{2K_r}{K_x})}$ (5). In cases where the light source is small and the pixels are far from the source, the equation is converges to 2. In cases where the source is large and the pixel is close to the source, the equation converges to 1. Thus, the part added to the equation will contribute to a more effective increase of the visibility level of the pixels in regions with low visibility, similar to the 4 neighboring average. Instead of using a constant coefficient as in logarithmic and force transformations, when the equation is created in this way, it gets special adaptive properties for night road images. The final form of the equation is given below (5).

The equation was applied to different night road images recorded by the researcher and collected from the internet. Examples of the general night road images obtained were shown in figure (see Fig.7), Video 2 (clickhere) and Video 3 (clickhere). In addition, the developed equation was applied to the images containing the detail (human, animal, and etc.) in the regions with low visibility. The operation of the proposed method is given in figure (see Fig.6). The resulting images were shown in figure (see Fig.8 and Fig.9).

$$s(i,j) = \left(\left(1 + e^{-pFour_R(i,j)/255}\right) \Big/ \left(1 + e^{-(\frac{Kx-2K_r}{20})}\right) \right) r(i,j) \tag{4}$$

$$s(i,j) = \left((1 + e^{-pFour_R(i,j)/255})(1 + e^{-(\frac{2K_r}{K_x})}) \bigg/ \left(1 + e^{-(\frac{Kx - 2K_r}{20})}\right) \right) r(i,j) \qquad (5)$$

$$s(i,j) = \left((1 + e^{-pFour_R(i,j)/255})(1 + e^{-(\frac{2K_r}{K_x})}) \bigg/ \left(1 + e^{-(\frac{Kx - 2K_r}{20})}\right) \right) r(i,j)$$

Nearest light source (K)

K_r K_x

$$pFour_R(i,j) = r(i,j) * \begin{pmatrix} 0 & 0.25 & 0 \\ 0.25 & 0 & 0.25 \\ 0 & 0.25 & 0 \end{pmatrix}$$

4 neighboring pixels average
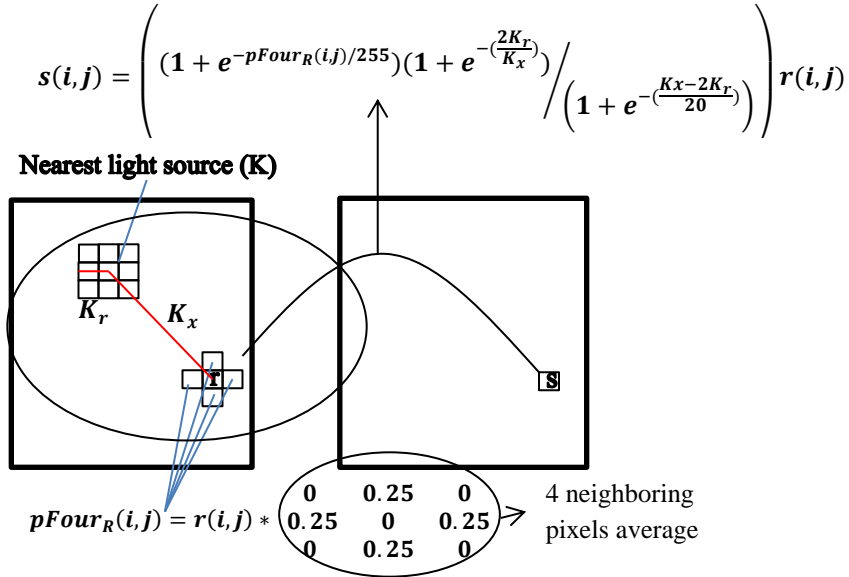
Fig. 6. Operation of the proposed method

IV. RESULTS
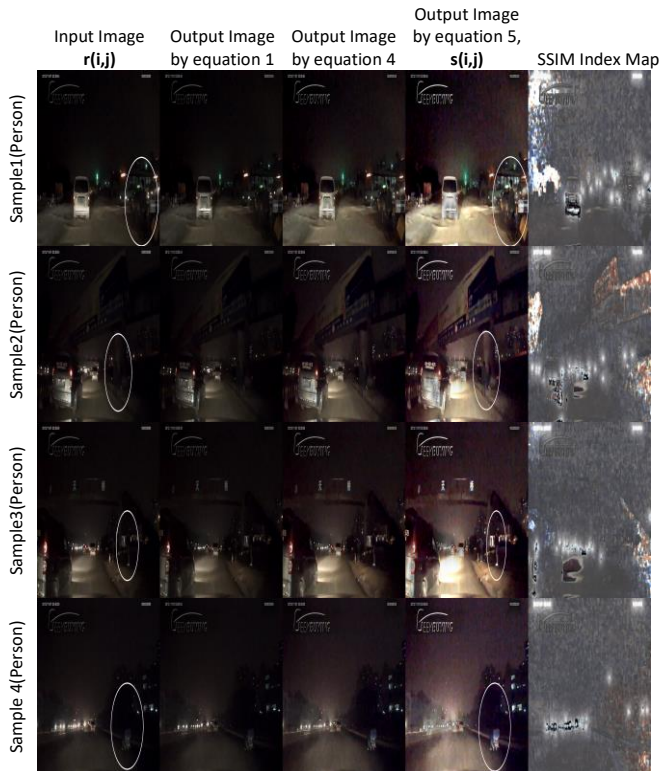
Fig. 7. Night Road Image Enhancement Study Sample Images (General Images) [31,32,33,34]

Figure (see Fig.7) and video 1 examined, of the developed method is seen that stable and good results on night road images. Image at the stage of improvement is processed separately for each pixel. It is considered that if necessary work is done, it can be used as image filter.

When examined in figure (see Fig.8 and Fig.9), it has been clearly observed that the level of visibility within the image of human/animal/object in areas of low visibility is increased.

In the study, it has been tried to develop an image enhancement method to increase the visibility level in the regions with low visibility on night road images. At the same time, this method should ensure reduces glare in the regions where glare occurs, or should ensure at least the glare does not increase.

As a result, the expectation in the output image is generally a decrease in the pixel brightness values of the regions around the light sources. In addition, it is aimed to increase the brightness value in dark regions where visibility is low. Especially in the output image, changes in the pixel values in the regions with these characteristics are expected.
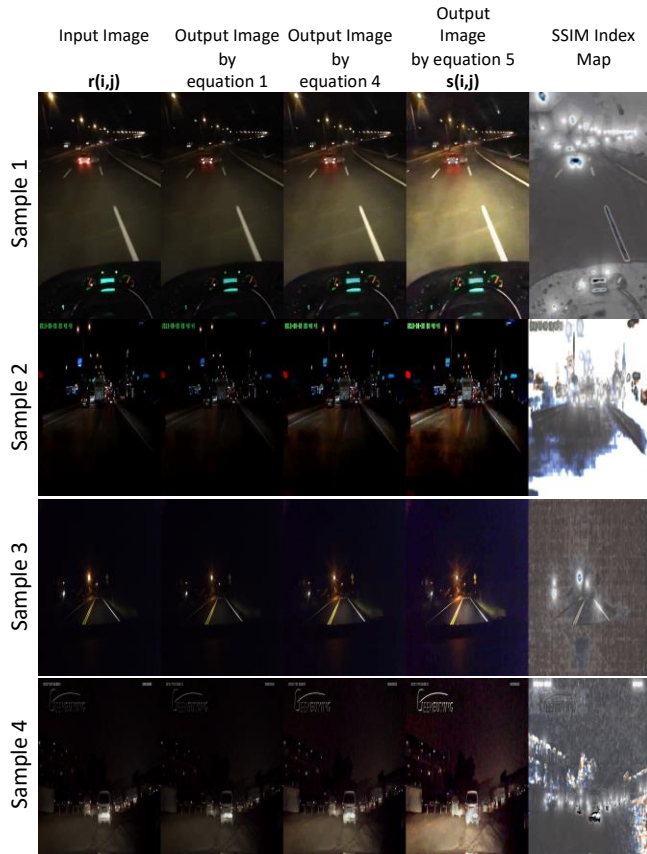
Fig. 8 Night Road Image Enhancement Study Sample Images (Images Containing Detail in Dark Area for pedestrian)[33]
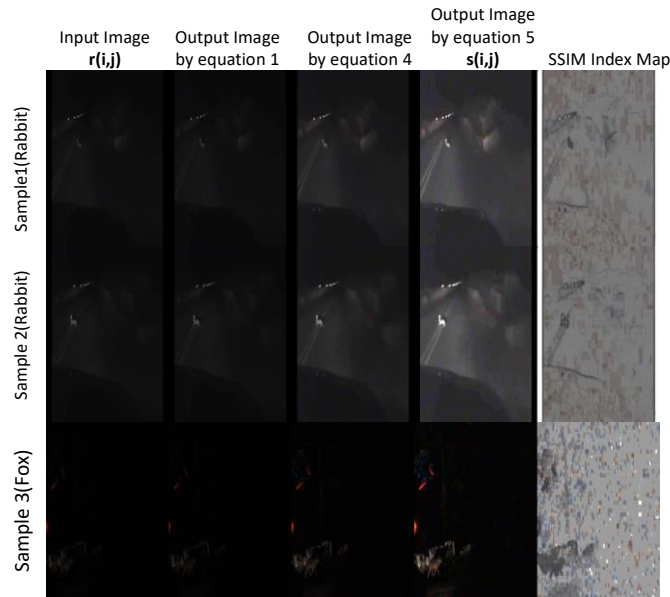
Fig. 9. Night Road Image Enhancement Study Sample Images (Images Containing Detail in Dark Area for animal)[35,36]

Structural similarity maps include changes in pixel values. For this reason, the structural similarity map is created of the output images which was obtained. Brightness, contrast, and structural components are used when evaluating structural similarity [29]. The Structural Similarity Index Maps (SSIM) contain visual information about the regions that have been modified by processing the output and input images together. It is considered that it would be meaningful to evaluate the results of SSIM index map and output image together in the specific image enhancement studies as in the study. Because the location of the change of pixel values is important in specific image enhancement studies. SSIM and mean SSIM equations are given below (6),(7),(8),(9),(10). SSIM defined as [29]:

$$SSIM(x,y) = [I(x,y)]^\alpha * [c(x,y)]^\beta * [s(x,y)]^\gamma \qquad (6)$$

$$I(x,y) = \frac{2\mu_x\mu_y + C_1}{\mu_x^2 + \mu_y^2 + C_1} \qquad (7)$$

$$c(x,y) = \frac{2\sigma_x\sigma_y + C_2}{\sigma_x^2 + \sigma_y^2 + C_2} \qquad (8)$$

$$s(x,y) = \frac{\sigma_{xy} + C_3}{\sigma_x\sigma_y + C_3} \qquad (9)$$

If $\alpha = \beta = \gamma = 1$ and $C_3 = C_2/2 \Rightarrow SSIM(x,y)$ can be written as follows.

$$SSIM(x,y) = \frac{(2\mu_x\mu_y + C_1)(2\sigma_{xy} + C_2)}{(\mu_x^2 + \mu_y^2 + C_1)(\sigma_x^2 + \sigma_y^2 + C_2)} \qquad (10)$$

The structural similarity is calculated for each pixel and the structural similarity is generated in the index map. In the study, the structural similarity index maps were created by using input and output images and given in figures (see Fig.7, Fig.8, and Fig.9). The structural similarity index maps have value of 1 in unchanged pixels. If the value is in the changing takes a value between 0-1. If the change in the pixel value is small, it produces a value close to 1, and the change in the pixel value is big, it produces a value close to 0. Thus, the regions where the change is very high are expressed as dark, and the regions where there is little change are expressed as light colors. Figures (see Fig.7, Fig.8, and Fig.9) output images and the SSIM index map together examined, there is no seen change in the regions around the light sources or there is seen change in the direction of glare reduction. Whereas, in regions with low visibility (dark), it is seen that there is more change (in the direction of increasing the level of brightness).

The structural similarity mean (mean SSIM) can be taken in order to give an overall quality measure of the image studied [24,29]. The mean SSIM equation (11) is given below for color images.

Mean SSIM defined as [29]:

$$mean\ SSIM(x,y,z) = \frac{1}{M*N*3}\sum_{i=1}^{M}\sum_{j=1}^{N}\sum_{k=1}^{3} SSIM(x_i,y_j,z_k) \tag{11}$$

Mean SSIM quality values are given in Table 1.

In addition, peak signal to noise ratio (PSNR) was used as the criterion of success in the evaluation of the study. PSNR adaptive histogram equalization [17,28,30] is widely used as a measure of success in studies. The PSNR is based on the input and output images, and acts as the error between the input image pixel value and the output image pixel value. For this reason, it is reasonable to use it as an appropriate quality criterion for image enhancement studies which are not expected to have very large variations between the pixel values of the input and output images. However, PSNR cannot be expected to be a good quality criterion in improvement studies where pixel values are expected to vary greatly. PSNR and MSE equations are given follows (12),(13). PSNR quality values are given in table 1. PSNR is defined as [30]:

$$PSNR = 10log_{10}\left[\frac{(L-1)^2}{MSE}\right] \tag{12}$$

MSE is defined as [28]:

$$MSE = \frac{1}{MN}\sum_{i=1}^{i=M}\sum_{j=1}^{j=N}[X(i,j)-Y(i,j)]^2 \tag{13}$$

Table 1 Mean Stuructural Similarity Value (mean SSIM) and Peak Signal to Noise Ratio (PSNR)

	Mean SSIM	PSNR
Figure 7 Sample1	0.4280	11.9640
Figure 7 Sample2	0.7620	22.4063
Figure 7 Sample3	0.3425	20.1995
Figure 7 Sample4	0.4100	15.5745
Figure 8 Sample1(Person)	0.4158	12.5919
Figure 8 Sample2(Person)	0.4008	14.4469
Figure 8 Sample3(Person)	0.3722	13.4063
Figure 8 Sample4(Person)	0.3699	13.9977
Figure 9 Sample1(Rabbit)	0.4870	15.8951
Figure 9 Sample2(Rabbit)	0.4891	15.4841
Figure 9 Sample3(Fox)	0.5651	28.4071

Generally, quality criteria are expected to be high in image enhancement studies. This is also the case for PSNR [17,28,30] and SSIM [24]. High PSNR and mean SSIM values mean that the amount of change in pixels is low. For example, when there is no change between input and output pixel values, PSNR takes infinite and SSIM takes 1. So they get the maximum value they can get. Therefore, it is generally considered appropriate to take reasonable values in line with the changes expected from the improvement process. In image enhancement studies, the quality criteria obtained from the methods that are expected to do the same work are compared [16,17,24,27,28,29,30]. In this study, a specific study was performed to improve night road images, so no comparison could be made with any method. However, it can be said that PSNR and SSIM values are within reasonable limits when compared with the values in studies using PSNR and mean SSIM [17,24,28,30].

REFERENCES

[1] K. W. Gish, M. Shoulson, & M. Perel, 2002. "Driver behavior and performance using an infrared night vision enhancement system" Presented at the 80th Annual Meeting of the Transportation Research Board, Washington, D.C.

[2] F. Xu, X. Liu, and K. Fujimura, (2005) "Pedestrian Detection and Tracking with Night Vision" IEEE Trans. Intelligent Transportation Systems, vol. 6, no. 1, pp. 63-71, Mar. 2005. https://doi.org/10.1109/TITS.2004.838222

[3] O. Tsimhoni, J. Bärgman and M.J. Flannagan (2007) "Pedestrian Detection with near and far Infrared Night Vision Enhancement", LEUKOS, 4:2, 113-128

[4] D. Olmeda, C. Premebida, U. Nunes, J.M. Armingol, A. de la Escalera, (2013) "Pedestrian detection in far infrared images", Integr. Comput. Aided Eng. 2013, 20, 347–360. https://doi.org/10.3233/ICA-130441

[5] A. González, Z. Fang, Y. Socarras, et al. (2016) "Pedestrian detection at Day/Night time with visible and FIR cameras", a comparison 820 Sensors, 16 (6) (2016) :1-820:11. https://doi.org/doi:10.3390/s16060820

[6] G. Wang, Q. Liu, Q. Wu, (2016) "Far-infrared pedestrian detection for advanced driver assistance systems using scene context", Optical Engineering 55(4), 043105 (21 April 2016). https://doi.org/10.1117/1.OE.55.4.043105

[7] K. Bengler, K. Dietmayer, B. Faerber, et al. (2014) "Three decades of driver assistance systems: review and future perspectives, IEEE Intell. Transp. Syst. Mag., 2014, 6, (4), pp. 6–22 https://doi.org/10.1109/MITS.2014.2336271

[8] S. Mahlke, D. Rösler, K. Seifert, J.F. Krems, M. Thüring (2007) "Evaluation of six night vision enhancement systems: qualitative and quantitative support for intelligent image processing", Human Factors 49 (3), 518–531. https://doi.org/10.1518/001872007X200148

[9] V. Asari, A. Livingston, M. Zhang, H. Ngo and L. Tao, (2005)"A Multi-sensor Image Fusion and Enhancement System for Assisting Drivers in Poor Lighting Conditions," 34th Applied Imagery and Pattern Recognition Workshop (AIPR'05)(AIPR), Washington, DC, 2005, pp. 106-113. https://doi.org/10.1109/AIPR.2005.9

[10] H.A. Burley, R. J. Sweet, (1991) "Night vision system with color video camera", US5001558A * General Motors Corporation. US Patent 5,001,558

[11] Robert Tamburo, Eriko Nurvitadhi, Abhishek Chugh, Mei Chen, Anthony Rowe, Takeo Kanade, Srinivasa G. Narasimhan, "Programmable Automotive Headlights" Computer Vision – ECCV 2014. ECCV 2014. Lecture Notes in Computer Science, vol 8692. pp 750-765 Springer, Cham

[12] A. Borkar, M. Hayes, M. T. Smith, and S. Pankanti, (2009) "A layered approach to robust lane detection at night,"inProc.IEEEWorkshopComput.Intell. Vehicles Vehicular Syst., Apr. 2009, pp. 51–57. https://doi.org/10.1109/CIVVS.2009.4938723

[13] Pomerleau D (1997) "Visibility estimation from a moving vehicle using the RALPH vision system", In: Proceedings of the IEEE Conference on Intelligent Transportation Systems, Boston, Mass., November 1997, p403 https://doi.org/10.1109/ITSC.1997.660594

[14] PELI, E. 1990. "Contrast in complex images" J. Opt. Soc. Am. A 7, 10 (October), 2032–2040. https://doi.org/10.1364/JOSAA.7.002032

[15] S. M. Pizer, E. P. Amburn, J. D. Austin, R. Cromartie, A. Geselowitz, T. Greer, B. H. Romeny, J. B. Zimmerman, K. Zuiderveld, "Adaptive histogram equalization and its variations", Comp. Vis. Graph. Image Process., vol. 39, no. 3, pp. 355-368, 1987. https://doi.org/10.1016/S0734-189X(87)80186-X

[16] T. Kim, J. Paik, "Adaptive contrast enhancement using gain-controllable clipped histogram equalization", IEEE Trans. on Consumer Electronics, vol. 54, no. 4, pp. 1803-1810, November 2008. https://doi.org/10.1109/TCE.2008.4711238

[17] Liyun Zhuang, Yepeng Guan, 2018, "Adaptive Image Enhancement Using Entropy-Based Subhistogram Equalization" Computational Intelligence and Neuroscience, Volume 2018, Article ID 3837275, 13 pages, https://doi.org/10.1155/2018/3837275

[18] N. Hautière, J.-P. Tarel, D. Aubert, E. Dumont, "Blind contrast enhancement assessment by gradient ratioing at visible edgese",

Image Analysis & Stereology Journal, vol. 27, no. 2, pp. 87-95, june 2008. https://doi.org/10.5566/ias.v27.p87-95

[19] Tarel, J.P., Hautière, N., Caraffa, L., et al.: 'Vision enhancement in homogeneous and heterogeneous fog', IEEE Intell. Transp. Syst. Mag., 2012, 4, (2), pp. 6–20, https://doi.org/10.1109/MITS.2012.2189969

[20] X. B. Jin, J. Bao, and J. J. Du, "Image Enhancement Based on Selective - Retinex Fusion Algorithm" Journal of Software, vol. 7, no. 6, pp. 1187–1194, June 2012 https://pdfs.semanticscholar.org/2293/fd6124403f44e59134755064c6118989f180.pdf

[21] Z. Shi, M. M. Zhu, B. Guo, M. Zhao, C. Zhang, "Nighttime low illumination image enhancement with single image using bright/dark channel prior", EURASIP Journal on Image and Video Processing, vol. 2018, pp. 13, February 2018. https://doi.org/10.1186/s13640-018-0251-4

[22] Ji Wei, Qian Zhijie, Xu Bo and Zhao Dean, (2018) "A Nighttime İmage Enhancement Method Based On Retinex And Guided Filter For Object Recognition Of Apple Harvesting Robot" International Journal of Advanced Robotic Systems, January-February 2018: 1–12, https://doi.org/10.1177/1729881417753871

[23] R. Nivedha, W. Newton David Raj M.Tech., (2016) "Hardware Implementation Of Combining Image Enhancement And Roı Extraction For Night Time Images" Int. J. Advanced Networking and Applications Volume No: 8, Issue No: 4(Jan-Feb 2017), Special Issue-NCBSI-2016 https://www.ijana.in/specialissue.php#one

[24] Hulin Kuang, Xianshi Zhang, Yong-Jie Li, Leanne Lai Hang Chan, Hong Yan, (2017) "Nighttime Vehicle Detection Based on Bio-Inspired Image Enhancement and Weighted Score-Level Feature Fusion" IEEE Transactions on Intelligent Transportation Systems archive , Volume 18 Issue 4, April 2017 Pages 927-936, https://doi.org/10.1109/TITS.2016.2598192

[25] Allen M. Waxman, Eugene D. Savoye, David A. Fay, Mario Aguilar, Alan N. Gove, James E. Carrick, Joseph P. Racamato, "Electronic imaging aids for night driving: low-light CCD, uncooled thermal IR, and color-fused visible/LWIR", Proc. SPIE 2902, Transportation Sensors and Controls: Collision Avoidance, Traffic Management, and ITS, (17 February 1997); https://doi.org/10.1117/12.267163

[26] P. Didyk, R. Mantiuk, M. Hein and H.P. Seidel, (2008) "Enhancement Of Bright Video Features For Hdr Displays" Computer Graphics Forum, Volume27, Issue4 June 2008 Pages 1265-1274, https://doi.org/10.1111/j.1467-8659.2008.01265.x

[27] Gang Cao, Lihui Huang, Huawei Tian, Xianglin Huang, Yongbin Wang, Ruicong Zhi, (2017) "Contrast Enhancement of Brightness-Distorted Images by Improved Adaptive Gamma Correction" Computers & Electrical Engineering, Volume 66, February 2018, Pages 569-582, https://doi.org/10.1016/j.compeleceng.2017.09.012

[28] MinjieWan, Guohua Gu, Weixian Qian, Kan Ren, Qian Chen, Xavier Maldague, (2018) "Infrared Image Enhancement Using Adaptive Histogram Partition and Brightness Correction" Remote Sens. 2018, 10(5), 682; https://doi.org/10.3390/rs10050682

[29] Zhou Wang, Alan C. Bovik, Hamid R. Sheikh, and Eero P. Simoncelli, (2004) "Image Quality Assessment: From Error Visibility to Structural Similarity "IEEE Transactıons On Image Processıng, Vol. 13, No. 4, pp. 600-612, April, 2004. https://doi.org/10.1109/TIP.2003.819861

[30] Jing Rui Tang, Nor Ashidi Mat Isa, (2014) "Adaptive Image Enhancement based on Bi-Histogram Equalization with a clipping limit" Computers and Electrical Engineering 40 (2014) 86-103. https://doi.org/10.1016/j.compeleceng.2014.05.017

[31] TTY Motorlu Araçlar 2, https://vimeo.com/96782778. Last access date: 18.02.2019

[32] HD YOL KAMERASI GECE PERFORMANSI (şehir içi), https://www.youtube.com/watch?v=Icbl5wQDOFo. Last access date: 18.02.2019

[33] ARAÇ KAMERASI Full HD 1080P ARAÇ iÇi KAMERA GECE KAYIT VİDEOSU, https://www.youtube.com/watch?v=lRV4JQQ7wwI. Last access date: 18.02.2019

[34] Late Night Mountain Road Drive, https://www.youtube.com/watch?v=P49yLhhr0O0. Last access date: 18.02.2019

[35] Rabbit runs in front of car, https://www.youtube.com/watch?v=O1kMF6BCG2I. Last access date: 18.02.2019

[36] Riding towards Shimla ?? BE CAREFUL !! FOX spotted on highway, https://www.youtube.com/watch?v=teamtsm88cI. Last access date: 18.02.2019

BIOGRAPHIES

AUTHOR Village, Manisa, in 1971. Ph.D. degrees in Department of Electronic Computer Education from the Sakarya University, Turkey, in 2009 and 2015. He is currently a assistant professor of Computer Engineering in Tokat Gaziosmanpaşa University, Faculty of Engineering and Natural Sciences. His research interests; image processing, open source SmartCam, industrial applications, industrial low cost image processing, embedded systems, embedded operating systems.

A Comparative Study of PM Synchronous Generator for Micro Hydropower Plants

A. DALCALI

Abstract—**Developing technology and growing population are increasing the need of countries for energy every passing day. Renewable energy resources, which are an environmentally friendly and local solution alternative to fossil fuels, are seen to be a significant source of supply in this matter. Among renewable energy resources, hydroelectric energy is in an advantageous position with its reliable potential and sustainable production. With the purpose of utilizing small flowing waters such as rivers and streams and solving problems of access to interconnected grids in rural areas, micro-type hydroelectric power plants have a significant potential for countries. This study carried out the design and performance analyses of permanent magnet synchronous generators (PMSGs) with different numbers of poles for micro hydroelectric power plants. The generators' flux density values and total voltage harmonic distortions were examined. Additionally, the cogging torque magnitudes have been analyzed. The generators were loaded with nominal loads, and the time-dependent waveforms of phase voltages were obtained. By subjecting the obtained voltages to Fourier analysis, their harmonic spectrum was created. Finally, by considering the amount of active material used for the designs, their costs were compared.**

I. INTRODUCTION

THE NEED for energy resources is increasing every day due to decreased fossil fuel resources, increased environmental concerns and population density. This has made energy supply one of the most important issues of today. Renewable energy resources (RER) are a significant solution for all these problems. The popularity of renewable energy is increasing as fossil fuels lead to environmental pollution and are being exhausted. In the period of 2000-2009, there were increases of 76% in oil prices, 114% in natural gas prices and 136% in coal prices. It is projected for the period of 2015-2040 that there will be increases of 186.3%, 85.7% and 56.3% in oil, natural gas, and coal prices, respectively. Considering the projections, it is important to increase renewable energy resources. Renewable energy is considered as inexpensive,

ADEM DALCALI, is with Department of Electrical and Electronics Engineering, Bandırma Onyedi Eylül University, Bandırma, Balıkesir, Turkey,(e-mail: adalcali@bandirma.edu.tr).

https://orcid.org/0000-0002-9940-0471

local, and environmentally friendly energy. The main RERs may be listed as hydroelectric, biomass, geothermal, solar and wind energy. The most significant one among clean energy resources is hydroelectric energy [1,2] The main purpose of utilizing renewable energy resources is to reduce the emissions caused by fossil fuels, prevent global warming and climate change and achieve more effective usage of the assets of countries.

Hydroelectric energy plants are the most prevalently used plants in the world. They provide 19% of the world's electricity [3]. Hydroelectric power plants may be categorized based on their power. It is possible to categorize those with a power of 100 MW as large, those with a power of 15-100 MW as medium, those with a power of 1-15 MW as small, those with a power of 100 kW-1 MW as mini, those with a power of 5 kW-100 kW as micro and those with a power of less than 5 kW as pico-hydroelectric power plants [4,5]. While large-capacity hydroelectric power plants supply electricity for several consumers, mini and micro types of hydroelectric plants usually appeal to grid-independent users [6,7]. Large-scale hydroelectric plants have disadvantages such as high initial investment costs, long construction times, their disruption of ecological balance and the negative effects of their potential storage areas on life [8,9]. As opposed to large hydroelectric plants, there is no need to build a dam for micro hydroelectric plants. This prevents the disadvantages of high cost and long installation time. By achieving the right design in small-scale hydroelectric plants, the energy of flowing water may be directly converted into electricity with minimal harm on the environment [10,11]. Micro hydroelectric plants have a high efficiency, a high-capacity factor and a slow water velocity change regime. Turbine and generator selection is an important factor in micro hydroelectric power plants. Factors such as flow rate, head and slope of the water are effective in this selection. Another important parameter in turbine selection is the specific speed of the turbine [12,13]. These plants can operate independently from the grid or in connection with the grid. Small and micro hydroelectric plants use self-excited synchronous reluctance generators [10], PMSGs [14], and asynchronous generators [15]. However, as there is no separate field winding in asynchronous generators, there is a need for a group of capacitors that need to be connected in parallel to the generator. PM generators are frequently used in micro hydroelectric facilities. In small hydroelectric plants where PM generators are used, higher efficiency may be obtained in comparison to plants with asynchronous machines [16]. Considering the literature, this

study carried out designs, performance analyses and cost comparisons of PMSGs with pole numbers of 10 and 16 for micro hydroelectric power plants.

II. PERMANENT MAGNET SYNCHRONOUS GENERATOR

While designing electric machinery, the smallest volume, the lowest amount of material and the highest power density are desired. PMSGs are machines that have high power density, high efficiency and low torque ripple [17]. PM materials may be grouped as Alnico, ferrite and rare earth magnets. The quality of a PM is characterized by the maximum energy product that is obtained by multiplying the magnetic flux density $\left(\vec{B}\right)$ and the magnetic field strength $\left(\vec{H}\right)$. Neodymium magnets have high BH_{max} products and are prevalently used in electric machinery. By using these magnets, it is possible to obtain compact machines with a high air-gap flux density [18]. PM machines are frequently preferred especially for low-speed and variable-speed applications. Improvements in driver technology in parallel with the developments in elements of power electronics have increased the usage of PM machines [19,20].

The design of electric machinery starts with sizing equations. The size of the machine that are obtained as a result of sizing calculations are usually associated with a set of assumptions and expectations that are not directly specified in the equation. In this sense, in sizing, the experience of the designer has importance in terms of meeting expectations. The general equation that is used for sizing electric machinery [21,22]:

$$S = 11K_{w1} * \overline{B} * ac * \left(\frac{D}{1000}\right)^2 * \frac{L}{1000} * n \qquad (1)$$

In the equation, S is the power (VA), K_{w1} is the winding coefficient, $\vec{B}$ is the specific magnetic loading (Tesla), ac is the specific electrical loading (A/m), D is the stator diameter (mm), L is the outer length (mm), and n is the nominal speed (rpm). The remaining mathematical model of the PMSG, not present in this paper, may be found in detail [22,23]. The generators are 5 kW, internal-rotor, and surface-mounted magnets. Table I shows the detailed design parameters. From here on, the 10-pole generator will be referred to as Design A, while the 16-pole generator will be described as Design B.

TABLE I
DESIGN PARAMETERS

	Parameter	Design A	Design B
Stator	Stator outer/inner diameter(mm)	320/235	450/340
	Length (mm)	91.5	65.5
	Stator material	M19	M19
	Number of slots	60	96
	Skew	0.7	0.7
Rotor	Rotor outer diameter (mm)	233	338
	Rotor inner diameter (mm)	170	250
	Rotor material	M19	M19
Magnet	Embrace	0.7	0.7
	Offset	50	100
	Magnet material	N40UH	N40UH
	Magnet thickness (mm)	9.1	9.8

Fig. 1 shows the 3D model of the generators that have been designed.
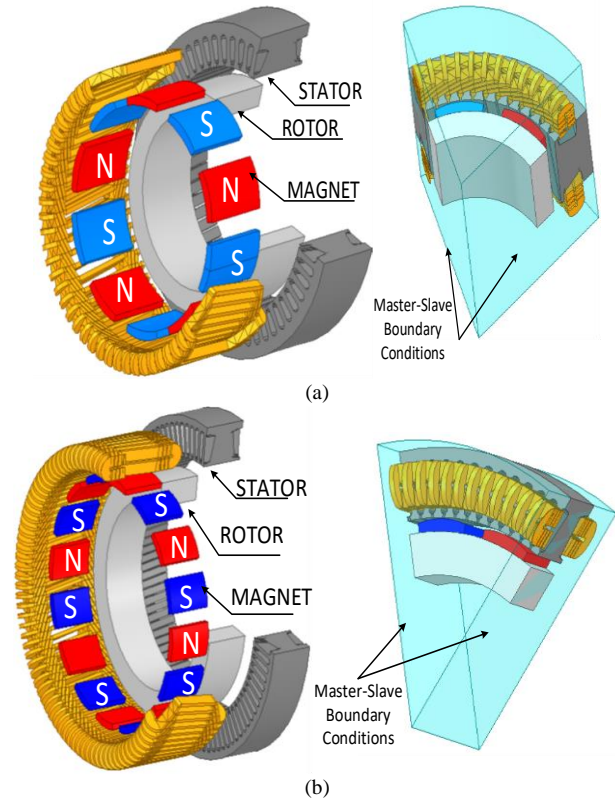

(a)

(b)

Fig.1. Exploded view of the generators, a) Design A, b) Design B

III. ANALYSIS OF THE PERFORMANCE AND COST OF THE DESIGNED GENERATORS

In generators that are designed, both the number of poles and the number of stator slots vary. The variation in these parameters leads to performance changes such as changes in the induced voltage and efficiency by changing the air-gap flux waveform. All these parameter changes determine the total amount of magnets and change the total cost of the generator. The design of electric machinery is complicated in its nature. Therefore, to obtain a satisfactory design, several interrelated problems need to be solved. Mathematics-based tools have been developed for solution of such complicated problems. One of the most effective ones among these is the Finite Element Method (FEM). FEM is a method that is used to obtain the solutions of amounts that are continuous in a certain region whose changes in the region where they are continuous may be represented by partial differential equations. By using this method, it is possible to obtain the electromagnetic parameters of a generator with high accuracy [24,25]. The mesh structure in the generators was created automatically with the help of a computer program. However, the density of the meshes was increased by the designer, particularly around the air gaps. In this study, the number of meshes created for Design A was 66482, whereas that for Design B was 74709. However, the point that requires attention here is that both generators were analyzed through the cross-section of a part to save time. Table II shows the

results of the analyses on the designs that were carried out with no-load and rated load.

TABLE II
ANALYSIS RESULTS

	Parameter	Design A	Design B
Nominal load	Output power (W)	5001	5001
	Efficiency (%)	92.3	92.4
	Total loss (W)	242.1	238.5
No load	Stator yoke flux density (T)	1.69	1.71
	Rotor yoke flux density (T)	1.03	0.56
	Cogging torque (Nm)	0.24	0.18

Considering the cogging torque values that occurred out of the interaction between the magnet and the stator slots in PMs, a lower cogging torque value was obtained in Design B with higher numbers of poles and slots as expected. The results of the analysis in the unloaded state showed the suitability of the core geometry that was created and the magnetic material that was selected. The flux density value at which the generator core is to be operated is determined based on the point under the saturation region where the permeability is the maximum. In this context, the results that were obtained were suitable for the criteria that were targeted. Analyses with FEM require long times of solution. By using the boundary condition of symmetry, 1/5 part of the 10-pole generator and 1/8 part of the 16-pole generator were obtained in the study. The analyses were carried out on these parts. In electric machinery, magnetic fields may be shown with Maxwell Equations:

$$\nabla \times \overline{E} = -\frac{\partial \overline{B}}{\partial t} \qquad \nabla \times \overline{H} = \overline{J} \qquad (2)$$

where, $\overline{E}$ is the electrical field strength, and $\overline{J}$ is the current density [26]. To define the magnetic vector potential in terms of magnetic flux density:

$$\overline{B} = \nabla \times \overline{A} \qquad (3)$$

The main formula of the vector potential for the magnetic field is shown:

$$\nabla \times (v\nabla \times \overline{A}) = \overline{J} \qquad (4)$$

In the equation, as the curve $B = f(H)$ is not linear, v shows variable conductance. The flux density distribution obtained on the generator core is obtained by Eq 5 and 6 [26]:

$$\frac{\partial}{\partial x}\left(v\frac{\partial A}{\partial x}\right) + \frac{\partial}{\partial y}\left(v\frac{\partial A}{\partial y}\right) + \frac{\partial}{\partial z}\left(v\frac{\partial A}{\partial z}\right) = -\overline{J} \qquad (5)$$

In 3D analyses, the components of the magnetic flux density value in the x, y and z axes are found as:

$$B = \sqrt{B_x^2 + B_y^2 + B_z^2} \qquad (6)$$

In 2D modeling, fringing and end winding effects are not properly accounted. Therefore, it is a sturdier approach to create a 3D model of the machine. It would be possible to design a more realistic generator in terms of implementation by also addressing the presence of such effects through 3D modeling. For these reasons, the generators were analyzed through their 3D models [24]. The magnetic flux distribution that was obtained in the transient analyses on the part cross-section models is given in Fig. 2.
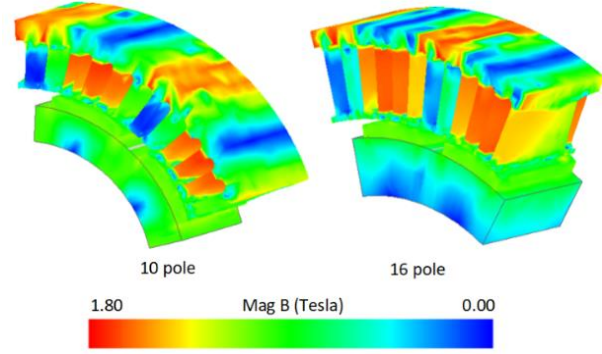
Fig. 2. Flux density distribution in part cross-sections

Because the saturation point of the M19-24G material is approximately 1.9 T, the distributions of flux obtained on the core indicate that the operation was taking place below the saturation point. Because flux concentrated on stator notches, the density of flux was found to be relatively higher there in comparison to the other areas. For the generators, whose suitable magnetic flux distributions were obtained, nominally loaded state analyses were carried out in the next step, and voltage waveforms were derived.
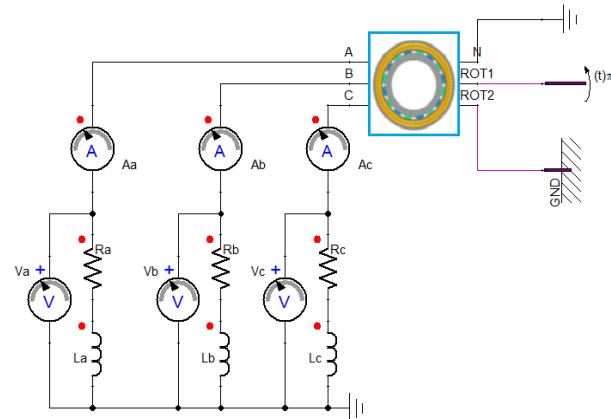
Fig. 3. Co-simulation model with nominal load

Nominal loads were attached to the generators, and their performances at the nominal speeds (600 rpm for Design A and 375 rpm for Design B) were applied. An ohmic value of 26 ohms and an inductive load of 27.42 mH are connected to each phase. The circuit schema that was created is presented in Fig. 3. Fig. 4 shows the phase voltage waveforms of both generators.

(a)

(b)

Fig. 4. Phase voltage, a) Design A, b) Design B

Harmonics are the full multiples of the fundamental frequency, and they lead to ripples in load current and voltage. Two types of harmonics as time and space harmonics may be considered for electric machinery. The ef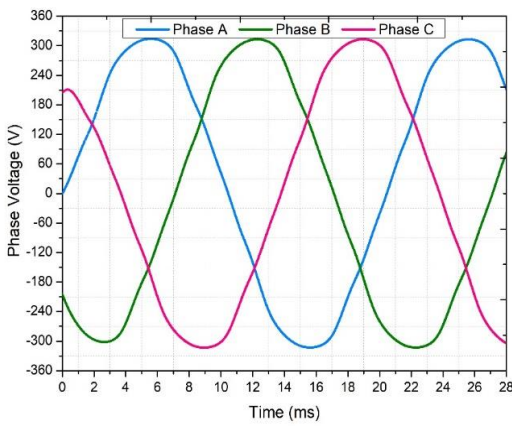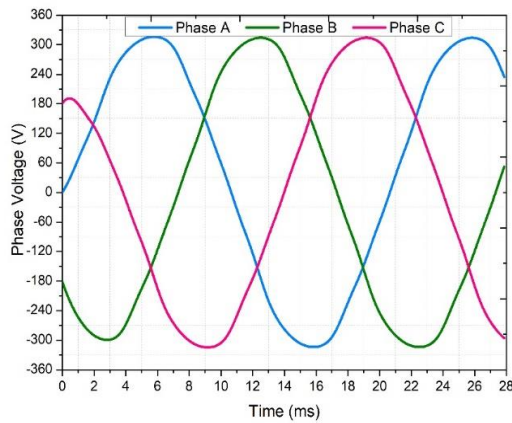fects of space harmonics may be changed by the physical changes to be made in the machine [23]. Analyses of the harmonic values of the designed generators need to be carried out. Fourier analyses of the generators may be calculated by using the graphical method. In this method, the Fourier coefficients may be derived by using [27].

$$A_n = \frac{2}{m} \sum_{k=1}^{m} \left(y_k \cos(n\theta_k) \right)$$
$$B_n = \frac{2}{m} \sum_{k=1}^{m} \left(y_k \sin(n\theta_k) \right)$$

(7)

In the equation, m is the number of vertical separations, and for the harmonic analysis to be sensitive, it needs to be at the maximum value. However, the number of operations increases as the number of separations increases [23]. The function of the phase voltage induced by the A_n and B_n coefficients is expressed by:

$$V(\theta) = \left(\sqrt{A_1^2 + B_1^2} \right) \cdot \left(\sin\left[\theta + \tan^{-1}\left(\frac{B_1}{A_1} \right) \right] \right) + \dots$$
$$+ \left(\sqrt{A_n^2 + B_n^2} \right) \cdot \left(\sin\left[\theta + \tan^{-1}\left(\frac{B_n}{A_n} \right) \right] \right)$$

(8)

The value of the phase voltage is expressed as some of the base component (1st harmonic) and harmonic components. As mentioned before, the distortions in the waveform of voltage are known as the Total Harmonic Distortion (THD) and expressed in %. The THD value is found by using [28]:

$$THD_V = \frac{\sqrt{\sum_{2}^{\infty} V_n^2}}{V_1}$$

(9)

Fourier analyses have been carried out using the MATLAB software (License No: 40692431) to obtain their harmonic spectrum. Fig. 5 features the harmonic spectrum of the designs.
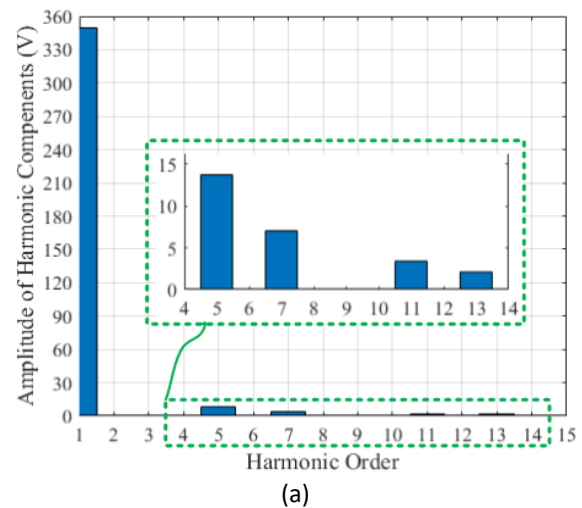
(a)
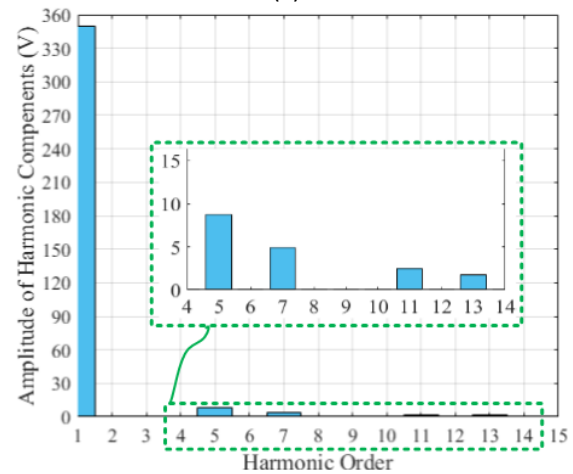
(b)

Fig. 5. Harmonic spectrum of the generators at phase voltage, a) Design A, b) Design B

At nominal loading, the harmonic distortions of the 16-pole

generator were relatively lower than those of the 10-pole generator. Design A had higher low-order harmonics than the other design. Machines with PMs have a significant disadvantage in spite of their efficiency and power density advantages. The cogging torque that occurs in machines with PMs can cause noise, vibration and have ripple of torque [29,30]. While the stator currents of both generators are zero, the variation of cogging torque with the rotor position is given in Fig. 6.

Fig. 6. Cogging torque variation of design

Design B with a higher number of poles and slots had a smaller cogging torque as expected. Because it had a greater number of slots and poles, the variation in its reluctance was reduced, and thus, the value of its cogging torque decreased.

Finally, cost analyses were performed on the generators whose magneto-static and transient performances were examined. As known, a large part of the cost in PM machines is created by the magnets. In the cost calculations, it was accepted that, N40UH: 95 $/kg, M19: 1.9 $/kg and Copper: 6 $/kg [21]. The material amounts that were used in the designs and their costs are shown in Table III.
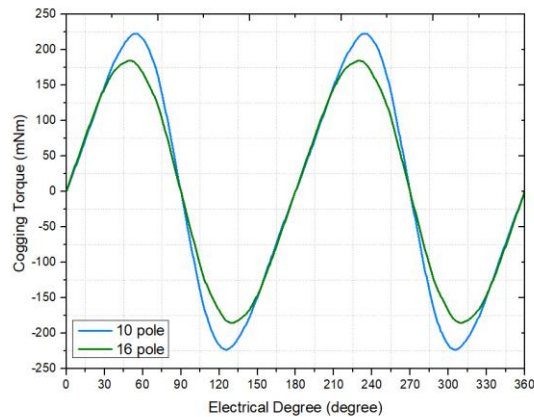
As N40UH-type magnets were used for both designs in the study, and magnet usage was expressed in kg. As seen in the table, changing magnet geometries lead to significant differences in the total material costs. Magnet cost has the largest share among the costs of active materials. Based on the costs, Design A is 16.34% more economical. The weights of the generators were 38.47 kg for Design A and 48.05 kg for Design B.

TABLE III
AMOUNTS OF MATERIALS THAT WERE USED AND TOTAL COSTS

Design	Magnet (N40)		Core Material (M19)		Coil (Copper)		Total Cost ($)
	Amount (kg)	Cost ($)	Amount (kg)	Cost ($)	Amount (kg)	Cost ($)	
Design A	2.82	267.9	25.56	48.56	10.09	60.54	377
Design B	3.19	303.05	32.67	62.07	12.19	73.14	438.26

IV. CONCLUSION

This study carried out the design and performance comparisons of PM multi-pole synchronous generators with the power of 5 kW that are suitable for micro hydroelectric power plants. For a fair comparison, the core and magnet materials of the generator were selected as the same. The analyses of the generators at nominal load and no-load showed that the flux density distributions were within the desired limits considering the core material that was used. In Design B, which had higher numbers of slots and poles, the cogging torque value was 25% less than that in Design A. Considering the total harmonic distortions of the voltages at the nominal load, Design B had lower harmonic components with the value of 2.73%. Although the provide similar efficiency values, designs with high THD values may lead to significant problems such as acoustic noise, vibration, and saturation at the core. Therefore, although the values of these generators with different numbers of poles such as efficiency and power factor could be close, THD values have a significant effect on the operational performance of the generator, and they need to be as low as possible. The 10-pole design required 26.21% less material usage than the 16-pole design. The amount of especially the magnets, which is a substantial component of costs, was relatively higher in the 16-pole generator. This situation is the main reason for the difference between the costs of the two designs. In terms of the total costs of the

materials that were used, Design A was 16.34% more economical. Considering the designs in general, Design B could produce the same power with approximately the same efficiency at a lower speed. Additionally, lower %THD could be obtained with the 16-pole design for the unloaded and nominally loaded states. However, a lighter generator and a lower-cost structure could be achieved by using less materials with Design A. Therefore, it would be a better approach for designers to consider several outputs rather than one output such as efficiency, cost and torque and assess their designs in this direction. With this study, it was aimed to provide a general idea for designers on the behaviors of PMSGs with different numbers of poles in both magnetostatics and transient state.

REFERENCES

[1] Electricity Generation Sector Report, Electricity Generation Corp., Ankara, Turkey, Tech. Rep. Jan. 2011.

[2] İ. Yavuz, H. Özbay, "Installation and Maintenance Processes in Wind Turbines: The Case of Bandırma." Journal of Engineering Sciences and Researches, vol. 2, 2, 2020, pp. 58-68.

[3] J.A. Laghari, H, Mokhlis, A. H. A. Bakar, H. Mohammad, "A comprehensive overview of new designs in the hydraulic, electrical equipments and controllers of mini hydro power plants making it cost effective technology." Renewable and Sustainable Energy Reviews, vol. 20, 2013, pp. 279-293.

[4] C.P. Jawahar, P.A. Michael, "A review on turbines for micro hydro power plant." Renewable and Sustainable Energy Reviews, vol. 72, 2017, pp. 882-887.

[5] B.A. Nasir, "Design of micro-hydro-electric power station." International Journal of Advanced Technology and Engineering Exploration, vol. 2, 5, 2013, pp. 39-47.

[6] S. Lajqi, N. Lajqi, B. Hamidi, "Design and construction of mini hydropower plant with propeller turbine." International Journal of Contemporary ENERGY, vol. 2, 1, 2016, pp. 1-13.

[7] A.T. Cordoba, D.G. Reina, P.M. Gata, "An evolutionary computational approach for designing micro hydro power plants." Energies, vol. 12, 5, 2019, pp. 1-25.

[8] M.M. Rahman, P. Chowdhury, M. N. Rahman, S. T. Mowri, M.A. Mamun, "Portable micro hydro electrical generator." IOSR Journal of Electric and Electronics Eng, vol. 6, 3, 2011, pp. 39-43.

[9] L. Belhadji, S. Bacha, D. Roye, "Modeling and control of variable-speed micro-hydropower plant based on axial-flow turbine and permanent magnet synchronous generator (MHPP-PMSG)." 7th Annual Conference of the IEEE Industrial Electronics Society, Melbourne, Australia, 2011, pp. 896-901.

[10] J Awad, H. Wadi, M., E., Hamdi, "A self-excited synchronous generator for small hydro applications." International Conference Energy, Environmental, Ecosystems, and Sustainable Development, 2005, pp. 1-5.

[11] S. Zeb, M. Ali, A. Mujeeb, H. Ullah, "Cost efficient mini hydro plant with low water head whirlpool design methodology for rural areas (micro hydro whirlpool power plant)." 2nd International Conference on Computing, Mathematics and Engineering Technologies, Pakistan, 2019, pp. 1-7.

[12] T.C. Yan, T. Ibrahim, N.M. Nor, "Micro hydro generator applied on domestic pipeline." International Conference on Electrical Engineering and Informatics, Indonesia, 2011, pp. 1-6.

[13] B. A. Nasir, "Suitable selection of components for the micro-hydro-electric power plant." Advances in Energy and Power, vol. 2, 1, 2014, pp. 7-12.

[14] B. Guo, S. Bacha, M. Alamir, A. Mohamed, "Variable speed micro-hydro power generation system: review and experimental results." 3ème édition du Symposium de Génie Electrique, Nancy, France, 2018.

[15] W. Ali, H. Farooq, A. U. Rehman, M. Jamil, Q. Awais, A. Mohsin, "Grid interconnection of micro hydro power plants: major requirements, key issues and challenges." International Symposium on Recent Advances in Electrical Engineering (RAEE), Islamabad, 2018, pp. 1-6.

[16] Z. Goryca, S. Rozowicz, K. Dabala, Z. Krzemien, "Design and tests of generators for micro hydro plants." International Symposium on Electrical Machines, Poland, 2017, pp. 1-4.

[17] B.O. Zala, V. Pugachov, "Methods to reduce cogging torque of permanent magnet synchronous generator used in wind power plants." Elektronika Ir Elektrotechnika, vol. 23, 1, 2017, pp. 43-48.

[18] N. Öztürk, A. Dalcalı, E. Çelik, S. Sakar, "Cogging torque reduction by optimal design of PM synchronous generator for wind turbines." International Journal of Hydrogen Energy, vol. 42, 28, 2017, pp. 17593-17600.

[19] H. Gör, E. Kurt, "Preliminary studies of a new permanent magnet generator (PMG) with the axial and radial flux morphology," International Journal of Hydrogen Energy, vol.11, 17, 2016, pp.7005-7018.

[20] O. Lyan, V. Jankunas, E. Guseınoviene, A. Pasilis, A. Senulis, A. Knolis, E. Kurt, "Exploration of a Permanent Magnet Synchronous Generator with Compensated Reactance Windings in Parallel Rod Configuration." Journal of Electronic Materials, vol. 47, 8, 2018, pp. 4437-4443.

[21] A. Dalcalı, "Cogging torque analysis in permanent magnet synchronous generators using finite elements analysis", International Transactions on Electrical Energy Systems, vol. 30, 10, 2020.

[22] Y. Duan, "Method for design and optimization of surface mount permanent magnet machines and induction machines." Ph.D. dissertation, Dept. Elect. Comp. Eng., Georgia Institute of Tech., USA, 2010.

[23] A. Dalcalı, M. Akbaba, "Optimum pole arc offset in permanent magnet synchronous generators for obtaining least voltage harmonics." Scientia Iranica, vol.24, 6, 2017, pp. 3223-3230.

[24] S.L. Ho, W.N. Fu, "Review and future application of finite element methods in induction motors." Electric Machines & Power Systems, vol. 26, 2, 1998, pp. 111–125.

[25] A. Alaeddini, H. Tahanian, A. Darabi, "Impact of Number of Phases on Electromagnetic Torque Characteristics of Transverse Flux Permanent Magnet Machines." Advanced Electromagnetics, vol. 8, 4, 2019, pp. 118-129.

[26] M. Akbaba, S.Q. Fakhro, "Field distribution and iron loss calculation in the reluctance augmented shaded pole motors using finite element method." IEEE Transactions on Energy Conversion, vol. 7, 2, 1992, pp. 302–307.

[27] C. Kocatepe, M. Uzunoğlu, R. Yumurtacı, A. Karakas, O. Arıkan, *Harmonics in Electrical Installations*, Istanbul, Turkey: Birsen Publication, 2003. (In Turkish).

[28] S.B. Efe, "Harmonic filter application for an industrial installation." 13th International Conference on Engineering of Modern Electric Systems (EMES), Romania, 2015, pp. 31–34.

[29] H. Gör, E. Kurt, "Waveform characteristics and losses of a new double sided axial and radial flux generator," International Journal of Hydrogen Energy, vol. 41, 29, 2016, pp. 12512-12524.

[30] S. Leitner, H. Gruebler, A. Muetze, "Cogging Torque Minimization and Performance of the Sub-Fractional HP BLDC Claw-Pole Motor." IEEE Transactions on Industry Applications, vol. 55, 5, 2019, pp. 4653-4664.

BIOGRAPHY

ADEM DALCALI received B.Sc. and M.Sc. degree from Gazi University, Ankara in 2010 and 2013, respectively. He received the Ph.D. degree in Electric and Electronics Engineering from Karabük University, Turkey, in 2017. From 2013 to 2017, he was a Research Assistant at Department of Electric and Electronics Engineering, Karabük University. He is currently an Assistant Professor at Department of Electrical-Electronics Engineering, Bandırma Onyedi Eylül University. His research interests wind energy and the numerical analysis of the electromagnetic field in electrical machinery.

Sequential Feature Maps with LSTM Recurrent Neural Networks for Robust Tumor Classification

C. BATUR ŞAHİN, B. DİRİ

Abstract— In the field of biomedicine, applications for the identification of biomarkers require a robust gene selection mechanism. To identify the characteristic marker of an observed event, the selection of attributes becomes important. The robustness of gene selection methods affects the detection of biologically meaningful genes in tumor diagnosis. For mapping, a sequential feature long short-term memory (LSTM) network was used with artificial immune recognition systems (AIRS) to remember gene sequences and effectively recall learned sequential patterns. An attempt was made to improve AIRS with LSTM, which is a type of RNNs, to produce discriminative gene subsets for finding biologically meaningful genes in tumor diagnosis. The algorithms were evaluated using six common cancer microarray datasets. By converging to the intrinsic information of the microarray datasets, specific groups such as functions of the co-regulated groups were observed. The results showed that the LSTM-based AIRS model could successfully identify biologically significant genes from the microarray datasets. Furthermore, the predictive genes for biological sequences are important in gene expression microarrays. This study confirmed that different genes could be found in the same pathways. It was also found that the gene subsets selected by the algorithms were involved in important biological pathways. In this manuscript, we tried an LSTM network on our learning problem. We suspected that recurrent neural networks would be a good architecture for making predictions. The results showed that the optimal gene subsets were based on the suggested framework, so they should have rich biomedical interpretability.

Index Terms— Biomarker discovery, Deep learning, Gene selection, Robustness, Tumor classification.

I. Introduction

MICROARRAY TECHNOLOGY is a technology with a high process capacity that can identify thousands of genes at the same time.

CANAN BATUR ŞAHİN is with the Department of Computer Engineering, University of Malatya Turgut Ozal, Malatya, Turkey (e-mail: canan.batur@ozal.edu.tr) 🆔 https://orcid.org/0000-0002-2131-6368

BANU DİRİ is with the Department of Computer Engineering, Yildiz Technical University, Istanbul (e-mail:diri@ce.yildiz.edu.tr).
🆔 https://orcid.org/0000-0002-6652-4339

It is used to identify disease-related genes by comparing gene expression in a diseased and normal cell. Obtaining pointer genes from high-throughput experiments instead of creating models provides advantages for biomarker discoveries. It can be used in gene expression profiling, the diagnosis of diseases, and pharmacogenetics areas. Some of the genes in gene expression data provide us with important information about disease diagnosis.

Feature selection methods generally influence the performance of biomarker discoveries. Pointer discovery needs a robust feature selection method for microarray datasets. The groups formed by the associated features are generally mentioned as intrinsic specific groups, such as functions, and present in high-dimensional datasets. The current research aimed to develop and assess a method of converging to co-regulated feature groups in microarray datasets, thus, addressing the problem of robust feature groups with high-accuracy classifications. The recent advancements in deep learning techniques in machine learning introduce a strong alternative to high-throughput experiments. The methodology in this research is the immune-based feature selection that is utilized for the discovery of optimal feature sets, enhancing robust tumor classification. The recent research efforts that have utilized feature selection methods include deep learning, feature selection, and classification of cancer microarray datasets. The in-depth investigation of feature selection to enhance the diagnosis of diseases will provide a significant contribution to the literature in the biomarker discovery domain. This study presented and tested a novel method of leveraging feature selection that resulted in the improved classification of tumor diagnosis.

In the study conducted by [1], a new framework of feature selection based on recurrent neural network (RNN) was suggested to select a subset of features. The suggested model was applied to select features from microarray data for cell classification. Feature selection models were implemented based on gated recurrent unit (GRU), long short-term memory (LSTM), RNN and bidirectional LSTM for microarray datasets. In the study carried out by [2], a deep neural network model was improved by feature selection algorithms in predicting various biomedical phenotypes. Five binary classification methylome datasets were selected to compute the prediction performances of CNN/DBN/RNN models by utilizing the feature selected by the eleven feature selection algorithms. The results showed that the Deep Belief Network (DBN) model

utilizing the features selected by SVM-RFE usually had the best prediction accuracy on the five methylome datasets.

In the research conducted by [3], a novel approach was established based on clustering-centered feature selection for the classification of gene expression datasets. According to the experiments, the suggested feature clustering support vector machine (FCSVM) was capable of achieving efficient performance on gene expression datasets.

In the research performed by [4], the most recent studies using deep learning to establish models for cancer prognosis prediction were reviewed. This study revealed that the application of deep learning in cancer prognosis was equivalent to or better in comparison with the current approaches.

In the study conducted by [5], a convolutional neural network (CNN) deep learning algorithm was investigated for the classification of microarray datasets. The promising results proved that CNN had superiorities in terms of accuracy and minimizing gene in classifying cancer.

In the research conducted by [6], the performance of deep neural networks for the classification of gene expression microarrays was analyzed. The experimental results suggested that deep learning needs high-throughput datasets to achieve the best performance.

In the study carried out by [7], deep learning-based algorithms were developed to make a tumor diagnosis, reveal biomarkers and genetic changes, pathological features. An overview showed that deep learning-based approaches for pathology gave promising results for big data.

The recent developments of robust biomarker techniques with deep learning introduce a strong alternative to tumor diagnosis. The principal contribution of the current manuscript is presented below:

1. The current study presents an extensive framework in which the learning and combination of features are carried out in a novel way, by establishing a biomarker discovery model.
2. The Artificial Immune Recognition (AIRS) algorithm was trained by deep learning-based approaches to sequentially learn biologically meaningful genes in order to predict a tumor diagnosis.
3. We leveraged the LSTM deep learning technique to capture the long context correlations in a cancer microarray dataset.
4. We optimized deep-learned features by utilizing LSTM recurrent neural networks (RNNs) to detect co-regulated specific groups, such as functions, in high-dimensional data.
5. We examined the possibility of utilizing Deep Neural Network (DNN) recurrent neural network models to learn disease-related genes, and then we used them for the prediction of important biological pathways.

In this study, LSTM-based AIRS version 1, LSTM-based AIRS parallel version 1, LSTM-based AIRS version 2, and LSTM-based AIRS parallel version 2 algorithms were developed to discover optimal biological gene sequences. The suggested

algorithms were compared with the traditional genetic algorithm and genetic algorithm-based artificial immune systems. All the experiments in this study used the microarray dataset.

The present research is structured in the following way. Section II summarizes the feature subset group. Sections III briefly explains the systems. Section IV describes the methodology and framework. Sections V and VI focus on the results and performance analysis, and the conclusions.

II. Feature Subset Group

Robust tumor classification was constructed with an ensemble gene selection framework. The framework uses feature subset groups comprised of the associated attributes. Feature groups are created using group formation algorithms that run separately on sub-samples of the training dataset. The bootstrap method was used to ensure the stability of training samples in the presence of variations. The associated feature groups were created with filter-based feature selection methods.

Density-based feature groups were created by kernel density estimation, which was calculated using equation (1). The kernel function is determined by the C_{j+1} formula to identify the consecutive locations of the kernel function. Kernel density estimates were made to locate dense feature groups, and then the most relevant groups were selected.

$$C_{j+1=} \frac{\sum_{i=1}^{k} fi\, K(\frac{c_j - fi}{h})}{\sum_{i=1}^{k} K(\frac{c_j - fi}{h})}\ ,\ j = 1,2,\dots \qquad (1)$$

In Eq. (1), variables h, k, f_i, and K represent the kernel bandwidth, the nearest neighbor number, the number of attributes in the dataset, any attribute that is represented by parameter f_i, and the kernel function, respectively.

The usefulness of attribute subsets in the CFG was identified by Eq. (2). The intuitive usability of a subset of S was based on the heuristic evaluation function.

$$\text{merit}_S = \frac{k * \text{rcf}}{\sqrt{k + (k-1) * \text{rff}}} \qquad (2)$$

Variables k, rcf, and rff represent the number of attributes, the mean attribute-class correlation, and the correlation between the mean attributes, respectively.

In Eq. (3), the information gain function identifies the significance of a given attribute in the full feature set. The entropy criteria were used to determine feature knowledge.

$$E = -\sum_{i=1}^{M} (f_t(i)\log(f_t(i))) \qquad (3)$$

Parameters f_t and M represent any attribute and the data numbers, respectively.

III. SYSTEMS

A. Long Short-Term Memory (LSTM)

LSTM is a variation of RNN architecture and one of the most effective solutions to sequence prediction problems because of the recognition of patterns in data sequences. Since LSTM possesses a certain type of memory, it can selectively remember patterns for a long time. It is quite a reasonable approach to predict the period with the unknown duration between important events. Fig. 1 demonstrates the architecture of the LSTM recurrent neural network. It comprises a self-recurrent connection and three gates, input, forget, and output, which are responsible for remembering things and manipulating the memory cell. Interactions between the memory cell and its environment are modulated by the mentioned gates. The input gate is responsible for adding information to the cell state. The forget gate allows the cell to remember or forget the cell's previous state. The output gate selects beneficial information from the current cell state and shows it out.
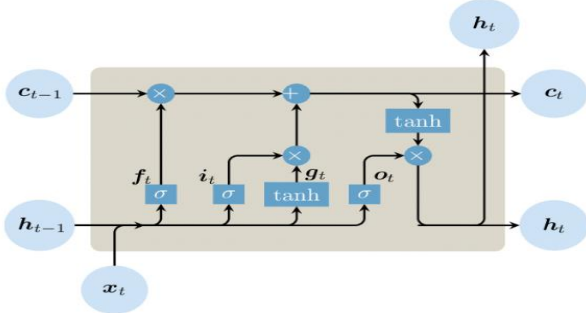

Fig. 1. Architecture of the LSTM Recurrent Neural Network [8].

Each LSTM block has input and output gates that learn to activate or deactivate to obtain new information, change the cell state, and activate it to affect other cells and network outputs. X(t) is an input for the antigenic pattern at time t. For each time series, one LSTM block changes the output of the new cell state ($\hat{C}$) at time t, which acts as the current cell state at time t. A tanh layer is added to $\hat{C}(t)$, which represents the new state of the cell at time t. Then, the old cell state C(t-1) is updated as C(t). The modulation and output gates are represented by g(t) and O(t), respectively.

B. Artificial Immune Recognition System (AIRS)

The artificial immune recognition system (AIRS) represents an intelligent system that is inspired by the natural immune system.

AIRS depends on the stages of initialization, memory cell recognition, resource competition, and the selection of memory cells. The normalization of the dataset is performed at the initialization stage in the range of [0, 1]. Then, the affinity threshold is computed using Eq. (4). The affinity threshold represents the average affinity between antigens in the training set. In Eq. (4), variables n, ag_i, and ag_j refer to the number of antigens in the dataset, any antigen, and the next antigen in the dataset, respectively. Antigens are trained in the artificial recognition ball (ARB) pool during the resource competition stage. The stimulation value is assigned to every ARB to compete for limited resources. Memory cells are selected at the end of the resource competition stage. The evolved memory cell pool indicates the quality of the classification process. The affinity between two antigens in the training set is calculated using Eq. (5). Eq. (6) calculates stimulation. If a memory unit and an antigen have the same class label, this refers to the stimulation value in affinity. If they have a different class label, this refers to the stimulation value in the Euclidean distance. In Eq. (6), m_c represents the memory cell.

Affinity threshold

$$= \sum_{i=1}^{n} \sum_{j=i+1}^{n} \left(\frac{Affinity\left(ag_i, ag_j\right)}{\frac{n(n+1)}{2}} \right) \qquad (4)$$

$$Affinity\left(ag_i, ag_j\right) = 1 - Eucliden\ distance\left(ag_i, ag_j\right) \qquad (5)$$

Stimulation

$$= \begin{cases} Affinity(m_c, ag_i) & if\ m_c.class = agi.class \\ 1 - Affinity & otherwise \end{cases} \qquad (6)$$

The first version of the artificial immune recognition system (AIRS1) utilizes the ARB pool as a permanent resource, and the mutation rate is determined by the user. The second version, AIRS2, utilizes the ARB pool as a temporary resource. Therefore, the complexity of AIRS2 is less, and somatic hypermutation is used, which means that the mutation rate is proportional to affinity. The parallel versions of AIRS are PAIRS1 and PAIRS2. The training datasets are separated into np number processes. The AIRS algorithm was run separately on each process and merged with the np memory pool.

C. Genetic Algorithm

The genetic algorithm (GA) represents a stochastic search model and optimization technique that mimics natural evolutionary mechanisms. GA is a population-based algorithm that evolves solutions on the basis of the principles of Darwinism. Each candidate solution is represented by the chromosome and has a fitness value indicating the quality of the solution to a problem. GA starts by generating a random population. Fitness-based selection determines the recombined parent chromosomes in the mating pool. Through crossover and mutation operators, offspring are produced for the next generation. The evolution of successive generations continues until the stopping criterion is achieved. At the final stage, the best solution to a problem is determined.

D. Genetic Artificial Neural Network with the Genetic Algorithm (ANN +GA)

The artificial neural network (ANN) represents a computational structure that models the neural structure of the human brain. Artificial neurons are the basic units, which are connected to weighted values, synapses. The structure

comprises input, hidden, and output layers. The input layer provides data to ANN. The hidden layer consists of units transforming input into something in the output layer. The feature subsets of ANN were created with DGF, CFG, and IGFG feature subset groups. The genetic algorithm (GA) was employed to estimate the best input parameters of ANN to train networks.

IV. METHODOLOGY AND SUGGESTED FRAMEWORK

The methodology was inspired by a theoretical model of the natural immune system, which describes the functioning and behavior of the immune system and has been an inspiration for a new artificial immune system (AIS).

The theoretical model hypothesizes that "a kind of internal restimulation keeps immune memory preserved for a long time" [9]. To model such an internal restimulation mechanism, this study used an LSTM recurrent neural network. The proposed framework was designed for the robust computation of long-sequence learning. The adaptive immune system is capable of remembering the same antigenic patterns over different periods. An associative immune memory was developed to remember gene sequences as robust patterns. This study developed a mechanism for sequence modeling in which biologically significant gene sequences could be effectively memorized. The immune memory of AIRS was developed based on this methodology to understand the "remember" behavior of the artificial immune system response. The underlying principle of the LSTM-based AIRS is to allow for the preservation of the subpopulation of surviving ARBs as long-lived unit cells. In the LSTM systems, values, for which durations are random and delays between significant events are unknown, can be remembered. The evolution of each ARB was performed with the LSTM block for long time series. All recognition cells were remodeled with LSTM gates during the training of the system and then treated with the metadynamics of AIRS. LSTM evolves sub-populations of memory cells and treats them as network inputs. The proposed framework formulates long-sequence learning problems with LSTM memory blocks, as shown below:

The output of the network h(t) is computed by utilizing the formula presented below. C_t^j refers to the memory amount of every j^{th} LSTM unit at time t.

$$h_t^j = \sigma_t^j \tanh(c_t^j) \qquad (7)$$

σ(t) denotes the output gate in which the memory content exposure is managed.

The output gate is expressed by the following equation:

$$\sigma_t^j = \sigma(W_0 X_t + U_0 h_{t-1} + V_0 c_t)^j \qquad (8)$$

σ represents the standard sigmoid function, while V0 represents a diagonal matrix. Ĉ(t) denotes a new memory content of the memory unit, which is updated by partially forgetting the current memory and adding new memory contents to c(t).

$$c_t^j = f_t^j c_{t-1}^j + i_t^j \hat{C}_t^j \qquad (9)$$

The novel memory contents are presented below:

$$\hat{C}_t^j = \tanh(W_c X_t + U_c h_{t-1})^j \qquad (10)$$

The current memory forgetting gate is modulated by f(t). Input gate i(t) modulates the addition degree of new memory content to the memory cell. V_f and V_i are diagonal matrices [10].

$$f_t^j = \sigma(W_f X_t + U_f h_{t-1} + V_f c_{t-1})^j \qquad (11)$$
$$i_t^j = \sigma(W_i X_t + i\, h_{t-1} + V_i c_{t-1})^j \qquad (12)$$

Fig. 2, Fig. 3, and Fig. 4 demonstrate the pseudocode of LSTM-AIRS, the general flowchart of the suggested model, and the framework of the LSTM-AIRS architecture, respectively.

Procedure: LSTM-AIRS

Step 1: {*InitializeAntibodyPool* (AntibodySet)}
Step 2: {*InitializeFeatureSet*(Ω)}
Step 3: [Train] {1...N} (Input Size)
Step 4: {*IntroduceAntibodyPool}* (Ab$_N$)
Step 4: FOR I← Iteration Number **DO**
Step 5: *Affinities* ← *{calcAffinities* (Ab$_i$)}
Step 6: Clone$_{num}$ ← *Select{Affinity* (Ab$_i$)}
Step 7: Fitness ←*Accuracy* (Feature set (Ω), Ab$_i$)
Step 8: Antibody$_{LSTM}$ ← *CreateLSTMMemory* (Ab$_i$, t, State_id)
Step 9: FOR (Ab$_i$ ∈ Clone$_{num}$)
Step 10: ClonesAntibodies ← (CloneandHypermutated (Ab$_i$))
Step 11: Clone*Affinities* ← *{calcAffinities* (Ab$_i$)}
Step 12: Fitness ←*Accuracy* (Feature set (Ω), Ab$_i$)
Step 13: {*UpdateAntibodyPool}* ← (Clone*Affinities*)
Step 14: Ĉ$_{LSTM}$ ←*UpdateLSTMMemory* (Antibody$_{DNN}$, t, State_id)
Step 15: State_id ← State_id+1
Step 16: C$_{LSTM}$ ←*UpdateLSTMMemory* (Ĉ$_{LSTM}$, t,State_id)
Step 17: END FOR
Step 18: best*Affinity* ← *{getBestAffinity* (Clone*Affinities*)}
Step 20: Ω* ← NewFeatureSet(C$_{LSTM}$, best*Affinity*)
Step 20: END FOR

Fig.2. Pseudocode of LSTM-AIRS

LSTM represents a variation of RNN cells, which is easier to train when the vanishing gradient problem is avoided. The vanishing gradient problem emerges during the training of RNNs with long sequential time series data, and the gradient of error concerning the model parameters at early time steps approaches zero. This indicates that it becomes more challenging for the model to learn long-term dependencies in the input time series. For each time series, the propagation of inputs occurs through the recurrent neural network with the memory cells that are newly calculated.
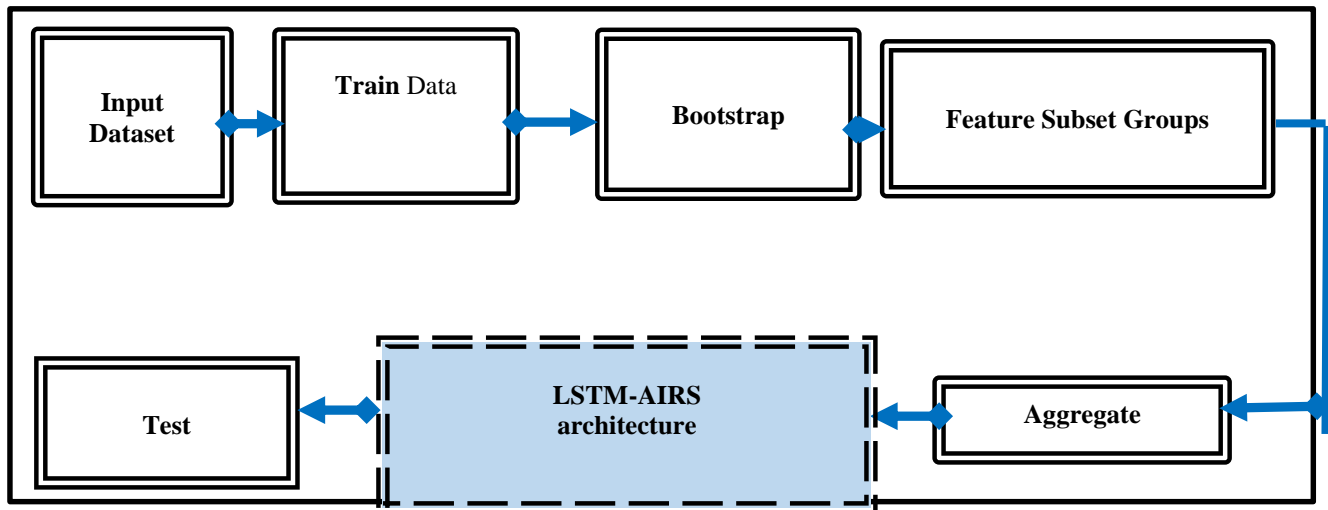
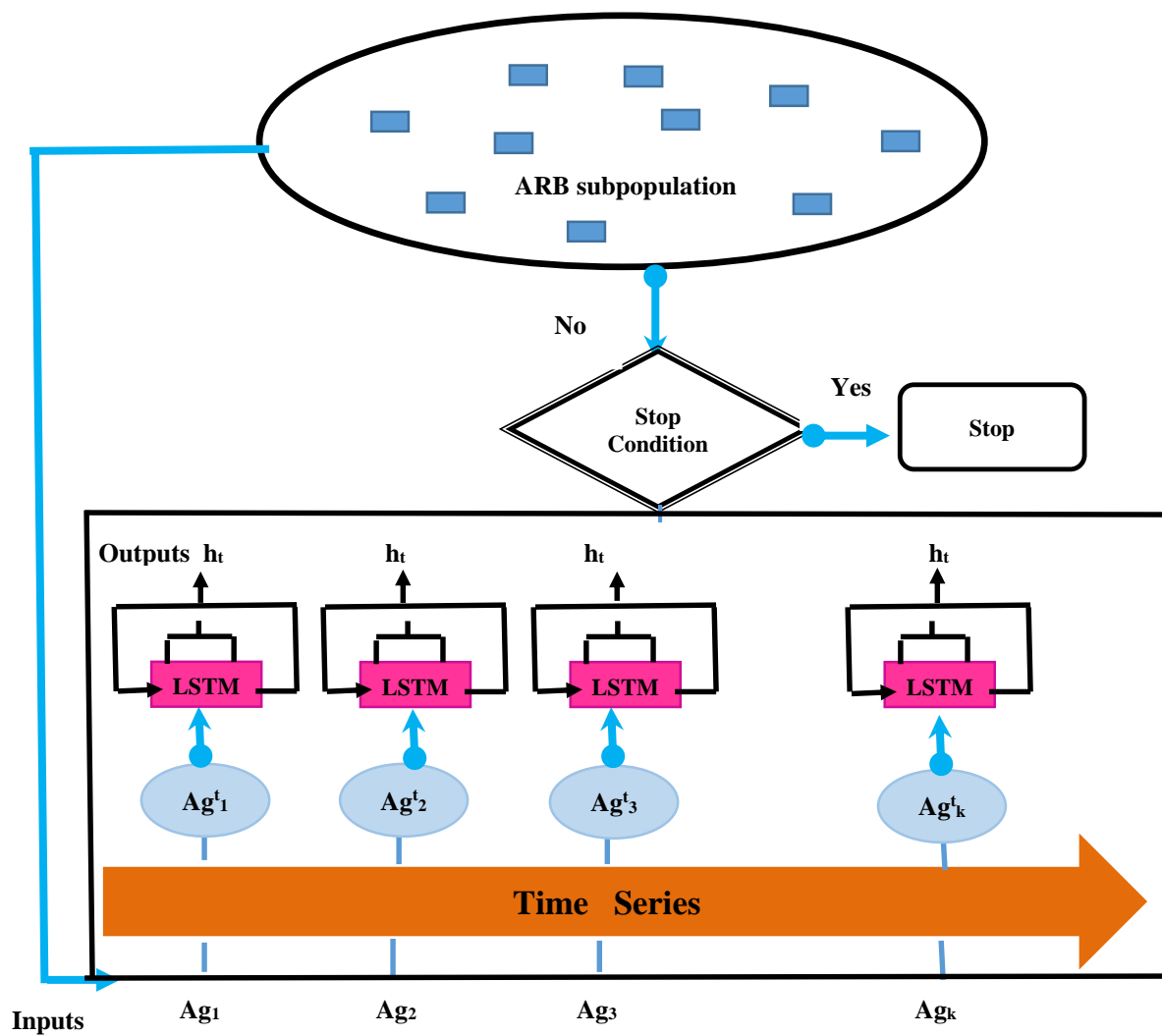Fig. 3. General flowchart of the suggested model

Fig. 4. Pseudocode of LSTM-AIRS

IV. RESULTS AND PERFORMANCE ANALYSIS

This study focused on the robustness of gene selection algorithms. Robust gene sequences were evaluated by the accuracy of each class computed using equation (13):

$$Accuracy = \frac{TP + TN}{TP + FP + FN + TN} \tag{13}$$

The characteristics of gene expression profile (GEP) datasets may cause over-fitting and bias selection problems if small gene sets are selected from large dimensional features. There may be a chance of finding high classification performance from small gene subsets in high-dimensional

datasets. Therefore, robust gene selection algorithms are required for GEP datasets [11]. Some predictor genes were reported in this part. The DAVID and REACTOME programs were used for the biological knowledge discovery of the selected genes. The biological information was extracted from the UNIPROT and NCBI ENTREZ databases. The k-NN and SVM classifiers were used directly as a classifier to measure the classification accuracy of optimal gene subsets. Ten-fold cross-validation was utilized to evaluate the classification model. It was aimed to find reliable accuracy on the training set and test set separately. The frequency measure was used as a measure of the significance of gene subsets in long sequences.

TABLE I
TUMOR-RELATED GENES FOR COLON, LUNG, AND PROSTATE DATASETS

Datasets		Colon Dataset				Lung Dataset				Prostate Dataset			
Algorithms	Group Type	SVM 10 CV on		KNN 10 CV on		SVM 10 CV on		KNN 10 CV on		SVM 10 CV on		KNN 10 CV on	
		Training Set	Test Set	Training Set	Test Set	Training Set	Test Set	Training Set	Test Set	Training Set	Test Set	Training Set	Test Set
LSTM-AIRS1	DGF	79.5	82.1	72.7	76.9	93.2	94.4	96.6	97.2	81.5	80.9	79.1	80.9
	CFG	75.4	79.4	71.4	76.4	82.1	86.1	80.8	88.8	71.9	70.7	77.4	79.8
	IGFG	72.5	76.9	74.3	80.7	84.4	88.1	82.6	83.3	68.4	69.6	75	77.1
LSTM-PAIRS1	DGF	75.4	79.4	71.4	75.4	**98.4**	**98.6**	**97.2**	**97.9**	70.4	72.1	74.1	83.9
	CFG	75.5	80.7	76.3	75.5	86.2	92.8	84.8	93.3	71.1	71.5	77.9	85.7
	IGFG	67.9	71.3	69.7	67.9	87.5	90.7	84.6	91.6	68.9	71	74.6	88.1
LSTM-AIRS2	DGF	81.6	84.6	75.5	79.2	90.7	91.6	89.8	91.6	75.3	76.1	79.1	80.9
	CFG	75.2	76.9	71.4	76.9	82	95.8	82.2	91.3	70.2	71.4	65.8	66.7
	IGFG	67.3	69.2	60	69.2	83.1	86.1	86.8	88.8	70	71.4	60.1	61.9
LSTM-PAIRS2	DGF	**89**	**92.3**	**85.3**	**91.2**	98.3	92.8	97.2	91.6	**92.1**	**84.4**	**88.4**	**76.7**
	CFG	80	86.2	58.7	90.5	82.7	91.6	80.6	91.6	89.5	84.4	87	79
	IGFG	71.4	68.6	71.2	74.5	88.9	97.2	87.5	94.4	72.9	71.5	69.7	70
GA	DGF	63.2	61.5	71.4	76.9	86.1	93.7	90.3	91.6	52.3	80.2	57.1	71.6
	CFG	63.2	69.2	61.2	67.8	82	86.1	78.6	90.8	38	51.8	46.9	61.9
	IGFG	62.7	66	60.8	65.3	82.7	88.8	81.3	89.7	61.7	61.9	59.7	63.5
ANN+GA	DGF	83.6	85.7	81.6	86	90	94.3	91.5	97.9	79.5	80.9	85.1	90
	CFG	71.4	82.6	75.3	87.1	89.2	93	79.3	91.7	65.4	71.5	59.2	79.2
	IGFG	68.9	70.9	66.9	69.8	83.4	95.5	91	91.6	69.3	70.2	53.1	71.6

In all tables, we marked in bold the jointly selected genes based on DGF, CFG, and IGFG for the tested methods. The selected gene sequences were analyzed based on the gene function and pathway analysis. For the colon dataset, the LSTM_PAIRS2 algorithm exhibited the best performance with the training accuracy of 89% and predicting accuracy of 92.3% using the SVM classifier and the training accuracy of 85.3% and predicting accuracy of 91.2% using the k-NN classifier

based on DGF. {R28608, T94993, L19437 (TALDO1), M82919 (GABRB3), T55780} is the selected gene subset in the colon dataset based on DGF. The results in Table 1 show important tumor-related genes preserved in long-lived unit cells. TP53 regulates the transcription of cell cycle genes and performs transcriptional regulation by TP53 pathways [12]. P53 plays an important role in colorectal cancers, and p21 is a critical effector of butyrate-induced growth arrest in colonic

TABLE II
TUMOR-RELATED GENES FOR SRBCT, LYMPHOMA, AND LEUKEMIA DATASETS

Datasets			SRBCT Dataset				Lymphoma Dataset				Leukemia Dataset			
Algorithms	Group Type	SVM 10 CV on		KNN 10 CV on		SVM 10 CV on		KNN 10 CV on		SVM 10 CV on		KNN 10 CV on		
		Training Set	Test Set	Training Set	Test Set	Training Set	Test Set	Training Set	Test Set	Training Set	Test Set	Training Set	Test Set
LSTM-AIRS1	DGF	80	81.5	75.6	78.9	81.7	82.6	81.6	94.4	73.3	83.2	78.7	87.7
	CFG	71.2	73	78.5	79.7	70.3	78.5	80.3	83.2	76	82	80	85
	IGFG	60	61.1	63.4	65.7	65.3	70	77.5	78.3	84.8	85.9	82.4	86.6
LSTM-PAIRS1	DGF	74.2	76.9	76.9	80	84.6	93.3	78.8	95.9	84.6	86.9	80	91.2
	CFG	72	73.8	70	79.6	72.4	78.3	73.4	76.9	77.1	82.5	79	87.3
	IGFG	59.8	68.4	56.7	67.3	70.2	81.6	70	72.7	76.2	86.6	79.8	85
LSTM-AIRS2	DGF	80	92.3	82.6	84.6	**91.8**	**92.3**	**93.8**	**94.6**	84.7	89.2	84.7	93.3
	CFG	74.2	75.4	72.1	76.4	80	84.1	77.2	82.7	77.1	86.6	73.9	93.3
	IGFG	61.3	65	67.3	69.1	81.4	84.6	77.3	92.3	72.4	86.6	68.9	71.9
LSTM-PAIRS2	DGF	**90.8**	**92**	**91.7**	**94.3**	**94.5**	**95.1**	**90.8**	**92.3**	**96.3**	**86.6**	**98.2**	**85.2**
	CFG	76.2	75	71	74.3	86.9	86.8	81.6	84.6	83.3	86.6	85.5	80
	IGFG	65	68	64.3	65.8	80.4	85.9	81.6	92.3	80.5	86.6	69.2	72.3
GA	DGF	66	76.9	68	69.2	81.6	84.6	83.6	92.3	86.6	90.2	80	85.9
	CFG	46	58	58	69.2	72.3	79.2	71.4	78.5	77.9	85.7	63.7	66.7
	IGFG	45.7	46.1	48	49.8	75.5	78.1	73.4	76.9	77.1	83.8	71.9	79.8
ANN+GA	DGF	78.5	82	74.3	86	83.3	90.8	89.7	96	**92.9**	**93.7**	**91.1**	**92.9**
	CFG	65.8	78.7	76	82.3	77.1	82.4	79.5	92.3	79.3	89	70.9	82.1
	IGFG	58.2	65.4	52	69.2	76.3	81.5	77.1	79.8	80	82.8	75.3	81.4

TABLE III
EXPERIMENT RESULTS FOR MICROARRAY DATASETS.

Classifiers	Group Type	Colon Dataset	Lung Dataset	Prostate Dataset	SRBCT Dataset	Lymphoma Dataset	Leukemia Dataset
MLP	DGF	79.2	83.4	72.1	70.6	82.7	83.5
	CFG	76.6	82.6	70.8	69.6	82.4	82.7
	IGFG	74.3	80.5	71.3	68.4*	80.6	81.5
LSTM	DGF	**84.7**	**89.6**	75.7	**77.6**	88.3	85.3
	CFG	82.1	87.4	74.3	75.3	87.8	85.3
	IGFG	77.9	84.5	72.4	73.8	85.7	78.5
GRU	DGF	82.6	88.2	**76.8**	78.1	**89.7**	**88.2**
	CFG	83.7	85.6	71.6	76.7	83.6	84
	IGFG	75.6	81.4	70.3	76.3	83.8	76.1

cancer cells. Activating transcription factor 4 (ATF4) is effective in colorectal cancer [13].

For the lung dataset, the LSTM_PAIRS1 algorithm exhibited the best performance with the training accuracy of 98.4% and predicting accuracy of 98.6% using the SVM classifier and training accuracy of 97.2% and predicting accuracy of 97.9% using the k-NN classifier with selection in the lung dataset based on DGF. The USP32P1, CD44, HCRTR2, TNFSF4, NUP98, CCNO, NCF2, and TCEB3-AS1 genes commonly involved in the metabolism of RNA and class I MHC mediated antigen processing and presentation pathways [14] are expressed in lung cancer.

In the prostate dataset, the highest classification performance was achieved through the LSTM_PAIRS2 algorithm with the

optimal gene set consisting of eight genes, LYL1 (39971_at), HSD17B3 (39978_at), BMPR2 (39998_at), SCARF1 (40034_r_at), ASIC2 (40317_at), DYNC1I1 (40319_at), HSPA4L (40354_at), and ITGA2B (40643_at)}, with the training accuracy of 92.1% and predicting accuracy of 84.4% using the SVM classifier and training accuracy of 88.4% and predicting accuracy of 76.7% using the k-NN classifier based on DGF. The SLC35A2 gene participates in seven different pathways. The ACD gene is involved in eleven different biological pathways, such as reproduction, meiosis, meiotic synapsis, and cell cycle pathways. The RPL10A gene is involved in 32 different biological pathways. The RPL10A gene is involved in SRP-dependent cotranslational protein targeting to membrane pathway and plays a role in proteins upregulated in prostate cancer. The RPL10A gene takes part in the base regulation of expression of SLITs and ROBOs. SLITs and ROBOs are expressed during the development of prostate cancer.

For the SRBCT dataset, the LSTM_PAIRS2 algorithm exhibited the best classification performance with the {GNAO1, DNAJA1, PSMB10, PRKCE6(PML), MDK, XRCC5} gene subset with the training accuracy of 90.8% and predicting accuracy of 92% using the SVM classifier and training accuracy of 91.7% and predicting accuracy of 94.3% using the k-NN classifier based on DGF. The selected gene, PSMB10, participates in the stabilization of p53, regulation of TP53 expression, p53-dependent G1 DNA damage response, and p53-dependent G1/S DNA damage checkpoint pathways. XRCC5 is X-ray repair cross complementing 5, ERCC2 is ERCC excision repair 2, TFIIH core complex helicase subunit [15], POLG is DNA polymerase gamma, catalytic subunit, EIF2S1 is eukaryotic translation initiation factor 2 subunit alpha.

For the lymphoma dataset, the results show that the LSTM_AIRS2 algorithm exhibited the best performance with the training accuracy of 91.8% and predicting accuracy of 92.3% using the SVM classifier and training accuracy of 93.8% and predicting accuracy of 94.6% using the k-NN classifier. The LSTM_PAIRS2 algorithm exhibited the classification performance with the training accuracy of 94.5% and predicting accuracy of 95.1% using the SVM classifier and training accuracy of 90.8% and predicting accuracy of 92.3% using the k-NN classifier while selecting the {GENE595X, CARP cardiac ankyrin repeat protein, GENE585X, TNNT1 troponin T1, skeletal, slow.GENE771X, Homo sapiens mRNA; cDNA } gene subset in the lymphoma dataset based on DGF. Type II transmembrane protein contains C-lectin domains and is related to DC-SIGN [16].

For the leukemia dataset the {ATP6V0C; ATPase, H+ transporting, lysosomal 16kDa, V0 subunit c, CTSD; cathepsin D lysosomal aspartyl peptidase, AKT1; v-akt murine thymoma viral oncogene homolog 1, CSRP1; cysteine and glycine-rich protein 1, TGFBI; transforming growth factor, beta-induced, 68kDa, CCND3; cyclin D3, SERPINB1; serpin peptidase inhibitor, clade B ovalbumin, member 1} gene subset was selected based on DGF by the LSTM_PAIRS2 algorithm with the training accuracy of 96.3% and predicting accuracy of 86.6% using the SVM classifier and training accuracy of 98.2% and predicting accuracy of 85.2% using the k-NN classifier.

Table 3 shows the experimental performance results of Multi-Layer Perceptron (MLP), Long-Short-Term Memory (LSTM), Gated Recurrent Unit (GRU) classifiers using Deep Learning 4j (DL4J). The results present the GRU and LSTM classifiers had best performances by 89.7 and 89.6 accuracies with Lymphoma and Lung datasets respectively based on the DGF feature group. Also, GRU classifier had accuracy 88.2 with Leukemia dataset based on the DGF feature group. The results of Table 3 presents the worst classification accuracy obtained by MLP classifier with SRBCT dataset with 68.4 accuracies based on the IGFG feature group.

Figure 5-7 show the classification performance of the algorithms on the basis of the datasets. The results showed the lung dataset obtained the best classification accuracy of 94.2% by the LSTM-PAIRS1 and ANN+GA algorithms using the k-NN classifier. At the same time, the prostate dataset obtained the lowest classification accuracy of 50.6% by the GA algorithm using the SVM-train and SVM classifier.
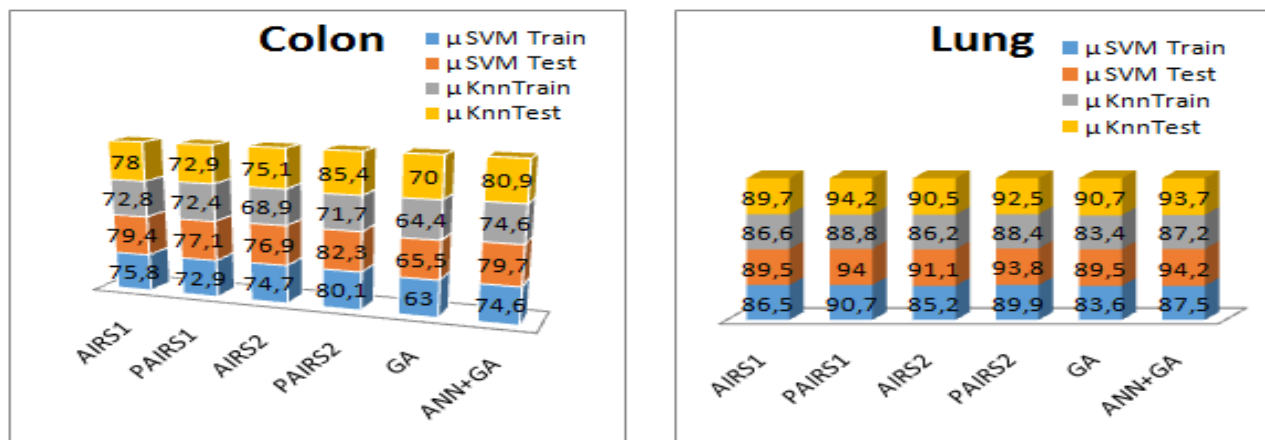

Fig. 5. Classification performance of the colon and lung datasets based on the algorithms
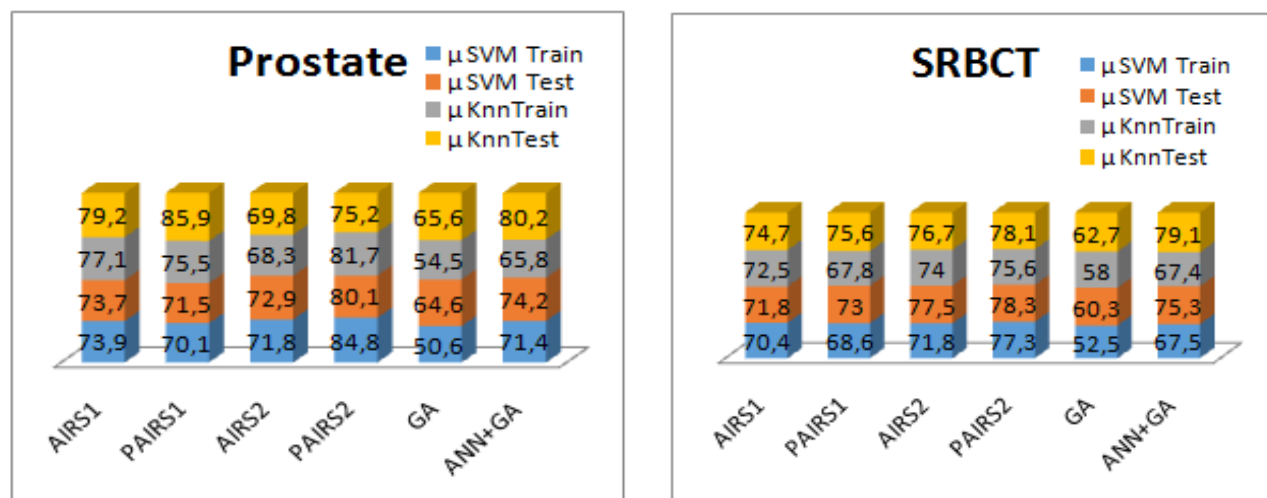
Fig. 6. Classification performance of the prostate and SRBCT datasets based on the algorithms
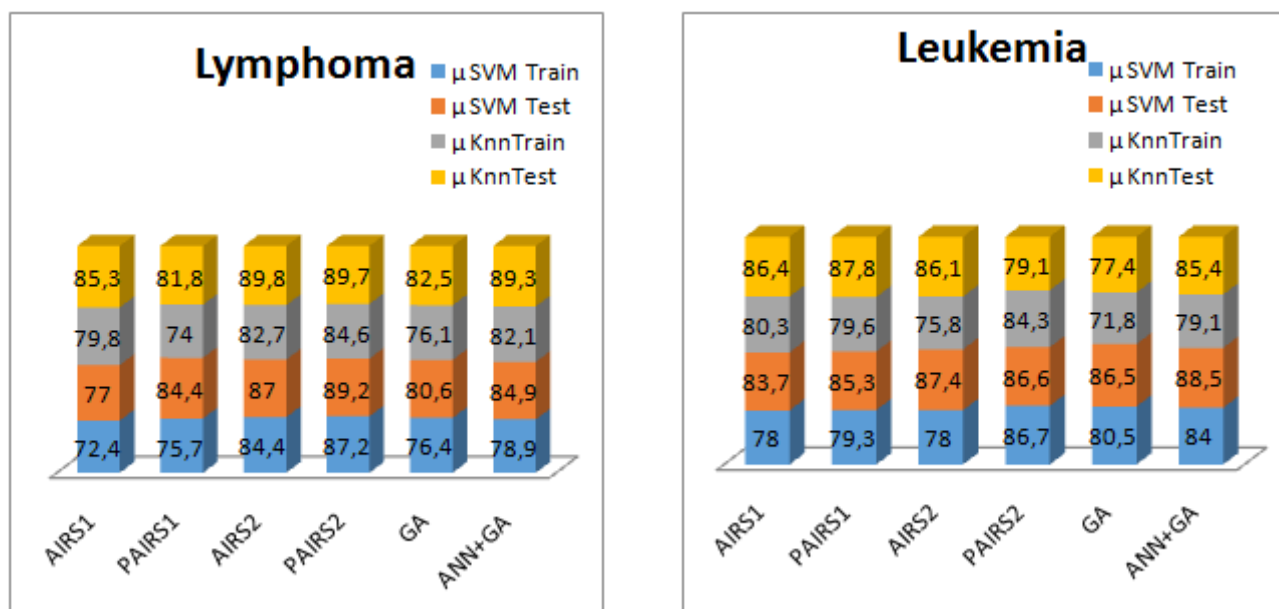

Fig. 7. Classification performance of the lymphoma and leukemia datasets based on the algorithms

V. CONCLUSION

The framework showed that predictive genes for biological sequences were important in gene expression microarrays. It was also found that the gene subsets selected by the algorithms were involved in important biological pathways. LSTM was used to learn sequences over time. The suggested framework was proposed for converting immune memory into an intelligent network system. The analysis of gene sequences was performed, and informative genes from each dataset were detected. This study confirmed that different genes could be found in the same pathways. Optimal gene subsets were obtained from six commonly used microarray datasets.

In future research, our aim is to investigate different deep neural network models (e.g., the BiLSTM network, CNN network) to improve the performance of the proposed model. Furthermore, it is crucial to evaluate the proposed methodology on other datasets. For future studies, we also aim to conduct an assessment of biomarker detection on different types of techniques presented for the detection of Coronavirus (COVID-19).

References

[1] Chowdhury S., Dong X., Li X.,"Recurrent Neural Network Based Feature Selection for High Dimensional and Low Sample Size Micro-array Data", IEEE International Conference on Big Data (Big Data), 978-1-7281-0858-2/19/$31.00, 2019.
[2] Chen Z., Pang M., Zhao Z., et al. "Feature Selection may Improve Deep Neural Network for the Bioinformatic Problem", Bioinformatics. Doi: 10.1093/bioinformatics/btz763, 36(5), 2019.

[3] Mabu A., Prasad R., Yadav R., "Gene Expression Dataset Classification Using Artificial Neural Network and Clustering-Based Feature Selection", International Journal of Swarm Intelligence Research. Doi: 10.4018/IJSR20200104, 2020.

[4] Zhu W.., Xie L., Han J., Guo X., "The Application of Deep Learning in Cancer Diagnosis", Cancers. *12*(3), 603; https://doi.org/10.3390/cancers12030603, 2020.

[5] Zeebaree D., "Gene Selection and Classification of Microarray Data Using Convolutional Neural Network", International Conference on Advanced Science and

Engineering (ICOASE), Doi: 10.1109/ICOASE.2018.8548836, 2018.

[6] Nava A. R., Sánchez J. S., Alejo R., Flores-Fuentes A. A., Rendón-Lara E., "The Application of Deep Learning in Cancer Diagnosis", Pattern Recognition, Doi:10.1007/978-3-319-92198-3_11, 2018.

[7] Jiang Y., Yang. M., Wang S., Li X.., Sun Y., "Emerging Role of Deep Learning-Based Artificial Intelligence in Tumor Pathology", Cancer Communications, doi: 10.1002/cac212012, 2020.

[8] Rubvurm M., Körner M., "Temporal vegetation modelling using long short-term memory networks for crop identification from medium-resolution multi-spectral satellite images", The IEEE Conference on Computer Vision and Pattern Recognition (CVPR), USA, 2017.

[9] Dasgupta D., Nino L.F., Immunological computation: theory and applications. 2009 by Taylor & Francis Group, LLC. Book, 2009.

[10] Chung Y., et al., "Empirical evaluation of gated recurrent neural networks on sequence modeling", Neural ComputAppl arxiv:1412.3555v1, 2014.

[11] Luque-Baena R.M., Urda D., Gonzalo Claros M., Franco L., and Jerez J.M., "Robust genesignatustes from microarray data using genetic algorithms enriched with biological pathway keywords", Journal of Biomedical Informatics, http://dx.doi.org/10.1016/j.jbi.2014.01.006, 2014.

[12] https://machinelearning-blog.com/2018/02/21/recurrent-neural-networks/

[13] https://www.cs.waikato.ac.nz/ml/weka/

[14] https://worldwidescience.org/topicpages/i/immunity-related+gtpase+irgml.html

[15] https://www.genecards.org/cgiin/carddisp.pl?gene=PCBP4

[16] http://www.bionewsonline.com/

[17] Loscalzo S., YU L., Ding C., "Consensus Group Stable Feature Selection", June 28–July 1, Paris, France, 2009.

[18] Loscalzo S., YU L., Ding C., "Stable Feature Selection via Dense Feature Groups", August 24–27, Las Vegas, Nevada, USA, 2008.

[19] Farhan M., Mohsin M., HamdanA., Bakar A.A., "An evaluation of feature selection technique for dentrite cell algorithm", IEEE, 2014.

[20] Schmidhuber, J., Wierstra, D., and Gomez, F. J. Evolino: "Hybrid neuroevolution/optimal linear search for sequence prediction". In Proceedings of the 19th International Joint Conference on Artificial Intelligence (IJCAI), pp. 853–858, 2005

[21] Ferreira A.j. (2014), "Feature selection and discretization for high-dimensional data", Phd Thesis.

[22] Mazel J. (2011), "Unsupervised network anomaly detection", Phd Thesis.

[23] Polat K., Güneş S., Sahan S., Kodaz H., (2005), "A New Classification Method for Breast Cancer Diagnosis: Feature Selection Artificial Immune Recognition System (FS-AIRS)", Berlin.

[24] Menon A. edited by. (2004). Frontiers of Evolutionary Computation, Kluwer academic Publishers, Pittsburgh, USA.

[25] Oh S., Lee J.S., Moon B.R. (2004). Hybrid Genetic Algorithms for Feature Selection.Vol. 26, No.11, November.

[26] Brownlee J. (2005). "Clonal Selection Theory & Clonalg the Clonal Selection Classification Algorithm (CSCA), Technical Report.

[27] Dudek G. (2012). "An Artificial System for Classification with Local Feature Selection", IEEE Transaction on Evolutionary Computation. December 2012, Czestochowa.

[28] Wang K., Chen K., Adrian A., (2014), "An improved artificial immune recognition system with the opposite sign test for feature selection", Knowledge-Based Systems, Taiwan.

[29] Daga M., Lakhwani K., (2013), "A Novel Content Based Image Retrieval Implemented By NSA of AIS", International Journal of Scientific & Technology Research.

[30] Farhan M., Mohsin M., Hamdan A., Bakar A.A., (2014), "An Evaluation of Feature Selection Technique for Dendrite Cell Algorithm", IEEE.

[31] Gu F., Greensmith J., Aickelin U., (2008), "Further Exploration of the Dendritic Cell Algorithm: Antigen Multiplier and Time Windows", ICARIS 2008.

[32] Wollmer M., Eyben F., Rigoll G., (2008), "Combining Long Short-Term Memory and Dynamic Bayesian Networks for Incremental Emotion-Sensitive Artificial Listening", Journal of Selected Topics in Signal Processing.

[33] Daga M., Lakhwani K., (2013), "A Novel Content Based Image Retrieval Implemented By NSA Of AIS", International journal of scientific & technology research

[34] Kalousis A., Prados J. and Hilario M., (2007), "Stability of Feature Selection Algorithms: a study on high-dimensional spaces", Knowledge and Information Systems.

[35] Saeys Y., Abeel T., and Peer Y.V. (2008), "Robust Feature Selection Using Ensemble Feature Selection Techniques". In Proceedings of the ECML Conference, pages 313-325.

BIOGRAPHIES

Canan BATUR ŞAHİN is an Assist. Prof. Dr. at Malatya Turgut Ozal University. She received her diploma and Ph.D. degrees in Computer Engineering from Yildiz Technical University. Her research interests include optimization, artificial intelligence, and software engineering.

Banu DİRİ is a professor at Yildiz Technical University, and she works on natural language processing. She authored more than 150 publications in this field. Her research interests include speech recognition, natural language processing, and machine learning.

RFID based Authorization Method for Computer Systems in Smart Library Environments

M. BAYGIN, O. YAMAN, A. C. TOPUZ and S. S. KALELI

Abstract—In recent years, intelligent systems have emerged with the concept of the Internet of Things. The purpose of intelligent systems is to use technological innovations to improve the quality of life of people. Smart systems are now being used almost everywhere. Concepts such as smart city, smart classroom, smart library, smart hospital and smart transportation have emerged. With the cameras, sensors and many other devices used in smart systems, data from the environment can be analyzed and remote control operations can be performed. In this study, RFID based authorization system has been developed in the publicly available computers used in smart libraries. In many places, as in universities, there are common computers or laboratory devices that can be used by everyone. The aim of this study is to ensure the common use of devices belonging to common use against existing users. The devices are controlled by an RFID based system developed for these devices. Using the ID cards of the students or staff, the person is authorized to use the devices for the defined period of time. This study has two main contributions. First, a modular system compatible with all electronic devices except the computer has been made by using RFID technology. The second is to provide a more efficient working environment by ensuring fair use of computers and other devices accessible.

Index Terms— Internet of Things, Library management systems, RFID, Smart library.

MEHMET BAYGIN, is with Department of Computer Engineering Ardahan University, Ardahan, Turkey, (e-mail: mehmetbaygin@ardahan.edu.tr).

https://orcid.org/0000-0002-5258-754X

ORHAN YAMAN, is with Department of Computer Engineering Firat University, Elazig, Turkey, (e-mail: orhanyaman@firat.edu.tr).

https://orcid.org/0000-0001-9623-2284

ARIF CEM TOPUZ, is with Department of Computer Engineering Ardahan University, Ardahan, Turkey, (e-mail: arifcemtopuz@ardahan.edu.tr).

https://orcid.org/0000-0002-5110-5334

SALIH SERKAN KALELI, is with Department of Business Management Ardahan University, Ardahan, Turkey, (e-mail: salihserkankaleli@ardahan.edu.tr).

https://orcid.org/0000-0003-2196-6050

I. INTRODUCTION

NOWADAYS, THE use of intelligent systems is generally aimed at regulating the work of end users and providing important advantages to the end user on time basis. In addition, the most important advantages of these systems are to save the end user from certain workloads, to enable the system to make decisions on its own, and to automate the periodic processes. From this point of view, it has been observed that serious problems and imbalances have been experienced especially in computer use by students. In addition, it was found out that the computer services provided by the library unit and generally provided for use in catalog scanning and research and development activities were used by the students against their purpose and the computers were constantly occupied due to this situation. In addition, the use of these computers as a personal computer by some students causes them to occupy them for hours and prevent a user from searching for catalogs or research activities.

Technological advances ensure that the existing systems are carried out quickly, reliably and consistently. It also plays a major role in the emergence of new systems. The technological devices produced to meet the requirements of the era continue to be inspired by the human mind. Thus, they have gained the ability to decide on their own by exceeding the feature of executing only the given command. These developments in almost every field have also started to be used in library systems. With the development of computer-aided search systems, the disadvantages of man-based systems were eliminated. Library software, which is widely used in our country, provides a fast and reliable service in many fields such as questioning, tracking, loan / return transactions and placement of books and documents. Moreover, with the protocols they use, they gathered the database and hardware resources known as necessity in the existing library automation under a single roof. Thus, the installation of a database and hardware was prevented over and over again in each area where the system was installed [1].

As a result of the researches, it has been found that RFID technology is used in many different fields and it is seen that it is one of these fields in its libraries [1-6]. In a study conducted for libraries using RFID technology, it was

provided to control the library as a whole by using Motorola MC9090 series handheld terminals. Each book in the library is equipped with a label and each of these books is assigned a separate electronic code, which is completely related to the database. Thanks to this developed system, a misplaced book, a missing book or undelivered books can be identified exactly. Furthermore, manual system was prevented with the developed system and problems in the library were minimized as much as possible [7].

RFID technology has an important place especially in the Internet of Things (IoT) concept [8, 9]. IoT is basically the process where devices can communicate between each other, share information and organize the working principle in this context [10, 11]. IoT applications take place in a wide range of areas [12, 13]. Some of these areas; health care, supply chain, logistics, mining, transport, firefighting, smart homes, building automation, smart cities and energy management [14-19]. Naturally, RFID technology plays an active role in almost all of these areas. Therefore, the concept of IoT and RFID are highly interrelated [20-23]. RFID, a core of IoT technology, was first used to identify friendly or enemy aircraft systems during the second world war [20]. This refers to a type of non-contact automatic identification system [21]. In other words, it identifies the object via radio frequencies and provides access to the associated data without the need for physical contact with any humanoid [22]. RFID systems are basically composed of 3 sections. These sections are RFID Tag, RFID reader and server sections, respectively. A block diagram summarizing the architecture and operating principle of RFID systems is given in Fig. 1.
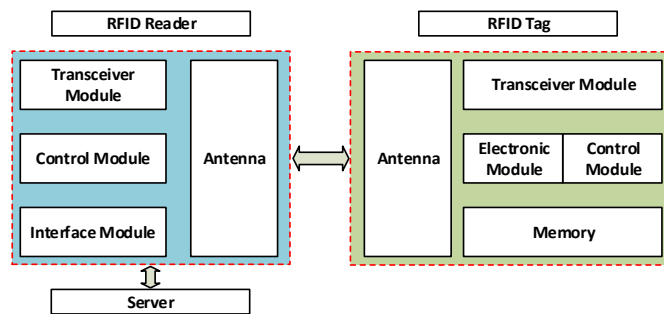

Fig. 1. RFID system architecture [22]

In another study on the subject, an RFID based application was developed for the medical health system. In practice, developed primarily for the purpose of medical confidentiality, patient ID, drug management and patient information are stored on RFID cards, and access is provided only to readers [24]. With RFID technology, the identification process allows the data to be collected and differentiated from each other by clarifying the characteristics of the object or living thing. Barcodes, smart cards and biometric technologies are widely used in recognition technology. The common feature of these systems is that they allow data to be received by contact or close distance. In RFID technology, data acquisition is provided by the object or living being within the range of the reader. In addition, physical problems such as impacts,

scratches caused by user-related problems in similar technologies make data retrieval difficult. RFID tags do not cause such problems. The possibilities of RFID technology are shown in Fig. 2.
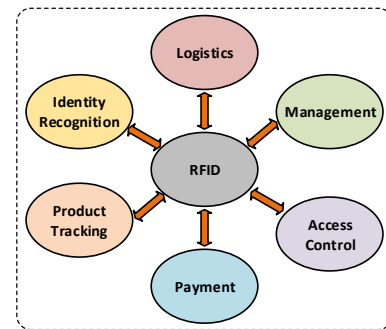

Fig. 2. The possibilities of RFID technology

II. PROPOSED METHOD

With this project, which is aimed to be developed and realized, all these situations are prevented and the computers used actively in the library unit are made smart and students are provided to use the computers in a more fair and orderly manner. With the hardware and software improvements to be realized within the scope of the project work, students can activate these computers with their own school ID cards, then use the computers for a period of time defined for each student and finally the system turns itself back to passive position. In the first stage of this proposed study, a hardware PCB board was developed. For this purpose, a card reader / writer interface has been developed and USB connection has been provided to the computers in the library unit. In the next stage of the system, software development process was applied for the computers in the library unit. With the help of this software, the Ethernet port of the computer is activated and the computer is ready for use by logging on to the card reader. In the last stage of the system, the software automatically shuts down the computer at the end of the specified period, the Ethernet port is disabled and the student's computer usage is terminated. A block diagram showing these stages and the relationship between these stages is given in Fig. 3.
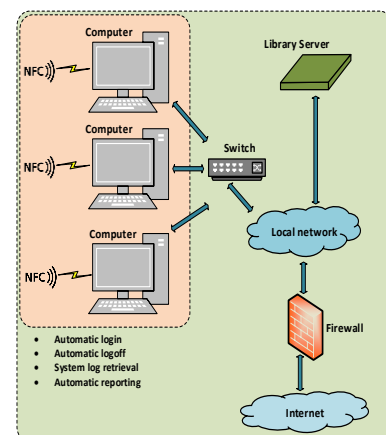

Fig. 3. A block diagram summarizing the proposed system

As shown in Fig. 3, the system expects to first read the user's ID card. With the designed ID card reading system, the information stored on the user's card is transmitted to the web service to be provided by the university over the local network. Upon the arrival of the student ID information to the web service, the query is performed in the database and information is obtained whether the student has the right to use the computer. Then, this information is returned to the computer in the library unit and the student is logged in through the software. After the user login, the system receives the date / time and starts to process the time for that student. The student can use the computer for a predefined period of time and after the expiration of the period, the computer turns itself off. The hardware and software unit developed in this study has a modular structure. Thus, it is aimed that card readers can be used in different units and areas in the following processes.

In the first stage of the proposed system, the hardware development process is completed. For this purpose, Arduino Pro Mini programming card is used primarily. The main reason for this is that these cards allow to recognize various additional cards and their cost is low. In addition, RFID RC522 series card reader which is compatible with these cards was used in the first stage. At this stage of the system, the integration of the processor and the RFID card series is provided and both read and write operations are performed from the student ID cards. In the next stage of the system, USB communication is made for these card readers to connect with the computer. Readers will be supplied with power via the USB line and a communication line will be installed. In the third stage of the system, a web service was prepared to communicate with the existing university server and to withdraw student information from the system. With this web service, the authentication process of the students who read their ID cards is performed. In addition, depending on the information taken, the time, date and time information defined for the students is recorded on the card and the student's session is started. In the fourth stage of the project work, a printed circuit board was prepared for the processor and rfid card and these cards were made compatible with each other on a single platform. In the fifth stage of the system, the previously prepared software and hardware modules will be brought together and the integration of the modules is ensured. In the sixth stage of the study, the product was packaged and made ready for use. The hardware connection of the developed system is given in Fig. 4.
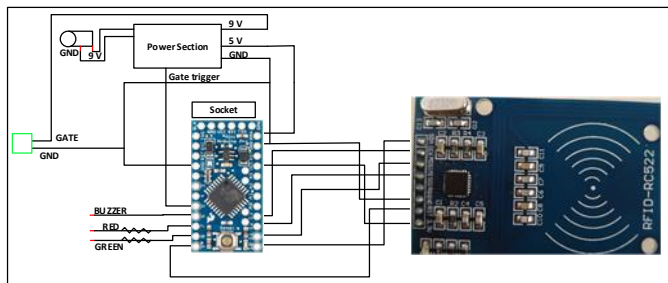

Fig. 4. Hardware connection of implemented system

As can be seen in Fig. 4, the hardware module of the system consists essentially of two parts. The first part is the processor part. This unit is the part that will process students' cards. The second part is RFID-RC522. With this equipment, the information in the student ID cards can be read and writing process can be provided by this card if necessary.

Another module of the system is the software section. On the software side, a platform is established to communicate with the university server. The information obtained through the hardware module from the student ID card is transmitted to the university server via a web service and the accuracy of the student ID card is ensured by the inquiry to be performed at that point. At this point, the user logs on to the computer with the information to be returned from the server and again, this login status and date, time information is processed on the student's card with the hardware module. A block diagram summarizing the steps of the software development process is given in Fig. 5.
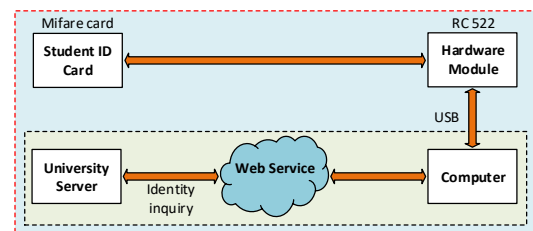

Fig. 5. Software block diagram of realized system

The final printed size of author photographs is exactly 1 inch wide by 1.25 inches tall (25 millimeters x 38 millimeters / 6 picas x 7.5 picas). Author photos printed in editorials measure 1.59 inches wide by 2 inches tall (40 millimeters x 50 millimeters / 9.5 picas x 12 picas).

III. EXPERIMENTAL RESULTS

Thanks to the intelligent computer control application performed in this study, students' use of computers is provided in a fair way, usage periods and movements are recorded and computers are made more secure. Especially considering the fact that illegal movements are frequently experienced in the virtual environment, it is extremely important to obtain information on which computer, on which days and hours the students use.

Experimental studies conducted are basically under two headings. The first of these studies is the hardware side of the system. On the second side of the system, simulation process of the developed hardware card was performed. These studies are presented in sub-sections below.

A. Hardware Module

The developed system can be integrated with existing ID cards and allows the system to be modified and used for many different purposes. Although the proposed study was developed for the library unit, it can be used in laboratory environments, university exits and collective environments such as dormitories upon request. Considering the limitations of the system, in order to be able to use the existing ID cards in this system, these cards must have 125 KHz Proximity Card feature and be open to read / write operations. In

addition, in order to use the developed system actively, a web service should be opened by the university server and student inquiry can be made through this web service. The names and models of the hardware used in the developed system are given in Table 1.

TABLE I
HARDWARE MATERIALS USED IN THE DEVELOPED SYSTEM

Name	Model
Programming Card	Arduino Pro Mini
Card Reader	RC522
Resistor	1K, 10K,
Capacitor	100nf, 470uf/25V, 1000uf/16V
Diode	1N4007
Transistor	BC337
Power	LM7805
Other	5V Relay, 5V Buzzer

PCB board was developed by using the hardware materials given in Table 1. The programming card on the PCB board is connected to the computer via USB interface. It provides automatic login and management by reading the students' ID cards. The prototype of the system developed in this study is given in Fig. 6.
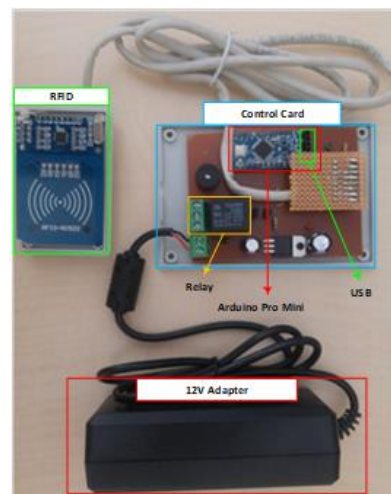

Fig. 6. Prototype of the system developed in this study

B. Simulation Results

In order to test the RFID based authentication method proposed in this study, a simulation was developed in MATLAB environment. During the simulation process, 6 different scenarios were planned. The scenario results made are given in Table 2.

TABLE II
SIMULATION RESULTS OBTAINED BY TESTING THE RFID SYSTEM

Scenario	Number of PCs	PC Usage Limit (min)	Number of Users [0-100]	Usage time limit in the current system(min)	Number of users who timed out	Total time in the normal process(min)	Total time elapsed with the developed system (min)	Difference (min)	Performance (%)
1	10	30	27	40	8	526	488	38	7,79
	20	30	28	40	9	644	599	45	7,51
	30	30	89	40	27	2043	1900	143	7,53
	40	30	16	40	3	318	294	24	8,16
	50	30	7	40	3	165	152	13	8,55
2	10	30	89	50	40	2339	1985	354	17,83
	20	30	53	50	11	1076	950	126	13,26
	30	30	68	50	25	1663	1433	230	16,05
	40	30	91	50	39	2314	1938	376	19,40
	50	30	84	50	38	2291	1879	412	21,93
3	10	30	53	60	23	1556	1192	364	30,54
	20	30	86	60	46	2749	2016	733	36,36
	30	30	18	60	10	569	429	140	32,63
	40	30	46	60	27	1518	1091	427	39,14
	50	30	35	60	18	1107	793	314	39,60
4	10	40	40	40	1	937	937	0	0,00
	20	40	45	40	4	1103	1103	0	0,00
	30	40	52	40	1	985	985	0	0,00
	40	40	37	40	0	803	803	0	0,00
	50	40	20	40	0	460	460	0	0,00
5	10	40	28	50	8	755	705	50	7,09
	20	40	13	50	3	329	319	10	3,13
	30	40	58	50	12	1400	1345	55	4,09
	40	40	82	50	14	2018	1959	59	3,01
	50	40	73	50	19	1988	1894	94	4,96
6	10	40	90	60	31	2665	2367	298	12,59
	20	40	20	60	9	701	611	90	14,73
	30	40	68	60	23	2178	1890	288	15,24
	40	40	90	60	35	2793	2476	317	12,80
	50	40	88	60	28	2718	2389	329	13,77

Calculations were made for five different computers for each scenario. In scenario 1, users' time to use computers is limited to 30 minutes for 5 different computers. The number of people using common computers was chosen randomly between 0 and 100 during the simulation of 5 different computers. The number of randomly selected users for Scenario 1 is limited to 40 minutes on computers. This limit value is set as 50 minutes for Scenario 2 and 60 minutes for Scenario 3. In Scenario 1, 27 people are randomly selected for a common use area with 10 computers, and their computers are chosen randomly between 0 and 40 minutes. As a result of this process, if the RFID based system is not used, a total of 526 minutes of time is needed for 27 users, while a total of 488 minutes is required in the RFID-based developed system. Thus, thanks to the developed system, 27 people made the best use of 10 computers in less time. When Scenario 2 is examined, computer usage times are randomly selected between 0 and 50 minutes in the current system. In the third scenario, it is chosen randomly between 0 and 60 minutes. When the first three scenarios are examined, it is seen that the advantage of the system developed when the computer usage time limit increases in the existing system. In scenario 4, the system computer usage time limit is equal to the current system computer usage time limit. Therefore, the advantage of the developed system is not clearly visible for the 4th Simulation. The advantage of the RFID system developed in other scenarios has been revealed. For 6 scenarios in the study, scenarios 1,2 and 3 and scenarios 4,5 and 6 were grouped within themselves. While the computer usage limit for the system developed in Scenarios 1,2 and 3 is 30 minutes, Scenarios 4,5 and 6 are 40 minutes. The average efficiency obtained in these grouped scenarios and the average gain from the whole simulation are presented in Table 3. According to these values, the success results of the method are shown in Fig. 7.

In figure 7-(a) the scenarios of Scenarios 1,2 and 3, that is, the computer usage limit in the developed system is 30 minutes, are given. Here, the "x" axis is the number of computers, the "y" axis is the computer usage time in the current system, and the "z" axis is the amount of time profited in the developed system. The unit of the "y" axis and the "z" axis are given in minutes. In Figure 7-(b), the success results of Scenarios 4,5 and 6 are given. The computer usage limit for the system developed in these scenarios is determined as 40 minutes. In the simulation, if the computer usage limit in the developed system is far from the computer usage limit in the existing system, the success of the system increases even more.

Thanks to the developed system, the number of computers and number of instantaneous users in the common use areas are optimized according to the usage time determined by the administrator. It provides the best and fair use of users from computers in the current common area. Thus, the limited number of computers in common areas are provided with the best service.

TABLE III
AVERAGE RESULTS BY SCENARIOS

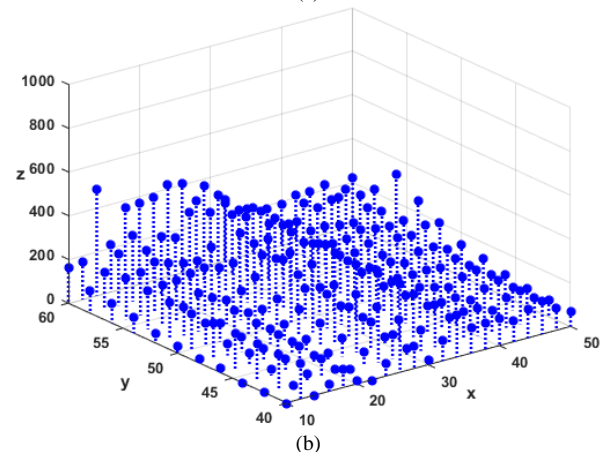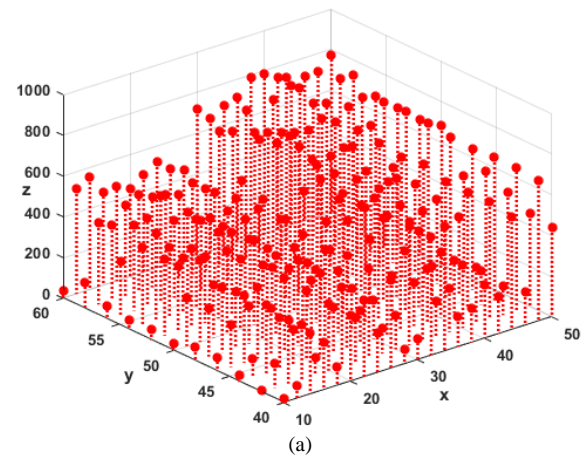| Scenario	Average Result (min)	Average for Groups (min)
1	52,6	
2	299,6	249,27
3	395,6	
4	0,0	
5	53,6	106
6	264,4	
General Avg.		**177,63**

(a)

(b)

Fig. 7. Displaying the success results of the scenarios in 3 dimensions
(a) Scenario 1,2 and 3 result (b) Scenario 4,5 and 6 result

IV. DISCUSSION AND CONCLUSIONS

With this study, RFID cards, which are frequently used in literature and in the market, are used for intelligent computer control application. As stated in the literature summary, intelligent systems have become an important part of our daily life. Given the operating principle of these systems, it is almost inevitable to use RFID card systems. With the developed RFID card reader system, fair computer usage of the students will be ensured and their usage on the computer can be observed. With the developed smart computer control application, the computers in Ardahan University library unit can be used more effectively and in a suitable way. In the use of these computers where there is no control mechanism in the current system, completely technological and smart solutions have become available. When the studies on the subject are examined in the literature, it is seen that the term

smart systems and industry 4.0 are generally encountered. In addition, it has been observed in the researches that the transactions carried out for this purpose are generally aimed at a specific purpose, the existing order is changed from the identity cards used to all electronic equipment and solutions are produced with very high budgets depending on this situation.

This system developed within the scope of the study was put into use as a pilot in the library unit of Ardahan University. This system, which is used in the library unit, regulates the students' use of computers, restricts illegal movements and limits unnecessary computer use. Studies have shown that RFID card systems are frequently used in campus areas such as book rental, bicycle rental, refectory and turnstile areas rather than libraries. With the proposed system, a different area is provided for the use of RFID cards within the campus. In addition, this system is planned to be used for different service points within the campus.

ACKNOWLEDGMENT

REFERENCES

[1] C. M. Roberts, "Radio frequency identification (RFID)," Computers & Security, vol. 25, no. 1, 2006, pp. 18-26.
[2] A. Ustundag. "The value of RFID," Springer London Limited, 2013.
[3] N. Saparkhojayev & S. Guvercin, "Attendance Control System based on RFID technology," International Journal of Computer Science Issues (IJCSI), vol. 9, no. 1, pp. 227-230, 2012.
[4] M. Dhanalakshmi & U. Mamatha, "RFID based library management system," Proceedings of ASCNT, pp. 227-234, Noida, India, 2009.
[5] K. Coyle, "Management of RFID in Libraries," The Journal of Academic Librarianship, vol. 31, no. 5, pp. 486-489, 2005.
[6] I. Markakis, T. Samaras, A. C. Polycarpou & J. N. Sahalos, "An RFID- enabled library management system using low-SAR smart bookshelves," International Conference on Electromagnetics in Advanced Applications (ICEAA), pp. 227-230, Torino, Italy, 2013.
[7] A. P. Renold & R. J. Rani, "An internet based RFID library management system," IEEE Conference on Information & Communication Technologies, pp. 932-936, Tamil Nadu, India, 2013.
[8] Z. Bi, Y. Liu, J. Krider, J. Buckland, A. Whiteman, D. Beachy & J. Smith, "Realtime force monitoring of smart grippers for Internet of Things (IoT) applications," Journal of Industrial Information Integration, vol. 11, pp. 19-28, 2018.
[9] H. Chen, "Applications of cyber-physical system: a literature review," Journal of Industrial Integration and Management, vol. 2, no. 3, 2017.
[10] F. Civerchia, S. Bocchino, C. Salvadori, E. Rossi, L. Maggiani & M. Petracca, "Industrial Internet of Things monitoring solution for advanced predictive maintenance applications," Journal of Industrial Information Integration, vol. 7, pp. 4-12, 2017.
[11] S. Fang, X. L. Da, Y. Zhu, J. Ahati, H. Pei, J. Yan & Z. Liu, "An integrated system for regional environmental monitoring and management based on internet of things," IEEE Transactions on Industrial Informatics, vol. 10, no. 2, pp. 1596-1605, 2014.
[12] J. H. Kim, "A review of cyber-physical system research relevant to the emerging IT trends: industry 4.0, IoT, big data, and cloud computing," Journal of Industrial Integration and Management, vol. 2, no. 3, 2017.
[13] C. T. Lai, P. R. Jackson & W. Jiang, "Shifting paradigm to service-dominant logic via Internet-of-Things with applications in the elevators industry," Journal of Management Analytics, vol. 4, no. 1, pp. 35-54, 2017.
[14] Y. Lu & L. X. Da, "Internet of Things (IoT) cybersecurity research: a review of current research topics," IEEE Internet of Things Journal, vol. 6, no. 2, pp. 2103-2115, 2018.
[15] G. Peretti, V. Lakkundi & M. Zorzi, "BlinkToSCoAP: An end-to-end security framework for the Internet of Things," International Conference on Communication Systems and Networks (COMSNETS), pp. 1-6, Bangalore, India, 2015.
[16] Z. Rashid, J. Melià-Seguí, R. Pous & E. Peig, "Using augmented reality and internet of things to improve accessibility of people with motor disabilities in the context of smart cities," Future Generation Computer Systems, vol. 76, pp. 248-261, 2017.
[17] L. D. Xu, E. L. Xu & L. Li, "Industry 4.0: state of the art and future trends," International Journal of Production Research, vol. 56, no. 8, pp. 2941-2962, 2018.
[18] L. X. Da, W. He & S. Li, "Internet of things in industries: A survey," IEEE Transactions on industrial informatics, vol. 10, no. 4, 2233-2243, 2014.
[19] L. Wang, L. X. Da, Z. Bi & Y. Xu, "Data cleaning for RFID and WSN integration," IEEE transactions on industrial informatics, vol. 10, no. 1, pp. 408-418, 2013.
[20] Z. Huixia, W. Fulin & S. Ruixia, "The application of the internet of things in China modern agriculture [j]," Chinese Agricultural Science Bulletin, vol. 27, no. 2, pp. 310-314, 2011.
[21] Y. Zhang, R. Yu, S. Xie, W. Yao, Y. Xiao & M. Guizani, "Home M2M networks: architectures, standards, and QoS improvement," IEEE Communications Magazine, vol. 49, no. 4, pp. 44-52, 2011.
[22] Y. Zhang, R. Yu, M. Nekovee, Y. Liu, S. Xie & S. Gjessing, "Cognitive machineto- machine communications: Visions and potentials for the smart grid," IEEE network, vol. 26, no. 3, pp. 6-13, 2012.
[23] K. Fan, P. Song & Y. Yang, "ULMAP: Ultralightweight NFC mutual authentication protocol with pseudonyms in the tag for IoT in 5G," Mobile Information Systems, vol. 2017, pp. 1-7, 2017.
[24] R. Want, "An introduction to RFID technology," IEEE pervasive computing, vol. 5, pp. 25- 33, 2006.

BIOGRAPHIES

MEHMET BAYGIN was born in Elazig, Turkey, in 1988. He received the B. S. degree in computer engineering from Firat University, Elazig, Turkey, in 2010, the M. S. degree in computer engineering from Firat University, Elazig, Turkey, in 2013, respectively and the Ph. D. degree in computer engineering from Firat University, Elazig, Turkey, in 2018. He is currently a assistant professor doctor in the Department of Computer Engineering, Ardahan University, Ardahan, Turkey. His research interests are image processing, computer vision, photovoltaic systems and heuristic methods.

ORHAN YAMAN was born in Elazig, Turkey, in 1990. He received B. S. degree in computer engineering from Firat University, Elazig, Turkey, in 2012, the M. S. degree in computer engineering from Firat University, Elazig, Turkey, in 2014, respectively and the Ph. D. degree in computer engineering from Firat University, Elazig, Turkey, in 2018. He works as expert in the Computer Center, Firat University, Elazig, Turkey. His research interests are image processing, fault diagnosis, computer vision, railway inspection systems and fuzzy systems.

ARIF CEM TOPUZ won bachelor, master and doctorate degree from the Department of Computer Education and Instructional Technology, Dokuz Eylul University in 2007, Marmara University in 2010 and Ataturk University in 2017, respectively. He has been working as an assistant professor at the Department of Computer Engineering, Ardahan University in Turkey. His research interests are distance learning, computer science education, artificial intelligence, and signal processing.

SALIH SERKAN KALELI was born in Erzurum, Turkey, in 1986. He got Bachelor's Degree in the Department of Business Management at Ataturk university, Erzurum, Turkey in 2009, the Master's Degree in Numerical Methods at Ataturk University in 2013, The PHD in the Department of Management Information Systems at Ataturk University in 2019. He is currently an assisstant proffessor doctor at the department of Office Management and Manager Assistance at Social Sciences Vocational School at Ardahan University, in Ardahan, Turkey. He is interested in such research areas as Optimisation, Statistics, Business Management.

A Dormand-Prince Based Hybrid Chaotic True Random Number Generator on FPGA

İ. KOYUNCU, H. İ. ŞEKER, M. ALÇIN and M. TUNA

Abstract— This study presents a Dormand-Prince-based hybrid chaotic True Random Number Generator Design (TRNG) that can be used for secure communication and cryptographic applications on Field Programmable Gate Array (FPGA). In this design, a chaotic oscillator unit has been implemented with an FPGA-based Sprott-Jafari chaotic oscillator model suitable with IQ-Math fixed point number and IEEE 754-1985 floating point number standards. Random numbers have been produced with the quantization of the results generated by the chaotic oscillator. XOR has been performed with FPGA-based ring oscillator structure on the post-processing unit so as to enhance the randomness. The differential equation of the chaotic system used in the TRNG design was modelled using Dormand-Prince numerical algorithm method. The design on FPGA has been realized in two separate number formats including 32-bit (16I-16Q) IQ-Math fixed point number standard and 32-bit IEEE 754-1985 floating point number standard. The realized design has been coded in VHDL, a hardware description language, and the Xilinx ISE 14.7 program has been used for the system design. The TRNG design has been synthesized and tested for the Virtex-6 (XC6VLX240T-1FF1156) FPGA chip. The maximum operating frequencies of the TRNG in 32-bit IQ-Math fixed point number standard and 32-bit IEEE 754-1985 floating point number standard reach 344.585 MHz and 316 MHz, respectively. The throughputs of the TRNG in 32-bit IQ-Math fixed point number standard and 32-bit IEEE 754-1985 floating point number standard have been obtained as 344 Mbit/s and 316 Mbit/s, respectively. 1 Mbit sequence has been generated by using TRNG system. Randomness analysis of the generated numbers has been performed in accordance with the NIST 800-22 tests and the generated numbers have successfully passed all of the tests.

Index Terms— **Dormand-Prince Algorithm, IQ-Math number standard, Chaotic System, FPGA.**

I. Introduction

Chaotic systems are defined as complex, nonlinear dynamical systems that are highly sensitive to initial conditions with irregular behavior [1].

Numerous national and international studies have been conducted on chaos and chaotic systems in recent years. Control [2], biomedical [3, 4], secure communication [5, 6], image processing [7, 8], fuzzy logic [9], artificial neural networks [10, 11], random number generators [12, 13], industrial control [14, 15], secure communication [16] and cryptography [17] can be given as examples of these studies.

Cryptography is defined as a series of techniques that need to be performed for data encryption and decryption due to its nature. The practice and study fields of chaotic signals include secure communication, cryptography and Random Number Generators (RNGs). Random numbers generated by RNG are used to form the initial vector, private and secret keys in cryptography. These keys can be produced as embedded off- or on-system. Off-system embedment weakens the security. Therefore, this is performed through digital circuits-based platforms such as hardware-based Digital Signal Processors (DSP) [18, 19], Application Specific Integrated Circuits (ASIC) [20, 21], and Field Programmable Gate Array (FPGA) [22, 23] to remove this disadvantage. True Random Number Generators (TRNGs) are essential for cryptology and secure communication practices. It is important for these random numbers used to display powerful statistical features, unpredictability and have regular distribution in terms of cryptography. The TRNGs have three main stages [24]. First stage includes the entropy resource which generates random numbers. Second stage includes quantification process which is described as generation of random number bits by using the randomness of entropy resource. Third stage includes post-processing blocks to strengthen statistical features [25].

Studies on FPGA-based chaotic TRNG studies are increasing in the literature [12, 26-37]. Koyuncu et al. [12] designed chaos-based TRNG design on Xilinx Virtex-6 FPGA using the Sundarapandian–Pehlivan chaotic system using the design based on RK4 numerical algorithm. In another study, Fischer et al. [27] realized the PLL based oscillator with

ISMAIL KOYUNCU is with Afyon Kocatepe University, Department of Electrical-Electronics Engineering, Afyon, 03100, TURKEY, (e-mail: ismailkoyuncu@aku.edu.tr).

https://orcid.org/0000-0003-4725-4879

H. IBRAHIM ŞEKER is with Sakarya University of Applied Sciences, Department of Electrical-Electronics Engineering, Graduate Education Institute, Sakarya 54187, TURKEY, (e-mail: hseker5@gmail.com).

https://orcid.org/0000-0002-5343-2419

MURAT ALÇIN is with Afyon Kocatepe University, Department of Mechatronics Engineering, Afyon, 03100, TURKEY, (e-mail: muratalcin@aku.edu.tr).

https://orcid.org/0000-0002-2874-7048

MURAT TUNA is with Kirklareli University, Vocational School of Technical Sciences, Kirklareli 39060, TURKEY, (e-mail: murat.tuna@klu.edu.tr).

https://orcid.org/0000-0003-3511-1336

FPGA chips. Avaroğlu et al. [29] implemented chaos-based post-processing on the ring oscillator based TRNG system on Altera FPGA board. Although the operating frequency of the design they realized was high as 450 MHz, the throughput decreased after the post-processing unit as 25 Mbit/s. Alçın et al. [31] designed ANN-chaos based TRNG on Xilinx FPGA. The operating frequency of the designed system is 231.616 MHz and the bit generation rate is 115.794 Mbit/s. Tuna et al. [32] implemented a dual entropy core TRNG design using hybrid ANN-based chaotic and ring oscillator structures on FPGA. Garipcan et al. [34] designed a hybrid TRNG on FPGA. In the hybrid system they designed, they used the ring system and the discrete-time chaotic maps system as the source of entropy. The discrete-time chaotic maps system operates as the slow oscillator and the ring system operates as the fast oscillator. The system has an operating frequency of 200 MHz and bit production rate of 15.4 Mbit/s. In Table 1, detailed information about TRNG designs and technical features designed on FPGA is given. As can be seen in the table, some studies have high operating frequencies, but bit generation rates decrease due to the algorithm used in the post-processing algorithm. The FPGA-based TRNG structure proposed in this study has the advantages of both high operating frequency and no reduction in throughput.

TABLE I
THE TECHNICAL PROPERTIES OF THE DESIGNED FPGA-BASED TRNGS IN RECENT YEARS

References		FPGA chip used	Designed Entropy type	Opr. Freq. (MHz)	Data rate (Mbit/s)
[12]	Koyuncu et al.	Virtex-6	Chaotic system	293	58.76
[26]	Wieczorek et al.	Spartan-3	Dual-metastability F/F	50	5
[27]	Fischer et al.	Altera Stratix	PLL oscillator	250	1.0
[28]	Lozach et al.	Virtex-2	Multi-ring oscillator	40	2.5
[29]	Avaroğlu et al.	Altera	Ring oscillator+chaos-based post-processing	450	25
[30]	Tuncer et al.	Cyclone IV	Ring oscillator	200	4.77
[31]	Alçın et al.	Virtex-6	3D ANN-based	231.61	115.7
[32]	Tuna et al.	Virtex-6	4D Hyperchaos+Ring	167.47	167.47
[33]	Kaya et al.	Quartus-II	Chua+RO-based PUF	------	------
[34]	Garipcan et al.	Altera	Chaotic map+Ring	200	15.4
[35]	Tuncer	Altera	Chaotic map+Ring	50	2.17
[36]	Prakash et al.	Virtex-6	4-D hyperchaotic system	370.894	185.447
[37]	Koyuncu et al.	Virtex-6	3-D chaotic system+Ring	464	464
This study		**Virtex–6**	**SJ Chaotic+Ring**	**316.756**	**316.756**

This study presents a TRNG design that uses 32-bit IEEE 754-1985 floating point number standard and IQ-Math fixed point number standard for cryptography and secure communication. The study has compared the chip statistics and operating frequencies of two different TRNG designs. The second section gives information about chaos and introduces the Sprott-Jafari chaotic system (SJCS). The SJCS was mathematically modeled and its time series and phase portraits were presented. The SJCS-based TRNG designs suitable with two separate number formats including 32-bit IQ-Math fixed point number standard and 32-bit IEEE 754-1985 floating point number standard were implemented on FPGA by using this chaotic system. NIST tests were performed for the random numbers obtained from the TGNR models of which designs were realized, and the results were presented in comparison.

II. DORMAND-PRINCE ALGORITHM AND SPROTT-JAFARI CHAOTIC SYSTEM

Chaotic systems are defined as complex, nonlinear dynamical systems that are highly sensible to their initial conditions with random irregular behaviors. Chaotic systems are defined with differential equations. The Eq. 1 presents a differential equation belonging to the SJCS. x, y and z in this equation are the chaotic state variables. The Eq. 2 presents the system parameters and initial conditions. Minor change on the system parameters and initial conditions may affect the chaotic behavior of the system at a considerable extent. Initial condition values of the chaotic system were determined to be x(0)=0, y(0)=3.9 and z(0)=0.7, and the system parameters were determined to be a=8.888 and b=4 [38].

$$
\begin{aligned}
dx/dt &= y \\
dy/dt &= -x + yz \\
dz/dt &= z + ax^2 - y^2 - b
\end{aligned}
\tag{1}
$$

$$
\begin{aligned}
a &= 8.888, b = 4 \\
x_0 &= 0, y_0 = 3.9, z_0 = 0.7
\end{aligned}
\tag{2}
$$

Chaotic systems are defined by differential equations and according to the relevant literature; the solutions of these differential equations can be modelled using various numerical algorithms such as Euler [39], Heun [40], RK4 [41] and RK5-Butcher [42]. In the presented study, the designed chaotic oscillator structure was modeled using the Dormand Prince (DP) numerical algorithm which generates more sensitive solutions than other methods.

Chaotic systems are sensitively dependent on the initial conditions and the system parameters. For this reason, changes in the system parameters and the initial conditions disrupt the chaotic behavior of the system. In other words, the system parameters and initial conditions in Eq. 2 in the SJCS system

are also specific to this chaotic system. When the parameters in Eq. 2 are changed, the chaotic dynamic behavior of the system changes. The system may not demonstrate a chaotic dynamic behavior when the specified parameter and initial conditions are out of range.

The Eq. 3 presents equation of the DP numeric algorithm [43]. Expressions that contain the derivative of a function as unknown are called differential equations. If an $f(x, y)$ function given as $f : \Re \rightarrow \Re$ and x, y $\in \Re$ and its derivative is defined and it is known, the values of function and its derivatives which are defined at yi and the function values at a distance of h= y_i +1- y_i from y_i for i=1 can be calculated using the Taylor series expansion. When DP numerical algorithm is examined, y_i is the initial values of the algorithm, y_i +1 is the first result value obtained by using the initial values, and h is the number of steps.

$$y_{i+1} = y_i + h(\frac{35}{384}k_1 + \frac{500}{1113}k_3 + \frac{125}{192}k_4 - \frac{2187}{6784}k_5 + \frac{11}{84}k_6)$$

$$k_1 = F(x_i, y_i)$$

$$k_2 = F(x_i + \frac{h}{5}, y_i + \frac{h}{5}k_1)$$

$$k_3 = F(x_i + \frac{3}{10}h, \left(y_i + \frac{3}{40}k_1 + \frac{9}{40}k_2\right)*h)$$

$$k_4 = F(x_i + \frac{4}{5}h, \left(y_i + \frac{44}{45}k_1 - \frac{56}{15}k_2 + \frac{32}{9}k_3\right)*h)$$

$$k_5 = F(x_i + \frac{8}{9}*h, \left(y_i + \frac{19372}{6561}k_1 - \frac{25360}{2187}k_2 + \frac{64448}{6561}k_3 - \frac{212}{729}k_4\right)*h)$$

$$k_6 = F(x_i + 1*h, \left(y_i + \frac{9017}{3168}k_1 - \frac{355}{33}k_2 + \frac{46732}{5247}k_3 + \frac{49}{176}k_4 - \frac{5103}{18656}k_5\right)*h)$$

$$k_7 = F(x_i + 1*h, \left(y_i + \frac{35}{384}k_1 + 0*k_2 + \frac{500}{1113}k_3 + \frac{125}{192}k_4 - \frac{2187}{6784}k_5 + \frac{11}{84}k_6\right)*h)$$

(3)

The literature has various analysis methods for the chaos analysis of dynamic systems. For example, Lyapunov exponents [45], frequency spectrum [46], time-series analysis [47], bifurcation diagram [48], phase portraits and power spectrum [49]. This study used phase portrait and time-series analyses for chaos analysis of the SJCS [50]. Fig. 1 presents the SJCS's phase portraits which were obtained using the Matlab-based DP numerical algorithm. The phase portrait of a chaotic system begins to fill its orbit over time in the phase space region, it never closes over and repeats continuously. If

the system fills the phase space in this way, it indicates that it has chaotic signs. Chaotic phase portraits of 3D chaotic system can be examined as x-y, x-z, y-z and x-y-z. Phase portraits of the SJCS chaotic system obtained using the Matlab program are given in Fig. 1. As can be seen from the figure, the phase portraits of the presented system show a chaotic behavior.

Due to the sensitive dependence of chaotic systems on initial conditions, different initial values given to the system can produce different chaotic signals in a certain time. Time series analysis of the system is performed to observe the chaotic signals produced with different initial values. In Fig. 2, x, y, z and x-y-z time series of the Matlab based SJCS chaotic system are given.

III. RING OSCILLATORS

Displayed Ring oscillators compose of an odd number of NOT gates which are connected consecutively. The output of each NOT gate is connected to the next gate and the output of last NOT gate is connected to the input of the first gate. Ring oscillators generate a square wave at a frequency depending on the delays of the ring to which it is connected. The frequency of the generated square wave changes based on the static and dynamic factors of the NOT gate constituting the ring. In other words, the operating frequencies of the signals generated by two ring oscillators arranged equivalently will not be same. This can be used to generate random bits. Fig. 3 represents the structure of the ring oscillator [37].

In this study, a ring oscillator that can operate in synchronization with the chaotic oscillator was designed. The random numbers, which were generated by the ring oscillator, designed on FPGA, and the chaotic system-based random numbers were combined in the post-processing stage. The aim of this process was to form TRNG structures that have more powerful statistical features as a result of the combination of two structures.
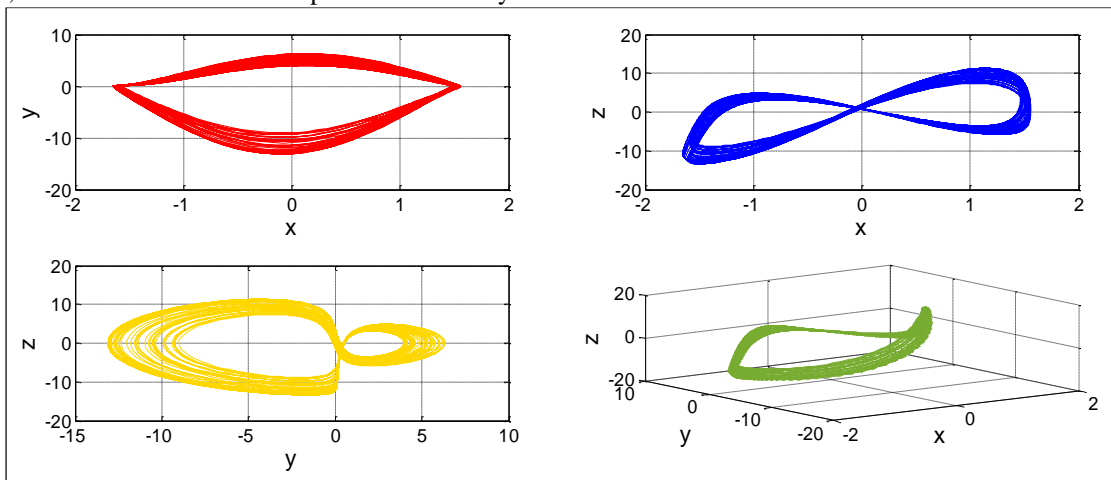

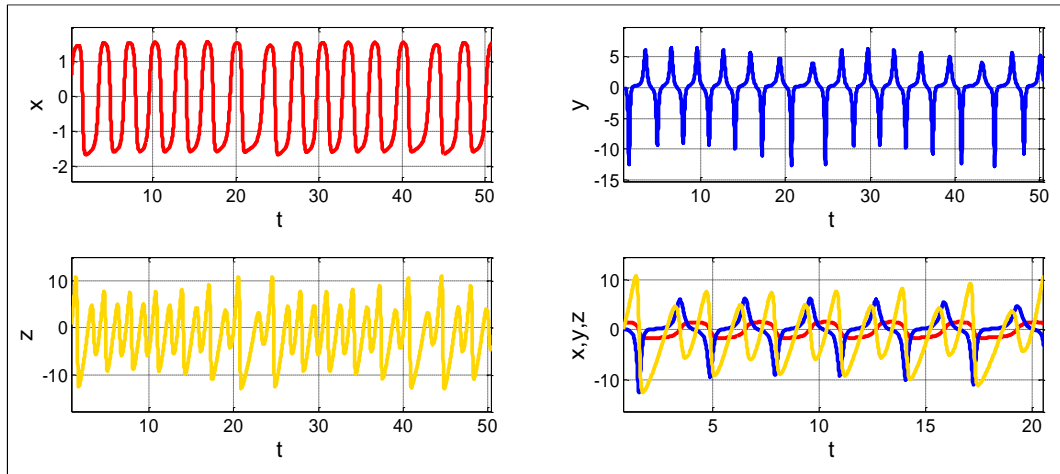Fig. 1. The SJCS's DP numeric algorithm-based phase portraits on Matlab.

Fig. 2. The SJCS's DP numeric algorithm-based time-series analysis on Matlab.
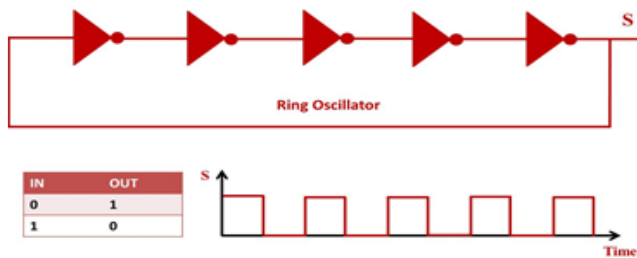

Fig. 3. Structure of the ring oscillator.

IV. CHAOTIC BASED TRNG DESIGNS ON FPGA AND RESULTS OF STATISTICAL TESTS

The SJCS-based TRNG was implemented to be operating on FPGA suitable with 32-bit (16I-16Q) IQ-Math fixed point number standard and 32-bit IEEE 754-1985 floating point number standard by using the DP numeric algorithm. The realized designs of TRNGs were coded using VHDL language. Main units used on the TRNG system design such as multiplier, adder, divider and subtractor were formed using the IP-Core Generator developed by Xilinx. The block diagrams of the recommended FPGA-based TRNGs that uses 32-bit IQ-Math fixed point number standard and SJCS-based 32-bit IEEE 754-1985 floating point number standard were similar. Fig. 4 presents the block diagram of the TRNG structure. 1-bit START signal on the input of the TRNG unit generates the signal to start the system, and 1-bit CLK clock pulse signal synchronizes the sub-units in the TRNG unit. 1-bit TRNG_SH signal on the output of the TRNG unit displays the value of 0 until the system result is ready and when the system result is ready, it displays the value of 1. 1-bit TRNG_RESULT indicates the signal that conveys the true random number values.

The proposed structure consists of four main parts including the SJCS oscillator unit, the random shredder function unit, the ring oscillator unit and the XOR unit. The SJCS oscillator unit generates the chaotic signals that TRNG needs. The random shredder function unit uses the fractional part values of x, y and z chaotic signals and makes random selection, and then sends the result to the XOR unit. A ring oscillator that operates in synchronization with the chaotic system is available. The ring oscillator generates 1-bit values and sends them to the XOR unit. At the last phase, XOR operation is applied to the chaotic signal-based random number and the numbers that are generated by the ring oscillator. KS_SH signal gets the value of '1' when the result of the chaotic signals is present and activates the random shredder function unit to which it is attached. On the other hand, RS_SH signal generates the value of '1' when random numbers are present and activates the XOR unit, thus making it operate.

The recommended SJCS-based TRNG design at two separate number formats, which were realized on FPGA, is synthesized on the Xilinx Virtex-6 (XC6VLX240T-1FF1156) chip. The design was coded in VHDL language in accordance with 32-bit (16I-16Q) IQ-Math fixed point number standard and 32-bit IEEE 754-1985 floating point number standard. Fig. 5 presents Xilinx ISE 14.7 simulation results of 32-bit IEEE 754-1985 floating point number-based TRNG design which were realized on FPGA. Fig. 6 presents Xilinx ISE 14.7 simulation results of 32-bit IQ-Math fixed point number-based TRNG which were realized on FPGA.

SJCS-based TRNG designs, which were made using DP numeric algorithm to operate on FPGA chips, were synthesized on the Xilinx Virtex-6 (XC6VLX240T-1FF1156) chip. The synthesizing process was performed using the Xilinx ISE Design Tools. Table 2 presents the chip statistics and operating frequencies of TRNG designs which were obtained following the Place & Route process. The maximum operating frequency of 32-bit IQ-Math fixed point number-based TRNG was 344.585 MHz and the throughput was 344.5 Mbit/s. The maximum operating frequency of the TRNG at 32-bit IEEE 754-1985 floating point number standard was 316.706 MHz and the throughput was 316.7 Mbit/s. The comparison of the chip statistics on Table 2 indicated that the TRNG that uses 32-bit floating point number standard used more chip

resources and had lower operating frequency than the TRNG that uses 32-bit fixed point number standard. However, floating point number standard can generate more sensible solutions than fixed point number standard. TRNG that uses 32-bit fixed point number standard used less chip resources and had higher operating frequency. The state of randomness and statistical features of the random number generators which will be used in cryptography and secure communication should be tested. One million data set, which generated by TRNG units, were recorded in a file. NIST 800-22 test was performed on these data and the results are given on Table 3.

NIST Test Suite is an internationally validated statistical test developed to determine whether the generated bit strings are random. In order for the bit stream to be accepted as random, it must pass all tests successfully. P-value, which is one of the most important parameters in these tests, is accepted as a measure of the randomness of the random sequences that are tested. For a random bit sequence, the P-value is close to 1, otherwise, the P-value is close to 0. In literature, P-value is generally accepted as 0.01. In other words, if the P-value is greater than 0.01, the bit sequences produced by the designed TRNG / PRNG are considered successful from the relevant test. As can be observed from Table 3, the bit sequences produced by the TRNG design presented in the study successfully passed the NIST Test Suite.
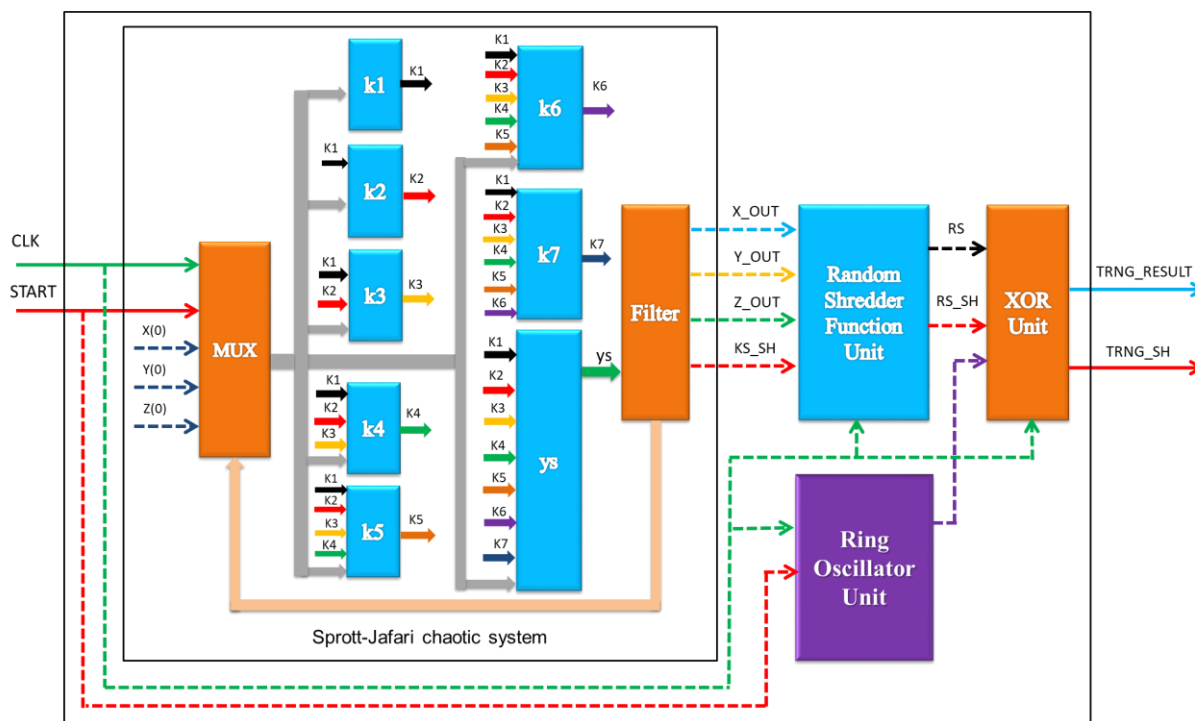
Fig. 4. Block diagram of the recommended SJCS-Ring-based TRNG design.
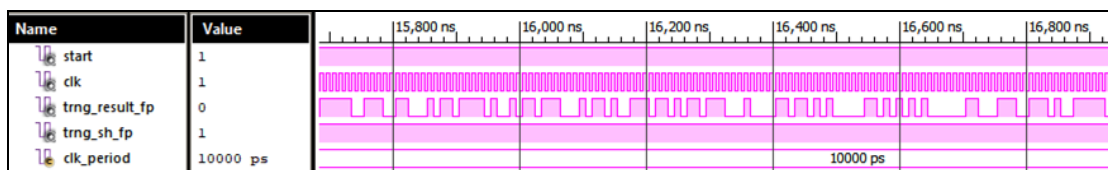
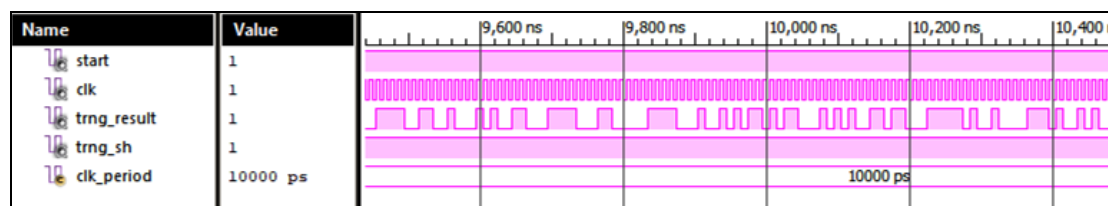Fig. 5. Simulation results of 32-bit IEEE 754-1985 floating point number-based TRNG.

Fig. 6. Simulation results of 32-bit IQ-Math fixed point number-based TRNG.

TABLE II
CHIP STATISTICS OF DORMAND-PRINCE-BASED HYBRID CHAOTIC TRNG USING 32-BIT IQ-MATH FIXED POINT AND 32-BIT IEEE 754-1985
FLOATING POINT.

Device Utilization	32-bit IQ-Math fixed point based TRNG		32-bit IEEE 754-1985 floating Point based TRNG	
	Used/Available	Utilization	Used/Available	Utilization
Number of Slice Registers	18507/301440	6 %	149071/301440	6 %
Number of Slice LUTs	14916/150720	9 %	147696/150720	97 %
Number of IOBs	4/600	1 %	4/600	1 %
Number of BUFG/BUFGCTRLs	1/32	3 %	1/32	3 %
Number of DSP48E1s	712/768	92 %	206/768	26 %
Max. Operating Frequency (MHz)	344.585		316.706	

TABLE III
NIST 800-22 STATISTICAL TEST RESULTS OF THE RECOMMENDED SJCS-BASED TRNG ON FPGA

NIST 800-22 Statistical Tests	Fixed Point Number Based TRNG		Floating Point Number Based TRNG	
	P value	Result	P value	Result
Frequency test	0.44367	Successful	0.96490	Successful
Block frequency test	0.62741	Successful	0.84124	Successful
Runs test	0.46871	Successful	0.37994	Successful
Longest-run test	0.72805	Successful	0.46004	Successful
Binary matrix rank test	0.61168	Successful	0.82406	Successful
Discrete fourier transform test	0.06511	Successful	0.25516	Successful
Non-overlapping templates test	0.03843	Successful	0.03077	Successful
Overlapping templates test	0.95936	Successful	0.75952	Successful
Maurer's universal statistical test	0.06970	Successful	0.36890	Successful
Linear complexity test	0.63663	Successful	0.18509	Successful
Serial test 1	0.43141	Successful	0.65730	Successful
Serial test 2	0.69996	Successful	0.28525	Successful
Approximate entropy test	0.53332	Successful	0.54052	Successful
Cumulative-sums test	0.13721	Successful	0.97330	Successful

V. CONCLUSIONS

In this study, a chaotic oscillator unit has been performed by modeling SJCS on FPGA in 32-bit IQ-Math fixed point number standard and 32-bit IEEE 754-1985 floating point number standard. Signals generated from the unit were sent to random shredder function unit and random numbers were obtained from the signals generated by the chaotic system. To strengthen the statistical features of these numbers and to increase the rate of randomness, they were sent to post-processing unit and XOR logic operation was performed following with the generation of true random numbers. The system was coded in VHDL using the Xilinx ISE 14.7 program. The design was then synthesized and tested for the Virtex-6 (XC6VLX240T-1FF1156) FPGA chip. The maximum operating frequencies of the TRNG in 32-bit IQ-Math fixed point number standard and 32-bit IEEE 754-1985 floating point number standard were 344.585 MHz and 316 MHz, respectively. The throughputs of the TRNG in 32-bit IQ-Math fixed point number standard and 32-bit IEEE 754-1985 floating point number standard were 344 Mbit/s and 316 Mbit/s, respectively. The sequence of 1 Mbit, which was obtained by realizing SJCS-based TRNG system both in 32-bit fixed point number standard and 32-bit floating point number standard on FPGA, was recorded in a file and was subjected to NIST 800-22 test, an international randomness test. The test results were successful. This study found that SJCS-based TRNG system, which was realized on FPGA, can be used in cryptology and secure communication.

REFERENCES

[1] T. Bonny, and Q. Nasir, "Clock Glitch Fault Injection Attack on an FPGA-Based Non-Autonomous Chaotic Oscillator," *Nonlinear Dynamics*, vol. 96, no. 3, pp. 2087–2101, 2019.

[2] J. S. Vaidyanathan, "Chaos in neurons and adaptive control of Birkhoff-Shaw strange chaotic attractor," *International Journal of PharmTech Research*, vol. 8, no. 5, pp. 956-963, 2015.

[3] A. Xiong, X. Zhao, J. Han and G. Liu, "Application of the chaos theory in the analysis of EMG on patients with facial paralysis," *Robot Intelligence Techlogy and Applications*, vol. 2, no. 274, pp. 805-819, 2014.

[4] H. Zhengxing, D. Wei, D. Huilong and L. Haomin, "Similarity measure between patient traces for clinical pathway analysis: problem, method, and applications," *IEEE Journal of Biomedical and Health Informatics*, vol. 18, no. 1, pp. 4−14, 2014.

[5] K. Zexin, S. Jiang, M. Lin, Q. Yanhui and J. Shuisheng, "Multimode synchronization of chaotic semiconductor ring laser and its potential in chaos communication," *IEEE Journal Quantum Electron*, vol. 50, no. 3, pp. 148-157, 2014.

[6] S. Çiçek, A. Ferikoğlu, and I. Pehlivan, "A new 3D chaotic system: dynamical analysis, electronic circuit design, active control synchronization and chaotic masking communication application," *Optik-International Journal for Light and Electron Optic*, vol. 127, no. 8, pp. 4024-4030, 2016.

[7] E. Tlelo-Cuautle, V. H. Carbajal-Gomez, P. J. Obeso-Rodelo, J. J. Rangel-Magdaleno and J. C. Nuñez-Perez, "FPGA realization of a chaotic communication system applied to image processing," *Nonlinear Dynamics*, vol. 82, no. 4, pp. 1879-1892, 2015.

[8] J. S. Khan and J. Ahmad, "Chaos based efficient selective image encryption," *Multidimensional Systems and Signal Processing*, vol. 30, no. 2, pp. 943-961, 2019.

[9] X. Wang, J. H. Park, K. She, S. Zhong and L. Shi, "Stabilization of Chaotic Systems With T–S Fuzzy Model and Nonuniform Sampling: A Switched Fuzzy Control Approach," *IEEE Transactions on Fuzzy Systems*, vol. 27, no. 6, pp. 1263-1271, 2018.

[10] M. Alçın, M. Tuna and İ. Koyuncu, "IQ-Math Based Designing of Fourth Order Runge-Kutta Algorithm on FPGA and Performance Analysis According to ANN Approximation," *Research International Journal of Advanced in Science Engineering and Technology*, vol. 5, no. 8, pp. 6523-6530, 2018.

[11] İ. Koyuncu, İ. Şahin, C. Gloster and N. K. Sarıtekin, "A neuron library for rapid realization of artificial neural networks on FPGA: A case study of Rössler chaotic system," *Journal of Circuits, Systems and Computers*, vol. 26 no. 1, pp. 1750015, 2017.

[12] İ. Koyuncu and A. T. Özcerit, "The design and realization of a new high speed FPGA-based chaotic true random number generator," *Computers & Electrical Engineering*, vol. 5, no. 8, pp. 203-214, 2017.

[13] S. Kaçar, "Analog circuit and microcontroller based RNG application of a new easy realizable 4D chaotic system," *Optik*, vol. 127, no. 20, pp. 9551-9561, 2016.

[14] L. dos Santos Coelho, "Tuning of PID controller for an automatic regulator voltage system using chaotic optimization approach," *Chaos, Solitons & Fractals*, vol. 39, no. 4, pp. 1504-1514, 2009.

[15] J. Lu, X. Yu and G. Chen, "Generating chaotic attractors with multiple merged basins of attraction: A switching piecewise-linear control approach," *IEEE Transactions on Circuits and Systems I: Fundamental Theory and Applications*, vol. 50, no. 2, pp. 198-207, 2003.

[16] Ü. Çavuşoğlu, A. Akgül, S. Kaçar, İ. Pehlivan and A. Zengin, "A chaos-based encryption algorithm over TCP data packet for secure communication," *Security and Communication Networks*, vol. 9, no.11, pp. 1285-1296, 2016.

[17] S. Akkaya, İ. Pehlivan, A. Akgül and M. Varan, "Yeni bir kaos tabanlı rastgele sayı üreteci kullanan banka şifrematik cihazı tasarımı ve uygulaması," *Journal of the Faculty of Engineering & Architecture of Gazi University*, vol. 33, no. 3. pp. 1171-1182, 2018.

[18] R. Kharel, K. Busawon, W. Aggoune and Z. Ghassemlooy, "Implementation of a secure digital chaotic communication scheme on a DSP board," *In 2010 7th International Symposium on Communication Systems, Networks & Digital Signal Processing*, 2010: pp. 212-216.

[19] T. Shi, G. Rui, Y. Zhang and S. Zhang, "Design Method for Duffing System Based on DSP Builder," *In 2012 International Conference on Systems and Informatics (ICSAI)*, 2012: pp. 121-124.

[20] M. Delgado-Restituto, A. J. Acosta and A. Rodríguez-Vázquez, "A mixed-signal integrated circuit for FM-DCSK modulation," *IEEE Journal of solid-state circuits*, vol. 40, no. 7, pp. 1460-1471, 2005.

[21] Ü. Güler and S. Ergün, "A high speed, fully digital IC random number generator," *AEU-International Journal of Electronics and Communications*, vol. 66, no. 2, pp. 143-149, 2012.

[22] T. Bonny, R. Al Debsi, S. Majzoub, and A. S. Elwakil, "Hardware Optimized FPGA Implementations of High-Speed True Random Bit Generators Based on Switching-Type Chaotic Oscillators," *Circuits, Systems, and Signal Processing*, vol. 38, no. 3, pp. 1342–1359, 2019.

[23] T. Bonny, and A. S. Elwakil, "FPGA Realizations of High-Speed Switching-Type Chaotic Oscillators Using Compact VHDL Codes," *Nonlinear Dynamics*, vol. 93, no. 2, pp. 819–833, 2018.

[24] E. Avaroğlu, and T. Tuncer, "Novel S-Box-Based Postprocessing Method for True Random Number Generation", *Turkish Journal of Electrical Engineering & Computer Sciences*, vol. 28, pp. 288–301, 2020.

[25] M. Tuna and C. B. Fidan. "A Study on the importance of chaotic oscillators based on FPGA for true random number generating (TRNG) and chaotic systems," *Journal of the Faculty of Engineering and Architecture of Gazi University*, vol. 33, no. 2, pp. 469-486, 2018.

[26] P. Z. Wieczorek and K. Golofit, "Dual-Metastability Time-Competitive True Random Number Generator," *IEEE Transactions on Circuits and Systems I: Regular Papers*, vol. 61, no. 1, pp. 134–145, 2014.

[27] V. Fischer, M. Drutarovsky, M. Simka, and N. Bochard, "High Performance True Random Number Generator in Altera Stratix FPLDs," *Field Programmable Logic and Application*, vol. 3203, pp. 555–564, 2004.

[28] F. Lozach, M. Ben-Romdhane, T. Graba, and J.-L. Danger, "FPGA Design of an Open-Loop True Random Number Generator," in 2013 Euromicro Conference on Digital System Design, 2013, pp. 615–622, doi: 10.1109/DSD.2013.73.

[29] E. Avaroğlu, T. Tuncer, A. B. Özer, B. Ergen, and M. Türk, "A novel chaos-based post-processing for TRNG," *Nonlinear Dynamics*, vol. 81, no. 1–2, pp. 189–199, 2015.

[30] T. Tuncer, E. Avaroglu, M. Türk, and A. B. Ozer, "Implementation of Non-periodic Sampling True Random Number Generator on FPGA," *Informacije MIDEM*, vol. 44, no. 4, pp. 296–302, 2015.

[31] M. Alcin, I. Koyuncu, M. Tuna, M. Varan, and I. Pehlivan, "A novel high speed Artificial Neural Network–based chaotic True Random Number Generator on Field Programmable Gate Array," *International Journal of Circuit Theory and Applications*, vol. 47, no. 3, pp. 365–378, 2019.

[32] M. Tuna, A. Karthikeyan, K. Rajagopal, M. Alçın, and İ. Koyuncu, "Hyperjerk multiscroll oscillators with megastability: Analysis, FPGA implementation and A Novel ANN-Ring-based True Random Number Generator," *AEU-International Journal of Electronics and Communications*, vol. 112, no. 2019, pp. 152941–10, 2019.

[33] T. Kaya, "A true random number generator based on a Chua and RO-PUF: design, implementation and statistical analysis," *Analog Integrated Circuits and Signal Processing*, vol. 102, pp. 415–426, 2020.

[34] A. M. Garipcan and E. Erdem, "Implementation and Performance Analysis of True Random Number Generator on FPGA Environment by Using Non-periodic Chaotic Signals Obtained from Chaotic Maps," *Arabian Journal for Science and Engineering*, vol. 44, no. 11, pp. 9427–9441, 2019.

[35] T. Tuncer, "The implementation of chaos-based PUF designs in field programmable gate array," *Nonlinear Dynamics*, vol. 86, no. 2, pp. 975–986, 2016.

[36] P. Prakash, K. Rajagopal, I. Koyuncu, J.P. Singh, M. Alcin, B.K. Roy, M. Tuna, "A Novel Simple 4-D Hyperchaotic System with a Saddle-Point Index-2 Equilibrium Point and Multistability: Design and FPGA-Based Applications," *Circuits, Systems, and Signal Processing*, vol. 39, pp. 4259–4280, 2020.

[37] İ. Koyuncu, M. Tuna, İ. Pehlivan, C. B. Fidan, and M. Alçın, "Design, FPGA implementation and statistical analysis of chaos-ring based dual entropy core true random number generator," *Analog Integrated Circuits and Signal Processing*, vol. 102, no. 2, pp. 445–456, 2020.

[38] S. Jafari, J. C. Sprott and F. Nazarimehr, "Recent new examples of hidden attractors," *The European Physical Journal Special Topics*, vol. 224, no. 8, pp. 1469-1476, 2015.

[39] M. S. Azzaz, C. Tanougast, S. Sadoudi, R. Fellah, and A. Dandache, "A new auto-switched chaotic system and its FPGA implementation," *Communications in Nonlinear Science and Numerical Simulation*, vol. 18, no. 7, pp. 1792–1804, 2013.

[40] M. Tuna, M. Alçın, İ. Koyuncu, C. B. Fidan, and İ. Pehlivan, "High speed FPGA-based chaotic oscillator design," *Microprocessors and Microsystems*, vol. 66, no. 2019, pp. 72–80, 2019.

[41] L. Merah, A. Pascha, A. Said and N. H. Mamat, "Design and FPGA implementation of Lorenz chaotic system for information security issues," *Application Mathematics Sciences*, vol. 7, pp. 237-246, 2013.

[42] İ. Koyuncu, A. T. Özcerit, and İ. Pehlivan, "An analog circuit design and FPGA-based implementation of the Burke-Shaw chaotic system," *Optoelectronics and Advanced Materials-Rapid Communications*, vol. 7, pp. 635-638, 2013.

[43] İ. Koyuncu, and H. İ. Şeker, "Implementation of Dormand-Prince based chaotic oscillator designs in different IQ-Math number standards on FPGA", *Sakarya Üniversitesi Fen Bilimleri Enstitüsü Dergisi*, vol. 23, no. 5, pp. 859-868, 2019.

[44] H. İ. Şeker, İ. Koyuncu, M. Tuna and M. Alçın, "Dormand-Prince Tabanlı SEA Kaotik Osilatör Tasarımının FPGA Üzerinde Gerçeklenmesi," *5th International Academic Research Congress*, Ankara, pp. 1-8, 2019.

[45] Z. Meng, G. Li, D. Yang, and L. Zhan, "A new directional stability transformation method of chaos control for first order reliability analysis," *Structural and Multidisciplinary Optimization*, vol. 55, no. 2, pp. 601-612, 2017.

[46] Y. Jiang, H. Zhu, and Z. Li, "A new compound faults detection method for rolling bearings based on empirical wavelet transform and chaotic oscillator," *Chaos, Solitons & Fractals*, vol. 89, pp. 8-19, 2016.

[47] Z. Tian, "Chaotic characteristic analysis of network traffic time series at different time scales," *Chaos, Solitons & Fractals*, vol. 130, pp. 109412, 2020.

[48] X. Chen, J. Hu, Z. Peng, and C. Yuan, "Bifurcation and chaos analysis of torsional vibration in a PMSM-based driven system considering electromechanically coupled effect" *Nonlinear Dynamics*, vol. 88, no. 1, pp. 277-292, 2017.

[49] D. Ding, Y. Weng, and N. Wang, "Dynamics analysis of a fractional-order delayed SBT memristive chaotic system without equilibrium points," *The European Physical Journal Plus*, vol. 134, no 444, pp. 1-7, 2019.

[50] S. Jafari, A. Ahmadi, A. J. M. Khalaf, H. R. Abdolmohammadi, V. T. Pham and F. E. Alsaadi, "A new hidden chaotic attractor with extreme multi-stability," *AEU-International Journal of Electronics and Communications*, vol. 89, pp. 131-135, 2018.

BIOGRAPHIES

İSMAIL KOYUNCU has an MSc from Abant Izzet Baysal University, Bolu-Turkey. He completed his doctoral research in the Department of Electrical and Electronics Engineering at Sakarya University, Sakarya-Turkey in 2014. Since 2017, he is an Associate Professor in the Department of Electrical and Electronics Engineering at Afyon Kocatepe University, in Afyon-Turkey. His main research interests are FPGA-based digital system design, chaos, TRNG and reconfigurable computing. He is also interested in FPGA-based artificial neural networks and computer graphics.

HALIL İBRAHIM ŞEKER was born in 1994, in Karaman, Turkey. He received the B.S. from Bozok University in 2017, and M.S. degrees, Electrical and Electronics Engineering from Afyon Kocatepe University in 2019, Afyon-Turkey. He is currently conducting his doctoral research in the Department of Electrical and Electronics Engineering at Sakarya University of Applied Sciences, Sakarya-Turkey. His research interests include chaos, FPGA-based digital system design and control theory.

MURAT ALÇIN received the BSc, MSc and PhD degrees in Electronic-Computer Teaching from the University of Marmara, Turkey, in 2006 and in 2009, and department of Electrical and Electronics Engineering at Sakarya University, in Sakarya-Turkey, 2017, respectively. From 2008 to 2012, he was an instructor in Abant İzzet Baysal University Electronic Technology Program at Bolu Vocational School, Bolu-Turkey. Since 2018, he is an Assistant Professor in the Department of Mechatronics Engineering at Afyon Kocatepe University, in Afyon-Turkey. His research interests include Neural Networks, Chaotic Systems and FPGA-based digital system design.

MURAT TUNA received his BSc and MSc in Electrical Education from Kocaeli University of Technical Education, in 2004, and Kocaeli University of Institute of Science, Kocaeli, Turkey, in 2008. He received his PhD in the Department of Electrical and Electronics Engineering at Karabuk University, Karabuk-Turkey in 2017. Currently, he is working at Kirklareli University in Turkey, Assistant Professor, since 2009. His main research topics include chaos, TRNG, FPGA-based digital system design and reconfigurable computing. He is also interested in mathematical model and control of nonlinear systems.

Antenna Selection and Detection Performance on Correlation Based Detection Systems

F. YAVUZ ILGIN

Abstract— **The increase data size transmitted in digital communication systems necessitates the use of high-capacity communication channels for the transmission of these data. To increase the channel capacity, MIMO systems are widely used. Antenna selection in MIMO systems is very important for efficient use of communication sources. Cognitive Radio systems generally aim to increase spectrum efficiency by using MIMO systems. Therefore, Cognitive Radio must find empty spectrum regions with spectrum detection methods. Spectrum detection performance is related to the antenna numbers in MIMO systems. Therefore, this study examines the effect of antenna numbers on detection performance in correlation-based detection method. Thanks to this study, the relationship between channel capacity, detection performance and antenna number for MIMO systems was investigated.**

Index Terms—**Antenna Selection, Cognitive Radio, Correlation based Spectrum Sensing, MIMO systems, Spectrum Sensing .**

I. INTRODUCTION

It is known that the amount of data transmitted in wireless communication systems is gradually increasing[1]. To transmit large amounts of data (for example DTV, 5G communication signal), more channel capacity is required[2]. Multiple Input Multiple Output (MIMO) wireless communication systems provide a significant improvement in system efficiency as they have multiple receiver-transceiver antennas[3]. One of the biggest advantages of MIMO systems is that their channel capacities are much higher than Sıngle Input Sıngle Output (SISO) systems[4]. However, MIMO systems contain amplifiers, analog-to-digital converters, mixers that are very expensive and complex. Despite these known disadvantages, MIMO systems are widely preferred due to their advantages. In MIMO systems, it is important to use the least antenna (both transmitter and receiver) to meet the system requirements[5].

In some communication applications, the use of multiple antennas is a necessity, not just because of the contribution

FATIH YAVUZ ILGIN, is with Department of Electrical Electronical Engineering Erzincan Binali YILDIRIM University, Erzincan, Turkey,(e-mail: (fyilgin@erzincan.edu.tr).

https://orcid.org/0000-0002-7449-4811

that MIMO systems can provide[6]. One of these applications is Cognitive Radio (CR) applications. The use of multiple antennas in multi-antenna CR systems is indispensable for some spectrum sensing models. For example, in eigenvalue and covariance based detection models, it is necessary to use multi-antenna in both transmitter and receiver[7]. However, there is no such requirement in the energy based sensing model. Basically, spectrum detection applications in CR systems are divided into classes such as single user-single antenna, single user-multi antenna or multi-user single antenna. Which method will be chosen to detect spectrum should be selected depending on some hardware requirements (number of users, antenna numbers) and communication environment. The main aim in spectrum sensing applications is to realize the most successful detection in the presence of the highest noise. Nevertheless , this process is not easy due to noise, fading and other disruptive effects in the wireless communication environment[8]. For this reason, various methods are proposed to ensure the most successful detection with the least user or antenna by using collaboration detection or some grouping algorithms[9]. The correlation-based detection method is very advantageous in terms of both computational cost and detection performance. In addition, the detection method used in this study detects as blind. That is, it does not need any prior knowledge for detection(for example: noise variance, modulation scheme).

Increasing the antenna numbers in spectrum sensing applications may increase detection performance, but increasing the antenna numbers is difficult in spectrum sensing applications. Because the antennas must be far enough from each other to not correlate with each other. On the other hand, the increase in the antenna numbers both increases the channel capacity and positively affects the detection performance.

Therefore, in this study, channel capacity-sensing performances are evaluated for correlation-based spectrum sensing in MIMO-OFDM systems. Thus firstly, theoretical information is given by channel capacity and correlation based spectrum sensing method for MIMO systems. Following, the relationship between antenna number and sensing performance in MIMO -OFDM based spectrum sensing method was investigated.

The organization of the study is as follows. Section 2 describes the antenna selection and channel capacity for MIMO systems. Cognitive radio and correlation-based spectrum detection is explained in chapter 3 and necessary

theoretical information is given. The results of the simulation studies made in section 4 are given. Chapter 5 is reserved for discussion and conclusion.

Some of the notation we use is as follows: superscript $(.)^T$ and $\mathbf{I}_L$ stands for transpose and the identity matrix of order $\boldsymbol{L}$ respectively. And $E(.)$ denotes expectation operation.

II. CHANNEL CAPACITY MIMO SYSTEMS

Suppose there is $N_t x N_r$ MIMO communication system, where N_t and N_r indicate the number of transmit and receive antennas, respectively. With this communication system, the maximum throughput achieved by transmitting $\min(N_t x N_r)$ number of parallel data stream, is given by[10]

$$B = log_2 \, det \left(\boldsymbol{I}_{N_r} + \frac{S}{\eta N_t} \, \boldsymbol{H}\boldsymbol{H}^T \right) \; bps/Hz \qquad (1)$$

where, $\boldsymbol{I}_{N_r} \epsilon \, C^{N_r x \, N_r}$ and $\boldsymbol{H} \epsilon \, C^{N_t x \, N_r}$ are the identity matrix and channel coefficient matrix, respectively. η and is the power spectral density of additive Gaussian noise with $\eta \sim N(0, \sigma_\eta^2)$. In addition S denotes the transmitted signal power.

Antenna selection technique aims to reduce the number of transmitting antennas without changing the system efficiency by using the channel information on the receiver. Optimum throughput is acquired through selection of best set of K antennas out of C_M combinations. Where M defines the number of transmit antennas to be used for transmission. Thus, the relationship between optimum system efficiency and antenna number is defined by Channel State Information (CSI) as follows[11].

$$B_M^{opt} = log_2 \, det \left(\boldsymbol{I}_{N_r} + \frac{S}{\eta N_t} \, \boldsymbol{H}_\gamma^{opt} \left(\boldsymbol{H}_\gamma^{opt} \right)^T \right) \; bpsHz \qquad (2)$$

where, B_M^{opt} is the channel capacity for optimally selected antenna number. The traditional MIMO system is given in Fig 1.
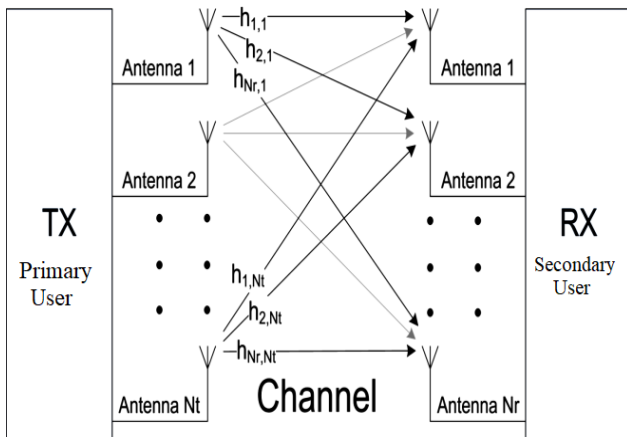
Fig. 1 MIMO communication system

As it is known, in addition to increasing the channel capacity, MIMO systems also reduce the negative effects of noise thanks to the spatial diversity of the antennas.

III. COGNITIVE RADIO AND BASIC SPECTRUM SENSING

Suppose there is a Primary Base Station (PBS) with N_t antenna and CR users within this coverage area. The purpose of CR users is to determine whether the PBS is active / passive. Thus, if PBS is passive, this communication band is used opportunistically by CR users. In this detection model, if the PBS has N_t antenna and M CR users, this system can be defined as a MIMO system[12].
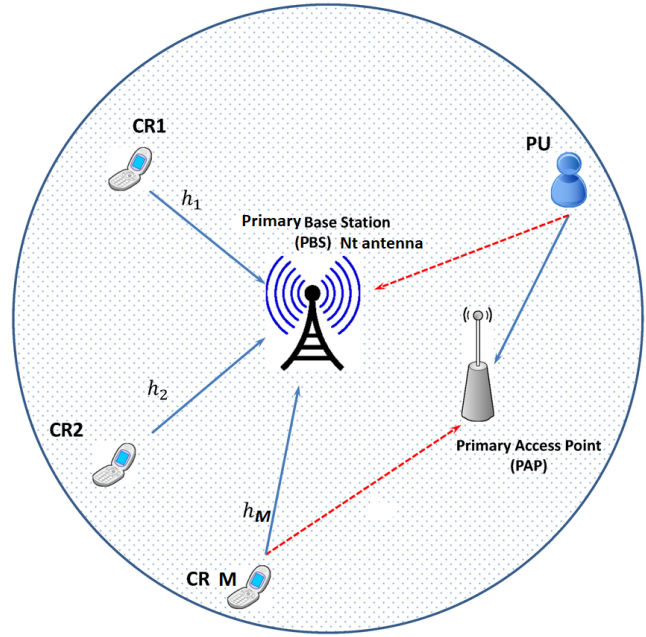
Fig. 2 Spectrum detection scenario for correlation based sensing

Basically the signal detection problem is to determine whether there is a embedded communication signal in the noise. In detection theory, this decision mechanism is explained by binary hypothesis testing. In binary hypothesis test, H_0 indicates that there is only a noise signal, H_1 indicates that it is a noise + communication signals. Mathematical decision making process is given below[13]

$$H_0 \; : \boldsymbol{y}(k) = \boldsymbol{\eta}(k) k = 1,2, \dots .3, K \qquad (3)$$

$$H_1 \; : \boldsymbol{y}(k) = \boldsymbol{h}(k)\boldsymbol{s}(k) + \boldsymbol{\eta}(k) \; \; k = 1,2, \dots .3, K \qquad (4)$$

.

Where $\boldsymbol{y}(k)$ is the form of the signal received from CR users (M numbers) stored in a matrix. For example, if M is the number of CR users and the number of samples is K, the size of the $\boldsymbol{y}(k)$ matrix will be MxK. In addition to this where $\boldsymbol{\eta}(k)$ denotes the independent and identically distributed (i.i.d.) circularly symmetric Gaussian (CSCG) white noise. $\boldsymbol{h}(k)$ and $\boldsymbol{s}(k)$ represents channel coefficient vector and primary user signal, respectively. In multi-antenna BR systems, spectrum detection is given by comparing the test statistic that varies according to the method with the threshold. The spectrum detection model for CR systems is given below.

$$y_m(k) = \psi \, h_m(k) \, s_m(k) + \eta_m(k) \quad m = 1,2,\dots 3, M \qquad (5)$$

Where $\psi = 1$ under H_1 and $\psi = 0$ under H_0, M represents the number of CR user. In order to make a spectrum decision, the threshold and test statistics are compared in correlation-based spectrum detection. This phenome can be expressed mathematically as follows[12].

$$TS_{cor} \underset{H_0}{\overset{H_1}{\gtrless}} \gamma_{cor} \qquad H_0 \text{ or } H_1 \qquad (6)$$

Where TS_{cor} and γ_{cor} define test statistics and threshold for correlation based detector, respectively.

A. Correlation Based Spectrum Sensing

Let $y_m(k) = s_m(k) + \eta_m(k)$ be the continuous-time received signal. Assume that we are interested in the frequency band with central frequency W and bandwidth f_c. We sample the received signal at a sampling rate f_s. Thus, consecutive signal vectors for $y_m(k)$, $s_m(k)$ and $\eta_m(k)$ are thus defined as follows.

$$y_m(k) = [y_m(k)\ y_m(k-1)\dots y_m(k-L+1)]^T \qquad (7)$$

$$s_m(k) = [s_m(k)\ s_m(k-1)\dots s_m(k-L+1)]^T \qquad (8)$$

$$\eta_m(k) = [\eta_m(k)\ \eta_m(k-1)\dots \eta_m(k-L+1)]^T \qquad (9)$$

Where L is defined as the smoothing factor. Specifies how many samples the spectrum detection process will be done with. Thus, the statistical covariance matrices of the received signal ($y(k)$) are defined as follows.

$$\mathbf{C}_{H_0} = E[\boldsymbol{\eta}(k)\,\boldsymbol{\eta}^{\mathbf{T}}(k)] \quad under \ H_0 \qquad (10)$$

$$\mathbf{C}_{H_1} = E[\mathbf{y}(k)\,\mathbf{y}^T(k)] \quad under \ H_1 \qquad (11)$$

Equation 10 can be written as a result of Equation 10 and Equation 11.

$$\mathbf{C}_{H_0} = \mathbf{C}_{H_1} + \sigma_\eta^2\,\mathbf{I}_L \qquad (12)$$

Where $\mathbf{I}_L$ denotes LxL identity matrix. According to Equation 12, if $y_m(k) = 0$, $\mathbf{C}_{H_1} = 0$. Therefore, all non-diagonal components of $\mathbf{C}_{H_0}$ are equal to 0. If there is a signal samples and the signal are correlated, $\mathbf{C}_{H_1}$ is not a diagonal matrix. Hence, some of the off-diagonal elements of $\mathbf{C}_{H_0}$ should be nonzeros. Denote r_{mk} as the element of matrix $\mathbf{C}_{H_0}$ at the m.th row and k.th column. Then the following test statistics can be written.

$$\delta_1 = \frac{1}{L}\sum_{m=1}^{L}\sum_{k=1}^{L}|r_{mk}| \qquad (13)$$

$$\delta_2 = \frac{1}{L}\sum_{m=1}^{L}|r_{mm}| \qquad (14)$$

At that time, under the H_0 , $\delta_1/\delta_2 = 1$. But under the H_0 , $\delta_1/\delta_2 > 1$. Consequently, ratio δ_1/δ_2 can be used to detect the presence of the signal.

B. Determination threshold for Correlation based Spectrum Sensing

To obtain the threshold value (under asymptotic conditions) the following equation can be written.

$$\lim_{N\to\infty} E(\delta_1) = \sigma_\eta^2 + \sigma_s^2 + \frac{2\sigma_s^2}{N}\sum_{l-1}^{L-1}(L-m)|\propto_l| \quad (15)$$

Where σ_s^2 denotes variance of PBS. Under H_0 ;

$$\delta_1/\delta_2 \approx E(\delta_1)/E(\delta_2) \qquad (16)$$

$$= 1 + (L-1)\sqrt{\frac{2}{\pi L}} \qquad (17)$$

As L approaches infinity, this ratio approaches 1. Thus, to obtain the threshold value, it should be continued with the conditional equation given below.

$$P_{fa} = P(\delta_1 < \gamma_{cor}\,\delta_2) \qquad (18)$$

$$= P\left(\delta_2 < \frac{1}{\gamma_{cor}}\,\delta_1\right) \qquad (19)$$

If δ_1 is written instead of Equation 19;

$$\approx P\left(\delta_2 < \frac{1}{\gamma_{cor}}\,1 + (L-1)\sqrt{\frac{2}{\pi N}}\sigma_\eta^2\right) \qquad (20)$$

$$= P\left(\frac{\delta_2 - \sigma_\eta^2}{\sqrt{\frac{2}{N}}\sigma_\eta^2} < \frac{\frac{1}{\gamma_{cor}}\left(1+(L-1)\sqrt{\frac{2}{\pi N}}\right)-1}{\sqrt{\frac{2}{N}}}\right) \qquad (21)$$

Equation 21 rearranged;

$$\approx 1 - Q\left(\frac{\frac{1}{\gamma_{cor}}\left(1+(M-1)\sqrt{\frac{2}{\pi N}}\right)-1}{\sqrt{\frac{2}{N}}}\right) \qquad (22)$$

Where

$$Q(t) = \frac{1}{\sqrt{2\pi}}\int_t^\infty e^{-u^2/2}du \qquad (23)$$

For a given P_{fa}, the associated threshold should be chosen such that[12];

$$\gamma_{cor} = \frac{1+(L-1)\sqrt{\frac{2}{M\,\pi}}}{1-Q^{-1}(P_{fa})\sqrt{\frac{2}{M}}} \qquad (24)$$

According to Equation 24 the threshold value depends on the number of CR users, L and P_{fa}. P_{fa} is a value set by the Federal Communication Committee (FCC). For CR systems, this value is 0.1.

IV. SIMULATION STUDIES

In this section, we will give some simulation results for spectrum sensing performance and channel capacity. The simulation studies in this study were simulated in MATLAB environment. During the simulation studies, P_{fa} is selected as 0,1. Because this value is the limit value determined by the International Communication Committee. Additionally, noise uncertainty factor was not included in simulation studies. Because the Correlation Based Spectrum detection method is not affected by noise uncertainty factor[14], [15]. Looking at the threshold given with Equation 24, it is seen that there is no noise variance component. The absence of noise power when calculating the threshold indicates that this method is not affected by noise uncertainty.

In Fig. 2, only channel capacity is given for MIMO systems without detection performance. As can be seen, the highest channel capacity is reached when the antenna numbers is highest and the noise level is lowest. Although the increase in the antenna numbers in MIMO systems affects the channel capacity positively, it may not be easy to use more antennas. As explained in the previous chapters, the increase in the antenna numbers increases the spatial diversity, so the MIMO system is more resistant to noise.
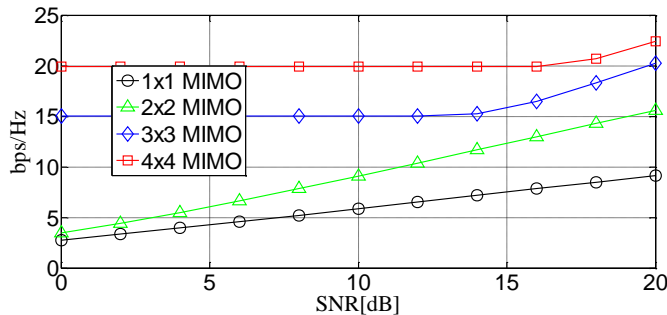
Fig. 3. Antenna versus channel capacity for MIMO syst

The antenna correlation should be at a minimum level in order to get maximum benefit from the spatial diversity. However, in many communication applications except CR applications, this may cause difficulties in practice, since the receiving antennas are located on the same receiver. In multi-user-single antenna CR applications, since each antenna is on a different user, maximum efficiency can be obtained from the spatial correlation.

One of the result graphics that constitute the main purpose of this study is given in Fig. 4. Where, the channel capacity for 4x4 and 6x6 MIMO systems is given along with the detection

performance (the red numbers in the boxes describe the detection performance). Where $P_d = P\left(\frac{\delta_1}{\delta_2} > \gamma_{cor}\right)$.
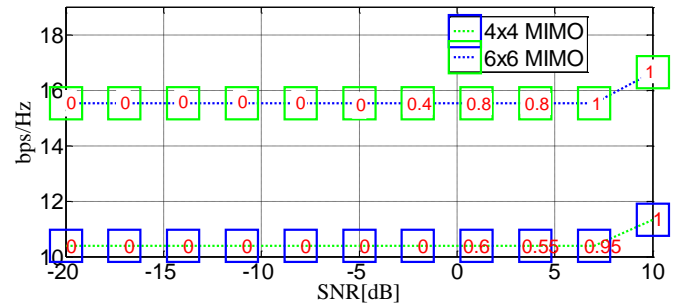
Fig. 4. Channel capacity versus P_d for 4X4 and 6X6 MIMO systems

When calculating P_d, Monte Carlo analysis was applied. Thus, according to the detection scenario given in Figure 2, spectrum detection is performed by creating 500 times random PBS signal and channel coefficients. The average of 500 detection results is calculated for P_d. First of all, it is seen that the detection performance for the same noise levels in 4x4 and 6x6 MIMO systems is directly proportional to the antenna numbers. For example, in the presence of 1 dB noise, detection performances are measured as 0.95 and 1 for 4x4 and 6x6 MIMO. Moreover, at noise levels higher than 0 dB, the 4x4 MIMO system has not made any accurate sensing at all. However, in a 6x6 MIMO system, it is seen that under - 2db noise, 0.4 probability correct detection is made.

The antenna numbers and detection performance are given in Figure 5 for 2x2 and 3x3 MIMO systems. Unlike Figure 4, the most striking difference is that both channel capacity and detection performance are significantly reduced. For example, in the presence of 10 dB noise, the detection probability was 1 for 4x4 and 6x6 MIMO systems. However, in Figure 5, it is observed that these values decrease to 0,7.
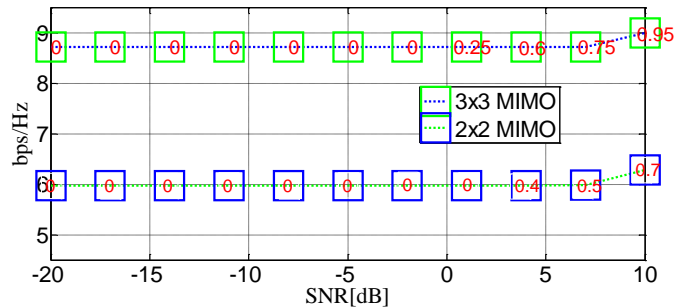

Fig. 5. Channel capacity versus P_d for 3X3 and 2X2 MIMO systems

See Table 1 P_d versus SNR for different antenna numbers. P_d and channel capacity are given separately for 5x5 and 8x8 MIMO systems that are not included in the graphs in Table 1 and Table 2.

TABLE I
SNR VERSUS P_d FOR DIFFERENT MIMO SYSTEMS

SNR	4x4	5x5	6x6	8x8
10 dB	1	1	1	1
5 dB	0.55	0.7	0.8	0.93
0 dB	0.6	0.65	0.8	0.91
-5 Db	0	0	0	0.2

TABLE II
CHANNEL CAPACITY VERSUS SNR DIFFERENT MIMO SYSTEMS

SNR	4x4	5x5	6x6	8x8
10 dB	14	15	22	28
5 dB	11	13	16	18
0 dB	11	13	16	18
-5 Db	11	13	16	18

As can be seen from the tables, the 8x8 MIMO system is the most successful antenna combination in both channel capacity and detection performance.

V. CONCLUSION

In this study, correlation based spectrum sensing and channel capacity are investigated for MIMO systems. In the simulation studies, the effects of the antenna numbers on detection performance and channel capacity in MIMO systems containing different antenna numbers are examined. Thus, simulation studies were carried out by applying Monte Carlo analysis according to the given detection scenario. As a result of these simulation studies, the increase in the antenna numbers has positive effects on both detection performance and channel capacity.

REFERENCES

[1]   B. B. Pradhan and L. P. Roy, "Ergodic capacity and symbol error rate of distributed massive MIMO systems over Rayleigh-inverse Gaussian fading channels using ZF detectors," *Phys. Commun.*, vol. 38, no. 77, p. 7777, Feb. 2020, doi: 10.1016/J.PHYCOM.2019.100906.

[2]   E. Dahlman, S. Parkvall, and J. Skold, *4G: LTE/LTE-Advanced for Mobile Broadband*. 2013.

[3]   M. Kang and M. S. Alouini, "Capacity of MIMO Rician channels," *IEEE Trans. Wirel. Commun.*, vol. 5, no. 1, pp. 112–122, 2006, doi: 10.1109/TWC.2006.1576535.

[4]   Y. Li, J. H. Winters, and N. R. Sollenberger, "MIMO-OFDM for wireless communications: Signal detection with enhanced channel estimation," *IEEE Trans. Commun.*, vol. 50, no. 9, pp. 1471–1477, 2002, doi: 10.1109/TCOMM.2002.802566.

[5]   M. Kowal, S. Kubal, P. Piotrowski, and R. Zieliński, "A simulation model of the radio frequency MIMO-OFDM system," *Int. J. Electron. Telecommun.*, vol. 57, no. 3, pp. 323–328, 2011, doi: 10.2478/v10177-011-0043-6.

[6]   C. Çiflikli and F. Y. Ilgin, "Covariance Based Spectrum Sensing with Studentized Extreme Eigenvalue," *Tech. Gaz.*, vol. 25, no. 6, pp. 100–106, 2018.

[7]   J. Wang, M. Ghosh, and K. Challapali, "Emerging cognitive radio applications: A survey," *IEEE Commun. Mag.*, vol. 49, no. 3, pp. 74–81, 2011, doi: 10.1109/MCOM.2011.5723803.

[8]   M. Matthaiou, M. R. McKay, P. J. Smith, and J. A. Nossek, "On the condition number distribution of complex wishart matrices," *IEEE Trans. Commun.*, vol. 58, no. 6, pp. 1705–1717, 2010, doi: 10.1109/TCOMM.2010.06.090328.

[9]   X. Liu, X. Zhang, H. Ding, and B. Peng, "Intelligent clustering cooperative spectrum sensing based on Bayesian learning for cognitive radio network," *Ad Hoc Networks*, vol. 94, 2019, doi: 10.1016/j.adhoc.2019.101968.

[10]   P. D. Arapoglou, K. Liolis, M. Bertinelli, A. Panagopoulos, P. Cottis, and R. De Gaudenzi, "MIMO over satellite: A review," *IEEE Commun. Surv. Tutorials*, vol. 13, no. 1, pp. 27–51, 2011, doi: 10.1109/SURV.2011.033110.00072.

[11]   N. Promsuwanna, P. Uthansakul, and M. Uthansakul, "Performance of antenna selection in MIMO system using channel reciprocity with measured data," *Int. J. Antennas Propag.*, vol. 2011, 2011, doi: 10.1155/2011/854350.

[12]   Y. Zeng and Y. C. Liang, "Spectrum-sensing algorithms for cognitive radio based on statistical covariances," *IEEE Trans. Veh. Technol.*, vol. 58, no. 4, pp. 1804–1815, 2009, doi: 10.1109/TVT.2008.2005267.

[13]   R. A. Davis, O. Pfaffel, and R. Stelzer, "Limit theory for the largest eigenvalues of sample covariance matrices with heavy-tails," *Stoch. Process. their Appl.*, vol. 124, no. 1, pp. 18–50, 2014, doi: 10.1016/j.spa.2013.07.005.

[14]   Y. Zeng and Y. C. Liang, "Eigenvalue-based spectrum sensing algorithms for cognitive radio," *IEEE Trans. Commun.*, vol. 57, no. 6, pp. 1784–1793, 2009, doi: 10.1109/TCOMM.2009.06.070402.

[15]   Y. He, T. Ratnarajah, E. H. G. Yousif, J. Xue, and M. Sellathurai, "Performance analysis of multi-antenna GLRT-based spectrum sensing for cognitive radio," *Signal Processing*, vol. 120, pp. 580–593, 2016, doi: 10.1016/j.sigpro.2015.10.018.

BIOGRAPHIES

FATİH YAVUZ ILGIN is an Associate Professor in the Department of Electric and Electronics Engineering, Ezincan Binali YLDIRIM University, Turkey. Her research interests include: Statistical signal processing, Cognitive Radio systems, detection theory.

K-Means Clustering Algorithm Based Arrhythmic Heart Beat Detection in ECG Signal

Ö. YAKUT, E. DOĞRU BOLAT and H. EFE

Abstract— **Disorders in the functions of the heart cause heart diseases or arrhythmias in the cardiovascular system. Diagnosis of cardiac arrhythmias is made using the Electrocardiogram which measures and records electrophysiological signals. In this study, a three-class, K-means clustering-based arrhythmia detection method was proposed, distinguishing the cardiac arrhythmia type Right Bundle Branch Block and Left Bundle Branch Block from normal heartbeats. Data from the MIT-BIH Arrhythmia Database were analyzed for clustering-based arrhythmia analysis. Feature Set 1 (FS1) was created by extracting the features from the Electrocardiogram signal with the help of QRS morphology, Heart Rate Variability and statistical metrics. The RELIEF feature selection algorithm was used for dimension reduction of the obtained features and Feature Set 2 (FS2) was obtained by determining the most appropriate features in FS1. Overall performance results for FS1 were 99.18% accuracy, 98.78% sensitivity, and 99.39% specificity, while overall performance results for FS2 were 95.37% accuracy, 92.99% sensitivity and 96.54% specificity. In this study, the computational cost was decreased by reducing the processing complexity and load, utilizing the reduced feature data set of FS2 and an arrhythmia detection method having a satisfactory level of high performance was proposed.**

Index Terms— **Arrhythmia detection, Electrocardiogram (ECG), K-means clustering, Machine learning, RELIEF feature selection algorithm.**

I. INTRODUCTION

ELECTROCARDIOGRAM (ECG) measures and records cardiac activity through electrical signals that are taken from the human body by non-invasive methods. An ECG shows the bioelectric activity of the heart. Fig. 1 depicts the

ÖNDER YAKUT, is with Department of Distance Education Research and Application Center, Kocaeli University, Kocaeli, Turkey, (e-mail: onder.yakut@kocaeli.edu.tr).

https://orcid.org/0000-0003-0265-7252

EMİNE DOĞRU BOLAT, is with Biomedical Engineering, Faculty of Technology, Kocaeli University, Kocaeli, Turkey, (e-mail: ebolat@kocaeli.edu.tr).

https://orcid.org/0000-0002-8290-6812

HATİCE EFE, is with Department of Information Technology, Kocaeli Metropolitan Municipality, Kocaeli, Turkey, (e-mail: haticefe@gmail.com)

https://orcid.org/0000-0002-8552-3075

waveform of a single heartbeat on the ECG recording [2]. The ECG signal is used by specialists to monitor the normal activity of the heart [1]. The depolarization and repolarization functions that occur as a result of stimulation of the heart muscle generate the ECG signal and periodic waves called the PQRST pattern (see Figure 1).
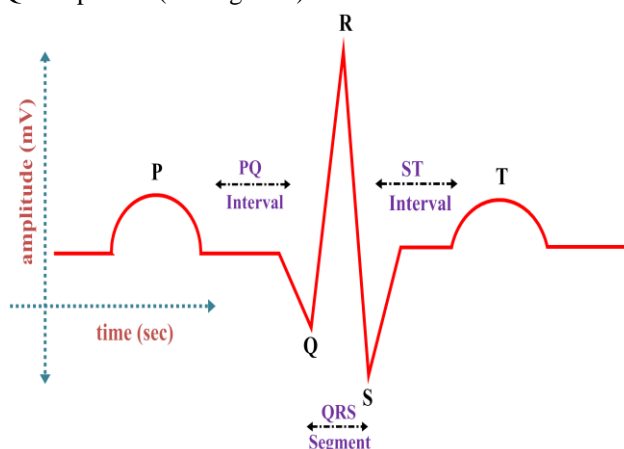
Fig.1. The waveform of the ECG signal [2]

The time intervals and/or waveform changes of a normal heartbeat shown in Fig. 1 may indicate the presence of various cardiac disorders. One of these heart disorders is an arrhythmia, a disorder of the sinus rhythm that is the normal heart signal. All of the problems derived from the generation or conduction of electrical excitation that provide the heart contraction are all collectively called "arrhythmias" [3]. A healthy heart contracts 60-100 times per minute.
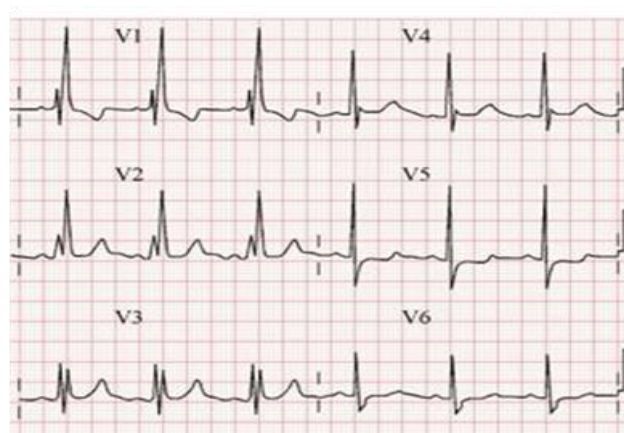
Fig.2. Example of Right Bundle Branch Block (RBBB) [4]
In the precordial leads (V1-V2-V3) showing the right side

of the heart, rSR' (prolonged S wave in V6) pattern or QRS complexes resembling an M shape are seen in Fig. 2 [4]. Fig. 2 shows the Right Bundle Branch Block (RBBB) beat example. The left ventricle is normally activated with the impulses travelling through the left bundle branch, and then the conduction passes to the Atrioventricular Node (AV node) and the right ventricle is activated with delay. The RBBB indicates a problem in the electrical conduction system of the heart. For a diagnosis of RBBB from ECG data the following signs should be present: the QRS duration should be over 120 ms; the S waves should be expanded in the V5-V6 band; there should be an M-shaped QRS complex; and there should be T wave inversion and ST depression in V1-V2-V3. Although RBBB may be present in healthy individuals, the rate of incidence of RBBB increases with age [4,5].
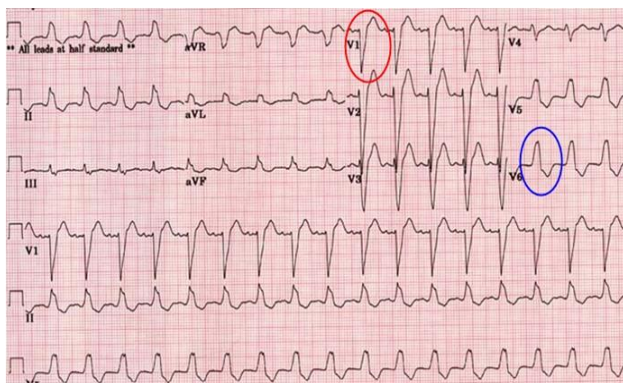
Fig.3. Example of Left Bundle Branch Block (LBBB) [8]

There can be many changes in the ECG signal components. The QRS and T waves are reversed in the direction as shown in Fig.3 depicting Left Bundle Branch Block (LBBB). In leads where the QRS wave is positive, the T wave may be negative. Negative T waves are abnormal in leads with negative QRS. The QRS complexes in the lateral leads may be in the form of an M-shaped, notched rS complex shown in Fig.3 [8]. LBBB is very important, since it can mask the diagnosis of myocardial infarction. In LBBB, the depolarization of the ventricles is delayed because the left ventricle is more slowly depolarized after depolarization of the right ventricle due to slower than normal right-to-left interventricular septal conduction [6]. Typical ECG parameters found in LBBB include: QRS duration of 120 ms or more; a large notched M-shaped R wave seen in DI, aVL, V5, V6; T and Q waves are on opposite sides; and no Q waves are seen in V5, V6 [7].

There are studies on arrhythmia diagnosis using clustering or classifier based algorithms in the literature. The study by Akdeniz [9] is of two phases. In the first stage, it was determined whether arrhythmia was present or not on the ECG data. In the second stage, classification was made of the arrhythmias that were detected. Time-frequency features were derived using various transformation techniques [9]. In the study by Ersoy [3], acceptable successful classification results were obtained using a multi-layered, artificial neural network that detected whether there was an arrhythmia symptom on the ECG signal [3]. Doğan et al. [10] proposed the Vortex Search

algorithm for fuzzy-based clustering of arrhythmia in the ECG signal using a metaheuristic approach. Donoso et al. [11] conducted a study of Atrial Fibrillation (AF) Clustering based on the ECG signal. In this study, they presented work which identified AF subclasses using K-means and hierarchical clustering algorithms [11]. Suganthy [12] in the proposed Fuzzy C Means (FCM) method calculated the heart rate from foetal electrocardiogram signals using clustering and grouping of the R peaks. Wang et al. [13] proposed a type 2 FCM algorithm used to determine early ventricular beats in the ECG signal. In the study by Yücelbaş [14], six different arrhythmia types were identified using hybrid classifiers formed by using multiple systems together. Features were prepared by applying wavelet transform on the data available from the Massachusetts Institute of Technology-Beth Israel Hospital (MIT-BIH) database [14]. Zhang et al. [15] extracted the wavelet features and classified electronic waveforms using the K-means clustering with a Hamming distance. Dallali et al. [16] proposed a classification of arrhythmias using wavelet transform, Heart Rate Variability (HRV) and FCM clustering. Hilavin et al. [17] suggested a K-Nearest Neighbour (KNN) based classification of five types of arrhythmias using the spectral features of the ECG signal. Yeh et al. [18] proposed a cardiac arrhythmia method, which was composed of three main stages using the FCM algorithm in ECG signals. Mohebbanaaz et al. [19] provided a summary of various studies in the literature, such as pre-processing, feature extraction, feature optimization and classification, used when classifying the arrhythmias in ECG signals. They compared performance analysis and methods. Yeh et. al. [20], proposed a method for analyzing the ECG signal to diagnose cardiac arrhythmias using the Cluster Analysis (CA) method. Korürek et. al. [21], classified ECG arrhythmias taken from the MIT-BIH Arrhythmia Database using Ant Colony Optimization (ACO) based cluster analysis. Jekova et. al. [22] compared the learning capacity and classification abilities of the KNN, Neural Networks (NN), Discriminant Analysis (DA) and Fuzzy Logic (FL) methods for arrhythmia classification. Christov et. al. [23] proposed Morphological Descriptors (MD) and Time-frequency Descriptors (TFD) techniques for heartbeat classification to extract heartbeat characteristics from ECG records.

In this study, using a novel clustering approach, a highly successful algorithm distinguishing normal, LBBB and RBBB beats of the ECG signal is described. Additionally, the computational load was decreased through reduction of the size of the feature data set.

II. MATERIALS AND METHODS

A. ECG Signal

ECG signals were obtained from the public MIT-BIH Arrhythmia Database [24]. In this database, there are 48 ECG recordings each of which is 30 minutes long. The ECG signal has ± 5mV amplitude and is sampled at 360 Hz. In the MIT-BIH Arrhythmia Database, a dataset of the beat types shown

in Table 1 was obtained using annotation files containing the location information of the R-peaks of the ECG signals.

TABLE I
DATA SET CREATED FOR DIAGNOSING ARRHYTMIC BEATS IN THE ECG SIGNAL

Beat Type	Number of beats	Record Number
Normal (N)	300	100
RBBB (R)	300	109
LBBB (L)	300	118

In the MIT-BIH Arrhythmia Database, record 100 for normal (N) beats, record 109 for RBBB (R) beats and record 118 for LBBB (L) beats were used. The number of beats with the related record numbers is given in Table 1.

B. Feature Extraction

In this study, the location of the R peaks in the ECG signal was obtained from the annotation files. Thus, the features including meaningful information about the heartbeats were extracted using these R-peaks and these features were used for the diagnosis of the arrhythmia types in the heartbeats of the clustering algorithm.

In the proposed system, a 50-sample window (24 samples before R peak and 25 samples after R peak) was located inside the R peak window. Thus, the locations of Q and S points were determined. The amplitudes of the QRS complex components and the QRS complex width were used as a feature.

Using the R-peak locations, the time interval $(RR_{(n)})$ between two consecutive R-peaks was calculated. HRV is the change between these intervals [1].
$RR_{(n)}$ is calculated as in Equation (1) [1].

$$RR_{(n)} = R_{(n+1)} - R_{(n)} \tag{1}$$

The feature of the selected beat is calculated as $RRnorm_{(n)}$, as in Equation 2, by normalizing the obtained $RR_{(n)}$ intervals in Equation (1) to the previous 10 $RR_{(n)}$ interval values.

$$RRnorm_{(n)} = \frac{\sum_{i=n-9}^{n} RR_{(i)}}{10} \tag{2}$$

$RRnorm_{(n)}$ represents the normalized $RR_{(n)}$ interval, n represents the index of the corresponding $RR_{(n)}$ interval location. Other features were calculated using the statistical and HRV metrics of the study by Yakut et al. [1]. In this study, feature vector Feature Set 1 (FS1) including 15 features was created as a result of the feature extraction process.

C. Feature Selection

In this study, the RELIEF feature selection algorithm proposed by Kira and Rendell [25] was used. RELIEF is a feature weight-based algorithm and inspired by instance-based learning [25]. The algorithm calculates the weights of the features using the input matrix and the output vector and performs the ordering according to the weights. When sorting, the features are weighted in order of importance, giving the

values between -1 and +1 to the weights of the corresponding features [27].

In this study, five of the 15 features which were used in the RELIEF algorithm were selected as RRnorm, RRmedian, QRSwidth, Qamplitude, and Samplitude, respectively, and feature vector Feature Set 2 (FS2) was generated.

D. K-Means Clustering

In this study, the K-means clustering algorithm, which is well described for solving clustering problems and based on unsupervised learning, was utilized. K-means is a simple and easy clustering algorithm classifying a given data set as input as a defined number of clusters (k clusters) [28].

The K-means clustering algorithm mainly consists of the following steps [28]:
Step 1 - The k-points are placed in the area represented by the clustered objects to form the initial group centroids;
Step 2 - Each object is assigned to a group that has the closest cluster center, depending on the distance metric used;
Step 3 - When objects are assigned to groups, the positions of group centers of k points are recalculated;
Step 4 - Repeat Step 2 and Step 3 until the positions of the group centers remain constant. When group centers are fixed, all objects are grouped according to the distance metric used.

III. EXPERIMENTAL STUDY

In this study, in the K-means clustering algorithm, the distance between objects and cluster centers was calculated using the Euclidean length metric. The proposed system was implemented using Matlab R2015b (The MathWorks, Inc., Natick, Mass., USA) software.

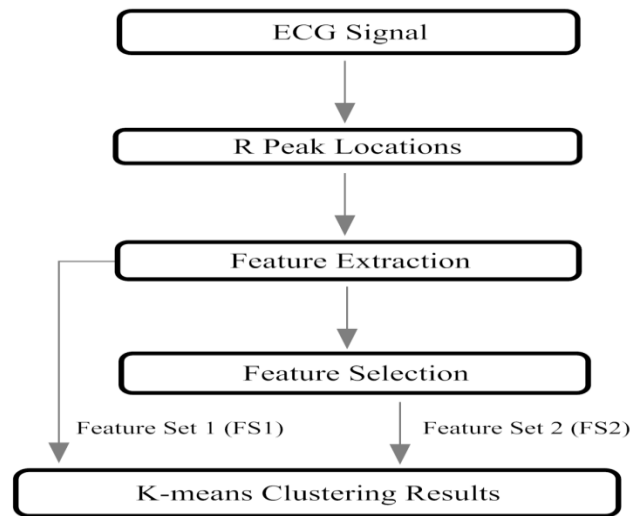### A. Diagnosis of Arrhythmic Heart Beats in the ECG Signal

Fig.4. Block diagram of the proposed system

The block diagram of the proposed system is shown in Fig. 4. The annotation file containing the locations of R-peaks of the ECG signal was obtained from the MIT-BIH Arrhythmia Database [24]. The locations of the obtained R-peaks were

used and FS1 was generated by extracting the features to diagnose arrhythmia from these peaks. These extracted features were subjected to a feature selection process using a size reduction algorithm and FS2 was created. Both of the generated feature data sets were applied to the clustering algorithm. In this study, the K-means clustering algorithm was used to distinguish Normal, LBBB and RBBB heartbeats from each other. The performance of arrhythmic heartbeat detection was assessed.

B. Performance Metrics

In the proposed system, the following metrics were used to measure the success of detecting arrhythmias in heartbeats of ECG signals [28,29].

Accuracy: Indicates the success of correctly detected beats belonging to a particular cluster. It is calculated as in Equation (3).

$$Accuarcy = \frac{TP + TN}{TP + TN + FP + FN} \times 100\% \qquad (3)$$

Sensitivity: It is the ability to accurately determine True Positive (TP) beats that belong to a particular cluster. It is calculated as in Equation (4).

$$Sensitivity = \frac{TP}{TP + FN} \times 100\% \qquad (4)$$

Specificity: It is the ability to accurately determine True Negative (TN) beats that belong to a particular cluster. It is calculated as in Equation (5).

$$Specificity = \frac{TN}{TN + FP} \times 100\% \qquad (5)$$

Explanation of abbreviations used in the above equations;
TP (True Positive): Indicates the total number of beats that are positive and that the algorithm gives a positive result.
TN (True Negative): Indicates the total number of beats that are negative and that the algorithm gives a negative result.
FP (False Positive): Indicates the total number of beats the algorithm gives positive result although it is negative.
FN (False Negative): Indicates the total number of beats the algorithm gives negative result although it is positive [28,29].

IV. EXPERIMENTAL RESULTS

In the proposed system, cardiac arrhythmia of the ECG signal was grouped using FS1 and FS2 data sets and K-means clustering algorithm, and the performance results of the proposed system are shown in Table 2 and Table 3. FS1 overall performance results are given in Table 2 and were: accuracy 99.18%; sensitivity 98.78%; and specificity 99.39%. The FS2 overall performance results are shown in Table 3 and were: accuracy 95.37%; sensitivity 92.99%; and specificity 96.54%, respectively. During simulation studies, the clustering process was repeated five times to ensure the reliability of the results.

TABLE II
K-MEANS CLUSTERING PERFORMANCE VALUES FOR FS1

Beat Type	Accuracy(%)	Sensitivity(%)	Specificity(%)
N	98.78	100.00	98.19
L	96.67	99.00	100.00
R	99.11	97.40	100.00
Overall Performance	99.18	98.78	99.39

In this study, the dimensionality reduction process was applied. Five features were selected from 15 features and the related performance results are given in Table 2 and Table 3.

TABLE III
K-MEANS CLUSTERING PERFORMANCE VALUES FOR FS2

Beat Type	Accuracy(%)	Sensitivity(%)	Specificity(%)
N	93.68	93.53	93.74
L	94.77	90.91	96.79
R	97.67	94.57	99.32
Overall Performance	95.37	92.99	96.54

In the proposed system, the graphs, shown in Fig. 5 and Fig. 6 illustrate the RRmedian and RRnorm features for the FS1 and FS2 feature data sets, respectively.
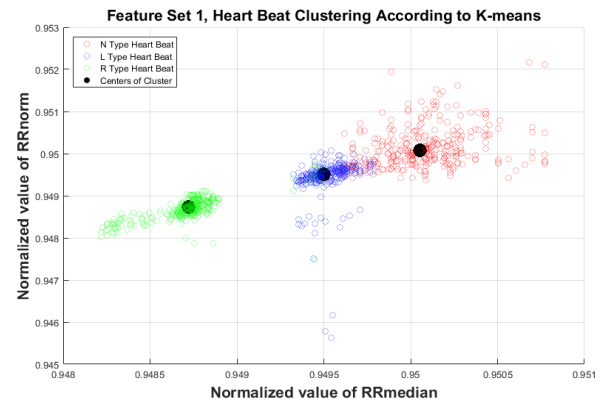
Fig.5. Clustering result for FS1, distribution of cluster centres and heartbeats according to RRmedian and RRnorm features

The cluster centers and distribution of heartbeats versus cluster centers are shown in Fig. 5 and Fig. 6. It is observed that the beats are clustered according to arrhythmia types in the ECG signal.
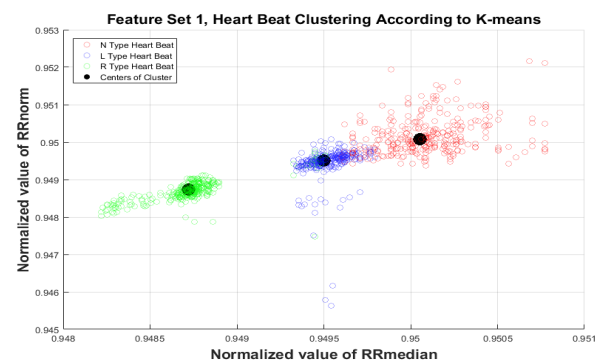

Fig.6. Clustering result for FS2, distribution of cluster centers and heartbeats according to RRmedian and RRnorm features

V. Discussion

The results shown in Tables 2 and 3 indicate that a high-performance system has been developed to detect arrhythmias due to either RBBB or LBBB in the heartbeat records of ECG measurements. However, when Fig. 5 and Fig. 6 are compared, it was observed that the heartbeats grouped in one cluster in Fig. 5 are grouped under other clusters in Fig. 6. This was due to some heartbeats not being sufficiently represented because of the dimensionality reduction of the features, which negatively affected the ability of the K-means clustering algorithm to achieve a correct prediction in some situations.

The FS1 data set consisted of 15 features. As a result of the feature selection process with the RELIEF method, five of these features, with high discrimination, were identified and the FS2 data set was created. Thus, because of the feature selection process, the FS2 data set was reduced to one third of the original FS1 data set. Reducing the size of the data set reduced the computational cost and therefore the computational load of the machine learning method. Since the size of the data set was reduced, the proposed method will consume less system resources, have a lower computational load and thus computational complexity will be reduced. This reduction in the size of the FS2 data set yields satisfactory results in terms of processing load and complexity. However, it was observed that the performance results are lower with a slight difference when compared to the more detailed FS1 data set. The obtained performance results show that the proposed system diagnoses heart arrhythmias at a satisfactory level.

Table IV shows a comparison of the proposed method described herein and classification methods in the literature [20-23]. When the results in Table IV are examined, it is evident that the FS1 data set has the highest sensitivity value when compared with cluster-based algorithms [20,21]. In addition, when the results of the FS1 dataset are compared with previous classification-based algorithms [22,23], they appear to be in the same range and give similar results.

TABLE IV
THE COMPARISON OF SENSITIVITY (%) RESULTS OF CLUSTERING AND CLASSIFICATION METHODS

Study	Method	N	L	R
Proposed Method	K-Means - FS1	100,00	99,00	98,78
	K-Means - FS2	93,53	90,91	92,99
Yeh et. al. [20]	CA	95,59	91,32	90,50
Korürek et. al. [21]	ACO	93,44	-	84,13
Jekova et. al. [22]	kNN	99,91	99,98	99,96
	NN	99,88	99,93	99,92
Christov et. al. [23]	kNN - MD	98,55	99,10	97,38
	kNN - TFD	98,89	98,92	94,77

When the results in Table IV are analyzed, it can be seen that the FS2 data set had the same range and similar sensitivity values when compared with earlier cluster-based algorithms [20,21]. In addition, the FS2 dataset appears to give weaker results compared to classification-based algorithms [22,23].

The ability of the features of the FS2 data set obtained after the dimension reduction to distinguish normal, LBBB- and RBBB-type beats has decreased. However, the result of the FS2 data set is satisfactorily high. When the results of the K-Means clustering method are compared in Tables II and III it is evident that the FS1 data set, containing three times as many features, provides better performance for arrhythmia classification than the FS2 data set.

The performance of the K-Means clustering method proposed in the present study has been compared with both clustering and classification methods in the literature. The performance of the current proposed method is comparable with earlier methods and is clearly and reliably proven.

It was concluded that the K-Means clustering method has similar detection capability with current methods in classifying normal, LBBB- and RBBB-type beats using both the FS1 and FS2 data sets.

In this study, normal, LBBB- and RBBB-type heartbeats were classified using the K-Means clustering method. Generally, classification methods are used to identify and classify arrhythmic heartbeats. It was shown that the K-Means clustering algorithm has the ability to classify arrhythmic heartbeats and a high-performance cluster-based arrhythmia diagnosis method is proposed.

VI. Conclusion

In this study, a method of distinguishing RBBB, LBBB and Normal beats in the ECG signal using the K-means clustering algorithm is proposed. The ECG signals and the locations of the R peaks were obtained from the MIT-BIH Arrhythmia Database. QRS morphology, HRV and statistical metrics were used to extract the features, creating FS1, and the most appropriate features were selected with the RELIEF dimensionality reduction algorithm, creating FS2. The K-means clustering algorithm was used to classify the arrhythmic ECG signals using FS1 and FS2 data sets, and the arrhythmic beat clustering analysis was performed. As a result of the classification, the overall performance results for FS1 were very good and comparable with previous, classification-based algorithms while the results obtained for FS2 were somewhat lower than for FS1 but were still acceptable for differentiation of normal, RBBB and LBBB heartbeats. In addition, use of the FS2 data set resulted in lower computational cost by decreasing the processing load and complexity, and a highly effective and successful arrhythmia diagnosis method has been proposed. In future studies, different data sets should be analyzed and the number of heartbeat types with arrhythmias should be increased. Morphological, time and frequency domain-based features could be extracted from the ECG signal using different methods and features can be selected using different algorithms. Different clustering methods with high classification performance may then be developed.

References

[1] O. Yakut, O. Timuş, E. D. Bolat, HRV analysis based arrhythmic beat detection using knn classifier, WASET Int. J. Biomedical and Biological Eng., 2016, 10(2), 60-63.

[2] Yakut, O., Solak, S., Bolat, E. D., Measuring ECG signal using e-health sensor platform., In International Conference on Chemistry, Biomedical and Environment Engineering, 7-8, October, 2014, Antalya, Turkey.

[3] E. Ersoy, ECG signals used on arrhythmia diagnosis with multilayer perceptron neural network, M.S. thesis, Dept. Mechatr. Eng., Gaziosmanpasa Univ., 2016.

[4] E. Tek, Right bundle branch block, Available: https://www.resusitasyon. com/sag-dal-blogu/, (date of visit: 21.09.2020).

[5] E. Burns, Right bundle branch block (RBBB), Available: https://litfl. com/ right -bundle -branch-block-rbbb-ecg-library/, (date of visit: 21.09.2020).

[6] B. P. Griffin, C. M. Rimmerman and E. J. Topol, The cleveland clinic cardiology board review, Lippincott Williams & Wilkins, ch.45, sec.8, 2007.

[7] D. Da Costa, W. J. Brady, and J. Edhouse, ABC of clinical electrocardiography: bradycardias and atrioventricular conduction block, British Medical J., 2002, 324(7336), 535-538.

[8] E. Tek, Left bundle branch block, Available: https://www. resusitasyon.com/ sol-dal- blogu/, (date of visit: 24.09.2020).

[9] F. Akdeniz, Classification of ECG arrhythmias using time-frequency based features, M.S. thesis, Dept. Elec. and Electron. Eng., Karadeniz Technical Univ., 2017.

[10] B. Dogan, T. Olmez, Fuzzy clustering of ecg beats using a new metaheuristic approach, In Proc. IWBBIO, 7-9, April, 2014, Granada, Spain.

[11] F. I. Donoso, R. L. Figueroa, E. A. Lecannelier, E. J. Pino, A. J. Rojas, Clustering of atrial fibrillation based on surface ecg measurements, In Proc. IEEE EMBC, 3-7, July, 2013, Osaka, Japan.

[12] Suganthy, M., Analysis of R-peaks in fetal electrocardiogram to detect heart disorder using fuzzy clustering, In Proc. IEEE 5th I2CT, 29-31, March, 2019, Bombay, India.

[13] Wang, X., Wang, S., Tang, Y., Li, B., A new two-type fuzzy c-means clustering algorithm for the diagnosis of ventricular premature beats, In Proc. IEEE MLBDBI, 8-10, November, 2019, Taiyuan, China.

[14] S. Yücelbas, Diagnosis of the heart rhythm disorders by using hybrid classifiers, M.S. thesis, Dept. Comp. Eng., Selcuk Univ., 2013.

[15] Y. Zhang, X. Zhao, Y. Sun, M. Liu, D. Shi, Waveform classification based on wavelet transform and k-means clustering, In Proc. ICMLC, 14-17 July, 2013, Tianjin, China.

[16] A. Dallali, A. Kachouri, M. Samet, Classification of cardiac arrhythmia using wt, hrv, and fuzzy c-means clustering, An Int. J. Signal Processing, 2011, 5(3), 101-109.

[17] İ. Hilavin, M. Kuntalp, D. Kuntalp, Classification of arrhythmias using spectral features with k nearest neighbor method, In Proc. SIU, 20-22 April, 2011, Antalya, Turkey.

[18] Y. C. Yeh, H. J. Lin, Cardiac arrhythmia diagnosis method using fuzzy c-means algorithm on ecg signals, In Proc. 3CA, 5-7 May, 2010, Tainan, Taiwan.

[19] Mohebbanaaz, Y. P. Sai, LV R. Kumari, A review on arrhythmia classification using ecg signals. In Proc. IEEE SCEECS, 22-23, February, 2020, Bhopal, India.

[20] Yeh, Yun-Chi, Che Wun Chiou, and Hong-Jhih Lin. Analyzing ECG for cardiac arrhythmia using cluster analysis, Expert Systems with Applications, 2012, 39(1), 1000-1010.

[21] Korürek, Mehmet, and Ali Nizam, Clustering MIT–BIH arrhythmias with Ant Colony Optimization using time domain and PCA compressed wavelet coefficients, Digital Signal Processing, 2010, 20(4), 1050-1060.

[22] Jekova, I., G. Bortolan, and I. Christov, Assessment and comparison of different methods for heartbeat classification, Medical Engineering & Physics, 2008, 30(2), 248-257.

[23] Christov, I., Gómez-Herrero, G., Krasteva, V., Jekova, I., Gotchev, A., & Egiazarian, K., Comparative study of morphological and time-frequency ECG descriptors for heartbeat classification, Medical engineering & physics, 2006, 28(9), 876-887.

[24] G. B. Moody, R. G. Mark, The impact of the MIT-BIH arrhythmia database, IEEE Eng. in Med. and Biol. Mag., 2001, 20(3), 45-50.

[25] K. Kira, L. A. Rendell, The feature selection problem: traditional methods and a new algorithm, In Proc. AAAI, 12-16 July, 1992, California, USA.

[26] Available: https://www.mathworks.com/ help/stats/relieff.html?s_tid =srchtitle, (date of visit: 11.10.2020).

[27] Available: https://home.deib.polimi.it/ matteucc/Clustering/ tutorial_html/kmeans.html, (Date of visit: 13.10.2020).

[28] O. Timuş, Sleep respiration disorders diagnosis and classification utilizing soft computing algorithms, PhD dissertation, Dept. Elect. Comp. Edu., Kocaeli Univ., 2015.

[29] Ö. Yakut, Classification of arrhythmias in ECG signal using soft computing algorithms, PhD dissertation, Dept. Biomedical Engineering, Kocaeli Univ., 2018.

BIOGRAPHIES

ÖNDER YAKUT received the B.Sc. and M.Sc. degrees in Electronics & Computer Education from Kocaeli University, Turkey, in 2008 and in 2012 respectively. He received Ph.D. degree in Biomedical Engineering from Kocaeli University, Turkey in 2018. The second B.Sc. degrees in Computer Science from Kocaeli University, Turkey, in 2020.

He is currently a software developer at Kocaeli University. His active research interests are signal processing, artificial intelligence, machine learning, cloud computing, embedded systems, sensor/actuator networks, engineering education.

EMİNE DOĞRU BOLAT received her M.Sc. degree in Electronics & Computer Education from Kocaeli University, Turkey in 1998 and Ph.D. degree in Electrical Education from Kocaeli University, Turkey in 2005.

She is currently working as a professor in Biomedical Engineering in Kocaeli University, Turkey. Her research interests are biomedical engineering, automation systems, industrial control, embedded systems and engineering education.

HATİCE EFE received her B.Sc. degree in Computer Engineering from Kocaeli University, Turkey in 2013. and M.Sc. degree in Industrial Engineering from Kocaeli University, Turkey in 2020.

She is currently working as a Computer Engineer at Kocaeli Metropolitan Municipality Information Technology Department, Turkey. Her research interests are computer engineering, decision analysis and decision theory.

Optimal Design of 3-phase Squirrel Cage Induction Motors Using Genetic Algorithm Based on the Motor Efficiency and Economic Evaluation of the optimal Model

M. REZAIEE NAKHAEI, R. ROSHANFEKR

Abstract— **There are different approaches to improve the efficiency of induction motors. In this paper, the considered approaches include, design of the rotor slot, rotor slot shape, and stator and rotor diameters which are applied on a 30-kW 3-phase, 4-poles, 48-stator slots, and 44-rotor squirrel cage induction motor. Comparison of analytical, simulation and experimental results confirm the proposed finite element method (FEM) based model of set-up induction motor. The sensitivity analysis of efficiency considering the variations of rotor slot dimensions, stator outer diameter, and stator and rotor diameters have been applied on the case-study. The results of the genetic algorithm (GA) based optimal design of the rotor slot dimensions showed a 0.32% improvement in motor efficiency. On the other hand, changing the motor core diameters has more effects on motor efficiency so that, when the stator and rotor outer diameters were increased simultaneously, the efficiency was increased by 0.55%. However, if the stator outer diameter just increased, motor efficiency increased by 0.76%. Finally, the economic evaluation was accomplished to validate the optimal approach of motor design for three cases of electricity consumption per kWh.**

Index Terms— **squirrel cage induction motor, geometric dimension, efficiency, optimization, economic evaluation**

I. INTRODUCTION

THE SQUIRREL cage induction motors are extensively used in many industrial fields and home applications because of their simple structure, reliability, low cost, robustness, less maintenance and ability to work in inimical environments. Since the starting torque in an induction motor is poor, there is a limitation to be used in some applications requiring high starting torque. One of the ways to increase the starting torque is adjusting the resistance and reactance of the rotor, especially the upper part of rotor slot resistance according to the skin effect in the motor startup. To reach this goal, it is necessary to design the rotor bars of the squirrel cage induction motor. The slot depth design is another procedure to improve the starting torque however, this design increases rotor slot leakage reactance and decreases motor efficiency [1-3].

Besides the low starting torque by induction motors, the efficiency of these motors should pay particular attention due to the wide applications in industry. According to the results of an investigation for the United State Federal Energy Administration, the electric motors consume 64% of the total electric consumption in the United-state. Thus, energy conservation requires focusing on electric motors, and their efficiencies [4, 5].

Many previous studies for increasing starting torque, efficiency, and power factor in induction motors have been carried out for a long time. As the rotor bar shape has more important effects on motor performance characteristics, there are many studies about rotor bar design. In some studies, to increase starting torque and efficiency or achieve a certain torque-speed curve, the rotor slot shape has been changed [1, 3-7]. In the other studies, the motor characteristics have been changed by using ways of adjusting slot dimensions and rotor slot area whereas the shape of the rotor slot has been maintained [8-11].

Besides, the aluminum die-cast is the way to fill the rotor bars and end rings. In this process, the porosity phenomena in bars and end rings of the rotor can occur. The porosity is proportional to the fill factor reversely. The results show that efficiency and starting torque will be increased by 1.92 %, and 11.93 %, whereas the fill factor is adjusted from 62% to 93%, respectively [12, 13]. But, in the industry, the fill factor is usually over 96 % and also it is difficult to model in software design.

The skewed rotor bars are employed to reduce the harmonic components of motor specifications. For instance, the total harmonic distortion (THD) of stator current with and without

MAHDI REZAIEE NAKHAEI, is with Department of Electrical Engineering University of Hakim Sabzevari, Sabzevar, Iran, (e-mail: mehdirezaei24@yahoo.com).

https://orcid.org/0000-0002-1008-2180

REZA ROSHANFEKR, is with Department of Electrical Engineering University of Hakim Sabzevari, Sabzevar, Iran, (e-mail: r.roshanfekr@hsu.ac.ir). Corresponding Author

https://orcid.org/0000-0002-6442-1571

the skewed model is 0.9% and 1.61%, respectively [14]. So, the skewed rotor has a significant effect on harmonic components. The novel skewed rotor presented in [15], decreases the radial electromagnetic force as well as the harmonics flux density amplitude for radial, circumferential, and axial component. Also, the noise of the motor in the improvement model is reduced.

The inclination of rotor bars which is different from the skewing of rotor bars has a significant effect on efficiency so that it is increased by 0.63% whereas the starting torque is increased only 0.63 % when the inclination angle adjusted from 0º to 25º [16]. However, the rotor bar inclination is limited when the number of rotor slots increases.

In the primary design of the induction motor, when the design process leads to lower efficiency than the desired value, the increase stator core is the way to increase efficiency [17, 18]. The stack length is one of the motor geometry parameters which was considered by [19] so that when the stack length is increased in different commercially manufactured induction motors, the efficiency is increased.

When using the material with a lower loss for core laminates and conductors, the efficiency has been increased. However, the selection of laminate and conductor material has been limited, and also it increases motor costs [20].

Generally, electricity generation is expensive for every government. With the high growth rate of electrical energy consumption, it is necessary to construct more power plants. Thus, this leads to an increase in the costs and pollution of the environment. To reduce the energy consumption with the industrial induction motors, the main goal of this article is the optimal efficiency design of 3-phase squirrel cage induction motors.

In this article, based on the mathematical equations related to geometric dimensions of induction motors, the motor performance characteristics have been determined. The motor performance results obtained from mathematical equations, model simulation using RMxprt-Maxwell software and experimental tests applied to a 30-kW 4-pole 3-phase squirrel cage induction motor have been compared. Also, different approaches with combination of the genetic algorithm have been applied to the model of the set-up motor as the conventional model to improve the motor efficiency. Finally, the economic evaluation of the optimal model has been considered to validate the optimal motor design approach.

II. ANALYTICAL BACKGROUND

The performance characteristics of induction motors are determined according to their geometric dimensions. In this section, the mathematical equations related to the motor efficiency and power factor are described in which they are proportional to the motor equivalent circuit [21]. The details of these equations have been presented in [22].

The Efficiency (η) is proportional to losses so that can be expressed using Eq. (1):

$$\eta = P_{out} / (P_{out} + P_{loss}) \tag{1}$$

where, P_{out} is rated output power, and P_{loss} is power losses of motor. The induction motor losses can be divided into the iron loss, stator copper loss, rotor copper loss, mechanical loss, and stray loss:

$$P_{loss} = P_{iron} + P_s + P_r + P_m + P_{stray} \tag{2}$$

where P_m is mechanical loss, P_{stary} is stray loss.

The stator copper loss depends on the resistance of stator (R_s) and motor rated current (I_n):

$$P_s = 3R_s I_n^{\,2} \tag{3}$$

Similarly, the rotor copper loss can be described as:

$$P_r = 3(R_r)_{S_n} I_m^{\,2} = 3R_r K_I^{\,2} I_n^{\,2} \tag{4}$$

where R_r is the resistance of rotor in the rated speed, I_n is rated current, and K_I is coefficient of stiffness stator mmf relative to the rotor.

The core loss P_{iron} consists of the fundamental P^1_{iron} and harmonic P^h_{iron} iron loss. The fundamental iron loss occurs only in the stator teeth (P^1_t) and stator yoke (P^1_y) due to the rotor frequency is low. The stator teeth fundamental loss P^1_t and the stator yoke fundamental loss P^1_y can be calculated approximately using Eq. (5) and (6):

$$P_t^1 \approx K_t \times P_1 \times (f_1 / 50)^{1.3} B_{ts}^{1.7} G_{ts} \tag{5}$$

$$P_y^1 \approx K_t \times P_1 \times (f_1 / 50)^{1.3} B_{ys}^{1.7} G_{ys} \tag{6}$$

where P_1 is specific losses in W/Kg at 1.0 Tesla and 50Hz, K_t is coefficient core loss augmentation due to the mechanical machining, f_1 is the fundamental frequency, G_{ts} is stator tooth weight, G_{ys} is stator yoke weight, B_{ts} is tooth flux density, and B_{ys} is yoke flux density.

Also, the harmonics iron loss P^h_{iron} includes both stator (P^h_s) and rotor (P^h_r) harmonic losses.

$$P_s^h \approx 0.05 \times 10^{-3} \tag{7}$$
$$\cdot ([(N_s (f_1 / p)(1 / (2.2 - B_{ts}))(K_{c2} - 1)B_g]^2 G_{ts})$$

$$P_r^h \approx 0.05 \times 10^{-3} \tag{8}$$
$$\cdot ([(N_r (f_1 / p)(1 / (2.2 - B_{tr}))(K_{c2} - 1)B_g]^2 G_{tr})$$

where B_g is air-gap flux density, N_s is number stator slot, K_{c2} is stator carter coefficient, K_{c1} is rotor carter coefficient, N_r is number rotor slot, and G_{tr} is rotor tooth weight.

In general, the power factor can be expressed using Eq. (9):

$$\cos \varphi = P_{out} / 3V_{ph} I_n \eta \tag{9}$$

where V_{ph} is phase voltage.

III. CASE STUDY

In this article, the case study is a 3-phase squirrel cage induction motor which consists of 4-pole, 48-stator slots, and 44-rotor slots with 30 kW rated power, 1474 rpm, and 380V. The outer diameter of the stator and rotor is 327 mm, and 210 mm, respectively and the core length of the motor is 230 mm. Also, the depth of stator and rotor slots are 26.8 and 38 mm, respectively.

Figure 1 shows the cross-section of the stator and rotor core. As shown in Fig. 1, the slot of the rotor is a half-slot type.

Also, the skewed rotor slot (3.48 degree) is employed to reduce the noise of motor as well as the harmonic components of motor performance characteristics.

According to the theoretical equations given in section II and motor geometrical dimensions, the performance characteristics of the set-up induction motor have been calculated. Also, the set-up induction motor as the conventional model has been simulated by RMxprt-Maxwell software based on the finite element method (FEM) [23]. The results of theoretical analysis, experimental test, and simulation applied on the conventional model have been presented in Table 1 where PF is the power factor, P_T is total losses, and T_m is maximum torque.

The experimental results presented in Table 1 have been performed in the evaluation and quality control section of Jovein Electrical Machines Industries Company (JEMCO). The purpose of this study is to improve the performance characteristics, especially the efficiency of the case study induction motor manufactured by JEMCO.

The determined performance characteristics given in Table 1, are relatively close to each other, except P_{iron}, η, P_s, and P_r. So that, the efficiency obtained from theoretical equations and experimental results is 91.14% and 91.52% respectively, however, it is 93.59 % by simulation results. The reason for the difference between these values in motor efficiency is the iron loss. The coefficient iron loss augmentation (K_t) due to the mechanical machining is considered in (5) and (6) to calculate the iron loss. Also, the opinion of professional engineers in the field of electric motor manufacturing is that the iron loss affected by mechanical machining becomes almost doubles. So, the efficiency obtained from software can be modified considering the K_t coefficient. Also, stator and rotor losses (P_s and P_r) in simulation and theory are different from experimental results. The fill factor of the squirrel cage induction motor rotor bars in the software is considered to be 100%, while in reality this coefficient is not 100%. In stator windings, in fact, the presence of stator slot insulations, the presence of wooden or plastic wedges at the top of the stator sot, and finally the end connection of the stator windings are reasons of a difference in the stator copper losses compared to the simulation that hasn't these cases.
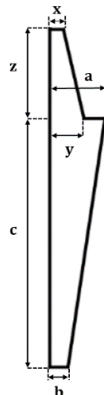
Fig.2. Rotor slot shape of the conventional induction motor

IV. SENSITIVITY ANALYSIS

In this section, the effects of rotor slot dimensions and the stator and rotor diameters on performance characteristics of the 30-kW induction set-up motor are analyzed. The result of sensitivity analysis is useful to choose a design method with appropriate variables and concentrates.

TABLE I
THE INDUCTION MOTOR PERFORMANCE CHARACTERISTICS OBTAINED FROM THEORETICAL ANALYSIS, EXPERIMENTAL TEST, AND SIMULATION RESULTS

Characteristics	Theoretical	Experimental	Simulation
P_{out} (kW)	30	30	29.99
V_{ph} (V)	380	380	380
I_n (A)	54.23	57.359	53.62
I_{start} (A)	230.21	226.65	234.22
speed (rpm)	1474	1474.31	1476
PF	0.92	0.871	0.90
P_{iron} (W)	1244	965	454.92
P_s (W)	742.8	909	770.77
P_r (W)	335.6	564	315.66
P_T (kW)	2.8	2.95	2.1
η (%)	91.14	91.518	93.59
f (Hz)	50	50	50
T_s (N.m)	330.36	482.4	339.82
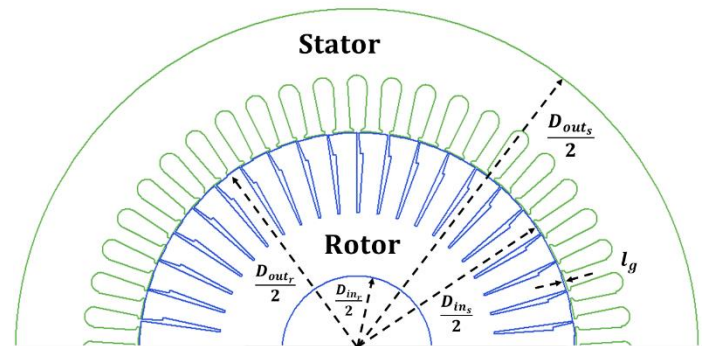
Fig.1. Cross-section of stator and rotor core related to the conventional model

A. Rotor slot dimensions

Since the induction motor is influenced by the skin effect at motor startup conditions, the current is concentrated in the upper part of the slot. Furthermore, at the motor rated conditions, the current flows of the whole slot. Hence various parts of slot and their area have effects on the performance characteristics of the motor. In this section, the effects of changing the values of the rotor slot dimensions along both width and depth are investigated on the motor efficiency, power factor and starting torque.

When each dimension of the rotor slot includes x, y, z, a, b, and c-dimension (Fig. 2) is changed, the area of the slot is no longer equal to the previous value. The current density of the rotor slot is changed when the area is changed. Due to current density variation, the rotor copper loss is changed as well as the motor efficiency. The conventional model efficiency is 93.59% refer to Table 1. The motor efficiency, power factor, and starting torque versus width and depth dimensions of the rotor slot are illustrated in Fig. 3, and Fig. 4, respectively.

Based on Fig 3-a, each part of the slot widths has a different

effect on motor efficiency so that the top part of the rotor slot width has no significant effect on efficiency. When the middle part width of the rotor slot is changed from 2mm to 12mm, the efficiency increases by 0.3%. Also, increasing the bottom part width results in a sharper decrease in motor efficiency in comparison with other parts.
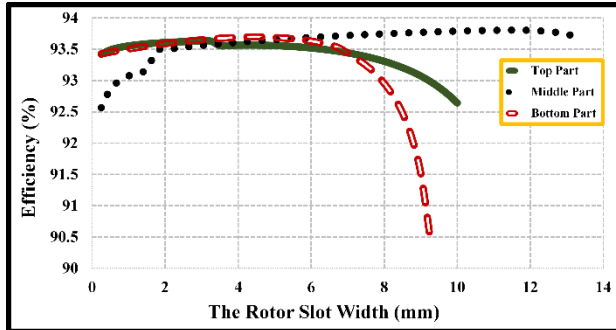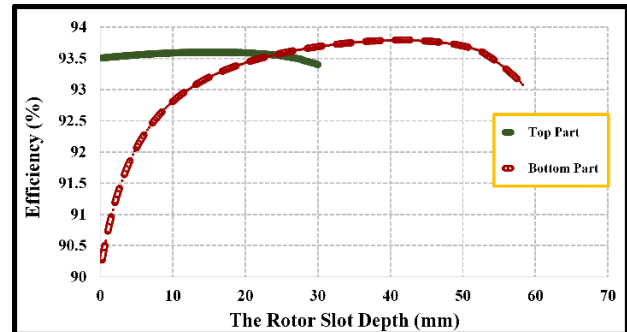

(a)
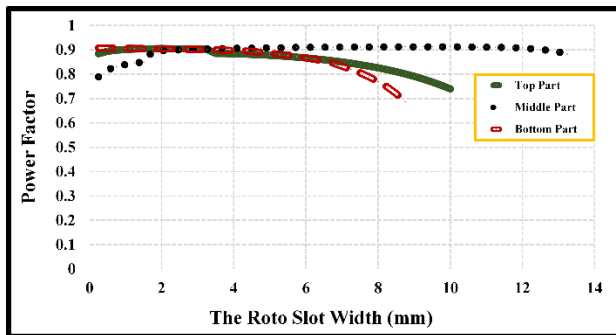
(b)
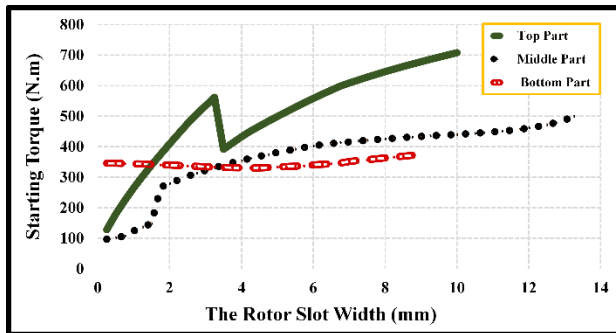
(c)

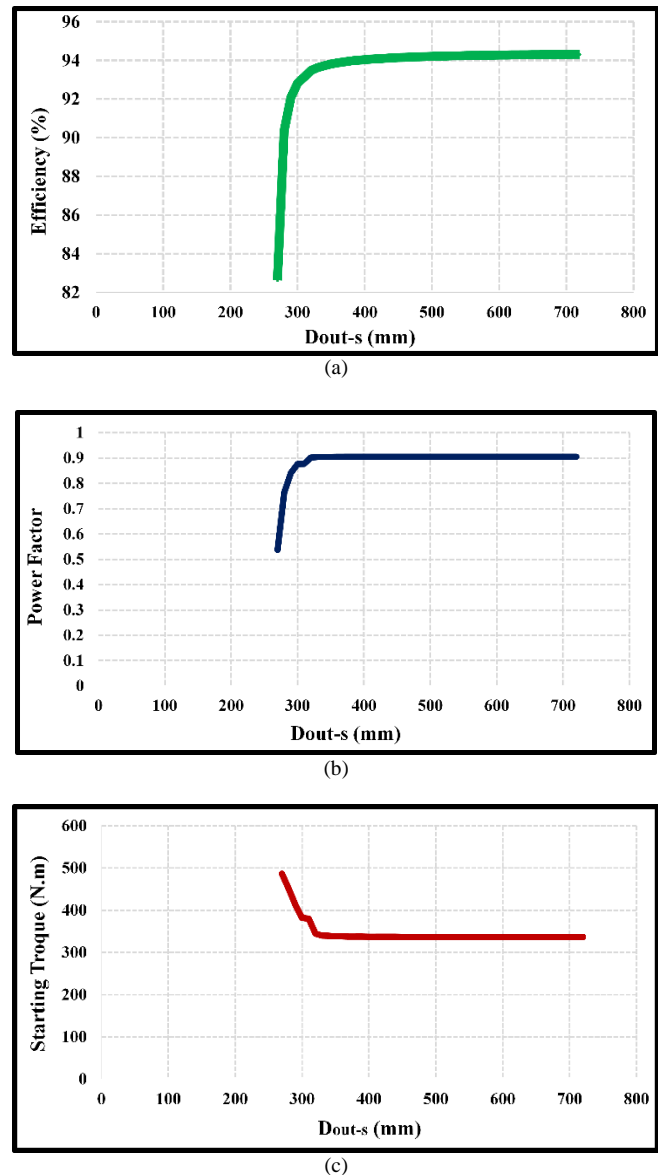Fig.3. Different part sensitivity of the rotor slot width on performance characteristics of the conventional model. (a)- Efficiency, (b)- Power Factor, (c)- Starting torque

Figure 3-b showed that the power factor is changed similar to efficiency. Also, the starting torque has different behavior against changing the different parts of the rotor slot width. The bottom part changing does not affect starting torque due to that the current is concentrated in the top part of the rotor slot. Hence, as shown in Fig. 3-c, the top part of the rotor slot has a great effect on starting torque whereas the top part width increases from 0.25mm to 10mm, the starting torque is increased by 483%. However, the efficiency is reduced amount of 0.96%.

According to Fig. 4-a, the efficiency related to the top part

of the rotor slot depth is almost constant. However, when the bottom part depth is increased from 0.25mm to 40mm, the efficiency was increased by 4%. The variations of the power factor have been depicted in Fig.4-b which is similar to the efficiency variations, but the starting torque is decreased when the top and bottom parts depth dimensions of the rotor slot are increased as shown in Fig. 4-c.

(a)
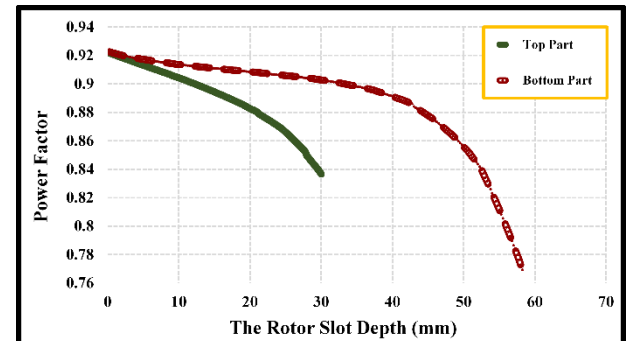
(b)
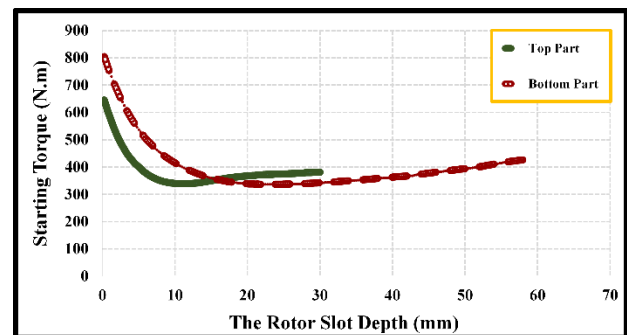
(c)

Fig.4. Different part sensitivity of the rotor slot depth on performance characteristics of the conventional model. (a)- Efficiency, (b)- Power Factor, (c)- Starting torque

Thus, all dimensions of the rotor slots have effects on the performance characteristics of the motor. It is needed a trade-off between different parts of the rotor slot (width and depth) to achieve an acceptable performance characteristic. So, a trade-off between efficiency, power factor, and starting torque is needed to choose the optimal point for $D_{out\text{-}s}$, $D_{in\text{-}s}$, $D_{out\text{-}r}$, and $D_{in\text{-}r}$.

B. Stator and rotor diameters

The stator inner diameter (D_{in-s}) is proportional to the ratio, which is defined as the ratio (K_D) of D_{in-s} to D_{out-s} (stator inner diameter). This ratio depends on the number of motor pole pairs (p). When the D_{out-s} is changed, the stator inner diameter, rotor outer diameter (D_{out-r}) and rotor inner diameter (D_{in-r}) can be calculated using Eq. (10)- (12):

$$D_{in-s} = K_D D_{out-s} \qquad (10)$$

$$D_{out-r} = D_{in-s} - 2l_g \qquad (11)$$

$$D_{in-r} \leq D_{out-r} - 2l_{slot} \qquad (12)$$

where l_g and l_{slot} are air-gap length and rotor slot depth, respectively.

(a)

(b)

(c)
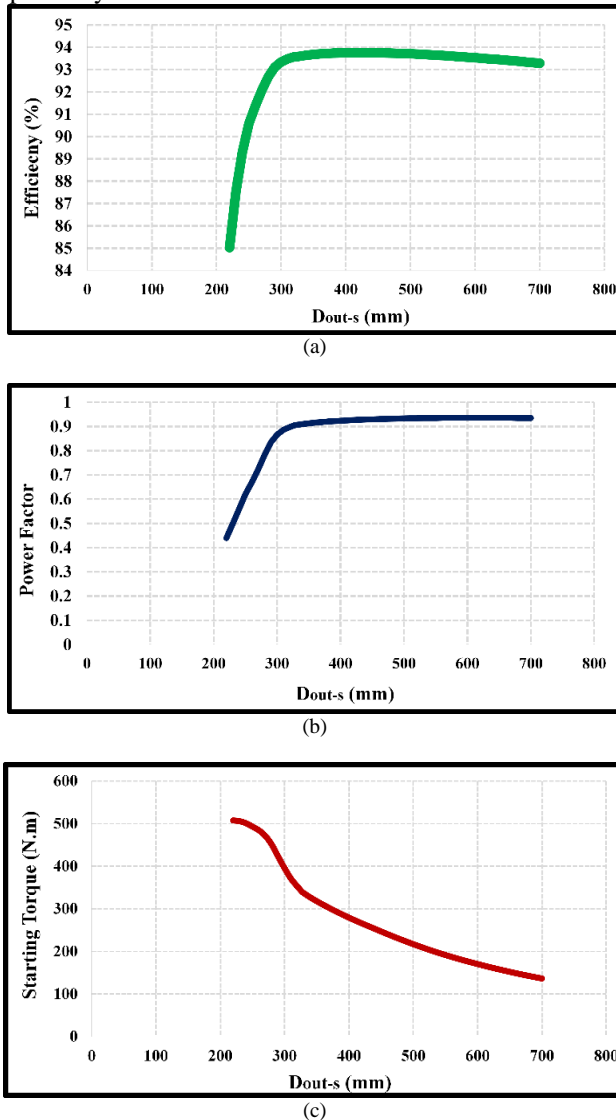
Fig.5. Sensitivity of the stator and rotor diameters simultaneously on performance characteristics of the conventional model. (a)- Efficiency, (b)- Power Factor, (c)- Starting torque

Based on the number of pole pairs in the conventional model ($p = 2$), K_D is considered 0.62. In this approach, since the stator outer diameter has been changed from 220 mm to 700 mm, also the air-gap length is 0.65mm, the D_{in-s}, D_{out-r}, have been changed from 136.4mm to 446.4, 135.1mm to 445.1mm, respectively.

The motor efficiency, power factor, and starting torque curve versus the stator and rotor diameters at the same time is depicted in Fig. 5. Although the enlargement of core diameter increases the motor efficiency, however the starting torque reduces. The power factor is changed similar to the efficiency curve.

C. Stator outer diameter

In this approach, the inner and outer diameters of the rotor and the inner diameter of the stator are constant at their initial values. The stator outer diameter is changed to analyze the effect of this variation on motor performance characteristics. The stator outer diameter has been changed from 270mm to 720mm. The efficiency, power factor, and starting torque curves versus the stator outer diameter (D_{out-s}) are depicted in Fig. 6.

(a)

(b)

(c)

Fig.6. Sensitivity of the stator outer diameters on performance characteristics of the conventional model. (a)- Efficiency, (b)- Power Factor, (c)- Starting torque

The results show that power factor and starting torque are constant when the D_{out-s} is larger than 350mm whereas efficiency is increased. However, in comparison with Fig. 5, the efficiency and starting torque decrease whereas the power factor increases.

V. APPROACHES OF MOTOR DESIGN

There are different approaches to improve the performance characteristics of induction motors. In this article, the approaches include design of rotor slot, rotor slot shape, stator and rotor diameters, and stator outer diameter are applied to the conventional model presented in section 3. The sensitivity analysis of rotor slot dimensions and stator and rotor diameters is accomplished. The genetic algorithm (GA) is employed to find the optimal geometric parameters in the proposed approaches according to the sensitivity analysis results.

A. Approach 1: Design of rotor slot

In this approach, the goal is to design an optimal rotor slot based on the rotor slot shape of the conventional model. The maximum motor efficiency has been chosen as the objective function. The optimization algorithm has six variables such as x, z, y, a, c, b which are dimensions of conventional model rotor slot (Fig. 2). The results of the GA optimization are presented in Table 2. The optimal rotor slot shape using GA is depicted in Fig. 7-b.

(a)   (b)
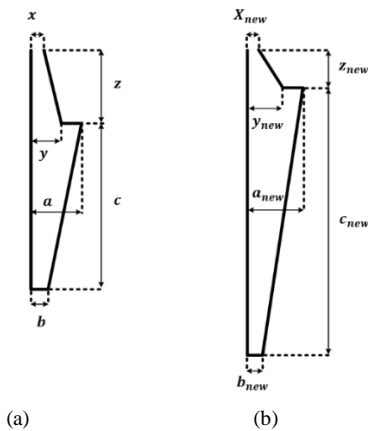
Fig.7. Rotor slot shape. (a)- Conventional model, (b)- Optimal model related to the approach 3

TABLE II
THE RESULTS OF GA OPTIMIZATION

Variables	Limit (mm)	Initial value (mm)	optimal value (mm)
x (mm)	0.75-2.25	1.5	1.509
z (mm)	5-15	10	5.900
y (mm)	1.75-5.25	3.5	4.605
a (mm)	2.9-8.7	5.8	7.876
c (mm)	14-42	28	38.039
b (mm)	1-3	2	1.549

The simulated performance characteristics of the optimal motor have been presented in Table 3. The results show that the optimal motor efficiency in this approach increases by 0.32% in comparison with the conventional motor efficiency. Besides, the starting torque increases by 18.13%, as well as the starting current by 31.36% in comparison with the

conventional model. Furthermore, the PF of the optimal decreases by 0.55% in comparison with the conventional motor PF.

TABLE III
THE INDUCTION MOTOR CHARACTERISTICS OF THE OPTIMAL ROTOR SLOT SHAPE RELATED TO APPROACH 1 IN COMPARISON WITH THE CONVENTIONAL MODEL (SIMULATION RESULTS)

Characteristics	Conventional	Optimal
η (%)	93.59	93.89
PF	0.904	0.899
I_{start} (A)	234.22	307.68
T_s (N.m)	339.82	401.45

B. Approach 2: Rotor slot shape

The shape of the slot is proportional to the leakage reactance of the slot which affects motor efficiency. Hence, in this approach, the rotor slot shape has been changed to investigate the effect of different slot shapes on motor performance characteristics considering constant slot area (134.2 mm^2). The motor performance characteristics related to the conventional model and each rotor slot shapes (shown in Fig. 8) are presented in Tables 4. According to the results, the highest efficiency is 93.63 % in I, III, and IV prototypes. In these cases, the efficiency increases by 0.04 % in comparison with the efficiency of the conventional model.

(I)   (II)   (III)   (IV)
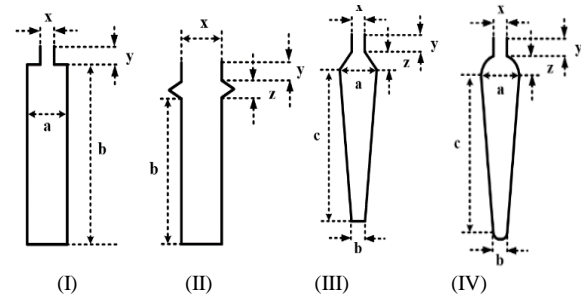
Fig.8. Five different prototypes of rotor slot shapes with the same area

TABLE IV
THE INDUCTION MOTOR PERFORMANCE CHARACTERISTICS RELATED TO APPROACH 2 BASED ON THE SHAPE IN COMPARISON WITH THE CONVENTIONAL MODEL (SIMULATION RESULTS)

Char.	Conv.	I	II	III	IV
η (%)	93.59	93.63	93.52	93.63	93.63
PF	0.904	0.918	0.876	0.912	0.912
I_{start} (A)	234.22	364.10	413.8	311.7	306.87
T_s (N.m)	339.82	512.72	647.66	472.74	468.72

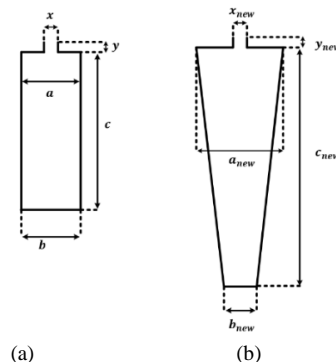(a)   (b)

Fig.9. Rotor slot shape. (a)- Prototype I, (b)- Optimal model of prototype I

To optimize the presented prototypes of the rotor slot shape, the objective function considered maximum motor efficiency. Figure 9 shows the prototype and GA-based optimal shapes of the case I. In this optimal slot shape, the motor efficiency increased amount of 0.25%, and 0.2% in comparison with the conventional model (Fig. 2), and the prototype case I, respectively. Also, the efficiency in the GA-based optimal shape of case II (Fig. 10) increases by 0.21%, and 0.29% in comparison with the conventional model, and the prototype case II, respectively. Figures 11, and 12 show the prototype and GA-based optimal shapes of cases III, and IV, respectively. The efficiency of the optimal model in Fig. 11 increases by 0.32%, 0.28% in comparison with the conventional model, and the prototype case III, respectively. Also, the efficiency in the GA-based optimal shape of case IV (Fig. 12) increases by 0.31%, and 0.27% in comparison with the conventional model, and the prototype case IV, respectively. The efficiency results in all considered cases in this approach have been illustrated in Fig. 13. As mentioned before, the sensitivity analysis of the rotor slot dimensions showed that the suitable slot shape for higher efficiency is the slot with a tight top, and bottom width, wide middle width, and deep depth. The results of the GA validate the sensitivity analysis results.

is expanded by about 58% in comparison with the conventional model. Also, the efficiency in the optimal motor is 94.1% which increased by 0.55% in comparison with the conventional model. Besides, the starting torque and power factor in the optimal motor have been almost constant.
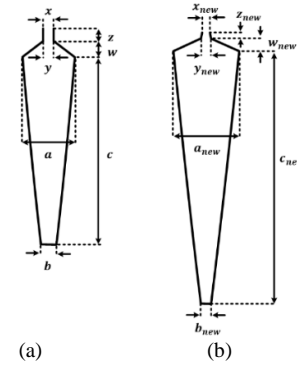
Fig.11. Rotor slot shape. (a)- Prototype III, (b)- Optimal model of prototype III
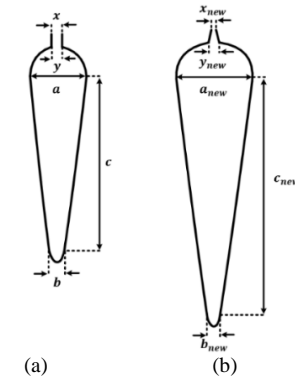
Fig.12. Rotor slot shape. (a)- Prototype IV, (b)- Optimal model of prototype IV

Fig.10. Rotor slot shape. (a)- Prototype II, (b)- Optimal model of prototype II

C. Approach 3: Stator and rotor diameters

1) changing of the stator and rotor diameters simultaneously

In this section, the objective function is maximum efficiency with considering four variables include $D_{out\text{-}s}$, $D_{in\text{-}s}$, $D_{out\text{-}r}$, $D_{in\text{-}r}$ whereas the shape and dimensions of rotor and stator slots remain as same as the conventional model. The linear constraints are expressed as follow:

$$D_{out-s} - D_{in-s} > 2l_{slot-s} \tag{13}$$

$$D_{in-s} - D_{out-r} > 2l_{g} \tag{14}$$

$$D_{out-r} - D_{in-r} > l_{slot-r} + l_{er} \tag{15}$$

where $l_{slot\text{-}s}$ is depth of stator slot, $l_{slot\text{-}r}$ is depth of rotor slot, and l_{er} is end-ring width.

The limits of the design variable and the results of the optimization algorithm is presented in Tables 5 and 6 respectively. The results show that the optimal motor volume

Fig.13. Comparison efficiency between prototype and optimal shape of slots related to the approach 2

2) changing of the stator outer diameter

In this section, if three variables include $D_{in\text{-}s}$, $D_{out\text{-}r}$, and $D_{in\text{-}r}$ have been considered constant whereas $D_{out\text{-}s}$ is changed as $2l_{slot\text{-}s} < D_{out\text{-}s} \leq 650mm$ based on the sensitivity analysis results in section 4.3, the highest efficiency is 94.3%. In this efficiency, $D_{out\text{-}s}$ is 650mm and also the efficiency is increased by 0.76% in comparison with the efficiency of the conventional model. In general, when the motor core become larger, the flux density, as well as the core loss is decreased and the efficiency is increased consequently. The results of

this investigation are summarized in Table 7. According to the results, the starting torque and power factor have been almost constant similar to the changing of the stator and rotor diameters simultaneously.

TABLE V
THE OPTIMAL DIAMETERS OF THE STATOR AND ROTOR RELATED TO APPROACH 3 (THE STATOR AND ROTOR DIAMETERS) IN COMPARISON WITH THE CONVENTIONAL MODEL

Diameters (mm)	Conventional	Limits	Optimal
D_{out-s}	327	163.5-490.5	411.1
D_{in-s}	210	105-315	208.4
D_{out-r}	208.7	104.35-313.05	207.1
D_{in-r}	72	36-108	96.9

TABLE VI
THE INDUCTION MOTOR PERFORMANCE CHARACTERISTICS OF OPTIMAL MODEL RELATED TO APPROACH 3-A IN COMPARISON WITH THE CONVENTIONAL MODEL (SIMULATION RESULTS)

Characteristics	Conventional	Optimal
η (%)	93.59	94.1
PF	0.904	0.902
I_{start} (A)	234.22	235.12
T_s (N.m)	339.82	342

TABLE VII
THE INDUCTION MOTOR PERFORMANCE CHARACTERISTICS OF THE STATOR OUTER DIAMETERS VARIATIONS RELATED TO APPROACH 3-B (SIMULATION RESULTS)

Characteristics	Conventional	Optimal
η (%)	93.59	94.3
PF	0.904	0.905
I_{start} (A)	234.22	232.99
T_s (N.m)	339.82	336.59

D. Compare the results of considered approaches

In this paper, three considered approaches have been applied on a 30-kW set-up squirrel cage induction motor to analysis the motor performance characteristics. These approaches with a combination of the genetic algorithm lead to an optimal model for set-up induction motor. The performance characteristics of the optimal motor related to each approach are presented in Table 8. Based on the motor efficiency (Fig. 14), the approach 3-B leads to the highest motor efficiency (94.3%) between all considered approaches. The increase of efficiency in approaches 1, 2, 3-A, and 3-B in comparison with the efficiency of the conventional model are 0.32%, 0.32%, 0.55%, and 0.76%, respectively.

The important manufacturing considerations of the optimal motor in all presented approaches are summarized in Table 9. These considerations include stator slot mold, rotor slot mold, aluminum weight, shaft diameter, bearings, motor cortex, and cooling system. In approach 1, and 2 the rotor slot dimensions are changed as well as the rotor slot mold and aluminum weight. In approach 3-A, when the diameters of the rotor and stator are changed simultaneously, the slot mold of stator and rotor, shaft diameter, bearings, motor cortex, and cooling system is changed. However, in the approach 3-B, since the outer diameter of the stator is changed, only the stator slot mold and the cortex motor are changed.
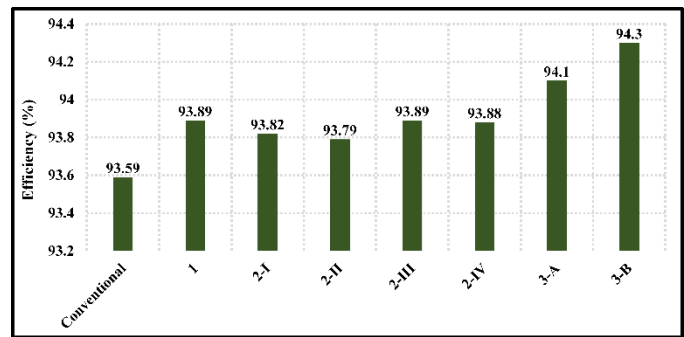
Fig.14. Comparison efficiency between considered approaches

TABLE VIII
THE INDUCTION MOTOR PERFORMANCE CHARACTERISTICS OF OPTIMAL MODEL RELATED TO THE CONSIDERED APPROACHES IN COMPARISON WITH THE CONVENTIONAL MODEL (SIMULATION RESULTS)

Characteristics	Conv.	App. 1	App. 2	App.3-A	App.3-B
η (%)	93.59	93.89	93.63	94.1	94.3
PF	0.904	0.899	0.912	0.902	0.905
I_{start} (A)	234.22	307.68	306.87	235.12	232.99
T_s (Nm)	339.82	401.45	468.72	342	336.59

TABLE IX
THE MANUFACTURING CONSIDERATIONS OF THE OPTIMAL MOTOR RELATED TO THE PRESENTED APPROACHES

Subject	App. 1	App. 2	App. 3-A	App. 4-B
Stator slot mold			✓	✓
Rotor slot mold	✓	✓	✓	
Aluminum weight	✓	✓		
Shaft diameter			✓	
Bearing			✓	
Motor cortex			✓	✓
Cooling system			✓	✓

In the approaches 1 and 2, due to the change in the dimensions of the rotor slot, in the process of producing the electromotor, the device that produces the rotor mold must be readjusted according to the new dimensions of the slot; However, this change in the dimensions of the rotor slot does not change the amount of material consumed by the rotor magnetic material. Also, due to the change in the dimensions of the slot, the amount of aluminum consumed in the rotor slots (rotor bars) increases, which will not cause problems in the production process and difficulties for electromotor manufacturers. In the approach 3, because all the geometric characteristics of the motor, including the rotor slot mold, stator slot mold, motor shaft, bearing and motor cortex are changed, it is necessary to adjust the molding machine for the rotor, as well as for the stator. Also, all parts must be re-machined, which increases the cost of production and operation of the devices. In addition, materials in the electromotor production increase, which increases motor costs. So, approach 3 is more difficult for the manufactures rather than approach 1 and 2. Also, the approach 4 due to the just changing in stator outer diameter is in a better position that the approach 3. In this approach the material consumption and motor cortex are changed. So, approach 1 and 2, Therefore, the approaches 1 and 2, then the approach 3 and then the approach 4 are considered from the lowest to the highest difficulty in the electromotor production process, respectively.

Thus, based on the motor efficiency and the manufacturing considerations, the optimal approach is approach 3-B. Hence,

the economic evaluation for this approach is accomplished in section 5.

VI. ECONOMIC EVALUATION

The simulation results obtained from four presented approaches in section 4 show that the starting torque increases in comparison with the conventional model. Although, the efficiency of the conventional motor is high so that it places into the IE2 group based on the IEC standard, however, in approach 4 the motor efficiency increases by 0.76 % in comparison with the conventional model. Although, the efficiency is increased by other approaches but the highest belongs to approach 4. In this approach, the stator iron part in the optimal model expand as well as the motor cost. So, the following economic evaluation has been employed to verify the optimal design of this approach [24].

The stator core price is calculated by specifying the net volume of the stator iron part. The core of 30-kW motor as a case study was made of sheets with grade m-470 which its price is 1.27 $ per kilogram.

The volume of stator slots should be subtracted from the volume of the stator core. Now, the volume of the stator iron part (V_{iron}) is:

$$V_{iron} = (S_s - S_r - S_{slot})L \tag{16}$$

where S_s is the stator area, S_r is the rotor area, S_{slot} is the area of stator slots, and L is core length.

The stator core weight (W_s) is calculated using Eq. (17):

$$W_s = V_{iron}\sigma_{iron} \tag{17}$$

The price of stator core based on 1.27$ per kilogram and motor energy losses in the conventional and optimal model related to approach 5 are presented in Table 10 and 11, respectively. The benefit of increased efficiency is calculated for three cases of electricity consumption cost include 0.0273$ (case 1), 0.0655$ (case 2), and 0.1$ (case 3) per kWh. This benefit is calculated according to the energy losses per year and it is assumed that the motor is powered on continuously during the year. The results show that the total cost of the optimal motor related to the approach 5 has been increased by 637.913$ in comparison with the conventional model due to an increase in stator core weight by about 435.7 kilograms.

This energy savings can be considered as an annual income (A) in the financial process. The residual value (F) of the motor after its useful life is considered to be 35 % of the initial value. Considering the time value of money, the number of interest periods (n) is determined using Eq. (18) [24].

$$-P(A/P, i\%, n) + A + F(A/F, i\%, n) = 0 \tag{18}$$

where P, F, A, and i are present worth, residual value, annual income, and interest rate, respectively. Also, the amount of $(A/P, i\%, n)$ and $(A/F, i\%, n)$ are determined in [25].

According to (18), the curves of the interest period number versus interest rates are depicted in Fig. 15 considering three cases for electricity consumption cost per kWh. As shown in this figure, the case 1 has no economic justification even at a low-interest rate. Regarding case 2, the results show that the optimal approach has economic justification for the interest

rate lower than 5% and also, case 3 has an economic justification for any interest rate. Thus, the optimal model extracted from approach 5 is an economical design if the electricity consumption cost per kWh is 0.1$. Furthermore, if the time value of money is regardless of the financial process, the number of interest periods is 8.9, 3.71, and 2.43 years whereas the electricity consumption cost per kWh is 0.0273$, 0.0655$, and 0.1$, respectively.

TABLE X
THE STATOR DIAMETER AND COST OF OPTIMAL MODEL RELATED TO APPROACH 5 IN COMPARISON WITH THE CONVENTIONAL MODEL

Parameters	Conventional	Optimal
$D_{out\text{-}s}$ (mm)	327	650
L (mm)	230	230
W_s (kg)	70.1	508.8
C_S ($)	88.073	647.576

TABLE XI
THE ENERGY AND COST OF LOSSES IN THE OPTIMAL MODEL RELATED TO APPROACH 5 IN COMPARISON WITH THE CONVENTIONAL MODEL FOR THREE CASES OF ELECTRICITY CONSUMPTION COST

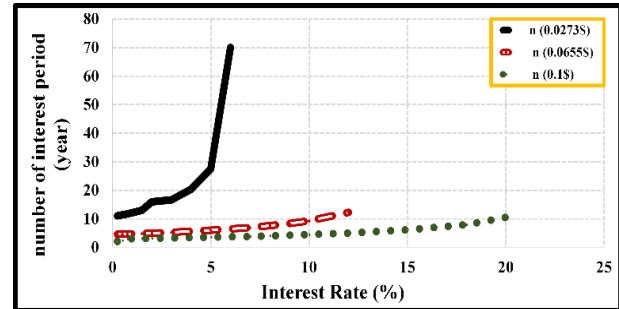| Energy losses	Conventional	Optimal
η (%)	93.59	94.3
P_T (kW)	2.1	1.8
Energy losses (kWh) [for 1 year]	18396	15768
Energy losses cost ($) [1 kWh = 0.0273$]	501.71	430.04
Energy losses cost ($) [1 kWh = 0.0655$]	1204.10	1032.09
Energy losses cost ($) [1 kWh = 0.1$]	1839.6	1576.8

Fig.15. Number of interest period curves versus interest rates related to the economic evaluation for three cases of electricity consumption costs per kWh

VII. DISCUSSION

The performance characteristics of set-up induction motor have been calculated according to the mathematical equations in which they are proportional to the motor equivalent circuit. The simulated results extracted from Maxwell software are close to the analytical results as well as the experimental results.

In this article, the goal is the optimal efficiency design of induction motors. The sensitivity of the rotor slot dimensions showed that the rotor slot with the tight top and bottom parts and with the wide middle part has the highest efficiency. Also, the sensitivity of the stator and rotor diameters showed that the efficiency is increased significantly when the motor core is expanded. Hence, three different approaches have been applied on a 30-kW, 4-pole, 3-phase squirrel cage induction motor to improve the motor performance characteristics such as efficiency, and starting torque. These approaches include

design of rotor slot (Approach 1), rotor slot shape (Approach 2), stator and rotor diameters (Approach 3).

The genetic algorithm is employed to find the optimal model in each considered approach. The optimal motor efficiency in approaches 1, 2, 3-A, and 3-B are 93.89%, 93.89%, 94.1% and 94.3%. Finally, approach 3-B is chosen as the optimal design approach. The economic evaluation of this optimal motor design is accomplished for three different cases of electricity consumption costs. The optimal model has less energy loss than the conventional model. But in the optimal model, the price is higher since the stator diameter of the motor is larger. The results show that the additional cost of the optimal motor is returned during 4 years with an interest rate of 5%.

REFERENCES

[1] Lee H. J., Im S.H., Um D. Y., Park G. S. (2018) A design of rotor bar for improving starting torque by analyzing rotor resistance and reactance in squirrel cage induction motor. IEEE Trans Magn 54(3)

[2] Khelfi H., Hamdani S. (2019) Induction motor rotor fault diagnosis using three-phase current intersection signal. Electr Eng, https://doi.org/10.1007/s00202-019-00894-7

[3] Parkash R., Akhtar M. J., Behra R. K., Parida S. K. (2014) Design of a three phase squirrel cage induction motor for electric propulsion systems. Third International Conference on Advances in Control and Optimization of Dynamical Systems, Kanpur, India

[4] Oraee H. (2000) A quantitative approach to estimate the life expectancy of motor insulation systems. IEEE Transaction on Dielectric and Electrical Insulation 7(6): 790-796

[5] Rengifo J., Alb´anez E., Benzaquen J. (2018) Full-load range in-situ efficiency estimation method for induction motors using only a direct start-up. XIII International Conference on Electrical Machines (ICEM), Alexandroupoli, Greece

[6] Kim H. M., Lee K. W., Kim D.G., Park J. H., Park G. S. (2018) Design of cryogenic induction motor submerged in liquefied natural gas. IEEE Trans Magn 54(3)

[7] Zhang D., Park C .S., Koh C. S. (2012) A new optimal design method of rotor slot of three-phase squirrel cage induction motor for NEMA class D speed-torque characteristic using multi-objective optimization algorithm. IEEE Trans Magn 48(2)

[8] Lee D., Jung H. C. (2018) Cost pattern value method for local search algorithms applied to optimal FEA-based design of induction motors. IEEE Trans Magn 53(11)

[9] Haisen Z., Jian Z., Xiangyu W., Qing W., Xiaofang L., Yingli L. (2014) A design method for cage induction motors with non-skewed rotor bars. IEEE Trans Magn 50(2)

[10] Lee G., Min S., Hong J .P. (2013) Optimal shape design of rotor slot in squirrel-cage induction motor considering torque characteristics. IEEE Trans Magn 49(5), Vol. 49, No. 5, May. 2013.

[11] Yetgin A. G. (2020) Investigation of the effects of stator slot permeance on induction motor and obtaining the best starting torque using permeance calculation. Canadian Journal of Electrical And Computer Engineering 43(1): 25-29

[12] Yun J., Lee S. B. (2018) Influence of aluminum die-cast rotor porosity on the efficiency of induction machines. IEEE Trans Magn 54(11)

[13] Yun J., Lee S., Jeong M., Lee S. B. (2018) Influence of die cast rotor fill factor on the starting performance of induction machines. IEEE Trans Magn 54(3)

[14] Kim D. J., Jung J. W., Hong J .P., Kim K .J., Park C .J. (2012) A study on the design process of noise reduction in induction motors. IEEE Trans Magn 48(11)

[15] Wang L., Bao X., Di C., Li J. (2015) Effects of novel skewed rotor in squirrel-cage induction motor on electromagnetic force. IEEE Trans Magn 51(11)

[16] Heo C. G., Kim H. M., Park G. S. (2017) A design of rotor bar inclination in squirrel cage induction machines. IEEE Trans Magn 51(11)

[17] Zhang D., Park C. S., Koh C. S. (2012) A novel method for multi-objective design and optimization of three phase induction machines. IEEE Trans Magn 48(2)

[18] Zhang D., Park C. S., Koh C. S. (2019) Design optimization of wound rotor induction motor using genetic algorithm. 5th Conference on Knowledge-Based Engineering and Innovation, Tehran, Iran

[19] Agamloh E. B., Boglietti A., Cavagnino A. (2013) The incremental design efficiency improvement of commercially manufactured induction motors. IEEE Transaction on Ind Appl 49(6): 2496 – 2504

[20] Mallik S., Mallik K., Barman A., Maiti D., Biswas S. K., Deb N. K., Basu S. (2017) Efficiency and cost optimized design of an induction motor using genetic algorithm. IEEE Trans Ind Elect 64(12): 9854-9863

[21] Boldea I., Nasar S. A. (2010) The induction machines design handbook. 2nd edition, CRC Press, USA.

[22] Haque M. (2008) Determination of NEMA design induction motor parameters from manufacture data. IEEE Trans Energ Conv 23(4): 997-1004

[23] Rengifo J., Romero J. (2018) Efficiency evaluation of indcuction motors supplied by VFDs. IEEE Third Ecuador Technical Chapters Meeting (ETCM), Cuenca, Ecuador.

[24] Varghese T., Rajagopa1 R. (2016) Economic and efficient induction motor controller for electric vehicle using improved scalar algorithm. 1st IEEE International Conference on Power Electronics, Intelligent Control and Energy Systems (ICPEICES), Delhi, India

[25] Oskounejad M. M. (1996) Economic engineering, economic evaluation of industrial projects. 7nd edition, Publishing center of Amirkabir university: CRC Press, Iran

BIOGRAPHIES

Mahdi Rezaiee Nakhaie was born in Kashmar, Iran, in 1994. He received the B.Sc. degree in power electrical engineering from Hakim Sabzevari University (HSU), Sabzevar, Iran in 2017, where also he is received the M.Sc. degree in HSU. His research interest is design of electrical machines, power system.

Reza Roshanfekr was born in Sabzevar, Iran, in 1980. He received the B.Sc. degree in power electrical engineering from Amirkabir University (AKU), Tehran, Iran in 2002, and the M.Sc. and Ph.D. degree from Iran University of Science and Technology (IUST), Tehran, Iran, in 2004 and 2017, respectively. He joined the electrical Group of the Department of Electrical Engineering at Hakim Sabzevari University in 2006, where he is Assistant Professor. His research interests are fault diagnosis in electrical machines, design of electrical machines, and power quality.

Electrification in Urban Transport: A Case Study with Real-time Data

İ.C. DİKMEN, Y.E EKİCİ, T. KARADAĞ, T. ABBASOV and S.E. HAMAMCI

Abstract— Electrification in urban transportation is becoming more popular, it is also becoming a necessity due to climate changes and sustainability issues. Trolleybuses are presenting an alternative for this purpose. Although their technology is a mature technology that has been used for decades, there are still some technical problems that need to be overcome. In this study, a technical method is presented for the conversion of trolleybus auxiliary power units. The electrification conversion demanded by the metropolitan public transportation company operating 22 trolleybuses in the province of Malatya is the replacement of diesel generators, used as auxiliary power units, with battery units capable of meeting the local operational requirements. For this purpose, a method is proposed and followed. At the first step of the implementation, real-time data has gathered from a trolleybus and this one round tour data is used to run on a scaled experiment. The setup has prepared as hardware and software to simulate the consumption on a scaled battery pack. Experimental results were interpreted with capacity and voltage restrictions resulting in the determination of battery chemistry and casing to be used. Then optimal battery placement was defined as a container loading problem and application was made with the first fit decreasing algorithm considering mass and volume restrictions. It was found that only two packing types out of six combinations are enough to form a battery pack within the mass and volumetric limitations. It is evaluated that the method adopted in this study can be used in conversion applications to be made in the future.

Index Terms— Auxiliary power unit, container loading problem, conversion, electrification, first-fit decreasing algorithm, trolleybus.

I. INTRODUCTION

VARIOUS TECHNOLOGIES have been developed for transportation. While animals were used for this purpose, a self-propelled vehicle was no more than a dream. Like with all inventions, somebody's dream came true. The first-ever self-propelled vehicle invented by French engineer and mechanic Nicolas Joseph Cugnot in 1769 [1]. That vehicle shown in Figure 1 is considered as the first steam-powered automobile; actually, it was a military cart intended for transporting cannons.

Electric-powered vehicles were always being popular since the invention of the electric motor. But the biggest challenge was and is still storing electric power on the vehicle. In 1799 Alessandro Giuseppe Antonio Anastasio Volta presented the system he discovered which is capable of storing electric power [2], [3]. This was the first battery, unfortunately, it was not suitable for a self-propelled electric vehicle not only because of its insufficient electrical properties but also its weight and volume. This was an engineering problem and could be solved in various ways. A German engineer named Dr. Ernst Werner von Siemens solved it in a wise way [4].

İSMAİL CAN DİKMEN, is with Department of Electric Vehicle Technologies Inonu University OSB Vocational School, Malatya, Turkey, (e-mail: can.dikmen@inonu.edu.tr).

https://orcid.org/0000-0002-7747-7777

YUNUS EMRE EKİCİ, is with Department of Electric Vehicle Technologies Inonu University OSB Vocational School, Malatya, Turkey, (e-mail: emre.ekici@inonu.edu.tr).

https://orcid.org/0000-0001-7791-0473

TEOMAN KARADAĞ, is with Department of Electric Electronic Engineering Inonu University, Malatya, Turkey, (e-mail: teoman.karadag@inonu.edu.tr).

https://orcid.org/0000-0002-7682-7771

TAHMURAZ ABBASOV, is with Department of Electric Electronic Engineering Inonu University, Malatya, Turkey, (e-mail: teymuraz.abbasov@inonu.edu.tr).

https://orcid.org/0000-0002-0290-8333

SERDAR ETHEM HAMAMCI, is with Department of Electric Electronic Engineering Inonu University, Malatya, Turkey, (e-mail: serdar.hamamci@inonu.edu.tr).

https://orcid.org/0000-0002-1868-6843

Fig.1. Steam Powered Automobile

The idea goes back to 1847 but realizations took some more time. Finally, Siemens presented his invention to the public April 29th 1882 in Halensee. He named his invention as ELECTROMOTE, shown in Figure 2. That was an electric

vehicle made with a four-wheeled horse cart and powered by two electric motors. These motors were rated 2.2 kW and mechanical power transmission was made via steel chains connected to the rear wheels. In order to fulfill the DC power needs, he made his move and installed an overhead line instead of a battery pack. This line was carrying 550 Volt direct current and was transferring it to the vehicle with an apparatus made of eight wheels. The apparatus moving along this bipolar cable served as a current collector [5]. So, he managed to create a fully electric transportation system. It was installed at the suburbs of Berlin between Halensee railway station (today known as Kurfürstendamm) and Straße No. 5 (today known as Joachim-Freidrich-Straße). This was the first trolleybus line in history [6].

The technology behind the trolleybus systems has not changed drastically since those days [7]. If one looks at today's modern trolleybuses can see that AC motors with inverters took place of DC motors, metal wheels changed to regular bus tires; this let trolleybuses navigate through regular roads instead of railways [8], [9]. Therefore, trolleybuses became more like buses, rather than trains. By this way trolleybuses can be used all over the residential areas.

Fig.2. Electktromote (Photo courtesy of Siemens AG)

In the last decades, regulations have been made to obtain more reliable, secure, and environmental transportation for the public while considering the global climate changes [10], [11]. The European Union has a target of 80% electrification of all public transport by 2030 [12], [13]. Moreover, countries targeting to phase out fossil fuel-powered vehicles by year Norway, 2025; Denmark, Iceland, Ireland, Israel, Nepal, Netherlands, Slovenia, Sweden, 2030; Scotland, 2032; Colombia, United Kingdom, 2035; British Columbia, California, Canada, France, Portugal, Spain, Sri Lanka, Taiwan (Province of China), 2040; Cabo Verde, Costa Rica, Japan, Mexico, 2050 [14].

Trolleybuses used for urban transportation is a taken step forward on this vision. But, some trolleybuses still have optional diesel auxiliary power units [15]–[17]. This unit helps to drive vehicles without connecting to the overhead line. It is used mainly while maneuvering on stucked roads or in

workshops. In addition, an extra inverter or converter system is not required as it operates on the same electronic systems [18]. But its most important duty is to letting the vehicle to move in case of power failure. These auxiliary power units may be diesel generators as well as battery packs [19]. Because of environmental issues and developing battery technologies, conversion of diesel generators to battery pack is became more important and more affordable [20]. In this regard, a case study is chosen as the main problem of this article.

II. MATERIALS AND METHODS

A. Method

In this paper, the following method has been adopted.
1 | Problem statement
2 | Numerical analysis
3 | Scaled hardware analysis (in 1.5% error range)
4 | Determination of battery case and pack type with power, voltage, and weight constraints
5 | Optimal battery placement with volume constraint

Here, first, the problem is presented. Then a numerical analysis has done. Due to commercial availability only lithium iron phosphate prismatic and 18650 case batteries or lithium manganese cobalt oxide batteries in 18650 casing were useable in this study. With these battery types, a scaled hardware analysis has conducted to prove that requirements are met. Afterward battery type and the casing have determined with respect to the results obtained. For the last step, a container loading problem has defined as an integer linear programming problem and solved by using the first fit decreasing heuristic algorithm.

B. Problem Statement

A trolleybus is an electric bus that gets its power from two wires in an overhead power line that is usually hung along the road [21], [22]. The reason for using two cables is that unlike trams, it is impossible to complete the circuit with a single cable due to the use of insulating rubber wheels [23]. The number of trolleybus systems worldwide is 286. Most of these systems are located in post-socialistic countries [24], [25].

Fig.3. Trolleybus (Photo courtesy of MOTAŞ)

Trolleybuses have been used in Turkey for many decades [26]. After a break for almost twenty years, in the spring of 2015, a new trolleybus project has been launched in Malatya city [27], [28]. In this study, the Trolleybus presented in Figure 3 and operated by Malatya Metropolitan Municipality Public Transportation Inc. will be taken into account for the case study. These vehicles have a motor of 320 kW and are 24.7 meters long. It also uses a diesel generator as an auxiliary system.

In order for the trolleybus to operate efficiently, the appropriate route must first be selected. The route is chosen according to the parameter of passenger density per kilometer in an hour. Therefore, it is determined that the best route is between the two main city locations on the two edges of the city in the east-west direction. These are Inonu University at the east of Malatya city and the City Bus Terminal at the west [28]. The route which is 38.2 km long and takes 96 minutes for a trolleybus to travel is shown in Figure 4.

Fig.4. Malatya city trolleybus route

In the first phase of the project, infrastructure works were completed and ten vehicles were purchased. These vehicles are equipped with two 160 kW electric motors and a 50 kW diesel auxiliary power unit. The weight of the generator is 600 kg. The fully loaded weight of the fuel tank placed separately from the generator is 50 kg. Therefore, 650 kg was determined as the weight constraint in the calculations to be made in this study. In vehicles equipped with a diesel generator as an auxiliary power system. In the second phase of the project, ten more vehicles were purchased but these vehicles are equipped with 110 kWh battery auxiliary power unit and have two 250 kW electric motors. First batch of the vehicles is having trouble with these generators. Because generators are not fully capable of powering these double articulated trolleybuses. Besides, regenerative braking energy (recuperation energy) cannot be used efficiently due to a lack of a proper energy storage system [29]–[31]. Therefore, it became necessary to convert these generators into battery blocks. In order to realize this purpose a numerical and experimental study was carried out with power constraint of minimum 110 kWh, voltage constraint of minimum 550 Volts, weight constraint of maximum 650 kg. and volumetric constraint of 1,1782 m^3.

C. Experimental Setup

All trolleybuses have a data recorder installed. These data recorders can collect speed, power, torque, acceleration, energy consumption, temperature, actual power, and recuperation power data with timestamps.
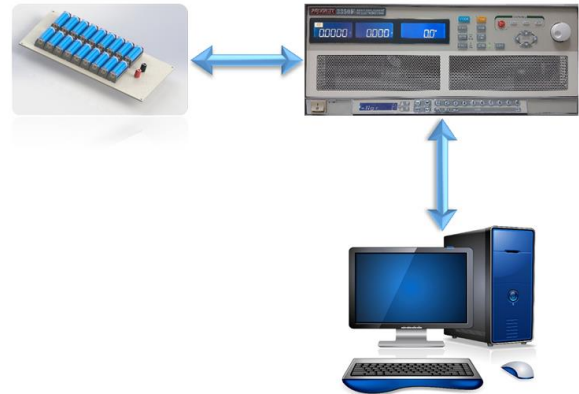
Fig.5. Experiment setup

As we have the real-time data of the vehicle for one tour, an experimental setup shown in Figure 5 is designed in order to run the real-time data in a scaled experiment. To scale down the real-time data, a hardware is designed and manufactured to place 18 cells in series, connected to a programmable electronic DC load. A software is also designed in LabVIEW for the electronic load to run a tour on the scaled battery pack.

III. SCALED EXPERIMENT

Real-time accelerator pedal data, vehicle speed and consumption data were obtained from the data loggers on the trolleybuses [32]. In Figure 6, the speed, acceleration and power consumption data of a trolleybus along a route are presented. As can be seen here, while the vehicle's two electric motors had total power of 320 kW, the maximum power consumption measured was 407.7 kW. The reason for this is other equipment that consumes energy on the vehicle. For example, Heating, Ventilating and Air Conditioning systems (HVAC). The speed of the vehicle is limited to 75 km/h and its positive acceleration is 1.5 m/s^2 by software. Negative acceleration varies according to the condition of the road, the braking characteristics of the driver. A maximum of -2.502 m/s^2 deceleration is measured. Additionally, due to road construction at the time, between 16.61 km and 18.77 km, the vehicle goes off-wire and is powered by the 50 kW generator. This is the reason why the vehicle's power consumption, acceleration and speed are limited during that time. While the vehicle moves with generator power, HVAC and other ancillary systems are limited by software so that more power can be supplied to the vehicle's traction system.
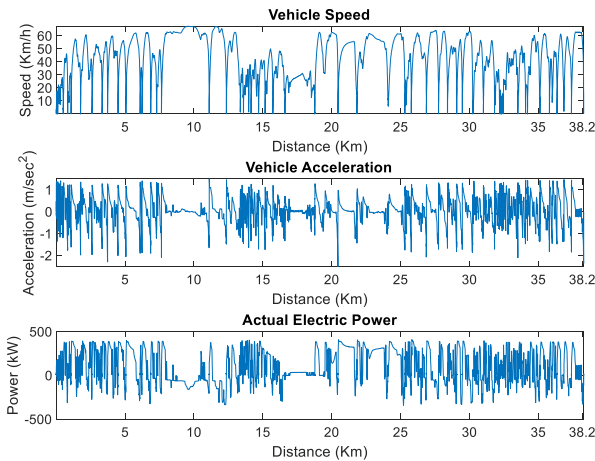
Fig.6. Real-time speed, acceleration and power data for one round

Two different battery groups with different chemical properties used for the scaled experiment. Type 1 is $LiNiMnCoO_2$ batteries and Type 2 is $LiFePO_4$ batteries which are rated 3.7V nominal voltage 3250 mAh capacity and 3.2V nominal voltage 1500 mAh capacity respectively. Both types are tested with a battery analyzer. It was found out that Type 1 batteries have 3230 mAh capacity while Type 2 batteries have only 730. Therefore, first experiment ran with datasheet values of the Type 2 batteries to show that the rated capacities written on them are not sound. Then the second experiment is run with the averaged data gathered from the first experiment in order to correct the data mismatch within real and datasheet values. Both experiments are halted due to batteries' rundown.
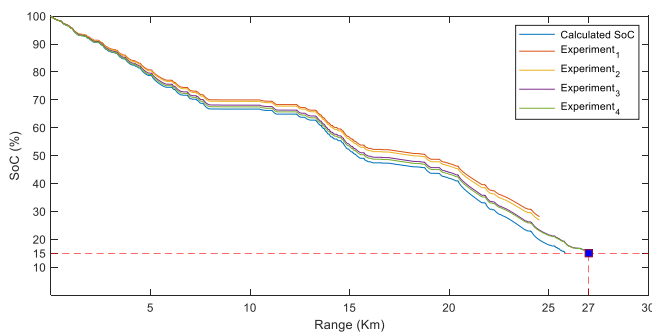
Fig.7. Calculated State of Charge (SoC) and experimental results

In the third experiment; data from the battery analyzer is used. It was found out that gathered data is much closer to the real-time data. On the fourth run Type 1 batteries are used with found parameters and results are presented in Figure 7. Mean Square Errors and Root Mean Square Errors of all four experiments are shown in Figure 8. The average error for this experiment is found to be 1.27%. So, it was accurate enough to calculate the battery capacity for the conversion purpose.
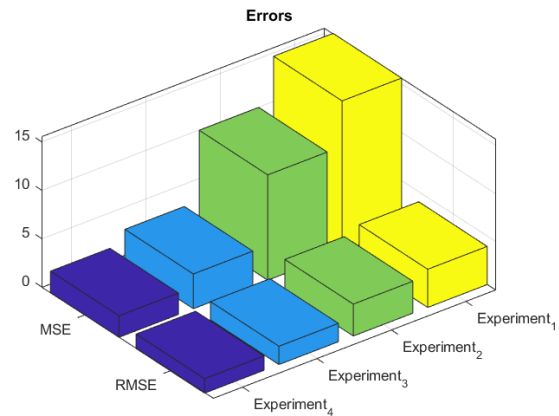
Fig.8. Experimental errors with respect to real-time data

IV. BATTERY PACKING

The diesel generator has to be disassembled to convert the auxiliary power unit of the trolleybus to a battery pack. In addition to the diesel generator, there is also a fuel tank that supplies fuel to this generator. While the conversion the volume and weight distributions are became constraints. For this reason, the optimum amount of battery that can fit into the generator compartment and how to pack these batteries in groups is a problem that needs to be solved.

TABLE I GENERATOR COMPARTMENT AND FUEL TANK DIMENSIONS

	Section	Dimension (cm)			Volume (m^3)
		L	W	H	
Fuel Tank	F	50	64	22	0,0704
Generator Compartment	1	132	55	40	0,2904
	2	100.6	74.6	95	0,7130
	3	35	74.6	40	0,1044

The generator compartment divided into sections and fuel tank are seen in Figure 9. For optimal battery placement calculations, the generator room is divided into three sections plus the fuel tank is taken into account. Dimensions of the sections and fuel tank are given in Table I.
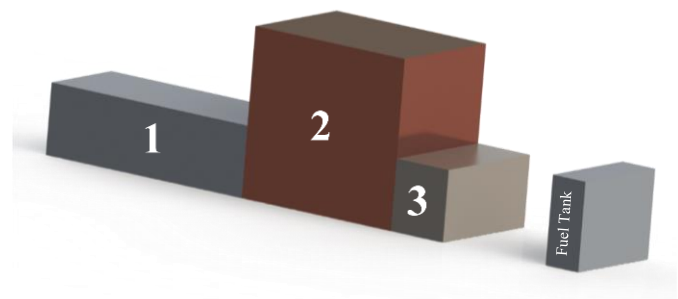
Fig.9. Generator compartment in sections and fuel tank

A. Battery Casing Type Determination

In this study, prismatic and 18650 packaged batteries are handled within the framework of technical competencies. When a battery pack of 110 kWh is made from prismatic batteries with different cell capacities that can be found commercially; volume and weight values are obtained as presented in Table II. As seen in Figure 10, even when using CALB SE200AHA

battery which is the most suitable type in terms of power/weight ratio; the weight of a 110 kWh battery pack calculated as 991 kg. So, this is 152.5% higher than the weight constraint of 650 kg. and cannot be used.

In addition, if the electrical and thermal harness on the batteries are also taken into account; the weight to be added to the vehicle exceeds one ton.

TABLE II DATASHEET DATA OF DIFFERENT TYPE BATTERIES FOR A 555 V PACK

Battery (LiFePO$_4$)	Capacity (Ah)	Volume (m^3)	Cell Voltage (V)	Weight (kg)	Power (kWh)	555 V Pack Total Voltage (V)	Number of Cells	Total Power (kWh)	Total Weight (kg)
WB-LYP40AHA	40	$9.89x10^{-4}$	3.2	1.6	0.148	555	174	22.2	278.4
WB-LYP60AHA	60	$1.41x10^{-3}$	3.2	2.3	0.222	555	174	33.3	400.2
WB-LYP100AHA	100	$2.67x10^{-3}$	3.2	3.3	0.37	555	174	55.5	574.2
WB-LYP130AHA	130	$3.5x10^{-4}$	3.2	5.2	0.481	555	174	72.15	904.8
WB-LYP160AHA	160	$3.6x10^{-4}$	3.2	5.8	0.592	555	174	88.8	1009.2
CALB CA180FI -	180	$4.5x10^{-3}$	3.2	5.8	0.666	555	174	99.9	1009.2
CALB SE200AHA	200	$3.06x10^{-4}$	3.2	5.7	0.74	**555**	**174**	**111**	**991.8**
WB-LYP300AHA	300	$6.2x10^{-3}$	3.2	10	1.11	555	174	166.5	1740

Considering that the generator weighs only 600 kg and the full weight of the fuel tank is 50 kg, the use of prismatic batteries in this study and placing them in the generator compartment is not possible due to the weight constraint. Therefore, in the continuation of the study, calculations will be made for 18650 case batteries.
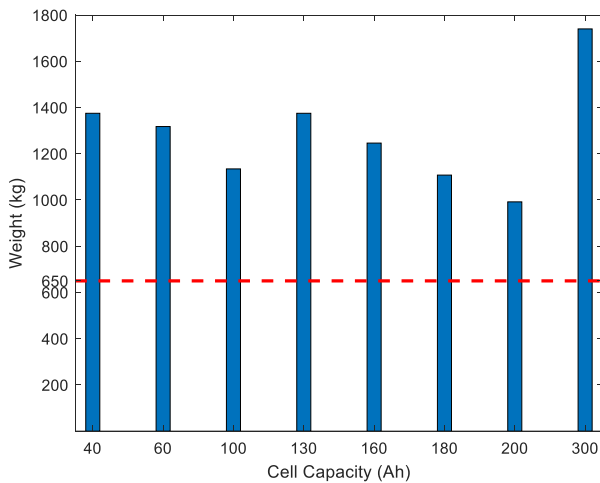
Fig.10. Weight to capacity comparison for 110 kWh or 555 Volt prismatic battery pack

B. Optimal Bin Packing

In this study, it was aimed to optimally place the 18650 battery group in the generator room. This problem is a well-known problem, named as Optimal Bin Packing problem which is classified as NP-hard problem [33]–[38]. Every battery pack

numbered i has three dimensions depth, width and height; represented as $\ell_{1i}, \ell_{2i}, \ell_{3i}$ $(i \in I)$. Each bin (compartment section) represented by b; also has three dimensions D_X, W_Y and H_Z where X, Y, and Z represent the axes of a Cartesian coordinate system. All battery packs and sections are assumed in rectangular form. Each battery pack has 6 rectangular facets. But there are only 3 distinct facets because opposing facets are identical. This means each of the three facets can be rotated orthogonally to obtain a new configuration; resulting in 6 different rotation configurations. The orientation of a pack with respect to the container section and the coordinate system is characterized by a binary variable, σ as in equation (1).

$$\sigma_{ai}^A := \begin{cases} 1; \ if \ pack \ i \ is \ placed \ with \ axis \ a, \\ \quad parallel \ to \ axis \ A \ of \ the \ section \\ \\ 0; \ otherwise \end{cases} \quad (1)$$

For each $i \in I$, for every axis $a \in O_{Pack} := \{1, 2, 3\}$ of a battery pack, and for every axis $A \in O_{Section} := \{X, Y, Z\}$ of section six different orientations are possible. Thus, i^{th} battery packs orthogonal placement can be written as;

$$\sum_{A \in O_S} \sigma_{1i}^A \leq 1, \quad \sum_{A \in O_S} \sigma_{2i}^A = \sum_{A \in O_S} \sigma_{1i}^A ,$$
$$\sum_{A \in O_P} \sigma_{ai}^A = \sum_{A \in O_S} \sigma_{1i}^A ; \ \forall A \in O_S \quad (2)$$

If $\sum_{A \in O_S} \sigma_{1i}^A = 1$, this means an edge of pack i is parallel to the one edge of the section. If $\sum_{A \in O_S} \sigma_{1i}^A = 0$, this means pack i is not placed in the section. The center point of a pack is taken as the allocation point ($x_i^X, x_i^Y, x_i^Z \in \mathbb{R}$). This coordinate has to fulfill at least non-overlapping and the containment conditions.

$$\ell_{ai} := \frac{1}{2} L_{ai}; \ \ a \in O_P \tag{3}$$

By using equation (4) the containment condition can be written as:

$$\sum_{a \in O_P} \sigma_{ai}^A \ell_{ai} \le x_i^A \le \sum_{a \in O_P} \sigma_{ai}^A (D_A - \ell_{ai}); \ \ A \in O_s \tag{4}$$

A binary variable is defined to model the non-overlapping condition. For each direction $A \in O_c$ and each pair of packs numbered i and j:

$$\rho_{ij}^A := \begin{cases} 1; \ pack \ i \ has \ to \ be \ placed \ before \ pack \\ \qquad\quad j \ in \ direction \ A \\ 0; \ otherwise \end{cases} \tag{5}$$

So, the non-overlapping condition for $i, j \in I, \ i < j$ and $A \in O_c$ can be modelled with the following restrictions.

$$D_A \rho_{ij}^A + \sum_{a \in O_P} \sigma_{ai}^A \ell_{ai} - \sum_{a \in O_P} \sigma_{ai}^A (D_A - \ell_{ai})$$
$$\le x_i^A - x_j^A \tag{6}$$
$$\le \sum_{a \in O_P} \sigma_{ai}^A (D_A - \ell_{ai}) - \sum_{a \in O_P} \sigma_{ai}^A \ell_{ai} - D_A \rho_{ij}^A$$

$$\sum_{A \in O_s} \left(\rho_{ij}^A + \rho_{ji}^A \right) \le \sum_{A \in O_s} \sigma_{1i}^A, \\ \sum_{A \in O_s} \left(\rho_{ij}^A + \rho_{ji}^A \right) \le \sum_{A \in O_s} \sigma_{1j}^A \tag{7}$$

$$\sum_{A \in O_s} \sigma_{1i}^A + \sum_{A \in O_s} \sigma_{1j}^A \le 1 + \sum_{A \in O_s} \left(\rho_{ij}^A + \rho_{ji}^A \right) \tag{8}$$

Here, equation (6) represents a conditions which ensures the minimum distance between allocated packs. Similarly, equation (7) and equation (8) represents a condition that limits σ and ρ variables to define a relevant combination of packs. From equation (4) and equation (6) one can write equation (9) in order to model the non-overlapping packs.

$$\sum_{a \in O_P} \sigma_{ai}^A \ell_{ai} - \sum_{a \in O_P} \sigma_{aj}^A (D_A - \ell_{aj}) \le x_i^A - x_j^A \\ \le \sum_{a \in O_P} \sigma_{ai}^A (D_A - \ell_{ai}) - \sum_{a \in O_P} \sigma_{aj}^A \ell_{aj} \tag{9}$$

$$\sum_{i \in I} g_i \left(\sum_{A \in O_s} \sigma_{ai}^A \right) \tag{10}$$

where g_i denotes the volume of pack i. This integer linear programming problem needs to be solved with the objective function equation (10) and restrictions equation (2), equation (8) for all $i, j \in I, \ i < j$. In order to solve this problem first fit decreasing (FFD) algorithm is used [39]–[41]. The pseudocode of the FFD algorithm is presented in Table III. To apply this algorithm to the problem an open-source solver named "CLP Spreadsheet Solver" is used. [42], [43].

TABLE III FFD PSEUDO CODE

FFD Pseudo Code
1: **Sort** All object in decreasing order
2: **for** All objects i = 1, 2, . . . , n **do**
3:    **for** All bins j = 1, 2, . . . **do**
4:       **if** Object i fits in bin j **then**
5:          Pack object i in bin j.
6:          Break the loop and pack the next object.
7:       **end if**
8:    **end for**
9:    **if** Object i did not fit in any available bin **then**
10:       Create new bin and pack object i.
11:    **end if**
12: **end for**

V. RESULTS AND DISCUSSIONS

Due to the technical specification requirements of the operator firm, 15% of battery power is needed to be reserved and a minimum 20 km range is expected. This study shows that with a battery auxiliary power of 110 kWh trolleybuses can travel 27 km. So, it is found to be 35% more than the required range as seen in Figure 7.

To achieve this goal this battery pack, have to be placed within the volume of the generator compartment; is found to be 1.1782 m³. A 18650 packed battery's volume, to fit in a rectangular form, is 2.8×10^{-5} m³. Thus, 42078 batteries can be placed in the compartment. There should be 150 units of 3.7 volt Li-Ion batteries in serial to form a 555 V battery. A combination of 150 series cells is shown in Figure 11. A pack of 150 batteries will have a 1.8 kWh capacity. To reach a 110 kWh capacity on a vehicle there should be 61 packs in parallel. To sum up, in order to fulfill the technical specs, a vehicle should have 150s61p of 3.7 V, 3250 mAh 18650 batteries. That means 9150 battery cells which are less than the compartment capacity. So, electronics and the heating-cooling system can easily be installed in the same area.

According to the capacity calculations and voltage

constraint, the batteries must consist of a minimum of 150 series cells. Therefore, different combinations of 150 serial cells were evaluated for optimal placement in the generator compartment. These combinations are 75x2, 50x3, 30x5, 25x6 and 15x10 as shown in Figure 11. The dimensions of these five packages, made up of 18650 batteries, are given in Table IV.

TABLE IV BATTERY PACK TYPE DIMENSIONS

		Dimension (cm)		
		L	W	H
Battery Pack Type	2x75	150	4	7
	3x50	100	6	7
	5x30	60	10	7
	6x25	50	12	7
	10x15	30	20	7

The battery, which consists of 150 serial cells in total, should have a capacity of 110 kWh, which is the minimum capacity constraint of this study. For this, a minimum of 61 parallel connections is required. The 61 parallel connections we obtained here have been identified as another constraint for optimal placement.
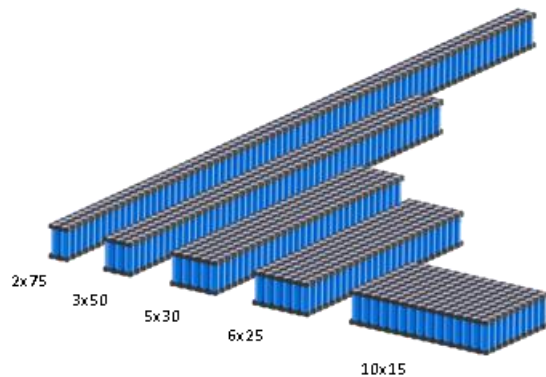
Fig.11. 150 Cells Li-Ion batteries in different packing combinations

In order to make calculations with the CLP Spread Sheet, the generator compartment was taken into account as three separate containers as Section 1, Section 2 and Section 3 as shown in Figure 9. In addition, since the fuel tank will also be removed, this section has also been evaluated for battery installation. At this point to solve that multi-objective optimization problem all constraints and objectives were determined. Hence, CLP Spread Sheet is run with the dimensions in Table I and Table IV, to provide minimum 110 kWh power, 555 Volts voltage, by fulfilling a maximum 650 kg weight constraint with an optionally minimum number of different battery pack types. The results obtained are presented in Table V.

TABLE V THE OPTIMAL SOLUTION

Optimal Placement			
		PCs	Kg
Battery Pack Type	2x75	0	0
	3x50	53	397,5
	5x30	42	240
	6x25	0	0
	10x15	0	0
Total		**95**	**637.5**

The optimal battery group, calculated to be 637.5 kg in weight, meets the 650 kg weight restriction. In addition, a minimum number of different battery pack types are targeted for cost and maintenance convenience. As a result of optimization, it has been shown that optimal placement can be made using only two different types of battery packs, 3x50 and 5x30.

VI. CONCLUSION

In this study, an analysis was performed to replace the diesel generator with more environmentally friendly and efficient lithium batteries for the trolleybus vehicles operated in Malatya city. Total battery pack capacity of second phase vehicles, generator compartment plus fuel tank volume, total weight and voltage of the diesel generator are taken as design restrictions. It is known that the battery group should have a capacity of 110 kWh because it is suitable for operation and is requested by the operator company for range considerations. For this purpose, a number of battery cells required to create a battery that will meet the design criteria, has been determined by the calculations made with the field data taken from the data logger of the vehicle. With the developed software and hardware, different simulation scenarios were analyzed one by one, resulting in the determination of cell chemistry and cell count. It has been shown numerically that the battery to be constructed using available prismatic batteries with the determined number of cells, does not meet design restrictions. For this reason, the study conducted with 18650 case batteries. The placement of battery packs in the generator compartment (bin loading problem) is defined as a linear integer programing problem with volume and weight restrictions. In order to solve that, first-fit descending heuristic algorithm is used. Finally, the shape and layout optimization of the cell packages that will be placed in the generator compartment has been made. According to the results obtained, 95 parallel packs, composed of only 3x50 and 5x30 packages, can be placed in the generator compartment. Using only two combinations of battery packs leads to cost, application and maintenance efficiency. With this study, it is shown that such conversion can be done within the requisitions of public transportation operating company. It is evaluated that the method used in this study can also be used in electrification applications to be made in the future.

REFERENCES

[1]   L. A. Manwaring, *The Observer's Book of Automobiles*, 12th Ed. Library of Congress catalog card # 62-9807, 1966.

[2]   M. Guarnieri, "The Big Jump from the Legs of a Frog [Historical]," *IEEE Ind. Electron. Mag.*, vol. 8, no. 4, pp. 59-61,69, 2014, doi: 10.1109/MIE.2014.2361237.

[3]   M. Guarnieri, "Looking back to electric cars," in *2012 Third IEEE HISTory of ELectro-technology CONference (HISTELCON)*, 2012, pp. 1–6, doi: 10.1109/HISTELCON.2012.6487583.

[4]   F. Maloberti and A. C. Davie, *A Short History of Circuits and Systems: From Green, Mobile, Pervasive Networking to Big Data Computing*. River Publishers, 2016.

[5]   L. Brunton, "The trolleybus story," *IEE Rev.*, vol. 38, no. 2, pp. 57-61(4), 1992, [Online]. Available: https://digital-library.theiet.org/content/journals/10.1049/ir_19920024.

[6]   U. Kreutzer and E. Blocher, "On the road – with electric power From the trolleybus to the eHighway." https://new.siemens.com/global/en/company/about/history/news/on-the-road-with-electric-power.html (accessed Mar. 26, 2020).

[7]   L. J. Brunton, "Why not the trolleybus?," *IET Conf. Proc.*, pp. 5-5(1), 2000, [Online]. Available: https://digital-library.theiet.org/content/conferences/10.1049/ic_20000265.

[8]   C. ELMAS, U. GUVENC, and M. U. DOĞAN, "Tire-Road Friction Coefficient Estimation and Experimental Setup Design of Electric Vehicle," *Balk. J. Electr. Comput. Eng.*, vol. 3, pp. 202–207, Dec. 2015, Accessed: Dec. 06, 2020. [Online]. Available: https://dergipark.org.tr/tr/pub/bajece/issue/36579/415720#article_cite.

[9]   S. Barsali, A. Bechini, R. Giglioli, and D. Poli, "Storage in electrified transport systems," in *2012 IEEE International Energy Conference and Exhibition (ENERGYCON)*, 2012, pp. 1003–1008, doi: 10.1109/EnergyCon.2012.6347716.

[10]   S. Tica, S. Filipović, and Predrag!, "Development of Trolleybus Passenger Transport Subsystems in Terms of Sustainable Development and Quality of Life in Cities."

[11]   L. C. G. Freitas, G. B. Lima, F. A. S. Gonçalves, G. A. Melo, C. A. Canesin, and L. C. de Freitas, "A novel single-phase HPF hybrid rectifier suitable for front-end trolleybus systems," in *2009 Brazilian Power Electronics Conference*, 2009, pp. 619–626, doi: 10.1109/COBEP.2009.5347751.

[12]   T. Held and L. Gerrits, "On the road to electrification – A qualitative comparative analysis of urban e-mobility policies in 15 European cities," *Transp. Policy*, vol. 81, pp. 12–23, 2019, doi: https://doi.org/10.1016/j.tranpol.2019.05.014.

[13]   M. Glotz-Richter and H. Koch, "Electrification of Public Transport in Cities (Horizon 2020 ELIPTIC Project)," *Transp. Res. Procedia*, vol. 14, pp. 2614–2619, 2016, doi: https://doi.org/10.1016/j.trpro.2016.05.416.

[14]   N. Medimorec, "E-Mobility Trends and Targets." [Online]. Available: https://slocat.net/e-mobility/.

[15]   M. Bartłomiejczyk, J. Dombrowski, M. Połom, and O. Wyszomirski, *Handbook Conversion of a Diesel Engine Bus*. Gdyni: Gmina Miasta Gdyni, 2012.

[16]   L. Bertoni, H. Gualous, D. Bouquain, D. Hissel, M.-. Pera, and J.-. Kauffmann, "Hybrid auxiliary power unit (APU) for automotive applications," in *Proceedings IEEE 56th Vehicular Technology Conference*, 2002, vol. 3, pp. 1840–1845 vol.3, doi: 10.1109/VETECF.2002.1040535.

[17]   UNECE, *General construction of buses and coaches*. Europe, 2020.

[18]   B. Ku and J. Liu, "Converter-Switching Surges: Railroad Vehicle Power Converter Impact Studies," *IEEE Veh. Technol. Mag.*, vol. 7, no. 3, pp. 57–66, 2012, doi: 10.1109/MVT.2012.2203409.

[19]   K. Rajashekara and Y. Jia, "An induction generator based auxiliary power unit for power generation and management system for more electric aircraft," in *2016 IEEE Energy Conversion Congress and Exposition (ECCE)*, 2016, pp. 1–7, doi: 10.1109/ECCE.2016.7854849.

[20]   D. Zhang, J. Jiang, L. Y. Wang, and W. Zhang, "Robust and Scalable Management of Power Networks in Dual-Source Trolleybus Systems: A

[21]   Consensus Control Framework," *IEEE Trans. Intell. Transp. Syst.*, vol. 17, no. 4, pp. 1029–1038, 2016, doi: 10.1109/TITS.2015.2492564.

[21]   VT/RTSC - Rail Transportation Standards Committee, *IEEE Recommended Practice for Terminology Used for Direct Current Electric Transit Overhead Contact Systems*. 2019.

[22]   J. Joyce, *British Trolleybus Systems*. London: Littlehampton Book Services Ltd, 1986.

[23]   C. S. Dunbar, *Buses, Trolleys and Trams*. Octopus Publishing Group, 2004.

[24]   Wikipedia, "List of trolleybus systems," 2020. https://en.wikipedia.org/wiki/List_of_trolleybus_systems.

[25]   P. Stepanov, "Characteristics of construction and operation of trolleybus systems in the wo," *Pr. Kom. Geogr. Komun. PTG*, vol. 22, no. 3, pp. 64–72, 2019, doi: DOI 10.4467/2543859XPKG.19.018.11284.

[26]   Wikipedia, "Public transport in Istanbul," 2020. https://en.wikipedia.org/wiki/Public_transport_in_Istanbul.

[27]   Rayhaber, "Malatya new Trambus line," 2013. https://en.rayhaber.com/2013/04/malatya-yeni-trambus-hatti/.

[28]   "Trolleybus usage by country." https://en.wikipedia.org/wiki/Trolleybus_usage_by_country#Turkey_2 (accessed Mar. 26, 2020).

[29]   J. Choi, J. Jeong, Y. Park, and S. W. Cha, "Evaluation of regenerative braking effect for E-REV bus according to characteristic of driving cycle," *Int. J. Precis. Eng. Manuf. Technol.*, vol. 2, no. 2, pp. 149–155, 2015, doi: 10.1007/s40684-015-0019-6.

[30]   D. Perrotta, B. Ribeiro, R. J. F. Rossetti, and J. L. Afonso, "On the Potential of Regenerative Braking of Electric Buses as a Function of Their Itinerary," *Procedia - Soc. Behav. Sci.*, vol. 54, pp. 1156–1167, 2012, doi: https://doi.org/10.1016/j.sbspro.2012.09.830.

[31]   E. Sindi, L. Y. Wang, M. Polis, G. Yin, and L. Ding, "Distributed Optimal Power and Voltage Management in DC Microgrids: Applications to Dual-Source Trolleybus Systems," *IEEE Trans. Transp. Electrif.*, vol. 4, no. 3, pp. 778–788, 2018, doi: 10.1109/TTE.2018.2844367.

[32]   Opperhill, "Real-Time CAN bus data recorder with SD card," 2019. https://copperhilltech.com/blog/realtime-can-bus-data-recorder-with-sd-card/.

[33]   A. Bortfeldt and G. Wäscher, "Container Loading Problems - A State-of-the-Art Review," Otto-von-Guericke University Magdeburg, Faculty of Economics and Management, 2012. doi: DOI:

[34]   M. R. Garey and D. S. Johnson, *Computers and Intractability; A Guide to the Theory of NP-Completeness*. USA: W. H. Freeman & Co., 1990.

[35]   E. Dube, "Optimizing Three-Dimensional Bin Packing Through Simulation," 2006.

[36]   R. Lewis, "A general-purpose hill-climbing method for order independent minimum grouping problems: A case study in graph colouring and bin packing," *Comput. Oper. Res.*, vol. 36, no. 7, pp. 2295–2310, Jul. 2009, doi: 10.1016/J.COR.2008.09.004.

[37]   G. Fasano, "Cargo Analytical Integration in Space Engineering: A Three-dimensional Packing Model BT - Operational Research in Industry," T. A. Ciriani, S. Gliozzi, E. L. Johnson, and R. Tadei, Eds. London: Palgrave Macmillan UK, 1999, pp. 232–246.

[38]   M. Padberg, "Packing small boxes into a big box," *Math. Methods Oper. Res.*, vol. 52, no. 1, pp. 1–21, 2000, doi: 10.1007/s001860000066.

[39]   B. S. Baker, "A new proof for the first-fit decreasing bin-packing algorithm," *J. Algorithms*, vol. 6, no. 1, pp. 49–70, 1985, doi: https://doi.org/10.1016/0196-6774(85)90018-5.

[40]   W. T. Rhee, "Stochastic Analysis of a Modified First Fit Decreasing Packing," *Math. Oper. Res.*, vol. 16, no. 1, pp. 162–175, Dec. 1991, [Online]. Available: http://www.jstor.org/stable/3689854.

[41]   G. Dósa, "The Tight Bound of First Fit Decreasing Bin-Packing Algorithm is *FFD(I)* ≤ 11/9*OPT(I)* + 6/9," in *Proceedings of the First International Conference on Combinatorics, Algorithms, Probabilistic and Experimental Methodologies*, 2007, pp. 1–11.

[42]   G. Erdoğan, "CLP Spreadsheet Solver." https://people.bath.ac.uk/ge277/clp-spreadsheet-solver/.

[43]   ]A. Ochoa Ortiz-Zezzatti, G. Rivera, C. Gómez-Santillán, and B. Sánchez–Lara, Eds., *Handbook of Research on Metaheuristics for Order Picking Optimization in Warehouses to Smart Cities*. IGI Global, 2019.

BIOGRAPHIES

İSMAİL CAN DİKMEN received the B.S. and M.S. degrees in Electronics Engineering from the National Defense University and Aeronautics and Space Technologies Institute, in 2002 and 2007 respectively. He is continuing his PhD studies on intelligent battery management systems for electric vehicles at Inonu University. Currently he is an instructor at Electric Vehicle Technologies department of Inonu University OSB vocational school. His research interests include electric vehicles, battery management systems, control theory, control system design, electronic circuit design, optimization methods and machine learning.

YUNUS EMRE EKİCİ is currently an instructor at Electric Vehicle Technologies department of Inonu University OSB vocational school. He is continuing his PhD studies. His research interests include electric vehicles, traction batteries, power electronics, powertrain systems, control theory and electric vehicles charging systems.

TEOMAN KARADAG Assist. Prof. in Department of Electrical and Electronics Engineering, Inonu University of Malatya, Turkey. He continues to work in the department, where he graduated, as an Asst. Professor Dr. since 2015. High and Low Frequency Electromagnetic Fields and Applications, Electric Vehicles and Battery Management Systems, Electric Vehicle Charging Stations are the main fields of his study.

TAHMURAZ ABBASOV was born in Karabag, Azerbaijan, 1958. He received the B.Sc. and the M.Sc. degrees from Moscow Automechanical Institute (Moscow State Technical University, MAMI) and the Ph.D. degree from University of Azerbaijan State Petrol Academy and Azerbaijan National Scientific Academy, all in Electrical Engineering, in 1981, 1991 respectively. Currently, he is a Professor of Electrical Engineering at Inonu University. He is also an academic member of American Chemical Society, He is member of two international journals. His research interests are in the area of Electromagnetic Fields and Technology, Magneto hydro Dynamics and Magnetic Fluids, Bioelectromagnetics.

SERDAR ETHEM HAMAMCI received the B.S. degree in Electronics Engineering from Erciyes University in 1992 and the M.S. and PhD. degrees in Electrical-Electronics Engineering from Firat University in 1997 and 2002 respectively. He is currently full professor at Electrical-Electronics Engineering Department at Inonu University, Malatya, Turkey. His research interest includes electric vehicles, control system design, fractional order systems, memristive systems and data mining.

Classification of the Agricultural Crops Using Landsat-8 NDVI Parameters by Support Vector Machine

E.ACAR, M.ALTUN

Abstract— **Along with the data obtained from the developing remote sensing technologies, the use of machine learning techniques is widely employed in classification at a more effective and precise level. In this study, support vector machines (SVM) technique, one of the machine learning approaches, was utilized with the help of data obtained from satellite image, and it was aimed to classify agricultural products. Moreover, lentil and wheat products were employed for object detection, and Landsat-8 satellite was preferred as satellite imagery. In order to determine the plant indexes in the image, Landsat-8 image of the development period of agricultural products dated May 6, 2018 was used and 98 sample points were taken with the help of GPS on the pilot area. After that, the position of these points were transferred to Landsat-8 satellite image employing the QGIS program and NDVI values were calculated from these points, which corresponds to Landsat-8 NDVI image pixels. The obtained NDVI values were then utilized in the SVM as inputs. As a result, the accuracy of the overall system for crop classification on the pilot area was computed as 83.3%.**

Index Terms— **Remote Sensing, SVM, Landsat-8, NDVI, Lentil, Wheat, Crop Classification**

I. INTRODUCTION

WE SENSE the world surrounding us with our five senses. We are able to perceive a lot of information around us remotely without requiring close contact by outer objects with our sense of sight and hearing. In this point, we are often using remote sensing. In general, remote sensing expresses the activities of observing, recording and sensing objects or events in remote positions [1].

EMRULLAH ACAR, is with Department of Electrical and Electronics Engineering University of Batman, Batman, Turkey, (e-mail: emrullah.acar@batman.edu.tr).
https://orcid.org/0000-0002-1897-9830

MÜSLİME ALTUN, is with Department of Electrical and Electronics Engineering University of Batman, Batman, Turkey, (e-mail: muslimealtun72@gmail.com).
https://orcid.org/0000-0001-9787-3286

The most up-to-date data about the land ensured by the remote sensing technology, merged with the Geographic Information Systems (GIS) technology, ensures a great convenience to the conventional techniques because it reaches its target faster, cheaper with limited labor [2].

Remote sensing systems can be categorized into two kinds as active and passive sensors. Of these, passive sensors enroll solar radiation emitted or reflected from the surface of earth. Photo cameras, electro-optic sensors, antenna sensors and thermal IR sensors can be thought as samples of passive sensors. Active sensors employ the energy, which sent from the sensor. They ensure their own energy towards the object to be investigated. The reflected energy from this object is then recorded and detected via the sensors. Active sensors can be employed in order to view the surface at any time regardless of the season. An instance of active detection is the radar that transmits an electromagnetic wave signal towards the object as well as measures and detects the backscattered signal [1].

Object detection and classification through machine learning in satellite images has recently become widespread. Support Vector Machines (SVM), one of the machine learning methods, have been among the highest performing approaches in the studies for object detection. SVM is a concept associated with a series of supervised learning methods in statistics and computer science. It is used for pattern recognition, data analysis, classification and regression analysis [3-4]. In this study, SVM model was preferred for crop classification since its capability and performance.

Many studies have been conducted in the literature using remote sensing data and machine learning approaches for object classification and detection [5-8].

In this study, two different agricultural products (lentil and wheat) were classified using Landsat-8 data, one of the optical remote sensors, and the SVM technique, one of the machine learning approaches. Landsat-8 satellite image used in the study was obtained in May 2018, which corresponds to the development period of the products. Parcels belonging to the village of Bıçakçı in Batman province, Turkey were selected as the study area. GPS coordinate points of 98 sample points over these parcels were then transferred to the pre-processed image. Finally, thanks to calculating the NDVI values, which corresponds to these points and employing them as inputs of SVM technique, the agricultural products (wheat or lentil) were classified with a high performance.

II. MATERIAL

In this section, the determination of the study area; the application of preprocessing to the Landsat-8 satellite image; the importing of the GPS coordinate points to the Landsat-8 image; the calculation of the corresponding NDVI values and finally the classification with machine learning technique are mentioned.

A. Pilot Area and Data Collection

As the study area, the agricultural land where lentil and wheat agricultural products were cultivated, covering an area of 2x2 km^2 within the borders of Bıçakçı Village of Batman Center, which is under the control of Batman Agriculture Directorate, was selected. GPS data of 96 different sample points (40 lentil and 56 wheat points) determined within the boundaries of the selected agricultural pilot area were employed in this study. In Figure 1, the Google Earth view of this study area and the distribution of GPS data of 96 sample points in the pilot agricultural area are shown.

(a)   (b)
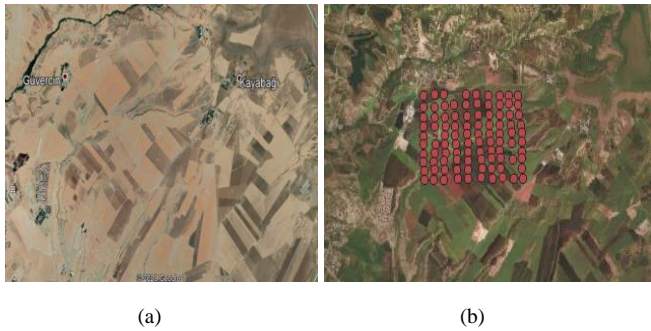
Fig.1. (a) Google Earth view of this study area (b) the distribution of GPS data of 96 sample points in the pilot agricultural area

In addition to the ground measurements, Landsat-8 data was utilized in order to generate NDVI parameters of the sample points.

B. Landsat-8 Image Preprocessing

The satellite image of the Landsat-8 OLI satellite used within the scope of this study was obtained from the website of the American Geological Service (USGS) with geometric and radiometric correction [9]. This image is in the Universal Transverse Mercator (UTM) coordinate system slice 35 and WGS84 datum. In the ENVI 5.0 software (Exelis Visual Information Solutions, Boulder, Colorado), band composition, band proportioning and image enhancement methods were applied to the data. Gaussian Distribution Method was used in the image enhancement process. In this method, the pixel values were spread over the 0-255 color range via histogram and the contrast values were increased. Band rationing is an image enhancement analysis method in which new pixel values are obtained by dividing the gray color value of a pixel in one band by the value of the same pixel in another band or by applying other mathematical operations [5, 10]. In addition, by using this image enhancement method, the spectral differences between the bands are enriched and the effect of the terrain roughness on the images is reduced.

C. Feature Extraction

In the feature extraction stage, one of the most important vegetation indexes, Normalized Difference Vegetation Index (NDVI), was computed from Landsat-8 image in order to form feature vectors for each sample point.

With the help of vegetation indices such as NDVI, it is possible to observe the plant diversity and vegetation density on the earth with remote sensing systems. In NDVI method, visible and near infrared regions of the electromagnetic spectrum were used [10-11].

In this study, the NDVI image was obtained by applying arithmetic operations (Equation-1) to the near infrared and red bands obtained from the Landsat-8 image, and the NDVI values of the 96 sample points on this image were then calculated.

$$NDVI = \left(\frac{NIR-RED}{NIR+RED}\right) \qquad (1)$$

Here, *NIR* and *RED* express the reflection values of the near infrared and red (visible) bands, respectively.

III. METHOD

In our study, a machine learning approach (SVM) was preferred to classify agricultural crops (lentil and wheat) utilizing the NDVI data, which obtained from the Landsat-8 image. The detailed information about SVM classifier is given as below.

A. Support Vector Machine (SVM)

Support Vector Machines (SVM) is a concept associated with a range of supervised learning methods in statistics and computer science. It is used for pattern recognition and data analysis as well as classification and regression analysis. The mathematical models of SVM have emerged in two classes for the classification of linear data at the first stage. In later times, new studies were conducted on the classification of nonlinear multi-class data. SVM, which tries to predict the most suitable transfer function to distinguish two different classes from each other and creates a hyper plane to separate them optimally [3, 12-13] as shown in Figure 2.
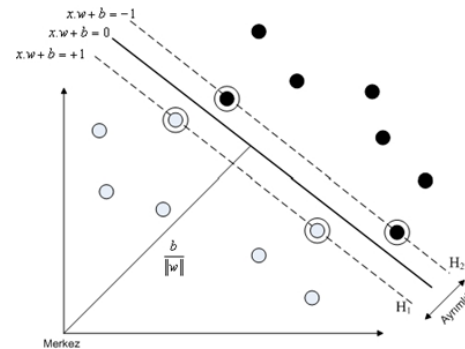
Fig. 2. The architecture of the linear SVM classifier

The aim of SVM is to ensure equal distance to both sample groups with the hyperplane. For the linear separability case, the differential hyperplane is defined in Equation-2.

$$g(\emptyset) = w^T x + b = \sum_{i=1}^{n} w_i x_i + b \qquad (2)$$

Here x, b and w denote input feature vector, bias and weight vectors, respectively.

IV. RESULTS AND DISCUSSION

In this section, the pre-processed Landsat-8 image and the NDVI image obtained from Landsat-8 image bands were presented. In addition, the data obtained from the NDVI image were passed through the training-test phase in the SVM technique and the performance values of the classification result were tabulated.

A. Obtaining NDVI Image

In this part, images of red (visible) and near infrared bands (band 4, band 5) to employ for obtaining NDVI image from the Landsat-8 image, which derived in 06.05.2018 are shown in Figure 3. These images were calculated in accordance with the NDVI formula specified in Equation 1, thanks to the raster calculator in the QGIS program. As a result of these operations, the NDVI image in Figure 4 was obtained. The obtained NDVI image was then converted into a "single band pseudo color layer" and shown in Figure 5. In addition, the import of GPS data to the image was carried out as shown in Figure 6.
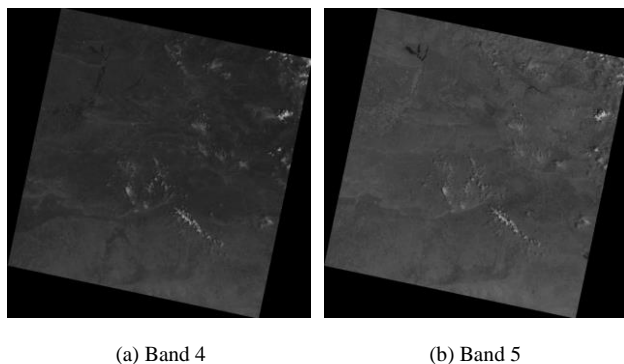
(a) Band 4   (b) Band 5

Fig. 3. Obtaıned Landsat-8 band images, which are (a) Band 4 (visible) and (b) Band 5 (near infrared)
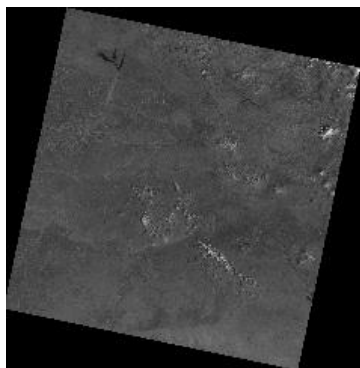
Fig. 4. NDVI image of the pilot area, which obtained in 06.05.2018
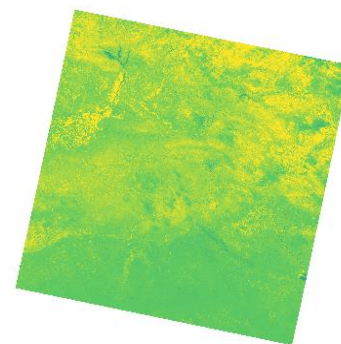
Fig. 5. Single band pseudo color layer (SBPCL) of the obtained NDVI image
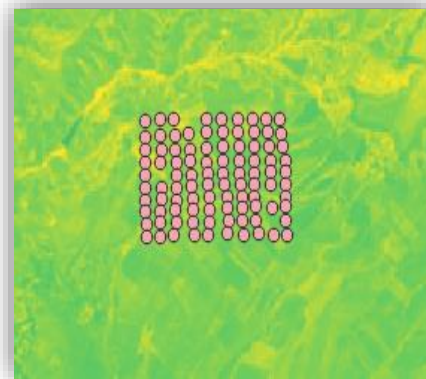
Fig. 6. The import of GPS data to the obtained SBPCL image

B. The Results of Crop Classification by Employing NDVI Parameters and SVM

At this stage, leave-one-out cross validation method was applied to the data obtained to calculate the performance value of the whole system and the results obtained were presented in Table-1 using performance metrics (Sensitivity, Specificity, Precision, Recall, F1 Score and Accuracy). Moreover, the confusion matrix of the recommended system was given in Figure 7.
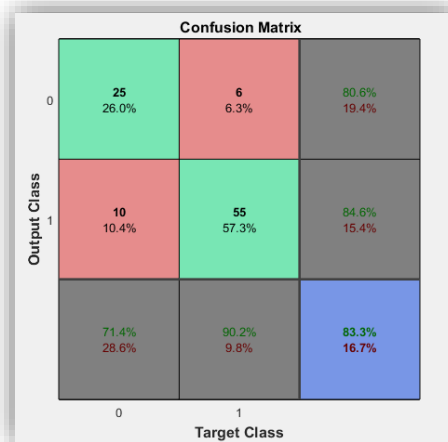
Fig. 7. The confusion matrix of the proposed system

As shown in both Figure 7 and Table-I, the best accuracy result was observed as 83.3 %, while other performance metrics are 90.1 % for sensitivity, 71.4 % for specificity, 84.6 % for precision, 90.1 % for recall and 87.3 % for F1 score.

From Table-II, it is possible to say that the result of the proposed study is successful when compared to the other literature studies.

TABLE I
PERFORMANCE METRICS BASED ON THE NDVI PARAMETERS AND SVM APPROACH

Performance Metrics	Results (%)
Sensitivity	90.16
Specificity	71.43
Precision	84.62
Recall	90.16
F1 Score	87.31
Accuracy	**83.33**

TABLE II
COMPARISON OF THE PROPOSED APPROACH BY THE OTHER LITERATURE STUDIES

Reference	Data Type	Approach	Results (%)
Our Study	Landsat-8	SVM	83.33
[5]	Sentinel-2A	Random Forest	93.10
[6]	Sentinel-2A	Random Forest	88.00
[8]	Landsat-8 & Sentinel-2A	Ensemble classifiers	90.00
[12]	LISS IV	SVM, ANN, SAM	[74.9-93.4]

V. CONCLUSION

Agricultural systems constitute an important economic sector in the Anatolian countryside and worldwide. In particular, the combination of remote sensing data and machine learning techniques can facilitate the detection of many agricultural products at very large distances in a short time with little cost. In this study, it has been proposed to classify two different agricultural products (lentil and wheat) by employing NDVI parameters obtained from Landsat-8 satellite images and SVM approach from machine learning techniques.

The results of the proposed system indicated that a high classification success was performed in order to classify the crops thanks to NDVI parameters. Moreover, considering the success rate, it was observed that the machine learning approach employed in the proposed crop classification system affected the overall performance significantly.

In the future, as a continuation of this study, it is planned to classify various products with different vegetation indexes and different machine learning methods. It is thought that this proposed study will contribute to the national economy, especially in agricultural states.

REFERENCES

[1] Q. Weng, "Introduction to Remote Sensing Systems, Data, Applications."Remote Perception of Natural Resources July 2013, pp 3-20

[2] Kavzoğlu, T., Çölkesen, İ.,"Remote Sensing Technologies and Applications." Sustainable Land Management Workshop In Turkey, 26-27 May 2011.

[3] Huang, J., Blanz, V., & Heisele, B. (2002, August). Face recognition using component-based SVM classification and morphable models. In *International Workshop on Support Vector Machines* (pp. 334-341). Springer, Berlin, Heidelberg.

[4] Koçyiğit, F., Çay, V. V., Dursun, Ö. O., & Akpinar, E. K. (2017). Prediction of thermal performance of designed different obstacles on absorber plates in solar air collectors by support vector machine. *European Journal of Technique*, *7*(2), 186-194.

[5] Kobayashi, N., Tani, H., Wang, X., & Sonobe, R. (2020). Crop classification using spectral indices derived from Sentinel-2A imagery. *Journal of Information and Telecommunication*, *4*(1), 67-90.

[6] Htitiou, A., Boudhar, A., Lebrini, Y., Hadria, R., Lionboui, H., & Benabdelouahab, T. (2020). A comparative analysis of different phenological information retrieved from Sentinel-2 time series images to improve crop classification: A machine learning approach. *Geocarto International*, (just-accepted), 1-20.

[7] Acar, E., & ÖZERDEM, M. S. (2020). On a yearly basis prediction of soil water content utilizing SAR data: a machine learning and feature selection approach. *Turkish Journal of Electrical Engineering & Computer Sciences*, *28*(4), 2316-2330.

[8] Chakhar, A., Ortega-Terol, D., Hernández-López, D., Ballesteros, R., Ortega, J. F., & Moreno, M. A. (2020). Assessing the Accuracy of Multiple Classification Algorithms for Crop Classification Using Landsat-8 and Sentinel-2 Data. *Remote Sensing*, *12*(11), 1735.

[9] Nasa U.S. Geological Survey. Landsat Data Continuity Mission ,February 2013, pp.1-17.

[10] A. Gönenç, " Comparison of NDVI and RVI Vegetation Indices Using Satellite Images. " 2019 Master Thesis, D.Ü, Institute of Science, Diyarbakır, 22-56

[11] Gonenc, A., Ozerdem, M. S., & Acar, E., (2019, July). Comparison of NDVI and RVI Vegetation Indices Using Satellite Images. In *2019 8th International Conference on Agro-Geoinformatics (Agro-Geoinformatics)* (pp. 1-4). IEEE.

[12] P. Kumar, D.K. Gupta, V.N. Mishra, R. Prasad, "Comparison of spectral angle matching algorithms for crop classification using support vector machine, artificial neural network, and LISS IV data." International Journal of Remote Sensing 2015.

[13] Olanloye, O. D., Olasunkanmi, O., & Oduntan, O. E. Comparison of Support Vector Machine Models in the Classification of Susceptibility to Schistosomiasis. *Balkan Journal of Electrical and Computer Engineering*, *8*(3), 266-271.

BIOGRAPHIES

EMRULLAH ACAR received the B.S. degree in electrical and electronics engineering from Çukurova University, Adana, Turkey in 2009. From 2008 to 2009, he was an exchange student in the electrical engineering from Linkoping University, Sweden. He received the M.S in electrical and electronics engineering from Istanbul Technical University, Istanbul and Dicle University, Diyarbakir, Turkey in 2012. After that, he received the PhD degree in electrical-electronics engineering from Gaziantep University, Gaziantep and Dicle University, Diyarbakir, Turkey in 2017.

He is an assistant professor at the Batman University of electrical-electronics engineering and is the head of electronics division. His research interest includes the digital image processing, machine learning and remote sensing applications.

Mr. Emrullah's awards and honors include the TUBITAK (The Scientific and Technological Research Council of Turkey) Grant, Erasmus Mobility Grant (Sweden) and Erasmus Internship Grant (Germany).

MÜSLİME ALTUN received the B.S. degree in electrical and electronics engineering from Gaziantep University, Gaziantep, Turkey in 2018. She received the M.S in electrical and electronics engineering from Batman University Batman, Turkey in 2021. Her research interest includes machine learning and remote sensing applications.

High Efficient Permanent Magnet Synchronous Motor Design, Electromagnetic and Noise-Vibration Analyzes

A. ŞAHİN, Y. ÖNER

Abstract—In this study, it was aimed to carry out the design, electromagnetic analysis and noise-vibration analysis of a 3 phase, high efficient surface mounted permanent magnet motor with power level of 7.5kW and 1500rpm speed. Using basic analytical formulas initial design geometry of motor was obtained. This first design geometry was investigated in detail by electromagnetic analyzes. In these electromagnetic analyzes, cogging torque, torque ripple, losses and efficiency parameters have been investigated. Then, modal and harmonic analyzes were carried out in order to interpret the effect of radial harmonic forces, obtained from electromagnetic analyzes, on the stator teeth on the noise and vibration parameters of the motor. According to analysis result of initial designed motor, it was aimed to reduce cogging torque, torque ripple, efficiency, noise and vibration parameters. It is thought that the improvement studies to be perform in the cogging torque will also have a positive effect on the torque ripple and vibration on the motor. By optimizing studies performed magnet and lamination geometry, new motor geometry has been obtained. Electromagnetic, modal, harmonic analyzes were made this new motor geometry. Analysis results of the new design and the first design were studied comparatively.

Index Terms—Cogging Torque, efficiency, noise, permanent magnet motor, vibration.

I. Introduction

P ermanent magnet synchronous are widely used in industrial application, electrical appliances and electrical vehicle applications. In addition to the widespread use of permanent magnet synchronous motors, with the increasing importance of energy efficiency throughout the world, many studies are carried out on these motors in academia and industry. These studies considering that the pulling force applied by the magnet in the rotor of these motors to the stator teeth causes the cogging torque. At the same time, there are many studies on the negative effect of torque ripple on motors and reducing this ripple. One of the most important issues emphasized in the studies is the efficiency of the motors. In permanent magnet synchronous machines, it is quite possible to obtain higher efficiency and power in smaller volumes compared to other traditional electric motors.

With the discovery of magnets such as ''Nd–Fe-B''(Neodymium Iron Boron) and ''Sm–Co''(Samarium Cobalt) with high remanence, high energy and high magnetic field intensity values as shown figure 1 that are subjected to demagnetization in early 1980s, studies on permanent magnet motors gained speed [1,2].
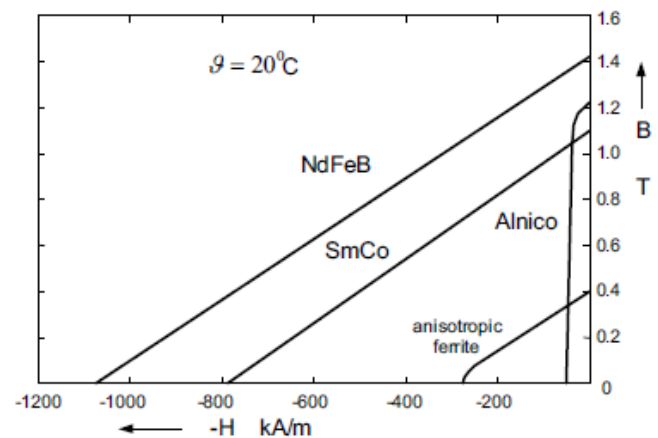
Fig.1. Demagnetization Curves of Different Magnet Materials [2]

These motors, which do not have conductors in their rotor, provide great advantages over other motor types both terms of efficiency and dimension with the use of high energy magnets such as ''Nd-Fe-B'' and ''Sm-Co''.

As with other electric motors in permanent magnet synchronous motors, the generation of noise and vibration is a subject that needs to be studied in detail. Noise and vibration in these motors are examined under three main titles as electromagnetic, mechanical and aerodynamic as shown figure2. Especially in the electric vehicles, aviation and servo industry, the generation of noise and vibration have high importance [3, 4, 5].

ATAKAN ŞAHİN, is with Department of Electrical Engineering University of Yıldız Technical University, Gamak Makina Sanayi A.Ş, Istanbul, Turkey,(e-mail: atknshn1@gmail.com).
https://orcid.org/0000-0001-5870-0147

YASEMİN ÖNER, with Department of Electrical Engineering University of Yıldız Technical University, Istanbul, Turkey,(e-mail: yoner@yildiz.edu.tr).
https://orcid.org/0000-0002-5310-6875

Electromagnetic noise and vibration occurs when radial electromagnetic forces in the air gap effect on the stator teeth. It is not possible to eliminate these forces, but these forces can be minimized. These forces cause the stator stack and the frame to be deformed over time due to the vibration effect [3,4,5].
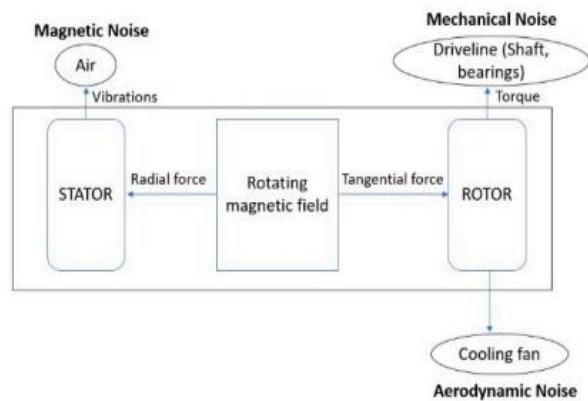

Fig.2. Generation of Noise and Vibration Origins in a Rotating Electrical Machine [5]

II. DETERMINATION OF DESIGN CRITERIA AND LAMINATION STRUCTURE

Fırstly, the minimum target efficiency value to be obtained in the analysis result was determined as %92,6 based on IEC 60034-30-1 efficiency standard of the motor, which will be designed at 230V phase voltage with IE4 efficiency class and 7.5kW power level at 1500rpm rotational speed. According the diameter of the motor frame maximum stator outer diameter is determined as 218mm. For 4 pole surface magnet synchronous motor number of stator slots was chosen as 36 and accordingly, it was decided to use a single layer distributed winding type. The surface magnet structure has been determined for design of rotor structure.

TABLE I
DESIGN PARAMETERS

Parameters	Value
Output Power (kW)	7.5
Speed (rpm)	1500
Phase Voltage (V)	230
Phase Current(rms) (A)	14.85
Target Efficiency (%)	92.6

III. INITIAL DESIGN

First, the main dimensions of the motor are determined by using basic motor analytical formulas. Then the stator lamination and winding arrangement were determined and rotor magnet dimensions were determined. Lamination geometry was obtained as shown figure 3 and dimensions were shown table II.
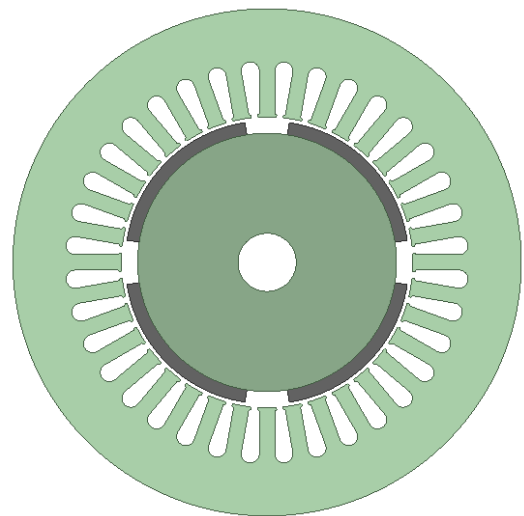
Fig.3. Stator and Rotor Structure

TABLE II
INITIAL DESIGN MOTOR DIMENSIONS

Parameter	Value
Stator Outer Diameter(mm)	218
Stator Inner Diameter (mm)	125
Stator-Rotor Stack Length (mm)	120
Slot Number	36
Slot Height (mm)	24
Stator Tooth Width (mm)	6.6
Airgap (mm)	1.5
Max. Magnet Thickness (mm)	5.5
Min. Magnet Thickness (mm)	5.3
Magnet Width (Electrical Degree)	144
Magnet Axial Length (mm)	120
Number of Turn in One Coil	19
Wire Diameter (mm)	1.02
Number of Wire	4
Steel Material	50JN400
Magnet Material	N45M

A. Initial Design Electromagnetic Analyzes

Electromagnetic analyzes were carried out in 2D with the finite element method using Ansys Maxwell software. In these analyzes made with sinusoidal current supply, moment, output power, flux - flux densities, cogging torque, losses and efficiency parameters are examined. In order to obtain more realistic results in analyzes to be perform, the mesh number was increased, as shown figure 4, by keeping the size of the mesh element thrown into the air gap and magnets.
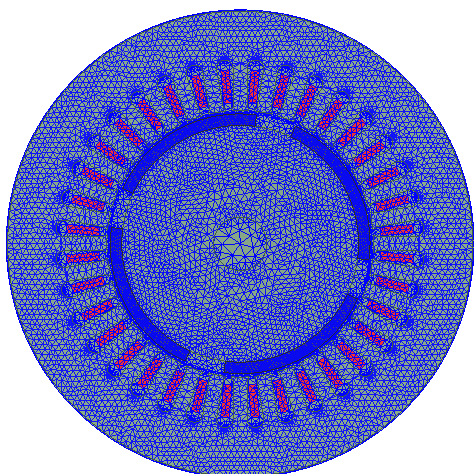
Fig.4. Mesh View

B. Torque Analysis

To obtain output power level of motor 7.5kW at 1500rpm speed;

$$T = \frac{P}{\omega} \qquad (1)$$

47.75Nm rated torque was obtained using the formula. Where P is the output power of the motor, ω is the angular velocity of the motor.
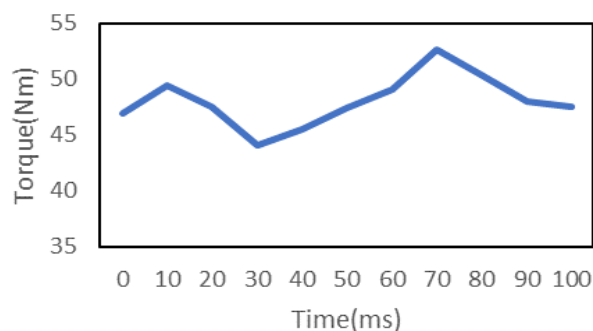
Fig.5. Torque Graph

TABLE III
Torque Values

Maximum Torque(Nm)	Minimum Torque(Nm)	Torque Ripple (%)
52.65	44.12	17.64

When the motor is operating under load at 1500rpm, the difference between maximum torque and minimum torque is clearly observed when the torque value is examined. Accordingly, torque ripple was calculated as 17.64% from figure 5.

C. Flux Density Analysis

It has been observed that the flux densities do not lead the 50JN400 electrical steel to the saturation point, as seen figure 6 and table IV, when the motor is fed with its nominal current and at nominal output power.
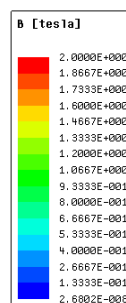
Fig.6. Flux Densities

TABLE IV
Max. Flux Densities

Parameters	Value (T)
Stator Yoke	1,6
Stator Tooth	1,73
Air Gap	1,16
Rotor Yoke	1,27

D. Determination of Losses

After the flux density analysis, the losses of the motor at the nominal power and speed were examined. Core and magnet losses were obtained by analyzing the finite element method. While calculating the copper losses, the stator winding temperature was accepted as 80°C in the thermal stability of the motor, and the copper losses were calculated according to the winding resistance at 80°C.
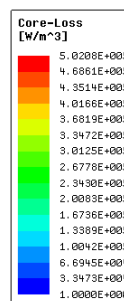
Fig.7. Core Losses
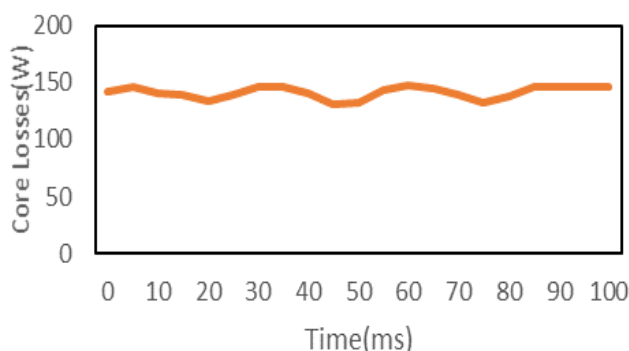
Fig.8. Core Losses Graph

When the iron losses became stable, 140.75W was obtained as the average value at figure 8 core losses graph. Efficiency value of motor was obtained summation of losses as seen table V.

TABLE V
Losses and Efficiency

Losses	Value
Copper Losses (W)	325,7
Core Losses (W)	140,75
Magnet Losses (W)	3,4
Friction and Windage Losses(W)	28
Additional Losses (W)	51
Total Losses(W)	548,85
Efficiency (%)	93,18

E. Cogging Torque Analysis

Cogging torque is the interaction between the stator teeth and the magnets when the phases are not supplied with current. Basically the strain felt when turning the shaft of the motor manually is called the cogging torque. Keeping this undesirable torque at the lowest possible value is very important in terms of torque ripple, noise and vibration [7,8].

$$T_{cogging} = \frac{1}{2} B_r \frac{l_m}{\mu_0 \mu_r} \frac{d\phi_r}{d\theta} \tag{2}$$

Here B_r is the magnet remanence value, μ_0 is the magnetic permeability of the air, μ_r is the relative magnetic permeability of the magnet, ϕ_r is the flux of the magnet, l_m is magnet thickness[6].
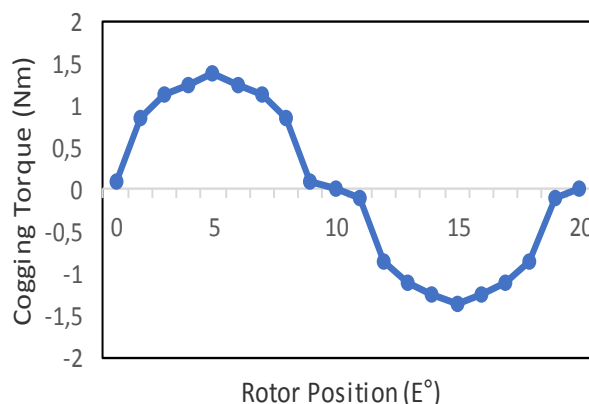
Fig.9. Cogging Torque Graph

The cogging torque of the motor was examined and the maximum cogging torque value was found to be 1.38Nm, and the peak to peak cogging torque value was found as 2.60Nm according to figure 9.

F. Noise and Vibration Analysis

One of the main causes of noise and vibration in electric motors is radial electromagnetic forces on the stator teeth. These electromagnetic forces cause vibration in the stator stack and cause both deformation and noise. Since electromagnetic forces cannot be eliminated theoretically and practically, minimizing these forces is very important for the life of the motor and driven load. Radial electromagnetic force density in the air gap according to the 'Maxwell Stress Tensor' equation

$$P_r(\theta, t) = \frac{b_r^2(\theta, t)}{2\mu_0} \tag{3}$$

it is calculated from the formula [4]. Where θ is the angular position of the stator, t time, μ_0 air gap magnetic permeability, air gap radial flux density $b_r^2(\theta, t)$.

G. Natural Frequency Analysis

Natural frequency is the frequency value that depends only on the elasticity and mass of an object and at which the object will vibrate continuously and in high amplitude when it is excited at a certain frequency. In this section, the natural frequencies of the stator geometry for different modes will be examined using Ansys Modal software.
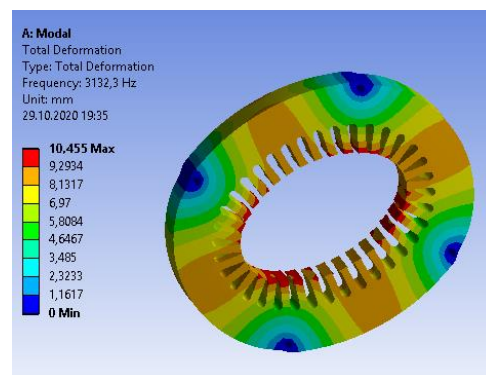
Fig.10. Natural Frequency in First Mode
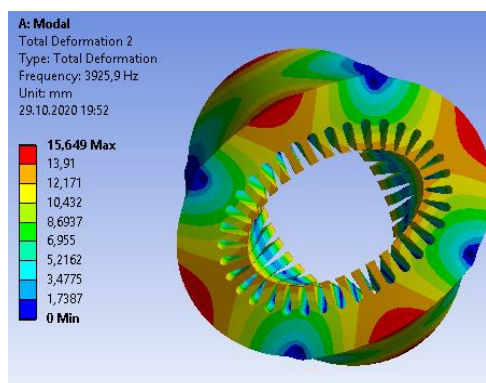
Fig.11. Natural Frequency in Second Mode
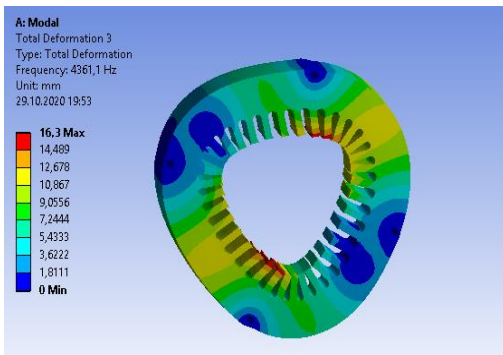
Fig.12. Natural Frequency in Third Mode

The natural frequency analysis results in the first 3 modes were examined. The natural frequencies were obtained from figures 10, 11, 12, as 3132.3Hz, 3925.9Hz, 4361.1Hz, respectively.

H. Harmonic Frequency Analysis

If the natural frequency of a geometry that makes forced vibrations under a dynamic force and the forced frequency are equal, the material goes into resonance and deformation. In this section, radial electromagnetic forces on the stator teeth are analyzed in Ansys Maxwell software. Then, these forces were transferred to the Ansys Harmonic Response software and the effects of electromagnetic forces on the motor on the stator teeth were analyzed with multiphysics.
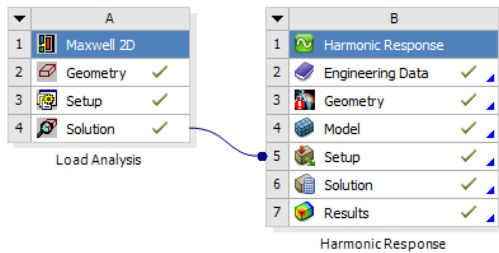
Fig.13. Multiphysics Analysis

TABLE VI
Forces on Stator Teeth

Frequency [Hz]	X Component Real [N]	X Component Imag [N]	Y Component Real [N]	Y Component Imag [N]
50	0,0040	0,0122	-0,0018	-0,0037
100	-133,21	-236,5	19,193	27,071
150	-0,0208	0,0067	-0,0054	-0,0131
200	-4,0502	-91,273	8,2426	9,7697
300	5,0297	-26,706	3,0731	4,5266
400	-10,966	-10,468	2,5416	-0,2752
500	-11,229	-14,374	4,1287	-0,4252
600	-2,2352	-11,996	3,1109	1,296
700	0,7360	-4,3094	0,9955	0,9029
800	-0,8957	-1,0045	0,3815	-0,4005
900	-0,5218	-0,8281	0,4090	-0,5105
1000	0,2447	-0,1527	0,0266	-0,0697
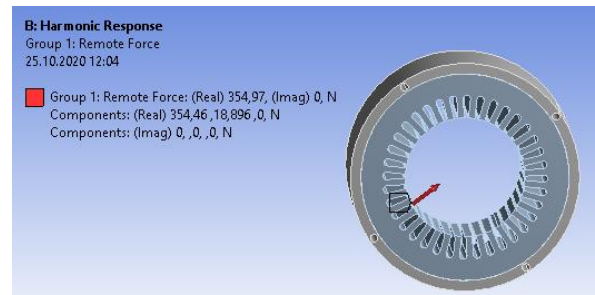
Figure.14. Illustration of the Force on a Stator Tooth
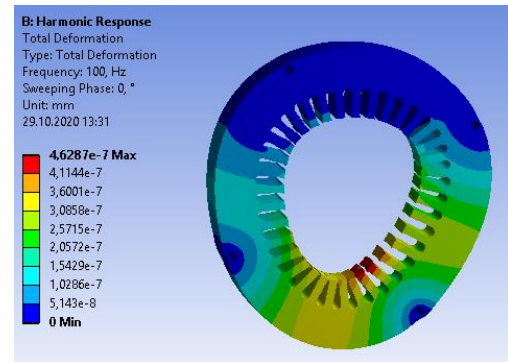
Figure.15. Deformation at 100Hz
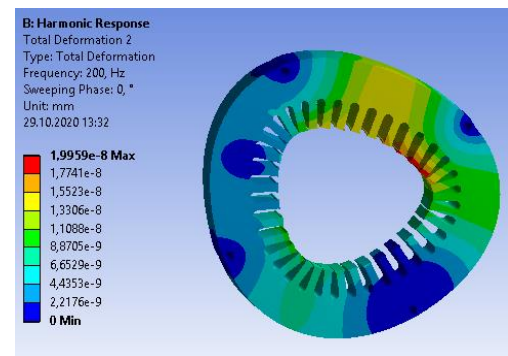
Figure.16. Deformation at 200Hz
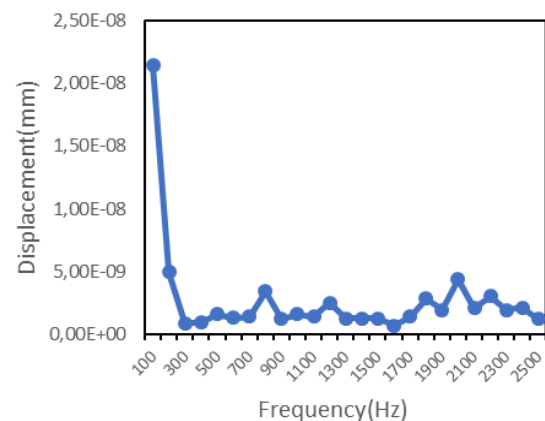
Figure.17. Frequency-Displacement Graph

Here, as seen figure 15, 16 and 17 the displacement values at certain frequencies resulting from the electromagnetic forces as shown table VI and figure 14 are basically the vibration values in the operating state of the motor. These vibrations, which are an energy source, cannot be noticed by the human

eye and can be measured with measuring devices. At the same time, these vibrations can be felt in the human ear by turning into noise, which is another source of energy, and can be measured with measuring devices.

IV. SECOND DESIGN

The final design was achieved by optimizing the design in order to make improvements in the cogging torque, torque ripple, efficiency, noise and vibration parameters of the permanent magnet synchronous motor. First of all, it was aimed to reduce the cogging torque and accordingly, torque ripple was also reduced. Magnet geometry has been optimized to reduce the cogging torque as shown figure 18.

TABLE VII
Second Design Parameters

Parameter	Value
Output Power (kW)	7.5
Speed (rpm)	1500
Phase Voltage (V)	230
Phase Current(rms) (A)	14.14
Target Efficiency (%)	92.6
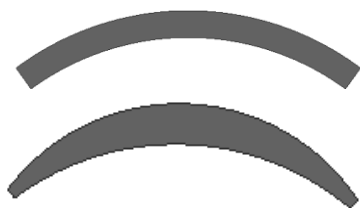
Figure.18. Magnet Geometry Optimization

TABLE VIII
Design 1&2 Motor Dimensions

Parameter	Design 1	Design 2
Stator Outer Diameter(mm)	218	218
Stator Inner Diameter (mm)	125	125
Stator-Rotor Stack Length (mm)	120	100
Slot Number	36	36
Slot Height (mm)	24	25,7
Stator Tooth Width (mm)	6.6	6
Airgap (mm)	1.5	1,5
Max. Magnet Thickness (mm)	5.5	8
Min. Magnet Thickness (mm)	5.3	2,2
Magnet Width (Electrical Degree)	144	155
Magnet Axial Length(mm)	120	100
Number of Turn	19	24
Wire Diameter (mm)	1.02	1
Number of Wire	4	4
Steel Material	50JN400	50JN400
Magnet Material	N45M	N48M

It is aimed to obtain the same power in a smaller volume by reducing the stack length of the motor. Accordingly, the need to increase the number of turns has emerged. If the stator slot area were left the same as the first design, we would have to

reduce the conductor cross section, and this reduction would increase the winding phase resistance, there would be a significant increase in copper losses. In order to prevent this, the stator slot area has been increased 'without ignoring the flux densities'.

A. Electromagnetic Analysis

In order to examine the effects of changing lamination and magnet geometry on the motor, the electromagnetic analyzes made in the first design were repeated and the results were examined comparatively.

B. Torque Analysis

The rated torque characteristic of the second design was examined and it was observed that the torque ripple decreased significantly compared to the first design as seen figure 19 and table IX.
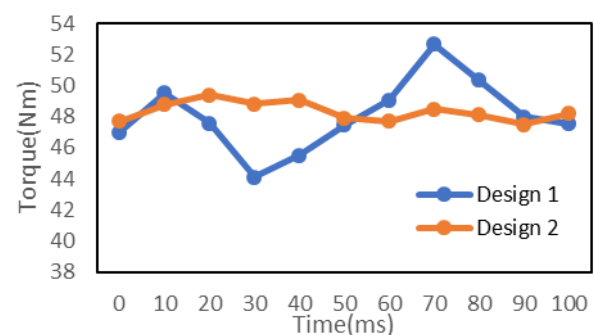
Figure.19. Torque Graphs

Table IX
Torque Values

	Maximum Torque(Nm)	Minimum Torque(Nm)	Torque Ripple (%)
Design 1	52,65	44,12	17,64
Design 2	49,4	47,5	3,9

C. Flux Density Analysis
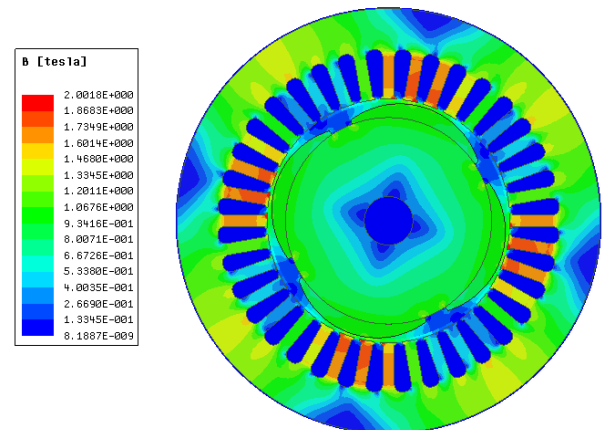
Figure.20. Flux Densities

Table X
Max. Flux Density Values

Parameter	Design 1(T)	Design 2(T)
Stator Yoke	1,6	1,5
Stator Teeth	1,73	1,77
Airgap	1,16	1,13
Rotor Yoke	1,27	1,2

It has been observed that the flux densities in design 2 do not lead the 50JN400 electrical steel to the saturation point, as seen figure 20 and table X.

D. Determination of Losses

In the second design, the volume of the motor was reduced, the stator-rotor axial length was decreased, the magnet volume was increased, and the iron losses of the motor, which could achieve 7.5kW output power with less phase current, were significantly reduced as seen figure 21. With the reduction of iron losses, an improvement has been made in the efficiency parameter as seen table XI.
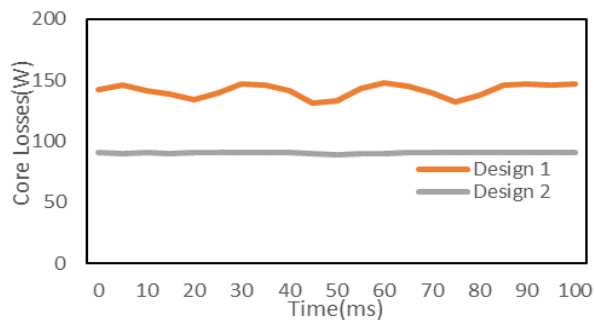
Figure.21. Core Losses Graph

Table XI
Comparative Result of Losses

Losses	Design 1	Design 2
Copper Losses (W)	325,7	340
Core Losses (W)	140,75	89,67
Magnet Losses (W)	3,4	1,19
Friction and Windage Losses(W)	28	28
Additional Losses (W)	51	51
Total Losses(W)	548,85	509,86
Efficiency (%)	93,18	93,63

E. Cogging Torque Analysis

After optimizing the magnet geometry in the first design, it is observed that the cogging torque obtained in the second design is significantly reduced as seen figure 22 and table XII.
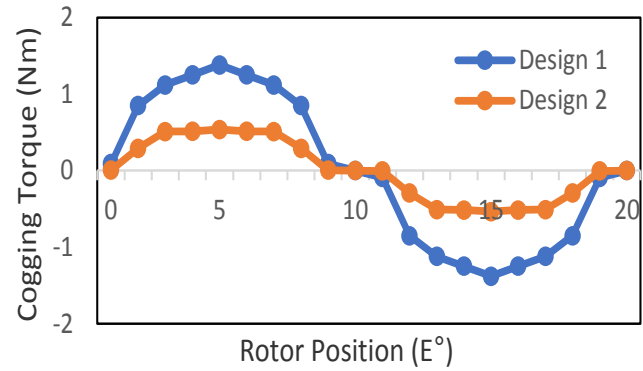
Figure.22. Cogging Torque Graph Design 1&2

Table XII
Cogging Torque Values

	Max. Cogging Torque(Nm)	Peak to Peak Cogging Torque(Nm)
Design 1	1,38	2,6
Design 2	0,537	1,07

F. Noise and Vibration Analysis

First, natural frequency analyzes of the stator stack fixed at 4 points were performed.
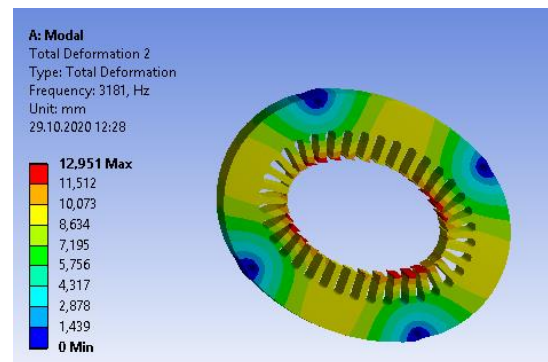
Fig.23. Natural Frequency in First Mode
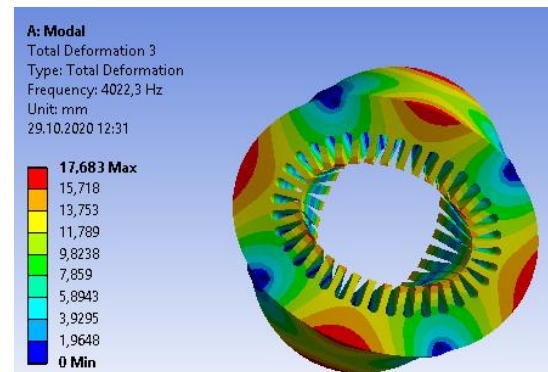
Fig.24. Natural Frequency in Second Mode
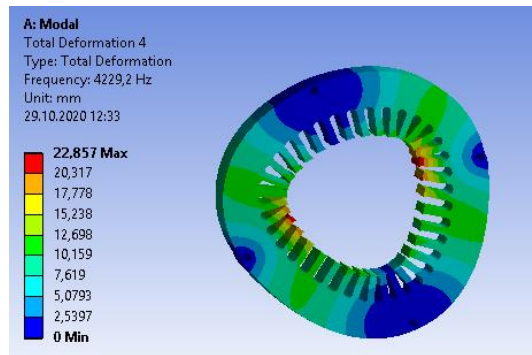
Fig.25. Natural Frequency in Third Mode

The natural frequency analysis results in the first 3 modes were examined. The natural frequencies were obtained as seen figure 23, 24 and 25 as 3181Hz, 4022.3Hz, 4229.2Hz respectively.

G. Harmonic Frequency Analysis

In this section, firstly, electromagnetic forces on stator teeth are analyzed. These forces were transferred to the Ansys Harmonic Response software and multiphysics analyzes were performed.
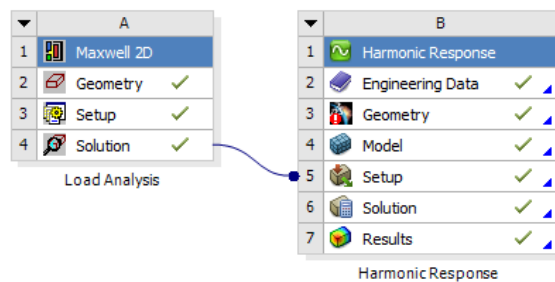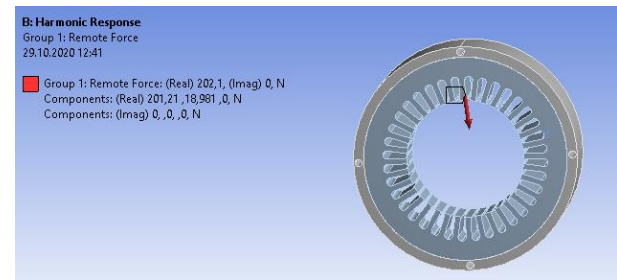

Fig.26. Multiphysics Analysis

Table XIII
Forces on Stator Teeth

Frequency [Hz]	X Component Real [N]	X Component Imag [N]	Y Component Real [N]	Y Component Imag [N]
50	0,0014	-0,0265	-0,0023	-0,0012
100	211,7	73,7020	13,547	20,6710
150	-0,0052	0,0103	-0,0011	0,0024
200	-23,9610	-2,4352	2,9854	-5,7988
250	-0,0016	0,0036	0,0013	0,0022
300	-3,2879	-7,6070	-1,1511	0,4653
400	-0,2876	-1,3666	0,2533	-0,3375
500	-1,1707	0,4757	0,1951	0,3020
600	-0,1889	-0,5597	0,2464	-0,1932
700	0,3106	-0,1428	0,1886	-0,0390
800	-0,2089	-0,0673	-0,0786	-0,0262
900	-0,2182	-0,0506	0,0404	-0,0931
1000	0,1428	0,1800	-0,2347	-0,0542

Figure.27. Illustration of the Force on a Stator Tooth
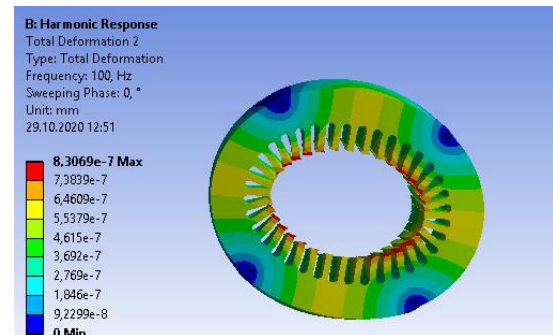
Figure.28. Deformation at 100Hz
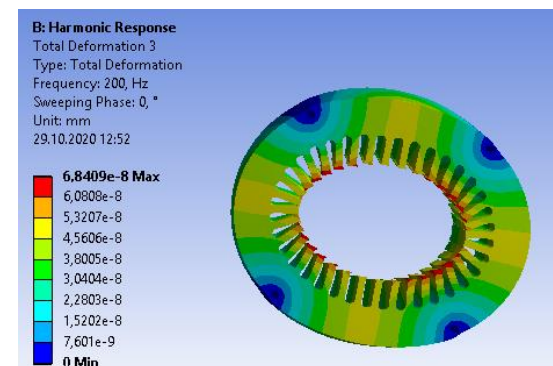
Figure.29. Deformation at 200Hz
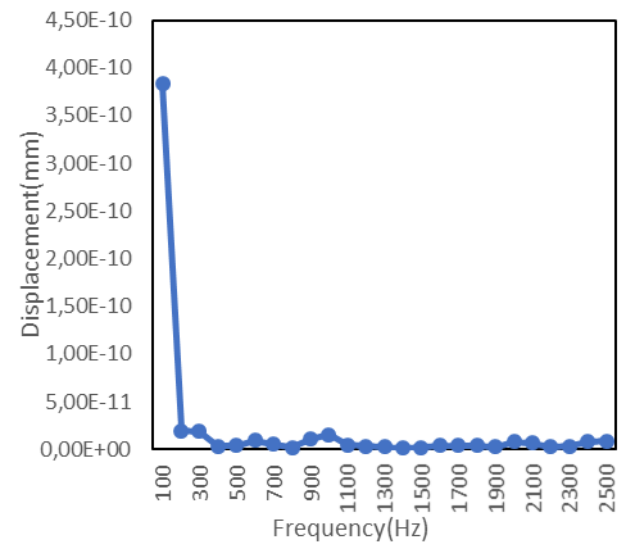
Figure.30. Frequency-Displacement Graph

Electromagnetic forces on stator teeth was shown at figure 27 and table XIII. The displacement, causes from electromagnetic

forces, values of the motor at certain frequencies as shown figure 28, 29 and 30. Under radial electromagnetic forces the displacement values design 1&2 were compared at table XIV.

Table XIV
Displacement Values for Design 1&2

Frequency(Hz)	Displacement(mm)	
	Design 1	Design 2
100	2.15×10^{-8}	3.83×10^{-10}
200	4.97×10^{-9}	1.96×10^{-11}
300	9.23×10^{-10}	1.92×10^{-11}
400	9.82×10^{-10}	3.54×10^{-12}
500	1.63×10^{-9}	3.99×10^{-12}
600	1.35×10^{-9}	9.13×10^{-12}
700	1.46×10^{-9}	5.29×10^{-12}
800	3.45×10^{-9}	1.88×10^{-12}
900	1.25×10^{-9}	1.10×10^{-11}
1000	1.66×10^{-9}	1.54×10^{-11}

The second design with lower cogging torque and torque ripple were obtained, the displacement values of the motor at the same frequency compared to the first design. Improvement work on the cogging torque and torque ripple also led to the reduction of radial electromagnetic forces on the stator teeth and the displacement of the motor under these forces was reduced. The fact that the displacement values are reduced also means that the noise and vibration values of the motor will be lower than the first design.

V. CONCLUSION

Within the scope of this study, the design and optimization of a 3-phase permanent magnet synchronous motor with 7.5kW output power and 1500rpm rotation speed for industrial applications was carried out. After the first design, finite element analysis was made and the performance results of the motor were examined. The design was optimized and a second design was made in order to improve the cogging torque, efficiency, noise and vibration parameters. As in the first design, both electromagnetic and structural analyzes of the obtained second design were performed using the finite element method, the results were analyzed comparatively. With this final design, the targeted improvements were made in the determined parameters and the motor design with smaller volume, higher efficiency, lower cogging torque, torque ripple, noise and vibration compared to the motor that was originally designed was realized.

ACKNOWLEDGMENT

REFERENCES

[1] D. Hanselman, "Brushless Permanent Magnet Motor Design." Second Edition, 2006.
[2] J. F. Gıeras, "Permanent Magnet Motor Technology." Third Edition, 2010.
[3] Y. Xie, Y. Xia, Z. Li, F. Li, "Analysis of modal and vibration reduction of an interior permanent magnet synchronous motor." Energies 12(18): 3427, September 2019.
[4] Y. Wang, H. Gao, H. Wang, W. Ma, "NVH optimization analysis of permanent magnet motor by rotor slotting", Vehicles 2(2): 287-303, May 2020.
[5] S. Sathyan, U. Aydin, A.Belachen, "Acoustic noise computation of electrical motors using boundary element method", Energies 13(1): 245, January 2020.
[6] Helder Sá Alves da Silva, ''Design for Manufacture of Brushless Permanent Magnet Synchronous Servomotors'', 2014.
[7] M. Chabchoub, I. B. Salah, G. Krebs, R. Neji, C. Marchand, "PMSM cogging torque reduction: Comparison between different shapes of magnet ", First International Conference on Renewable Energies and Vehicular Technology, 2012.
[8] M. Rizwan, M. Arun Noyal Doss, ''Reduction of cogging torque in pmbldc motor with reduced stator tooth width and bifurcated surface area using finite element analysis'', 2011
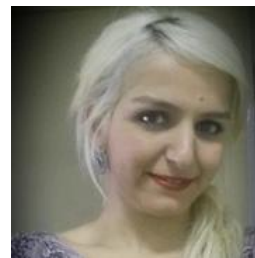
BIOGRAPHIES

ATAKAN ŞAHİN was born in 1995. He received the B.S. degree in electrical engineering from the Yıldız Technical University, İstanbul, in 2018. He has started M.Sc. at 2019 at Yıldız Technical University electrical engineering department, electrical machines and power electronics program.

He has been working at Gamak Makina Sanayi A.Ş R&D department as electrical design engineer since February 2019. His research and professional interests include: electrical motors design & optimization, advanced electromagnetic analysis, noise and vibration analysis, ac motor drives, electrical motors performance test systems.

YASEMİN ÖNER received the B.Eng., M.Sc., and Ph.D. degrees in electrical engineering from Yıldız Technical University, Istanbul, Turkey, in 2007, 2009, and 2013, respectively. She is currently Associate Prof. Dr. in Yildiz Technical University. Her research interests include analytical solutions for electrical machines.

Publication Ethics

The journal publishes original papers in the extensive field of Electrical-electronics and Computer engineering. To that end, it is essential that all who participate in producing the journal conduct themselves as authors, reviewers, editors, and publishers in accord with the highest level of professional ethics and standards. Plagiarism or self-plagiarism constitutes unethical scientific behavior and is never acceptable.

By submitting a manuscript to this journal, each author explicitly confirms that the manuscript meets the highest ethical standards for authors and coauthors

The undersigned hereby assign(s) to *Balkan Journal of Electrical & Computer Engineering* (BAJECE) copyright ownership in the above Paper, effective if and when the Paper is accepted for publication by BAJECE and to the extent transferable under applicable national law. This assignment gives BAJECE the right to register copyright to the Paper in its name as claimant and to publish the Paper in any print or electronic medium.

Authors, or their employers in the case of works made for hire, retain the following rights:

1. All proprietary rights other than copyright, including patent rights.
2. The right to make and distribute copies of the Paper for internal purposes.
3. The right to use the material for lecture or classroom purposes.
4. The right to prepare derivative publications based on the Paper, including books or book chapters, journal papers, and magazine articles, provided that publication of a derivative work occurs subsequent to the official date of publication by BAJECE.
5. The right to post an author-prepared version or an of ficial version (preferred version) of the published paper on an i nternal or external server controlled exclusively by t he author/employer, pr ovided that (a) such posting is noncommercial in nature and the paper is made available to users without charge; (b) a copyright notice and full citation appear with the paper, and (c) a link to BAJECE's official online version of the abstract is provided using the DOI (Document Object Identifier) link.

CONTENTS

BALKAN JOURNAL OF
ELECTRICAL & COMPUTER ENGINEERING

(An International Peer Reviewed, Indexed and Open Access Journal)